**UNIVERSITY OF SOUTHAMPTON**

FACULTY OF ENGINEERING, SCIENCE AND
MATHEMATICS

School of Ocean and Earth Sciences

# A High-Resolution Holocene Fault Activity History of the Aigion Shelf, Gulf of Corinth, Greece.

by

**Carol Jacqueline Cotterill**

This thesis is submitted for
**Doctor of Philosophy**

**July, 2006**

UNIVERSITY OF SOUTHAMPTON

# ABSTRACT

FACULTY OF ENGINEERING, SCIENCE AND MATHEMATICS

SCHOOL OF OCEAN AND EARTH SCIENCE

Doctor of Philosophy

# A HIGH RESOLUTION HOLOCENE FAULT ACTIVITY HISTORY OF THE AIGION SHELF, GULF OF CORINTH, GREECE.

by Carol Jacqueline Cotterill

The Gulf of Corinth is a continental rift in the western Aegean, Greece. It is the most active rift basin in Europe, with maximum N-S extension rates across the rift of ~15 mm yr$^{-1}$. The data presented in this thesis reveal the behaviour of the Aigion Shelf Fault, part of one of the active normal fault systems in the Gulf of Corinth, over the past ~12 kyr, using high-resolution seismic reflection and multibeam bathymetry datasets.

The Aigion Shelf Fault is part of an en echelon system comprising four basin bounding faults that control the southern margin of the Gulf of Corinth. It is a segmented, N-dipping normal fault, which overlaps and is active concurrently with the older Western Eliki Fault. It forms the southern boundary to a graben structure that narrows eastwards, which is bounded to the north by a S-dipping segmented fault. Approximately 500 m west of the shelf edge the graben geometry changes, with the Aigion Shelf Fault stepping north, and the S-dipping fault switching polarity to become N-dipping.

Sequence stratigraphic markers relating to the post-lowstand transgression and more recent progradational beach deltaics form the boundaries between three distinct seismic packages, enabling quantification of fault slip rates and changes in sediment deposition. Isopachs from five specific time periods show that the development of depocentres is predominantly controlled by faulting.

Displacement on the Aigion Shelf is distributed over a complex fault population. This is interpreted as a damage zone associated with the eastern tip of the Aigion Shelf Fault, formed through upward bifurcation of fault splays from a single structure at depth. The combined spatially averaged total slip rate for all the splays identified is $2.6 \pm 0.4$ mm yr$^{-1}$. The average vertical displacement rate on the Aigion Shelf Fault is ~$0.6 \pm 0.1$ mm yr$^{-1}$. Significant short-term spatial and temporal variability within the 12 kyr time period suggests the influence of segment boundaries, and periods of enhanced activity over 1 kyr timescales representing multiple earthquake cycles. Observation periods of >4 kyr are found to represent the longer-term displacement behaviour on the Aigion Shelf Fault.

The displacement profile of the Aigion Shelf Fault indicates that it is extends onshore. There is no apparent structural link between the main Aigion and Aigion Shelf Faults. However, a similarity in displacement rates and profiles suggest that both are immature structures that form part of the larger Aigion-Neos Erineos Fault system. Fault structure plots indicate that there has been no lateral fault growth over the Holocene, with burial and mortality of minor faults. Formation of growth wedges against both the Aigion Shelf Fault and S-dipping graben bounding fault indicate that the relative dominance of both faults has varied spatially and temporally.

**Graduate School of the**
**National Oceanography Centre, Southampton**

This PhD dissertation by

*Carol J. Cotterill*

has been produced under the supervision of the following persons

Supervisors

Dr. Lisa C. McNeill
Prof. Jonathan M. Bull
Dr. Timothy J. Henstock

Chair of Advisory Panel

Prof. Martin Sinha

Members of Advisory Panel

Dr. Lisa C. McNeill
Prof. Jonathan M. Bull
Dr. Timothy J. Henstock

# Contents

# List of Figures

# List of Tables

# DECLARATION OF AUTHORSHIP

I, **CAROL JACQUELINE COTTERILL**

Declare that the thesis entitled

**A High-Resolution Holocene Fault Activity History of the Aigion Shelf, Gulf of Corinth, Greece.**

and the work presented in it are my own. I confirm that:

- This work was done wholly or mainly while in candidature for a research degree at this University;
- Where any part of this thesis has previously been submitted for a degree or any other qualification at this University or any other institution, this has been clearly stated;
- Where I have consulted the published work of others, this is always clearly attributed;
- Where I have quoted from the work of others, the source is always given. With the exception of such quotations, this thesis is entirely my own work;
- I have acknowledged all main sources of help;
- Where the thesis is based on work done by myself jointly with others, I have made clear exactly what was done by others and what I have contributed myself;
- Parts of this work have been published as ;
  McNeill, L. C., Cotterill, C. J., Henstock, T. J., Bull, J. M., Stefatos, A., Collier, R. E. Ll., Papatheodorou, G., Ferentinos, G., and Hicks, S. (2005). Active faulting withi the offshore Gulf of Corinth, Greece: Implications for models of continental rift deformation. *Geology*, **33(4).** 241-244.

Signed:

Date:

# Acknowledgements

I would like to thank all the people who have made this thesis possible. In particular I would like to thank my primary supervisor, Lisa McNeill, for all her help, support and guidance throughout the past three years. I am also indebted to my other supervisors Jon Bull and Tim Henstock for their guidance and comments. I would also like to thank Richard Collier for his patience and assistance with my initial interpretations of the stratigraphy.

I am very grateful to all those involved with the data collection. Thanks to the crew of the R.V. Vasillios G, and to Aris Stefatos, George Ferentinos, George Papatheodorou and Aggeliki Georgiopoulou for acting as interpreters, and sharing their knowledge of the area. Thanks also to John Davies for his technical support and box packing skills!

And to my friends, my deepest thanks for sticking by me through the tough times. Without the encouragement and support, this process would have been so much harder. So thanks to Fletch, Charlie, Kate and Sam for always being there; to Squirrel for the early morning swimming sessions that made me realise there are worse things than writing up; to Lizzie, Zoe and Hannah for providing the light relief; and to Ele for her wise words that kept me sane!

And to my mother – thank you for your constant belief in me.

This work was funded by the Natural Environment Research Council (NER/B/S/2001/00269).

# Chapter 1

# Introduction

The development of continental rift zones has generated much investigation into, and debate concerning, distributions of extensional strain, tectonic evolution, normal fault geometry and interaction between different fault segments. Understanding fault geometry and displacement patterns, and the impact of interaction between different fault systems, is important when considering the mechanisms driving continental rifting, and the associated hazards from seismic activity and mass wasting / liquefaction for the coastal areas of rift zones.

By the nature of fault growth, through segment linkage or lateral propagation, a system may pass through numerous developmental stages. These stages are often ephemeral, leaving little indication as to how the geometry and displacement history of the fault system changed and evolved. However, high-resolution studies using stratigraphic analysis can help resolve changes in fault slip rates and geometry through space and time (e.g. Taylor et al., 2004; Bull et al., in press; Lamarche et al., in press).

With the data used in this thesis, it is possible to analyse the development of a fault system, looking at dominance of particular faults and segments, and investigating the evidence for both lateral and vertical growth, as well as looking at the interplay with surrounding fault systems. The data considered in this thesis come from a high-resolution seismic reflection survey, multibeam bathymetry survey and onshore geological fieldwork, conducted in the western to central Gulf of Corinth, Greece. The Gulf of Corinth is the most rapidly extending continental rift basin in Europe at the present time. There is a well-defined border fault system which controls the southern shoreline of the rift, creating a dramatic topography of uplifted footwall blocks. Re-working of deltaic sediments, uplifted in the footwalls of older faults, has provided a constant supply of sediments into the developing rift, ensuring that current fault activity in this developing rift basin has been recorded at a resolution enabling interpretation of fault evolution over both short-term and longer-term periods of observation (c.$10^2$ -$10^5$ years).

Previous studies conducted in the Gulf of Corinth have established approximate slip rates for the major faults (e.g. Armijo et al., 1996; McNeill and Collier, 2004). However, little is known about the potential variability in these rates, and the timescales over which this may occur, although authors including Pirazzoli et al. (1994), McNeill and Collier (2004) and Leeder et al. (2005) do indicate that displacement rates appear to have increased in the Holocene. It is also accepted that the faults in the Gulf of Corinth are formed of linked segments, and yet little is known about the scales of segmentation, and how quickly linked segments begin to behave as a coherent unit (Stewart and Vita-Finzi, 1996; McNeill and Collier, 2004).

This study will concentrate on the evolution of one major basin bounding fault system located along the southern margin of the Gulf of Corinth. The morphology and surface geometry of the fault, as well as the displacement profile, suggest that it is an immature system. A high sediment supply rate to the offshore Aigion shelf, where the fault is thought to extend towards the east, has created a high-fidelity, well-defined stratigraphic record of displacement associated with part of the Aigion Fault system over the past ~12 kyr.

Clear laterally extensive horizons, showing significant offset from the major faults, were mapped using high-resolution multichannel seismic reflection data. This record, combined with shallow survey depths of <80m across the shelf allowing acquisition of high quality high-resolution datasets, made it an ideal location for studying short-term (1000’s years) variations in fault activity, offering a unique insight into fault movements; firstly in an area where little is known about the developmental stages of basin bounding fault systems, and secondly over a short timescale (thousands of years), which is rarely considered when looking at well developed fault systems.

The aims of this thesis are to provide a detailed analysis of changes in fault behaviour and fault geometry over various discrete time periods within the past ~12ka. The seismic stratigraphy imaged enables a thorough analysis of sediment deposition patterns, highlighting areas of thickening / thinning of units, and the relationship to the faults. Through this it is possible to track changes in fault geometry and displacement, and determine whether or not faulting or sedimentation processes dominated.

It is also possible to determine vertical displacement rates, and thus slip rates, from the multichannel seismic reflection data, in addition to producing along strike displacement profiles. This enables a comparison between the offshore Aigion Fault system, and the onshore Aigion Fault system, as well as other faults within this part of the rift, to be carried out. (A thorough analysis of possible errors has ensured that a true representation of short-term fault displacement variability has been produced in this study). The ability to compare the geometry and displacement activity of the Aigion Fault with other regional faults means that for the first time, it will be possible to understand the differences in behaviour between an established border fault, and an evolving immature fault. What is particularly unique about this location is that the young Aigion Fault appears to have significant overlap with the still active, mature Western Eliki Fault, providing an excellent opportunity to assess the interaction between the two systems.

This chapter will establish the regional geological and tectonic history of the Aegean region; précis structural and extensional behaviour in the Gulf of Corinth; and review current thinking regarding normal fault populations, encompassing fault geometry and fault system development (including growth and propagation), before summarising the thesis structure.

## 1.1 REGIONAL GEOLOGY

### 1.1.1 Regional Tectonic Setting

The tectonic history of the Aegean region is complex. Figure 1.1 shows a simplified illustration of the major plate motions, illustrating the location of the Gulf of Corinth. Northward movement of the African plate resulted in subduction beneath the Eurasian plate, beginning at approximately 60 Ma, with a current N-S convergence rate of 1 cm yr$^{-1}$ (e.g. Hatzfeld, 1994; Armijo et al., 1996). Teleseismic travel time tomography (e.g. Spakman et al., 1988; Hatzfeld, 1994; Tiberi et al., 2000 and 2001) and studies of microseismicity (e.g. Papazachos et al., 2000) have imaged the subducting African plate, moving from shallow subduction to steeply plunging, beneath the Gulf of Corinth.

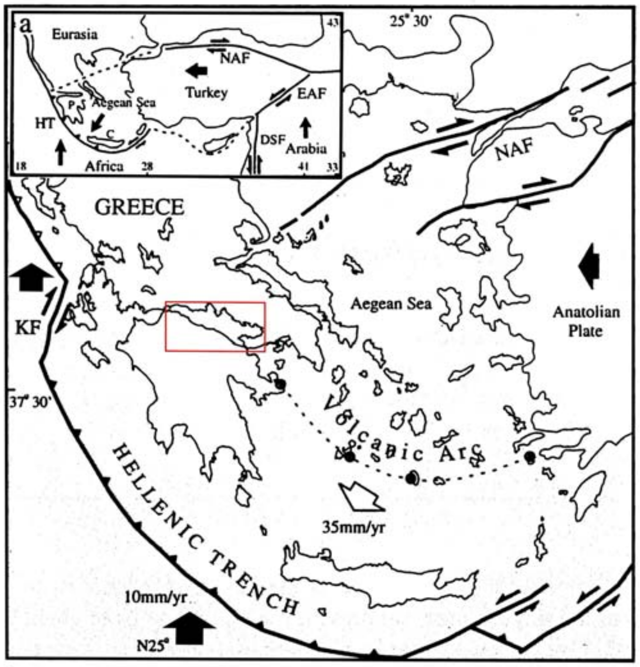

**Figure 1.1:** Map illustrating the movements of the main tectonic plates relative to the stable Eurasian Plate. Red Box indicates the location of the Gulf of Corinth. NAF = North Anatolian Fault, EAF = East Anatolian Fault, KF = Kefallonia Fault, DSF = Dead Sea Fault, P = Peloponnesus, C = Crete. (After Doutsos and Kokkalas, 2001).

Movement of the Arabian plate northwards has caused compression around the Black Sea (McClusky et al., 2000), resulting in a westerly extrusion of Turkey, relative to the Eurasian plate. This movement is currently taken up along the dextral strike-slip North Anatolian Fault (NAF), and results in the south-westerly movement of the Aegean-Anatolian microplate, relative to the Eurasian plate (Taymaz et al., 1991; Hatzfeld, 1994; Doutsos and Kokkalas, 2001). The northward moving African plate began to subduct underneath the south-westerly extruding Aegean-Anatolian microplate at ~13 Ma. Current NE-SW relative convergence rates of 3–5 cm yr$^{-1}$ have been measured at the Hellenic trench, (Davies et al., 1997).

## Rift Localisation

Approximately 15 Ma, the Hellenic Belt collapsed, possibly due to gravitational instabilities (Armijo et al., 1996; Tiberi et al., 2000). It is hypothesised that this created necking axes orientated E-W / ENE-WSW, resulting in pinch and swell structures. This, combined with thinning of the lithosphere due to back-arc extension (Doutsos et al., 1988), may have resulted in rift localisation and the initial formation of back-arc grabens, including the Gulf of Corinth and the Evvia Basin (Briole et al., 2000).

Extension has been occurring in the back-arc region of the Hellenic trench since ~10 Ma (e.g. Armijo et al., 1996). By ~1 Ma, it is hypothesised that the process zone caused by the transtensional stresses and deformation pattern from the laterally propagating NAF encompassed the Gulf of Corinth (Armijo et al., 1996; Armijo et al., 1999; Flerit et al., 2004) accelerating extension, however evidence of such an acceleration has not been confirmed by field studies.

However, there is also a disparity between areas of crustal instability established in the Miocene and the actual path taken by this rift basin as it has propagated over time (Tiberi et al., 2000) (Figure 1.2). Tiberi et al. (2000) believe that rupture may have initiated in the thinned crust found in the eastern Gulf, but instead of rupturing continuing along the original NW orientation, the rift began to propagate in a more westerly orientation due to the influence of the underlying geological nappe, possibly associated with the Hellenides.

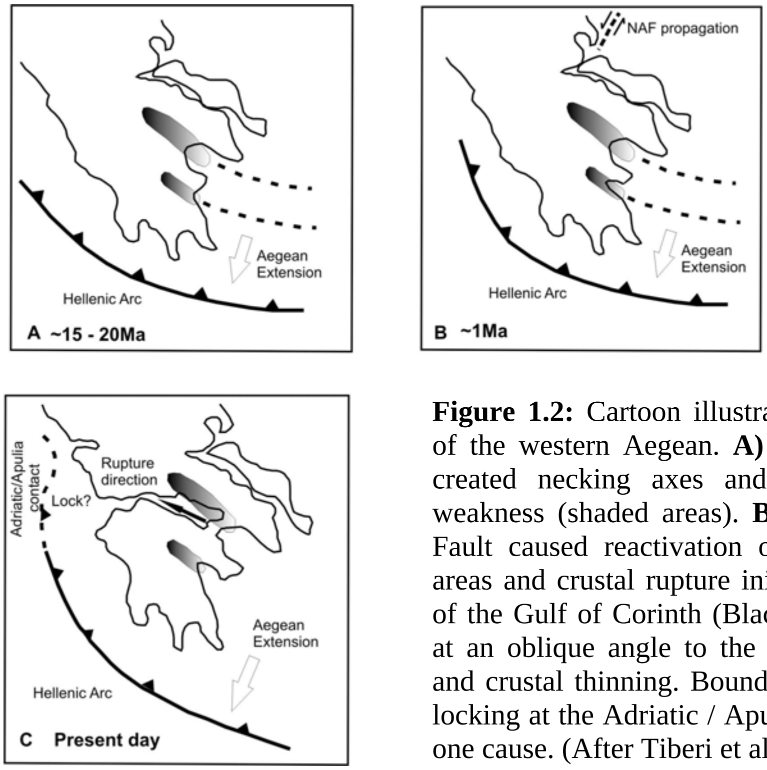

**Figure 1.2:** Cartoon illustrating the evolution of the western Aegean. **A)** Aegean extension created necking axes and areas of crustal weakness (shaded areas). **B)** North Anatolian Fault caused reactivation of these weakened areas and crustal rupture initiated. **C)** Rupture of the Gulf of Corinth (Black arrow) occurred at an oblique angle to the areas of weakness and crustal thinning. Boundary conditions and locking at the Adriatic / Apulia contact may be one cause. (After Tiberi et al., 2001).

### 1.1.2 The Gulf of Corinth

The Gulf of Corinth, Greece, is situated at the western margin of the Aegean extensional province (Figure 1.1), within one of the most actively extending and highly seismic regions globally, (e.g. Le Pichon and Angelier, 1981; Armijo et al., 1996; Briole et al., 2000). The gulf trends N120°E and is 110 km long and 30 km across at its widest point (Figure 1.3). Using gravity inversion and teleseimic tomography, Tiberi et al. (2000) and (2001) describe perturbations such as boudinage features and crustal thinning in the eastern Gulf. Crustal thickening in the western Gulf occurred as an isostatic response to building of the NW-SE trending Hellenides. There is therefore an E-W gradient in crustal thickness along the Gulf, ranging from 25 km in the east to 40 km in the western Gulf (Tiberi et al., 2001).

The central-western Gulf obliquely cuts N160° trending folds and thrusts associated with the Hellenide Orogeny (Doutsos and Poulimenos, 1992; Armijo et al., 1996; Sorel, 2000). Therefore, the extensional topography overprints that of the Hellenic Belt / Alpine evolution fabric, suggesting that rifting here began post 15 Ma, i.e. after the formation of the Hellenides. It has previously been described as an asymmetric half graben for most of its length, with a north-dipping en-echelon border fault system, (BFS), dominating the topography along the southern coastline (Armijo et al., 1996). However, seismic profiles presented by Stefatos et al. (2002), McNeill et al. (2005a), and conclusions drawn by Moretti et al. (2003), show that the fault geometry is more complex. The asymmetry of the Gulf alters along its length, becoming more graben-like in the central Gulf before reversing polarity in the western Gulf (Figure 1.4) (McNeill at al., 2005). Figure 1.4, profile F, illustrates this, and is supported by multichannel seismic reflection profiles collected by McNeill et al. (2005a) (see Chapter 3, Figure 3.3).

Seismic stratigraphic data suggests that the geometry of the rift has changed with time (Sachpazi et al. 2003). The central Gulf was initially controlled by a S-dipping fault on the northern margin, however the symmetry shifted, with a N-dipping fault on the southern margin taking over, producing a symmetrical graben rather than the half-graben geometry. They suggest that the southern basin bounding faults are now controlling extension, activating over time in an east to west progression.

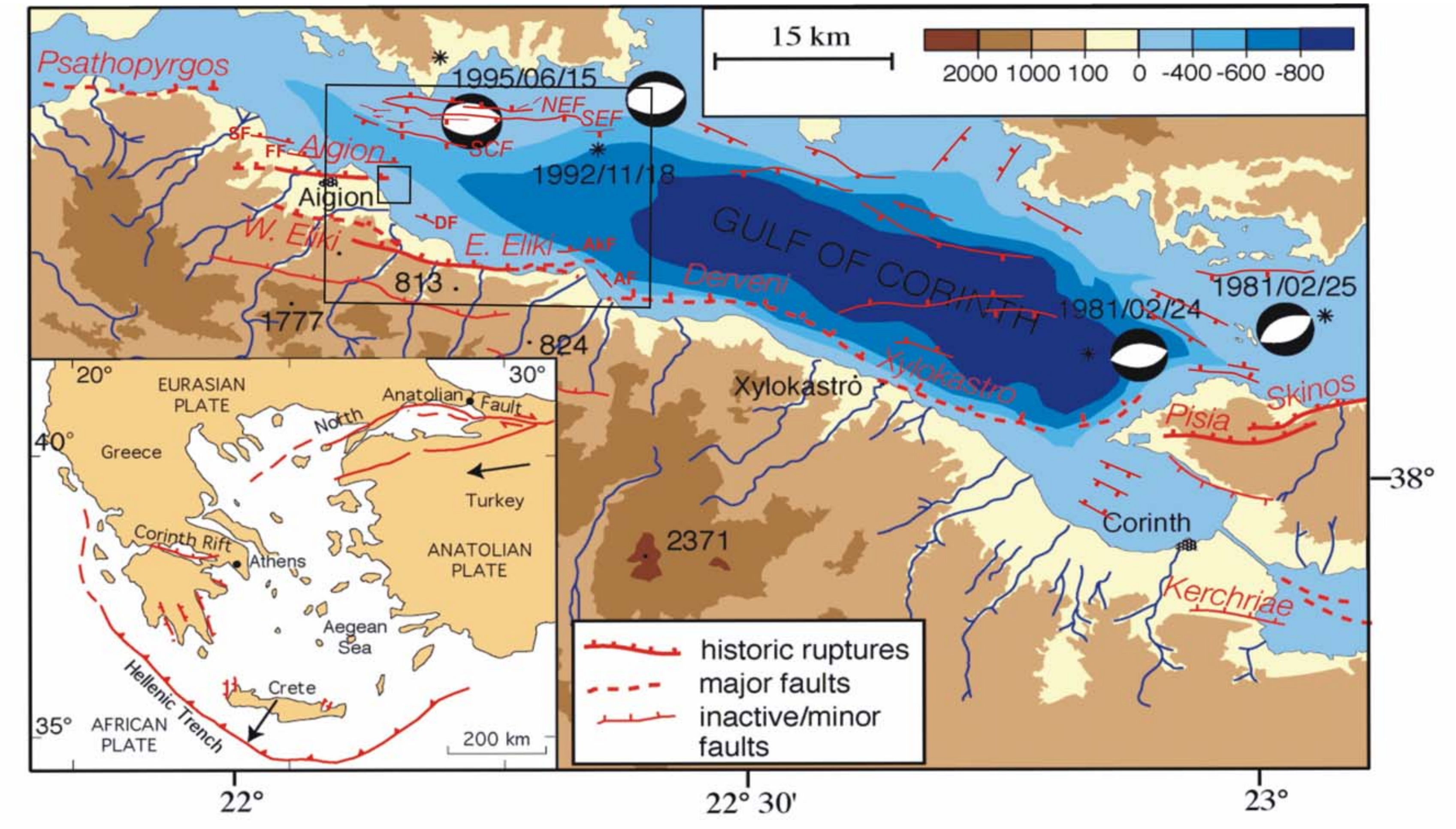

**Figure 1.3:** Map of the Gulf of Corinth with inset showing its location within the Aegean tectonic regime. Black boxes indicate the location of the regional survey (Chapter 3) and the detailed Aigion survey (Chapters 4 - 7). Faults from McNeill et al. (2005a); Stefatos et al. (2002); Palyvos et al. (2004).FF = Fassouleika Fault; SF = Selianitika Fault; DF = Diakopta Fault; AkF = Akrata Fault; AF = Aegira Fault. Focal mechanisms from Taymaz et al. (1991) and Bernard et al. (1997). Modified from McNeill and Collier (2004).

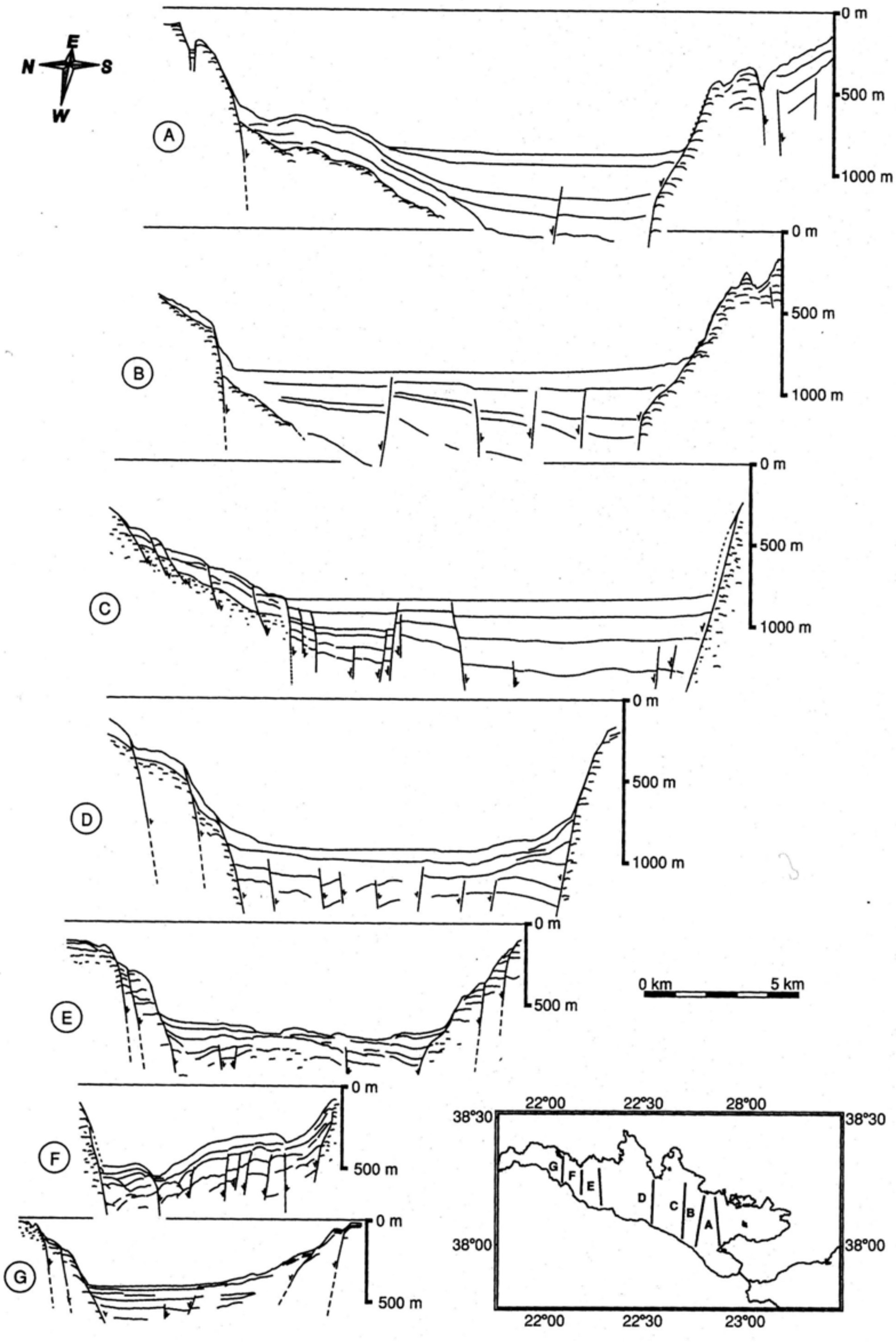

**Figure 1.4 :** Cross sections taken across the Gulf of Corinth show the change in structural geometry. A – C show a half graben geometry with the dominant faults lying to the south. D & E show a more symmetrical profile, whilst F & G show a shift in polarity of the graben, with the dominant faults now lying to the north. (from Stefatos et al., 2002).

Major offshore faults in the western Gulf (McNeill et al., 2005a) show wedge shaped sedimentary growth strata deposited during the Quaternary, and evidence of subsided paleoshorelines. Both of these features can be used to quantify regional fault development and fault displacement rates (Chapter 3).

Briole et al. (2000) believe that the zone of deformation in the Gulf of Corinth varies east to west, from a diffuse zone at the eastern end through a central zone, ~15-20 km, wide to a narrow zone, ~10-15 km, wide in the western Gulf, located in the offshore Gulf. However, whilst deformation in the offshore rift may be superficially narrower, it is known that there is significant active fault deformation onshore in the western Gulf. This would indicate that although the offshore deformation zone is narrower, the total deformation zone is similar to that observed across the eastern Gulf.

The gulf displays continental shelf, slope and abyssal plain provinces, reaching a maximum depth of ~820 m (e.g. Heezen et al., 1966; Stefatos et al., 2002). The southern side displays delta-front-slope-fan-apron and river-canyon-fan deposits, whilst the relatively sediment starved northern side has gentler slopes and elongated slope deposits (e.g. Leeder and Gawthorpe, 1987; Ori, 1989; McMurray and Gawthorpe, 2000). High resolution seismic surveys have revealed an axial channel that is fed by numerous canyons from the southern side, and ponding of sediments against major S-dipping offshore faults located on the northern margin of the western Gulf of Corinth (Stefatos et al., 2005; McNeill et al., 2005a).

### 1.1.3 Extension in the Gulf of Corinth

Surveys indicate that back-arc extension in this region is primarily concentrated across the Gulf of Corinth, with networks north of the gulf indicating significantly lower strain rates being accumulated (Ambraseys & Jackson, 1997; Clarke et al., 1998). The Gulf shows an average N-S geodetically measured extension rate of ~10 mm $yr^{-1}$. However, rates vary significantly along the length of the gulf (e.g. Billiris et al., 1991; Davies et al., 1997; Clarke et al., 1998), with Clarke et al. (1997) estimating 4 mm $yr^{-1}$ extension in the east, compared to a maximum recorded extension of 15 mm $yr^{-1}$ in the western Gulf (Briole et al., 2000). Measurements of seismic strain release conducted over the same monitoring period as the GPS surveys, although commensurate in the eastern gulf, can only account for 20-50% of the GPS extension observed in the western Gulf (e.g. Davies et al., 1997). Likewise, calculations of slip on major onshore faults in the western Gulf can only account for 20 – 50% of the geodetic extension (e.g. De Martini et al., 2004; McNeill & Collier, 2004).

Various hypotheses have been put forward to explain the discrepancy between GPS observed extension rates and the measured extension resulting from both coseismic and aseismic release on the major faults. These include a decrease in the seismogenic layer thickness from east to west (Rigo et al., 1996; Clarke et al., 1998); an increase in the contribution of smaller faults, hosting earthquakes of Ms<6 in the western Gulf, (Papatheodorou & Ferentinos, 1997); the influence of the observation period within the seismic cycle, with impending seismic release balancing the measurements out (Clarke et al, 1998); or contribution to extension from un-accounted for offshore fault systems (Briole et al., 2000). The greater extension rates are accommodated on either a low-angle detachment fault, resulting from the disparity between the direction of rift propagation and the orientation of weakened crust (e.g. Rigo et al., 1996; Tiberi et al., 2000), or as a result of flat slab subduction and trench rollback (Sachpazi et al., 2003; Leeder et al., 2003).

Billiris et al. (1991); Davies et al. (1997) and Clarke et al. (1998) all found that the GPS networks used in their studies were unable to resolve strain rates < 2 x $10^6$, with the network spacing representing twice the spacing of active faults. This means that the geodetic data are unable to distinguish local activity around individual faults, and so can only provide an overview of extensional activity. Therefore it is possible that the calculation of seismic release from major faults is omitting the contributions from smaller faults that the geodetic surveys include.

### 1.1.4 Faulting in the Gulf of Corinth

The southern side of the gulf is controlled by a series of normal, en-echelon N-dipping faults (Figure 1.3) (e.g. Armijo et al., 1996; Hatzfeld et al., 1996; Tiberi et al.,

2001) (Figure 1.3). Five main segmented fault systems (Psathopyrgos, Aigion, Eliki, Derveni and Xylokastro) dominate the southern side of the Gulf, having total lengths of 15 – 25km (McNeill & Collier, 2004). There are also additional minor faults of between 3.3 and 10km in length, that also step in an en-echelon fashion (e.g. Diakopta, Akrata, Aegira, Selianitika and Fassouleika) proposed by Stefatos et al. (2002) and Palyvos et al. (2005) (Figure 1.3). These may be isolated fault systems, although Palyvos et al. (2005) believe that at least two of these five are linked to the Aigion Fault system at depth.

The northern side of the gulf displays minor onshore S-dipping faults, with a subsiding coastline and downward flexure (Armijo et al., 1996; Sorel, 2000; Stefatos et al., 2002). Major offshore S-dipping faults, controlling the northern margin, have been identified in the western Gulf (McNeill et al., 2005a).

Analysis of syn-tectonic sedimentation suggests that the oldest faults in the western gulf are of Pleistocene age (Sorel, 2000). Faulting on the southern side has migrated northwards over time, with faults deactivating and uplifting in the footwall of new faults (e.g. Dart et al., 1994; Sorel, 2000; Goldsworthy and Jackson, 2001). Gravity surveys indicate that the main depocentres in the gulf have remained stationary over time, relative to the north-stepping faulting (King, 1998). This suggests that the rift basin is narrowing with time despite continued regional extension, and not migrating northwards mirroring the movement of fault activity.

The Eliki Fault is a major fault in the western gulf, whose activity is well documented (e.g. Koukouvelas et al., 2001; Micarelli et al., 2003; McNeill & Collier, 2004; De Martini et al., 2004). It has two main segments, both of which are c. 15 – 20 km in length. Between them is a right-stepping transfer, located at the Kerynitis River (Figure 1.5). Displacement on the two segments appears uniform, with no obvious lows associated with the transfer zone, as indicated by uplifted marine terraces (McNeill and Collier, 2004). These terraces, the oldest of which is proposed to be ~500 ka, based on the correlation between sea-level curves and uplift rates on the oldest dated terrace (~200 ka) indicate that this is a well established, major basin bounding fault. However, extension on the Eliki Fault of 2-4 mm yr$^{-1}$ can only account for <30% of the 15 mm yr$^{-1}$ geodetic extension measured (McNeill and Collier, 2004).

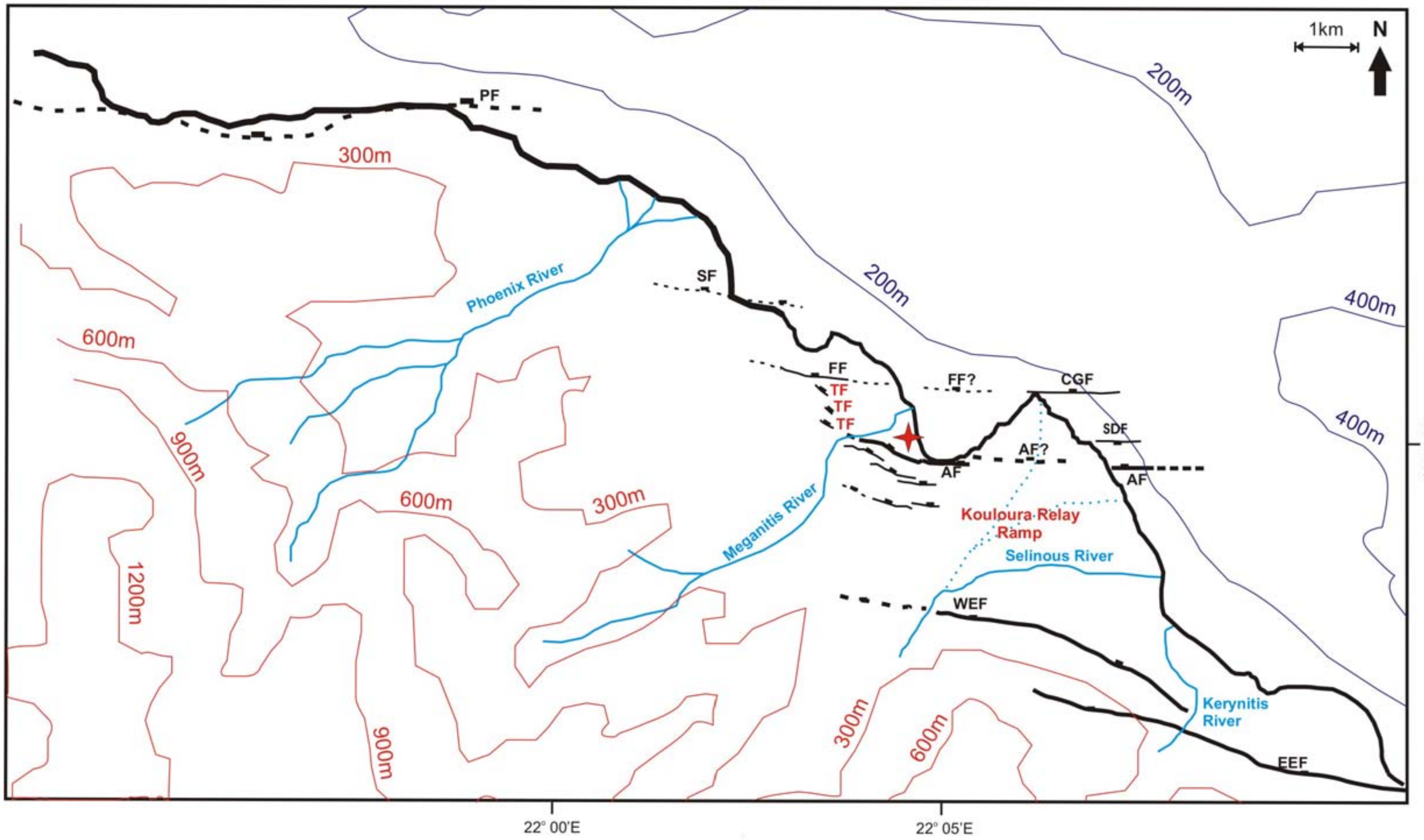

**Figure 1.5:** Location map showing the relative position between the mapped onshore fault systems and the offshore fault imaged in this study. The red star indicates the location of the onshore borehole AIG10.

AF = Aigion Fault (Koukouvelas, 1998; Palyvos et al, 2005); FF = Fassoulieka Fault, SF = Selenitika Fault, TF = transfer fault zone, PF = Psathopyrgos Fault (Palyvos et al, 2005); EEF & WEF = Eastern and Western Eliki Fault (McNeill and Collier, 2004); CGF = Cape Gyftissa Fault (McNeill et al, 2005); SDF = S-dipping fault imaged during this study.

### 1.1.5 Aigion Fault

The Aigion Fault is one of the en-echelon, roughly east-west striking, N-dipping normal faults that border the southern Gulf of Corinth (e.g. Palyvos et al., 2005) (Figure 1.3). Correlation of marine terraces uplifted in the footwall of the Aigion Fault to known dates (De Martini et al., 2004), gained through dating of corals and bivalves, suggest the fault is a young (<0.5ka). This is supported by both the morphology and geometry of the fault.

It has been proposed that the onshore fault consists of three segments (Koukouvelas & Doutsos, 1996; Koukouvelas, 1998), although the existence and position of the eastern-most of these three segments is difficult to confirm as there is no topographic expression. The mapped trace of the topographically distinct onshore Aigion Fault is ~10 km long in total, with a defined scarp reaching ~150 m height in the town of Aigion (Koukouvelas, 1998; Pantosti et al., 2004;). Offshore, there is a possible extension of the Aigion Fault, of ~1.5 km in length (this study; Stefatos et al., 2002; Pantosti et al., 2004; McNeill et al., 2005a). The onshore surface trace exhibits a dip of between 50-60$^o$ (De Martini et al., 2004; Pantosti et al., 2004; Rettenmaier et al., 2004).

The Aigion Fault is located ~4 km north of the Western Eliki Fault (Figure 1.3 & Figure 1.5), and is active concurrently with the Western Eliki Fault (De Martini et al., 2004). However, it is not known whether changes in displacement rates and growth associated with the maturing of the Aigion Fault are resulting in a gradual decline of activity on the Western Eliki Fault, or whether both systems are maintaining their slip rates.

The displacement profiles of the Eliki and Aigion Faults suggest that there is significant variation between them. McNeill and Collier (2004) show relatively uniform uplift over much of the Eliki system, based on the constant elevation of a marine terrace, with slight tapering off of displacement towards the tips. Initial analysis of displacement on the Aigion Fault indicates that it has a regular increase in displacement towards a central point of maximum displacement (Chapter 6; Micarelli et al., 2003). Possible explanations for this apparent change in fault displacement behaviour may be that the

Aigion Fault is a relatively immature fault and we are still seeing development of the length / displacement relationship; or that there is an inherent structural fabric that causes the faulting style to alter at this point.

Marine terraces uplifted in the Aigion footwall suggest long-term uplift rates for the onshore fault of 1.05–1.2 mm yr$^{-1}$ (De Martini et al., 2004; Pantosti et al., 2004). However estimated slip rates range from 2-7 mm yr$^{-1}$ (McNeill and Collier, 2004; McNeill et al., 2005b) to 9-11 mm yr$^{-1}$ (De Martini et al., 2004). The discrepancy between the two sets of slip rates is primarily due to the uplift:subsidence ratios used. McNeill and Collier (2004) used an uplift:subsidence ratio of 1:2-3.2, whilst De Martini et al. (2004) used a ratio of 1:3, as identified by Pantosti et al. (2004). Koukouvelas (1998) however, suggest a ratio of 1:2 for the Aigion Fault; Armijo et al. (1996) suggest 1:2.7-3.5 for the border faults; King (1998) suggest 1 : 2.2-2.6; and Collier (unpubl. data) suggest a ratio of 1 : 2 – 2.6 for the Skinos Fault in the eastern Gulf of Corinth. The ratios are predominantly based on correlations between uplifted marine terraces, available dated samples and the sea-level curve, therefore significant variations within the interpretation of data by different authors can impact on later slip rate calculations.

Palyvos et al. (2005) document NW-SE trending transfer faults linking the western Aigion Fault to the Fassouleika Fault - one of two intermediate faults that lie between the major N-dipping Aigion and Psathopyrgos Fault systems (Figure 1.5). No transfer structures have been documented at the eastern offshore tip of the Aigion Fault however. Koukouvelas and Doutsos (1996) suggest that the significant overlap between the Aigion and Western Eliki Faults (~5 km) causes tilting of the delta between them, which they have called the Kouloura Relay Ramp.

The presence of a CORSEIS Borehole (AIG10) situated in Aigion (Figure 1.5) has provided syn-rift sedimentological data from the hangingwall of the Aigion Fault, penetrating the fault plane at a depth of ~760 m (Rettenmaier et al., 2004; Lemeille et al., 2004). Bore-holes/cores located in the offshore footwall of the Aigion Fault show the stratigraphy to a maximum depth of ~60 m (Schwartz & Tziavos, 1979; Soter et al., 2001). Both provide a means to correlate the seismic stratigraphy imaged in this study with sedimentary units that have been described, and in some cases, dated.

### 1.1.6 Seismic Hazards

Understanding the nature of segmentation along the Aigion Fault, changes in behaviour and fault geometry following linkage of segments, and whether or not segment boundaries act as impediments inhibiting full surface rupture along the fault trace, may further the understanding of how earthquake events affect this vulnerable coastal area.

Both historical and modern records detail evidence of numerous earthquakes, resulting in hazards such as liquefaction, tsunami inundation, landslides, coastline change, ground fissures / cracks, building damage, and gas or fluid expulsion through sand volcanoes, that have affected the Aigion area (e.g. Lekkas et al., 1996; Papatheodorou & Ferentinos,1997; Soter, 1999 and Hasiotis et al., 2002) including 373BC, 1861AD, 1888AD and most recently 1995AD. Ancient historians reported that the earthquake in 373BC caused the submergence of the ancient town of Heliki, located to the SE of modern day Aigion, due to fault subsidence (Lekkas et al., 1996). Schmidt (1875) reported the effects of the 1861 earthquake on the Eastern Eliki Fault, indicating that liquefaction was a major hazard in this region. Lekkas et al. (1996) and Koukouvelas (1998) reported up to 10 m of coastline retreat, liquefaction and numerous ground fissures associated with the 1995 Aigion earthquake, which occurred on an offshore fault. As the coastal population and agricultural and industrial activity have grown, the potential effect of seismic hazards linked to coseismic activity has become increasingly severe.

Paleoseismological trenching on the western section of the onshore Aigion Fault trace has yielded an earthquake recurrence interval of ~360 years (Pantosti et al., 2004). This fits with data published by Collier et al. (1998) for the Skinos Fault in the eastern Gulf, where a maximum recurrence interval of 330 years was established. However, deformation modelling by Briole et al. (2000) calculated recurrence intervals of 250 ± 50 years across the Eliki / Aigion Faults and 70 ± 10 years for the offshore faults in this area. The second interval appears to be remarkably accurate when compared to other studies, and may represent analysis of data that only covers a small period of the seismic cycle, instead of providing a representative overview of long-term activity.

The model presented by Briole et al. (2000) also indicates that ~70% of energy released from earthquakes at the longitude of Aigion occurs offshore, supporting the previously discussed hypothesis that significant deformation occurs offshore in the western Gulf (Briole et al., 2000; McNeill et al., 2005a).

### 1.1.7 Extension on a Low Angle Detachment Fault?

It has been debated by many authors (e.g. Rigo et al., 1996; Tiberi et al., 2001; Gautier et al., in press) that the increase in measured geodetic extension in the western Gulf is accommodated on a low-angle detachment fault (Figure 1.6) onto which high-angle faults such as the Aigion Fault sole.

Dips of normal faults in the Gulf of Corinth are generally between 50-60$^o$, with movement on dips less than this generally being attributed to aseismic activity (e.g. Jackson, 1987). Fault plane solutions generally show 45-60$^o$ dipping fault planes in the Gulf (e.g. Jackson et al., 1982; Roberts & Jackson, 1991; Hatzfeld et al., 2000; Gautier et al., in press). However, some authors suggest that focal mechanisms indicate this may decrease to ~30$^o$ in the west (Rigo et al., 1996; Hatzfeld et al., 1996), with microseismicity dipping northwards at ~15$^o$. Ambiguity in the interpretation of fault plane mechanisms however makes it difficult to distinguish between the 30$^o$ and 60$^o$ planes, indicating that the apparent decrease in proposed fault dips in the west may be misleading.

Teleseismic modelling of the 1995 Aigion earthquake gave a S-dipping angle at depth of 33$^o$ with an error of 12$^o$, but the authors note that a good fit can only be produced when relaxing the hypocentral depth constraints (Bernard et al., 1997). This suggests that seismic activity on low-angle normal faults may occur in the western gulf. Results obtained by Gautier et al. (in press) suggest that there is a defined N-dipping low-angle surface underneath the Gulf (Figure 1.6). Projecting the Aigion and Eliki Fault planes down to depth sees them soling onto this structure at ~8 km depth (Gautier et al., in press). It is possible for normal faults that sole onto a detachment fault to deactivate as extension continues, and new faults activate, as a result of fault block rotation and locking.

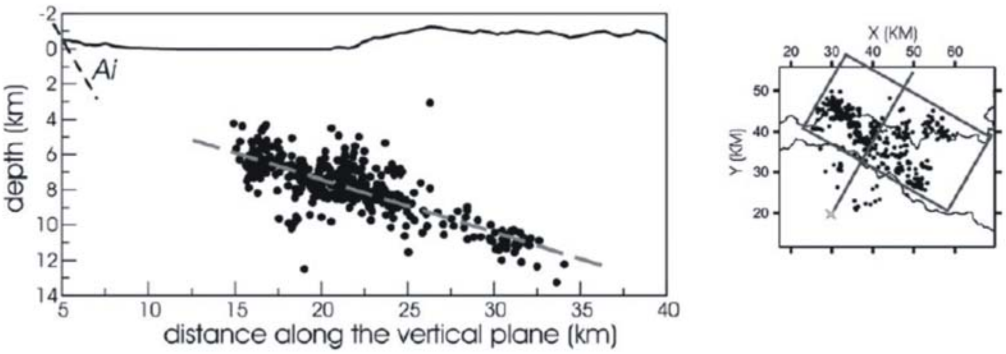

**Figure 1.6:** Illustration of the spatial distribution of seismicity in the western Gulf of Corinth, showing the location of the Aigion Fault relative to the events. Dashed grey line shows a linear regression, and suggests the presence of a low-angle detachment; Ai = Aigion Fault (Gautier et al., in press).

However, if faulting is distributed across the western Gulf on a number of offshore faults that have similar slip rates to the Aigion and Eliki Faults (McNeill et al., 2005a), the discrepancy between the geodetic extension and the fault related extension can be accounted for without a low angle detachment fault. In this case the microseismicity may represent the transition between the brittle and ductile layers in the crust instead of marking a low-angle detachment.

## 1.2 NORMAL FAULT BEHAVIOUR

Normal faults forming in rift environments commonly experience rapid (<1 Ma) changes in behaviour, including episodes of intense activity followed by periods of quiescence, spatial migration of activity between sub-parallel faults, and strain partitioning resulting in temporary and permanent inactivity (Jackson, 1999; Goldsworthy and Jackson, 2001). They commonly exhibit a wide range of trace lengths, often being composed of many linked segments (e.g. Trudgill and Cartwright, 199l; Machette et al., 1991). Analysis of syn-tectonic sedimentation and stratigraphic depocentres laid down throughout the evolution of a fault population can help interpret the temporal development of a system, addressing issues such as do length displacement ratios remain constant or fluctuate throughout fault development, how does segmentation and linkage affect fault behaviour, and how/when does strain localisation and partitioning occur across a system.

### 1.2.1 Fault Populations

Crustal strain in extensional regimes is often accommodated by fault populations, comprising numerous faults ranging in fault size (over several orders of magnitude), and degree of connectivity (e.g. Walsh et al., 2001). In many cases there appears to be a power-law relationship in fault populations between size and frequency (e.g. Scholz and Cowie, 1990; Walsh et al., 1991; Cartwright et al., 1995; Yielding et al., 1996), modelled by:

$$N \geq {}_{S} = cS^{-D} \tag{1.1}$$

Where S = maximum length or displacement of a fault, D = fractal dimension of a fault population, c = size of the sample being analysed and $N \geq_{S}$ = number of faults in that population having a size equal to or greater than S.

Faults that are part of the same population will generally maintain a similar length/displacement scaling relationship (Cowie and Scholtz, 1992). The power-law relationship is also useful in estimating the contribution of unobserved faults within an area due to the effects of “truncation” and resolution limitations (Scholz and Cowie, 1990; Yielding et al., 1996). Truncation occurs when either large scale faults are omitted from the survey sample or smaller faults lie below the resolution limits of the survey method.

It has been observed that young fault populations will have significantly greater numbers of smaller magnitude faults. However, as a fault system matures, and accrues displacement and length through segment linkage or radial propagation, the power-law relationship either ceases as strain localises onto a single dominant fault causing mortality of minor faults (Nicol et al., 1997; Walsh et al., 2001; Walsh et al., 2003a), or the power-law exponent decreases as fault strain increases on a smaller number of larger faults (Cladouhos and Marrett, 1996).

Meyer et al. (2002) analysed a fault population from the Timor Sea, where extensional faulting began ~6 Ma. They document rapid initial extension over the initial 1 – 2 Myr of rifting, during which individual faults rapidly established their initial lengths, which then remained relatively constant. Most of the faults reached 80% of their final length during this early period, but only accrued between 10-30% of their final displacement, so presenting an under-displaced profile. The second phase encompassed accrual of displacement and minimal lateral propagation, with strain localisation occurring during a third phase, causing mortality of minor faults and a concentration of regional strain across fewer larger faults. By the youngest mapped horizon (1.3 Ma), ~2/3 of the original faults mapped at the start of extension had disappeared.

Walsh et al. (2003a) analysed data from the northern North Sea. The fault population power-law relationship was found to develop a non-power law "tail" on each younger horizon, coinciding with the linkage of some faults into larger systems spanning the survey area, and subsequent mortality of the smaller faults. Strain localisation occurred over a ~10Myr period.

The Meyer et al. (2002) and Walsh et al. (2003a) studies show the effects of strain partitioning across a system, associated with linkage and fault segmentation. They also indicate that length / displacement ratios may vary substantially over the evolution of a fault system.

In the study area, there are numerous faults on the Aigion Shelf, ranging in both size and length. It is therefore important to ascertain whether they are part of the same population, and inter-connected, or whether they are behaving independently of each other. Therefore any variability between the displacement rates calculated in this detailed short-term study (Chapter 6) and longer-term rates suggested for the more established faults (e.g. Armijo et al., 1996; McNeill and Collier, 2004) may identify a transitory stage of fault development.

### 1.2.2 Fault Growth - Propagation and Linkage

Faults typically grow through radial propagation and/or segment linkage. Lateral growth on isolated faults can occur as a result of both coseismic and aseismic release (e.g.

Walsh and Watterson, 1987), increasing both displacement and length proportionally. However, faults often interact and link to form larger complex systems. In this scenario, growth will not only be governed by seismic activity and aseismic creep, but also by the kinematics involved when the stress regimes from adjacent faults interact (e.g. Pollard and Segall, 1987; Burgmann et al., 1994; Peacock, 2002).

Studies incorporating both geological data and numerical modelling have indicated that there is a length / displacement relationship:

$$d_{max} = cL^n$$

where $d_{max}$ = maximum cumulative displacement, c = constant based on rock properties, L = maximum linear fault length and n = exponent value ranging from 0.5 – 2 (Young-Seog and Sanderson, 2005). On isolated faults, maximum displacement will occur at the centre of the fault, with a linear tapering of displacement to zero at the fault tips (e.g. Young-Seog and Sanderson, 2005). When faults begin to interact and link, models predict that displacement maxima move towards the point of interaction, and displacement rapidly drops off towards the fault tips, due to the interaction between adjacent stress fields (Peacock and Sanderson, 1996). Figure 1.7 illustrates the two methods of fault growth and the associated displacement profiles.

Trudgill and Cartwright (1994) and Cartwright et al. (1996) examined aerial photographs and structural maps of Canyonlands, Utah, mapping fault segments ranging from ~300 m - >10 km in length. Segment boundaries were recognisable by changes in strike or an abrupt offset along strike. An example displacement profile appeared to indicate a single fault structure, with maximum displacement located towards the centre of the fault system. However, locations of high variability within this overall profile (Figure 1.8) were found to coincide with breached relay structures (Trudgill and Cartwright, 1994; Cartwright et al., 1996).

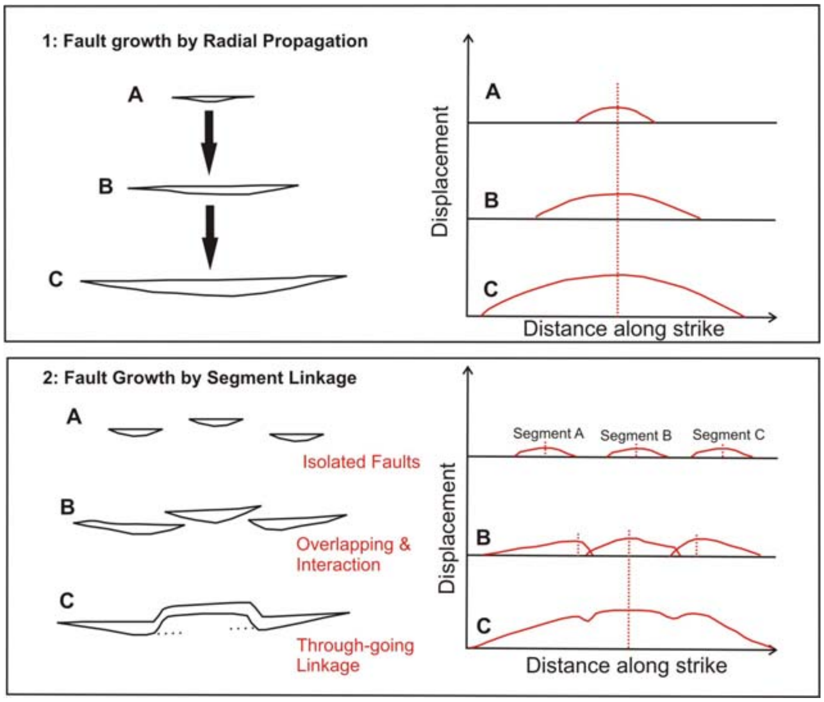

**Figure 1.7:** Illustration of two methods of fault growth and the resulting length / displacement profiles. **1)** Fault growth by radial propagation. Dashed red lines indicate the location of maximum displacement. It can be seen that the profile maintains a bell-shaped curve, with maximum displacement always located at the centre of the fault. **2)** Fault growth by segment linkage. As the faults grow, initially by radial propagation, they begin to overlap and interact. This causes maximum displacement to move towards the point of interaction. Finally the segments link, forming a profile that is indicative of a single fault, but with displacement lows indicating the positions of relic segment boundaries. (After Cartwright et al., 1995).

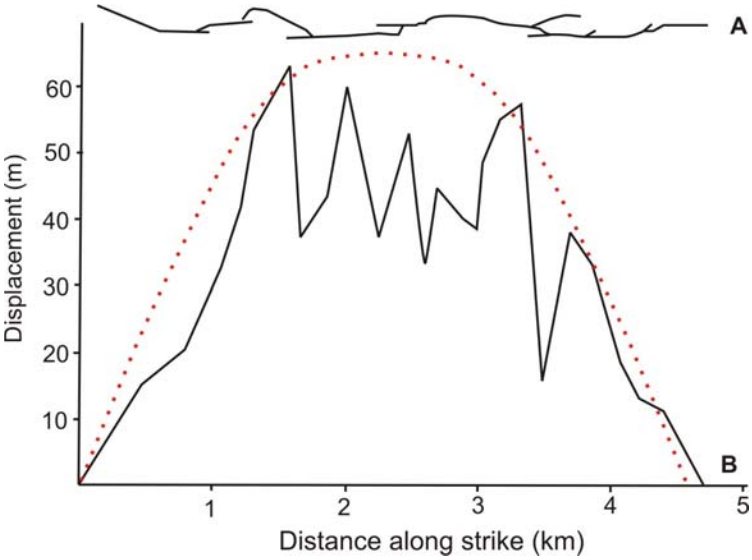

**Figure 1.8:** Illustration from Cartwright et al. (1996) showing the displacement profile along a segmented fault system.

**A)** Fault segment geometry

**B)** Displacement profile. Dotted red line shows a typical bell-shaped profile of an isolated fault.

Once through – going linkage has occurred, the displacement profile will retain minima that indicating the positions of relic segment boundaries (e.g. Peacock and Sanderson, 1991; Cartwright et al., 1995; McLeod et al., 2000). However, at some locations, the transfer of displacement between segments was taken up on subsidiary faults that ran parallel to the main faults (Trudgill and Cartwright, 1994), producing a displacement high at segment boundaries instead of a minimum.

Goldsworthy and Jackson (2001) state that sub-parallel faults may show displacement variations that indicate strain is migrating between faults on either a permanent basis, or episodically, on timescales that are relatively rapid. This suggests that strain can be transferred periodically between adjacent, sub-parallel faults if a segment boundary on one is acting as an asperity, in addition to longer term permanent partitioning of strain onto more established through-going faults.

Accurate analysis of fault growth and displacement profiles can be affected by: resolution and censoring (e.g. Walsh and Watterson, 1988); extent and contribution from damage zones surrounding the main fault (Peacock and Sanderson, 1991; Knott et al., 1996; Peacock, 2002;); drag and rotation of sediments in proximity to the fault (e.g. Trudgill and Cartwright, 1994; Mansfield and Cartwright, 1996); and the maximum length of the surface trace of fault displacement measured (e.g. Walsh and Watterson, 1988), as this can often be shorter than the true length at depth on a developing system. These factors will be addressed, wherever possible, throughout the error and displacement analysis conducted in this study (Chapters 4 and 6).

Field studies often show a wide scatter in length / displacement data points. Cartwright et al. (1995) believe that some of the scatter can be explained by the cycle of fault interaction, growth, and finally linkage (Figure 1.9). As two segments link, the increase in length can cause under-displacement relative to the length / displacement ratio. Displacement is accrued until the ratio is restored, and the fault begins to behave as an isolated structure again, growing laterally as well as accruing vertical displacement. This periodic deviation from the idealized linear length / displacement relationship creates a step-like pattern (Figure 1.9).

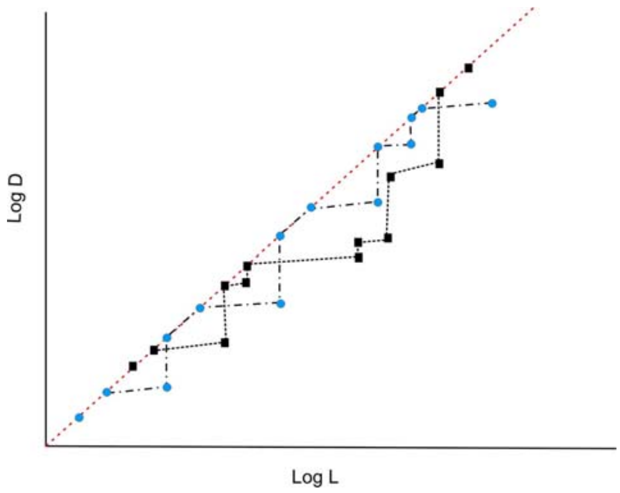

**Figure 1.9:** Illustration of the step-like displacement profile produced by segment linkage, where L = fault length and D = fault displacement. The dashed red line indicates idealized fault growth, showing a linear relationship between length and displacement. Linkage between segments causes deviations from this line due to periodic under-displacement relative to length. The degree of deviation is dependant on the length and number of segments involved. (After Cartwright et al., 1995).

Another hypothesis to explain scatter in field data is put forward by Peacock and Sanderson (1991). Fault segment linkage will increase a fault's ability to release strain, and so in order to maintain the regional strain rate, the displacement rate on other faults may slow or cease completely. This adjustment may take time to occur, and so pre and post-linkage length / displacement ratios may be variable (Peacock and Sanderson, 1991), departing from the idealized length / displacement ratio predicted by numerical modeling.

Periods of quiescence, earthquake clustering and the chosen period of observation may mean that the slip rates estimated for a segmented system may not match the rates required to create the long-term fault morphology (Cowie and Roberts, 2001). Likewise, longer periods of observation may not reveal short term variability in displacement rates, which can identify the initiation of fault interaction and linkage (e.g. Mansfield and Cartwright, 2001).

This study provides a unique opportunity to the study short-term variability of a young fault system developing within an established continental rift. Longer-term fault activity has been studied on neighbouring faults, such as the Eliki Fault (Armijo et al., 1996; Micarelli et al., 2003; McNeill and Collier, 2004; McNeill et al., 2005b), but this is the first opportunity to address very short timescale variations that can then be compared to the long-term fault behaviour of the established faults.

### 1.2.3 Modelling of Fault Behaviour

Many authors have used numerical and analytical modelling to investigate fault development. It can help aid understanding of fault behaviour and evolution where truncation, lack of exposure or erosion have prevented detailed field studies being conducted.

Numerous models exist, ranging in complexity from simple elastic single slip events (e.g. Pollard and Segall, 1987) to more complex, multiple slip, multiple segmented models (e.g. Peacock and Sanderson, 1991; Cartwright et al., 1995). Single slip event models on isolated faults predict a bell - shaped profile (e.g. Cowie and Scholz, 1992), where inelastic deformation occurs at the fault tips due to yield strength exceeding stress at the tip. The single slip profile has been shown to be self-similar over a wide range of fault lengths (Dawers et al., 1993), although this is only achieved if the whole fault ruptures. Cowie and Shipton (1998) predict that even on an isolated fault, length / displacement ratios may vary with time if only sections of the fault slip or rupture during any one earthquake event.

Models involving multiple segments and some form of segment interaction produce length / displacement profiles that are asymmetric, with displacement maximas canted towards the point of interaction (Peacock and Sanderson, 1991; Cartwright et al., 1995). Interactions between fault tips can inhibit lateral propagation (Walsh et al., 2002). As the stresses increase, bifurcation at the fault tip is common, with sub-parallel faults forming (Childs et al., 1996; Scholz, 2002). Walsh et al. (2002a) present a model where interaction between neighbouring faults inhibits lateral tip propagation, producing high displacement gradients at the tips.

Walsh et al. (2003) indicate that segments may grow out of a single fault plane through surface bifurcation, thereby appearing to be discrete faults, but actually behaving as a coherent system at depth. The length / displacement relationship for this model of evolution produced a scatter of data points similar to that also observed by Cartwright et al. (1995). Cartwright et al. (1995) suggest that the scatter will reduce with time, as displacement accrues on a system that is temporarily pinned at the tips (Cartwright et al., 1996) due to the proximity of neighbouring faults.

Whilst modelling can give a good approximation of time-averaged fault behaviour, factors such as lithology, rheology, underlying structural fabric, interaction with other faults, variation in far-field stresses and frictional properties (e.g. Burgmann et al., 1994; Knott et al., 1996; Walsh et al., 2001; Peacock, 2002) mean that no model has been able to fully explain the variability in length / displacement relationships observed in field studies over shorter time periods.

### 1.2.4 Rift Obliquity

The geometry of faulting within a rift is often influenced by the angle between rift orientation and extension direction ($\alpha$). If the rift runs orthogonal to the direction of extension, experimental clay modelling has shown that long, straight border faults will dominate (e.g. Clifton et al., 2000). However, oblique rifts tend to develop more segmented en-echelon border fault systems that are orientated obliquely to the rift, with a high density of intra-rift faults orientated obliquely to the direction of extension (Figure 1.10) (Withjack and Jamison, 1986; McClay and White, 1995; Clifton et al., 2000;). This is supported in the field by Boccaletti et al. (1998), who identified two distinct sets of faults in the Ethiopian Rift, with a N30$^o$E – N40$^o$E trending border fault system and the intra-rift Wonji belt trending N-S to N20$^o$E.

The Gulf of Corinth, with a rift trend of N120$^o$E and a N-S extension direction (Avallone et al., 2004) has an angle of $\alpha$ =60$^o$, fitting the definition of an oblique rift. The well-defined border faults along the southern Gulf of Corinth appear to fit the model predictions, forming segmented en-echelon systems that run slightly obliquely (N90$^o$E) to the rift orientation (N120$^o$E) (Le Pourhiet et al., 2003). The model prediction from Clifton et al. (2000) indicates that there should be a high number of intra-rift (offshore) faults (Figure 1.10).

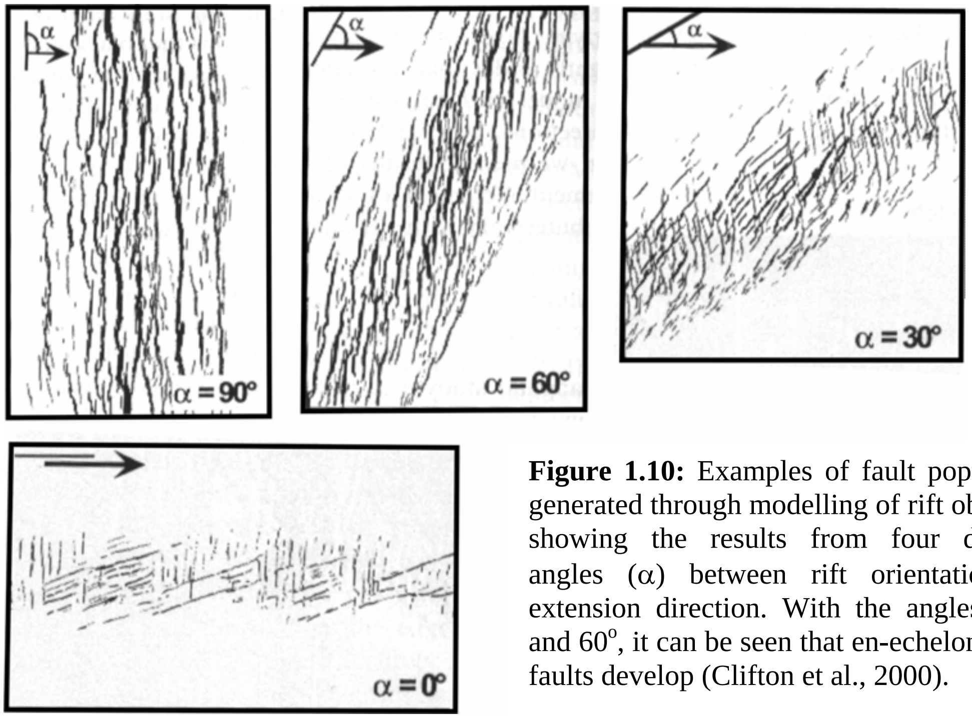

**Figure 1.10:** Examples of fault populations generated through modelling of rift obliquity, showing the results from four different angles (α) between rift orientation and extension direction. With the angles of 30 and 60$^o$, it can be seen that en-echelon border faults develop (Clifton et al., 2000).

However, McNeill et al. (2005a) and Stefatos et al. (2002) do not image the high-density of intra-rift faults predicted. Instead, McNeill et al. (2005a) image major, individual intra-rift faults, which appear to be associated with specific features, such as an uplifted basement horst, or axial channel. This may be a result of the underlying geological nappe associated with the Hellenide Orogony, which was not accounted for in the Clifton et al. (2000) model, suggesting that the inherited shape of the rift dominates the development of fault geometry.

## 1.3 THESIS OVERVIEW

This thesis uses high-resolution multichannel seismic reflection profiles and multibeam bathymetry to interpret fault growth and behaviour, both spatially and temporally, over short timescales. Through thorough analysis of all possible sources of error, and subsequent calculation of realistic error margins, detailed analysis of seismic stratigraphy, and correlation to existing datasets, it is possible to identify any significant variability in short timescale fault displacement within the longer-term fault profile.

Data from the region of the proposed eastward offshore extension of the Aigion Fault were collected and processed using standard techniques (Chapter 2). Chapter 3 presents interpretations of both multichannel seismic reflection and multibeam bathymetric data, in the form of a Geology paper, covering the western Gulf of Corinth. It gives a regional overview of fault distribution and seafloor morphology, prior to concentrating on the Aigion shelf survey area. The interpretation of faulting presented in Chapter 3 provides evidence of significant offshore faults in the western Gulf of Corinth, including a major horst bounding system, and a sub-surface fault controlling an axial drainage channel that is orientated ~E-W in the centre of the western Gulf.

Chapter 4 addresses the seismic stratigraphy imaged, and identifies four horizons that can be laterally correlated across the Aigion shelf area, ranging in date from 11.5 ± 1 ka to 3.5 ± 0.5 ka. A detailed error analysis is described, looking at the cumulative effects of uncorrelated errors including velocity picking, horizon picking and age assignment, on each of these horizons, resulting in an error range of 9% - 17%. The use of seismic character in linking the depositional architecture to sea-level behaviour and systems tract formations is discussed.

Chapter 5 describes the geometry of the faults during the Holocene based on the four horizons identified within the seismic reflection profiles. Using these horizons to generate isopachs of four discrete time intervals, it will investigate changes in sediment distribution, and relate to eustatic sea-level behaviour and tectonic activity.

Chapter 6 provides a quantitative view of fault displacement over discrete time periods. Not only does this enable an assessment of segmentation and possible linkage over time, but it provides estimated displacement rates that can be used as a comparison with data from onshore surveys in the region.

Chapter 7 investigates sedimentary and mass wasting processes related to faulting, that result in the formation of features not observed / preserved in the onshore environment in this locality. It suggests methods of formation for these features, and looks at whether or not changes in morphological size of these features are dependant on changes in seismic activity or preservation limitations.

Chapter 8 integrates the discussions related to the previous five chapters, and draws the findings together to discuss the evolution of the offshore Aigion Fault, and place those findings within a regional context. The evolution and geometry of the fault system are analysed both spatially and temporally, to determine whether or not the fault imaged is an extension of the onshore Aigion Fault system or a discrete fault. Displacement data gained from published material encompassing analyses of uplifted marine terraces, trenching and mapping of fault traces, combined with analysis of topography from Greek maps, are used to help analyse the continuity of behaviour between the offshore and onshore faulting. The displacement profile of the onshore and offshore Aigion Fault is then compared to an older fault within the Gulf of Corinth, and typical behaviour from faults in other extensional provinces, to help identify whether its behaviour is unique, due to location / lithology, or merely represents a stage in the development of basin bounding fault systems. Chapter 9 summarises the main conclusions that can be drawn from this thesis, and identifies areas of future work that lead on from the data presented in this thesis.

This study, due to its high-resolution nature and analysis of recent geological activity over much shorter timescales than usual, offers a unique view into the behaviour of a developing normal fault system, in a continental rift setting.

# Chapter 2

# Data Sources and Methodology

This chapter introduces the marine multichannel seismic reflection (MCS) and multibeam bathymetric data used in this thesis. It describes the processing of both datasets, explaining any particular stages in detail, where appropriate.

These data were collected during a marine survey using the R/V Vasillios G, in the Gulf of Corinth, Greece, in order to investigate spatial and temporal Holocene fault growth behaviour and related sedimentary deformation, with a view to quantifying slip rates and strain distribution in the western Gulf of Corinth. Detailed analysis of the Aigion Fault system was undertaken to investigate the early stage development of a rift-bounding fault system in the Gulf of Corinth, in order to more fully understand the generic development of continental rift basins.

Multichannel, high-resolution pseudo 3D seismic reflection data were collected where the offshore Aigion Fault was proposed to be located, and over the offshore transfer zone between the Aigion and Western Eliki Faults, indicated in Figure 2.1. Regional multichannel seismic reflection profiles and multibeam bathymetric data were acquired across the western and central Gulf. Tie-lines were run into a giant piston core site collected from the Marion Dufresne on an earlier cruise in the central Gulf, (Moretti et al., 2004), and to an onshore borehole at Aigion harbour drilled by the Corinth Rift Laboratory (e.g. Lemeille et al., 2004; Rettenmaier et al., 2004).

It has been suggested that the border fault systems in this region rarely show any sign of hard linkage or interaction and little overlap. However, the onshore Aigion Fault appears to deviate from this behaviour, having a significant overlap with the Western Eliki Fault (McNeill and Collier, 2004; De Martini et al., 2004; McNeill et al., 2005b), with both faults being concurrently active through the Holocene.

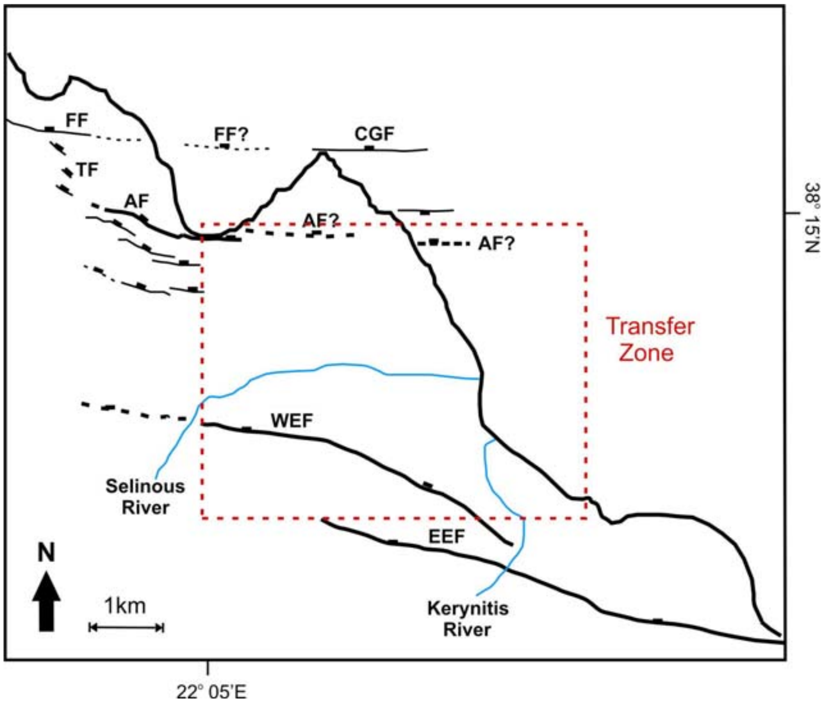

**Figure 2.1:** Location map illustrating the transfer zone between the Aigion Fault and the Eliki Fault system (red box). Onshore faults taken from Palyvos et al. (2005); McNeill et al. (2005b) and Koukouvelas (1998). AF = Aigion Fault; CGF = Cape Gyftissa Fault; FF = Fassouleika Fault; WEF = Western Eliki Fault; EEF = Eastern Eliki Fault; TF = Transfer fault zone.

This is a unique situation in the Gulf of Corinth. It is hoped that these data will help start to explain whether this is due to a change in the geology and strain distribution across the western gulf, or if we are seeing a developmental stage of these basin bounding faults, with transfer of activity passing from a slowly deactivating fault system onto a developing, currently immature system. The high-resolution data will also be used to analyse syn-tectonic sedimentation patterns and quantify fault displacement rates and variability in fault activity over the past ~12ka.

## 2.1. CRUISE R/V VASILLIOS G

A geophysical cruise was carried out using the R/V Vasillios G from July 5th to July 16th 2003. The cruise was a collaborative undertaking involving: the National Oceanography Centre, Southampton, UK; the University of Patras, Greece; and Leeds

University, UK. The seismic profiles consisted of a regional survey covering the western and central Gulf of Corinth, and a pseudo 3D survey across the offshore eastern Aigion Fault system. During the 10 survey days approximately 40 km of Boomer data, 173 km of Sparker data and 375 km$^2$ of multibeam data were collected. Figure 2.2 illustrates the equipment setup on the survey vessel.

## 2.2 NAVIGATION

The coordinate system used was UTM, Zone 34 North. Location fixes were recorded in UTM with time in milliseconds. Differential GPS data was taken from the EGNOS satellite navigation system. Two additional GPS antennas also supplied navigational information.

The differential correction was combined with the input from two GPS antenna's and the pitch, roll and heading data received from the Applanix military grade Inertial Measurement Unit (IMU), located below the waterline at the ship's centre of gravity. This navigation signal was then split, and recorded by both the multibeam acquisition system and HYDROpro navigation software. At times of DGPS failure, due to reasons unknown, a Trimble system mounted on the bridge was used as an alternative for HYDROpro. These intermittent DGPS dropouts resulted in estimated navigational accuracy reducing to +/-4m. As the Navigation and seismic acquisition systems were not linked, the UTC time recorded was synchronised on a daily basis between the DGPS signal, HYDROpro software, POS/MV and the seismic acquisition system at the initial power-up stage, prior to data collection.

All offsets between the survey equipment and the GPS and DGPS antenna's were measured with reference to the IMU (Appendix A).

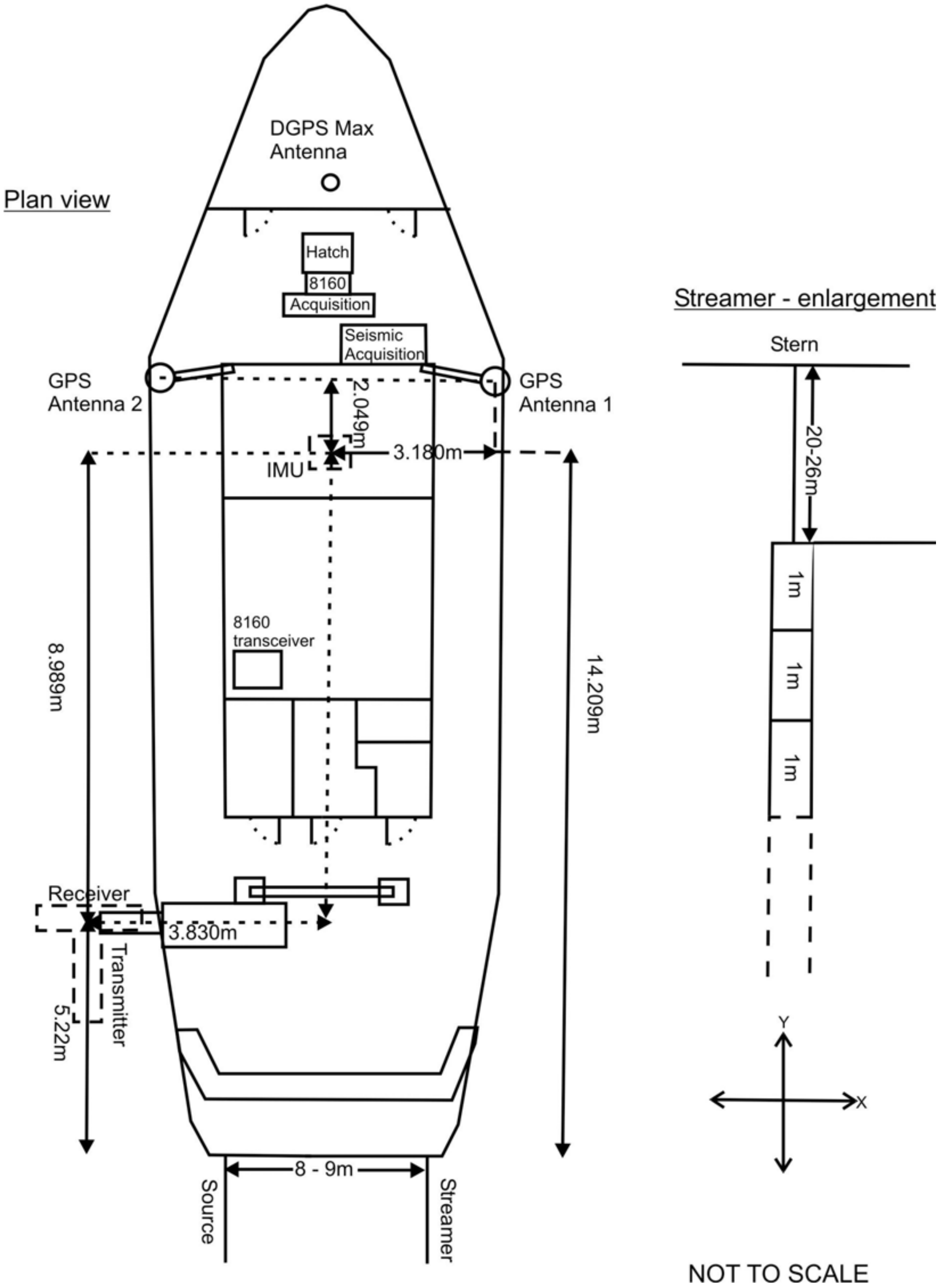

**Figure 2.2:** Plan of equipment layout on the M.V. Vasillios G. Offsets between navigational antennaes, the Inertial Motion Unit (IMU) and 8160 swath head are shown. Enlargement shows the offset between the active sections of the hydrophone streamer and the stern of the vessel, and the spacing between each active section of the streamer.

## 2.3 SURVEY STRATEGY

A regional seismic survey covered an area approximately 12.5 x 30 km, encompassing the western and central Gulf. 10 Sparker lines were collected running across the Gulf of Corinth from NW–SE and SW-NE, with an average length of 12 km, in water depths ranging from c.15 to 800 m (Figure 2.3). In addition, survey lines were run to the positions of known cores, one located just onshore at Aigion harbour, (AIG10, Corinth Rift Laboratory), the other being core 10-MD01-2477 collected from the Marion Dufresne, located at 38$^{o}$ 13.28’ N / 22$^{o}$ 33.53’E. The AIG10 profile (line 15) ran from the north of the Gulf, in a SW direction into the Aigion harbour area, and was approximately 7.5 km in length. The 10-MD01-2477 tie-line was approximately 40 km long, and crossed all of the regional sparker lines, with the exception of line 5, running from West – East along the centre of the Gulf.

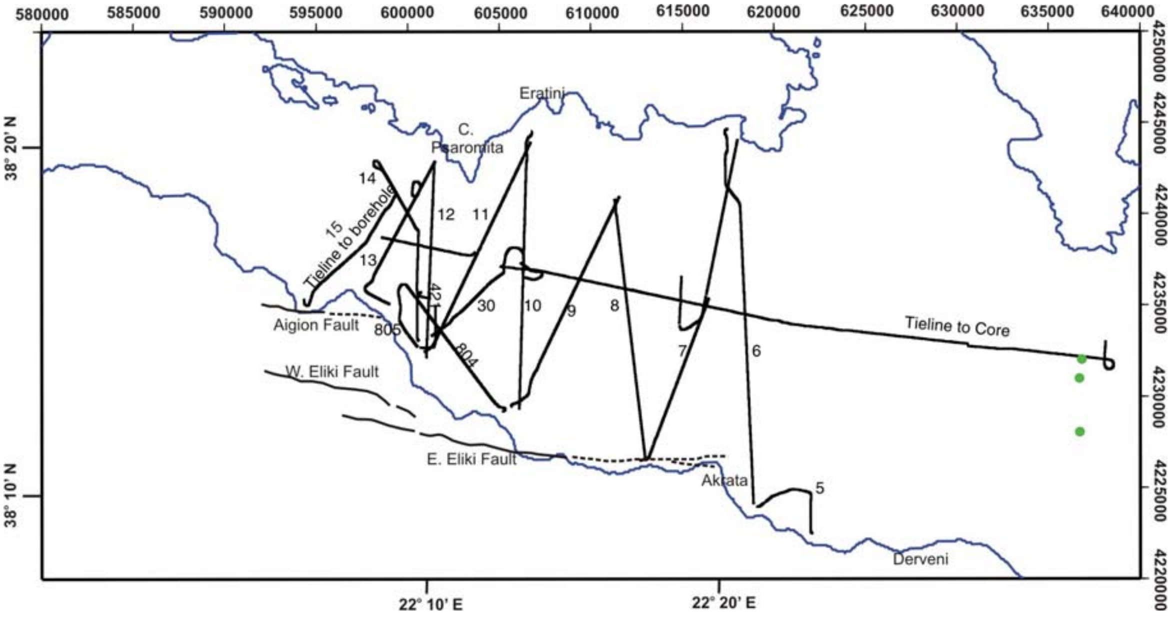

**Figure 2.3:** Plot of the Sparker seismic reflection survey lines run, providing profiles across the Gulf of Corinth. The green circles indicate the positions of giant piston cores taken by the Marion Dufresne (Moretti et al., 2004). Locations are shown in both UTM (Zone 34N) and Latitude / Longitude.

A detailed, multichannel pseudo 3D Boomer and Sparker seismic reflection survey was centred on the shelf situated to the east of the known onshore Aigion Fault (Figure 2.4). It covered an area of approximately 2 x 1.5 km, in water depths ranging from ~10- 90 m at the shelf edge. Twenty parallel N-S Boomer lines with an average length of 1.5 km were initially run perpendicular to the fault, with a line separation of 100 m. The first line was 350 m from the shoreline. An additional 5 Boomer lines with an average length of 1km were then run within the initial grid lines, at 25 m line spacing, to investigate the offshore fault tip in more detail. Three Boomer tie-lines running E–W parallel to the fault were run; two located within the hanging-wall and one within the foot-wall. One N–S Sparker line of 1.5 km length was run as the furthest offshore line within the detailed Boomer area. Two additional Sparker lines were run in this detailed area, with an average length of 2.5 km, orientated NW - SE. Regional Sparker lines 11 and 12 also terminated in the detailed Boomer survey area, aiding the interpretation of the detailed area within a more regional context.

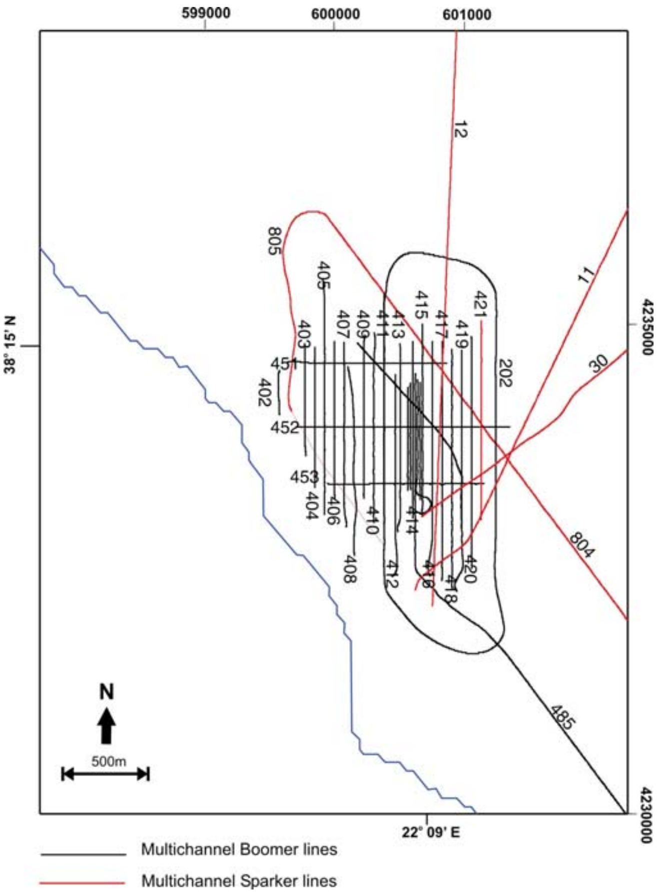

**Figure 2.4:** Plot of the multichannel seismic reflection lines run across the offshore Aigion shelf, conducted as a pseudo 3D survey. N-S lines are run at 100m spacing, with additional lines at 25m spacings. Lines 451 and 452 lie within the hanging-wall of the proposed offshore extension of the N-dipping Aigion Fault, whilst 453 lies within its footwall. Multichannel reflection Sparker lines tie this survey area into the regional survey area (Chapter 3).

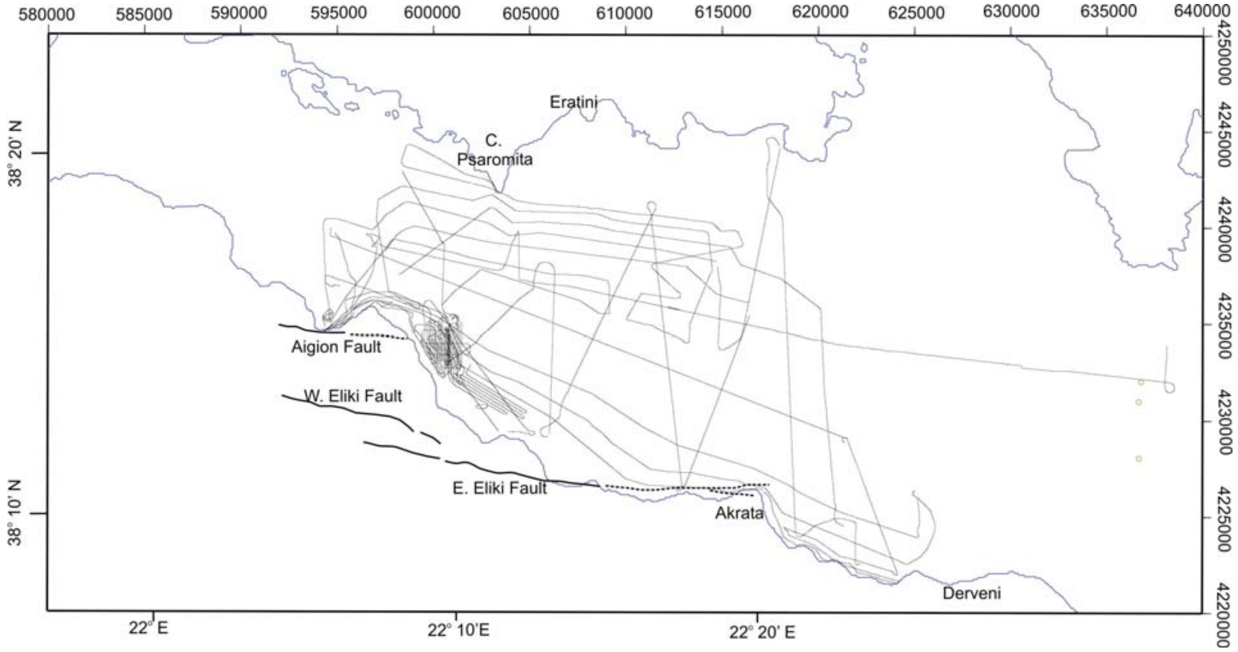

**Figure 2.5:** Plot of the Reson 8160 swath bathymetry survey lines run, showing location in both UTM (Zone 34N) and Latitude / Longitude coordinates. Green circles indicate giant piston cores taken by the Marion Dufresne (Moretti et al., 2004).

Multibeam bathymetry was collected from Aigion Harbour in the west to the western offshore tip of the Derveni Fault system in the east (Figure 2.5). Overlap of data ranged between 30 – 100%, with coverage coming to within 100’s of metres of the shoreline. The multibeam system was often run in conjunction with seismic acquisition, so using the seismic reflection survey lines instead of specific multibeam survey lines. The system was also run during transit to and from specific seismic survey areas in order to achieve maximum coverage of the complete region.

## 2.4 MULTICHANNEL SEISMIC REFLECTION DATA (MCS)

This section will describe the data acquisition methods and the processing techniques for both the MCS and navigation datasets.

### 2.4.1 Data Collection

For the regional Sparker survey lines an Applied Acoustics Squid 2000 catamaran-based Sparker, with a CSP3000 power supply set to 2200J per shot was used. The shot interval ranged from 1.55–3.3 seconds, however the regional lines were generally run at 2.75 seconds.

For the Boomer pseudo 3D survey, an Applied Acoustics catamaran and AA200 boomer plate was used, with the CSP3000 capacitor. The source setting was 300J, with a shot interval ranging from 0.53 – 1.35 seconds depending on seabed depth and stratigraphy imaged.

The data was recorded using a 60 m long bespoke hydrophone, consisting of 60 1 m active sections, each consisting of 7 hydrophone elements. There were 10 m inactive sections both before and after the active length, with an additional 50 m deck lead in. The streamer was deployed from the starboard side, with a distance of between 20 – 26 m between the stern of the vessel and the first active section. It was towed at ~0.25 m below the surface. Both the Boomer and Sparker sources were hand deployed from the port side at the stern, and towed between 20 – 22 m behind the stern at the surface.

Logging for both surveys was onto a Geometrics Strataview R60 seismograph with a marine controller, connected by a 100Mbit Ethernet cable. There was no preamplification between the hydrophone and seismograph input. Triggering was via a bespoke unit consisting of a temperature compensated, free running clock, with a split cable running to both the CSP300P capacitor and the Strataview system. Deep-water recording delays were introduced via the Strataview system. The data was backed up onto 4 mm tape in SEG-D format using two DDS4 DAT drives.

As both sources used were towed at the surface, there was no obvious vertical mis-tie between the horizons imaged in the Sparker and Boomer profiles collected. This has enabled the analysis of the detailed survey area to be incorporated into a more regional overview.

### 2.4.2 Data Processing

The multichannel seismic reflection processing involves processing both navigation and seismic trace data. Seismic SEG-D trace data were combined with navigation data using FORTRAN, UNIX and GMT scripts. The resultant output file was incorporated into the seismic trace headers, and the geometry between the source and 60 hydrophone sections assigned within ProMAX. The same processing stages were used for both the regional Sparker and pseudo 3D Boomer surveys, with different parameters applied, chosen to suit the frequency content of each source.

The complete processing flow followed in ProMAX is summarised in Figure 2.6. Detailed descriptions of settings within each step, where applicable, can be found in Appendix B, however the major processes are summarised below.

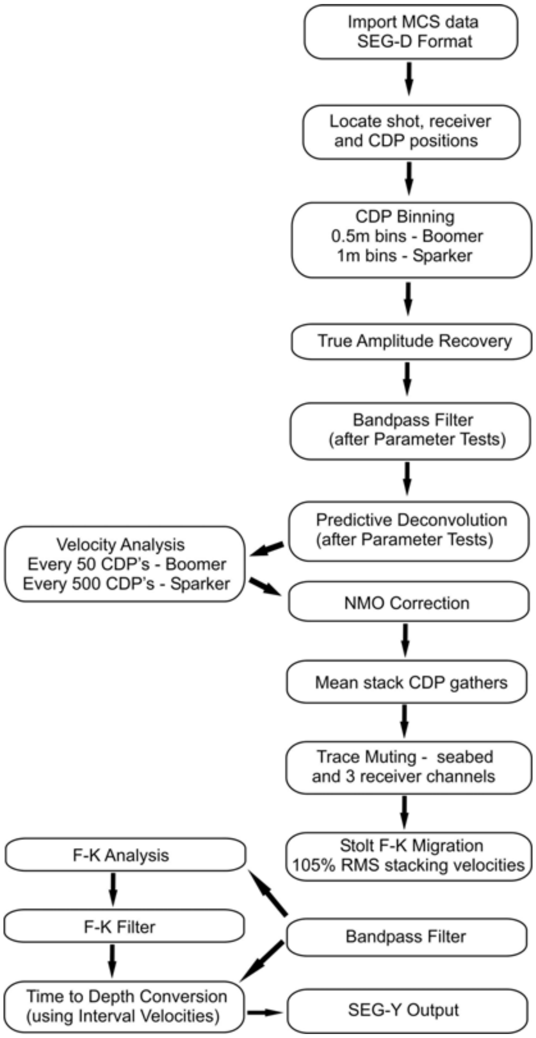

**Figure 2.6:** Multichannel seismic reflection processing flow used to process both the Boomer and Sparker datasets. Details of the settings used in each step can be found in Appendix B.

### Source and Streamer Location – Geometry assignment

The geometry for the MCS data was assigned using a 2D Marine Geometry Spreadsheet. Layback from the navigational IMU to the source and receiver were measured prior to the survey commencing. The acquisition geometry is illustrated in Figure 2.7 A & B.

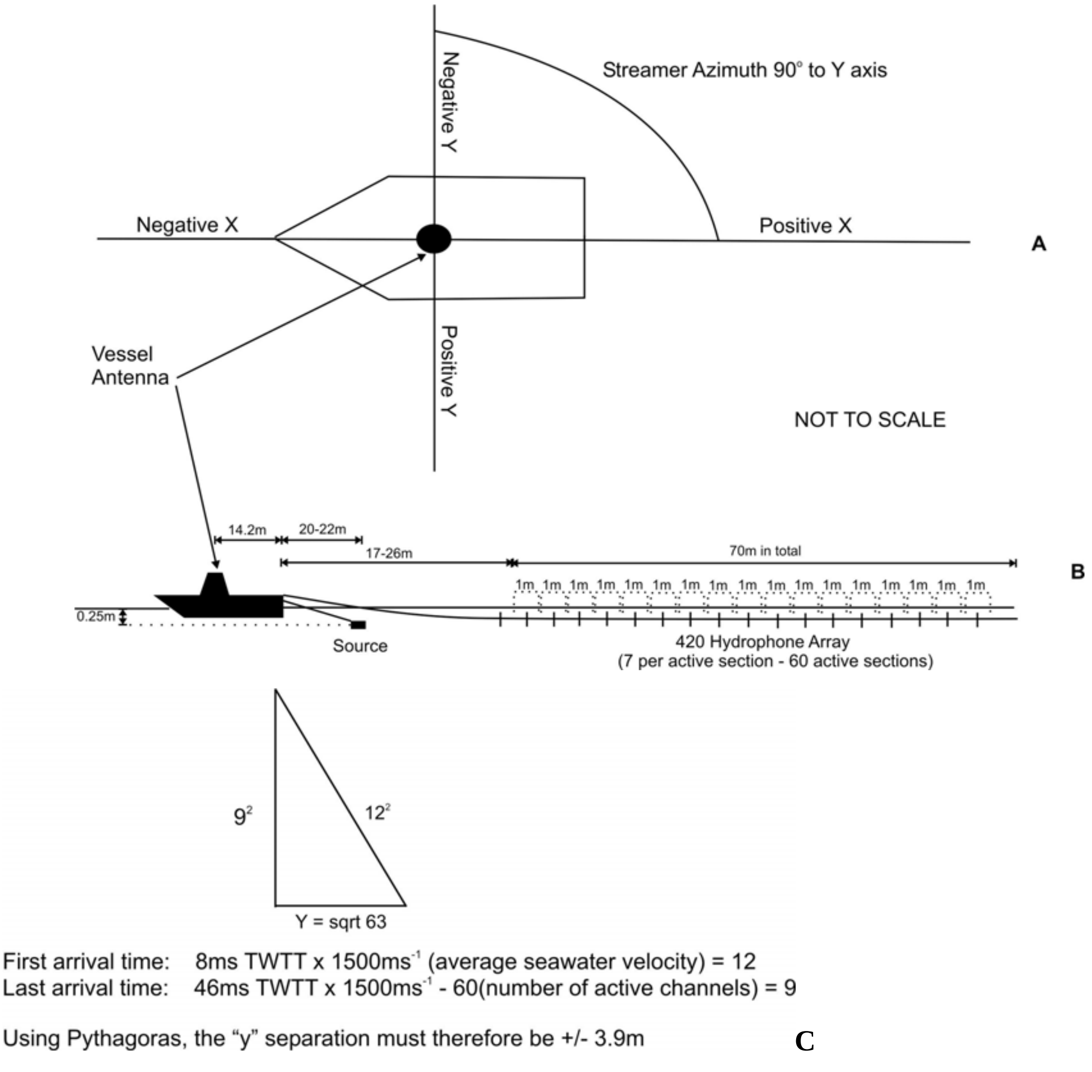

First arrival time: 8ms TWTT x $1500ms^{-1}$ (average seawater velocity) = 12
Last arrival time: 46ms TWTT x $1500ms^{-1}$ - 60(number of active channels) = 9

Using Pythagoras, the "y" separation must therefore be +/- 3.9m

**Figure 2.7:** MCS acquisition geometry. **A)** Plan view showing positive and negative orientations relating to the geometry spreadsheet. Exact source to first active receiver distances (x) and source receiver separations (y) are detailed in Table 2.1. **B)** Side view showing distances from the primary antenna to source and receiver. **C)** Example of how x and y offsets used in the 2D Marine Geometry Spreadsheet were calculated using first and last arrival times.

Offsets, in positive and negative x and y co-ordinates were entered into the spreadsheet, along with the number of active channels, receiver azimuth and channel spacing. The offsets were calculated using first and last arrival times (ms TWTT) as illustrated in Figure 2.7C. Using these answers, the y separation between source and the first active channel was calculated. Table 2.1 details the x and y offsets applied to each line of the Boomer pseudo 3D survey.

The CDP spacing was assigned during the binning process. Horizontal resolution in a seismic reflection survey is half the detector spacing. With the detailed Boomer survey conducted on the Aigion Shelf, the bin size chosen was 0.5 m, in order to optimise the horizontal resolution. However, on the regional Sparker survey the bin size chosen was 1 m, due to the increase in the Fresnel zone with deeper water depths. This resulted in fold coverage of between 17 – 20 for the Boomer profiles, and 8 for the Sparker profiles.

| Survey Line | X | Y | Survey Line | X | Y |
|---|---|---|---|---|---|
| **403** | 12.8 | 10 (+5, -5) | **414** | 12.7 | 9 (+4.5, -4.5) |
| **404** | 12 | 5.8 (+2.9, -2.9) | **485** | 12 | 8 (+4, -4) |
| **405** | 12 | 7.8 (+3.9, -3.9) | **484** | 12 | 7.8 (+3.9, -3.9) |
| **406** | 12 | 9 (+4.5, -4.5) | **483** | 12 | 5.8 (+2.9, -2.9) |
| **407** | 12.7 | 7.2 (+3.6, -3.6) | **415** | 13.5 | 10 (+5, -5) |
| **408** | 12 | 7.8 (+3.9, -3.9) | **416** | 13.5 | 8.4 (+4.2, -4.2) |
| **409** | 12 | 7.8 (+3.9, -3.9) | **417** | 13.5 | 8.4 (+4.2, -4.2) |
| **410** | 12.7 | 9 (+4.5, -4.5) | **418** | 12.7 | 9 (+4.5, -4.5) |
| **411** | 12 | 7.8 (+3.9, -3.9) | **419** | 14 | 10 (+5, -5) |
| **412** | 12 | 7.8 (+3.9, -3.9) | **420** | 13.5 | 9.2 (+4.5, -4.6) |
| **413** | 12 | 7.8 (+3.9, -3.9) | **451** | 12 | 9.2 (+4.6, -4.6) |
| **488** | 12 | 5.8 (+2.9, -2.9) | **452** | 12 | 5.8 (+2.9, -2.9) |
| **487** | 13 | 10 (+5, -5) | **453** | 12.7 | 9 (+4.5, -4.5) |

**Table 2.1:** X and Y offsets, applied during the geometry assignment process, for each of the MCS reflection Boomer profiles used in this study.

## Frequency Filtering

Interactive Spectral Analyses were run for each line. From the results, parameter tests were run to identify the four corners chosen for the minimum phase Ormsby Bandpass Filter applied to both the Boomer and Sparker profiles (Figure 2.8). The Nyquist frequency for the Boomer data is 4000Hz. However, in order to maximise the detail revealed, and due to the very clear images produced from the un-processed data, it was decided to adopt corner frequencies of 100-200-5000-6500Hz, thus ensuring all high frequency signals were passed through the filter. The best corner frequencies for the Sparker data were 50-150-2200-3600Hz. Bandpass filters were run using the same corner frequencies both pre- and post- migration.

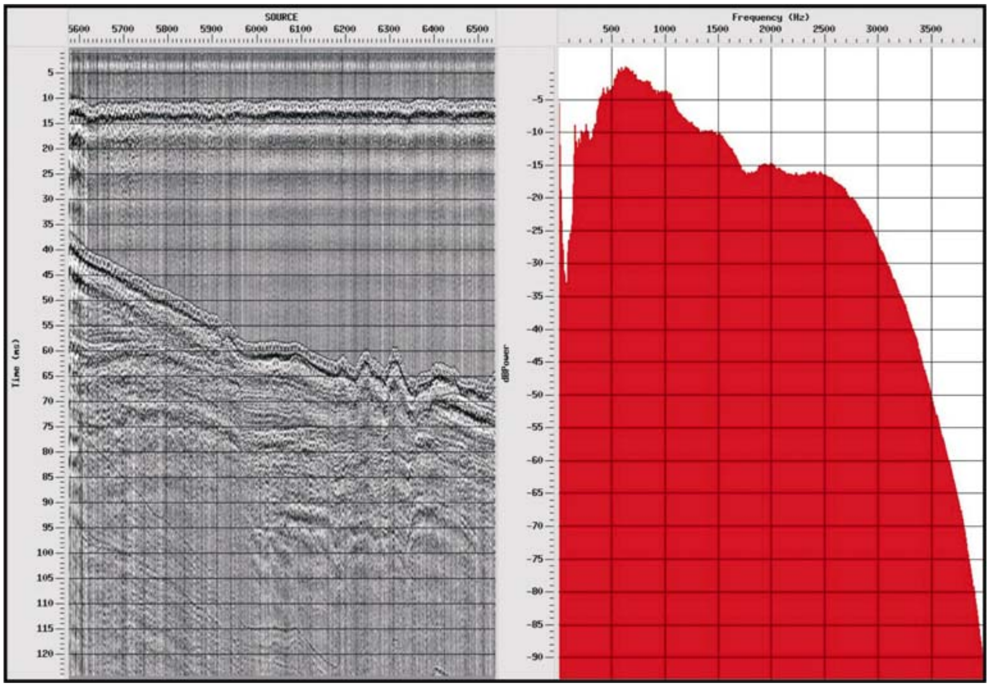

**Figure 2.8:** Sample Spectral Analysis from the Boomer MCS reflection data following geometry assignment. Parameter tests were run on each line to assess the corner frequencies that were most suitable to use. Frequencies chosen were 100-200-5000-6500Hz.

### Inverse Filtering

A minimum phase predictive deconvolution was applied to remove convolution effects due to the source signal, geophones and the previous frequency filtering. Again, parameter tests were performed to select the most appropriate deconvolution window.

An operator length of 4 ms and a predictive distance of 1 ms was applied to all of the Boomer and Sparker traces within the pseudo 3D survey area (Figure 2.9). This increased the resolution at depth by filtering much of the high frequency noise, although it decreased resolution in the upper parts of some profiles. Interpretation therefore utilised both deconvolved and non-deconvolved profiles. A post migration deconvolution with an operator length of 1.5 ms and a predictive distance of 0.75 ms was applied to remove any effects caused by migration, but found to have negligible effect.

The regional Sparker survey was found to benefit from the application of two separate minimum phase predictive deconvolution filters. The first, with an operator length of 15 ms and a gate distance of 1.5 ms removed any streamer ghost. The second, with an operator length of 8 ms and a gate distance of 3.5 ms reduced any remaining intrinsic effects caused by migration.

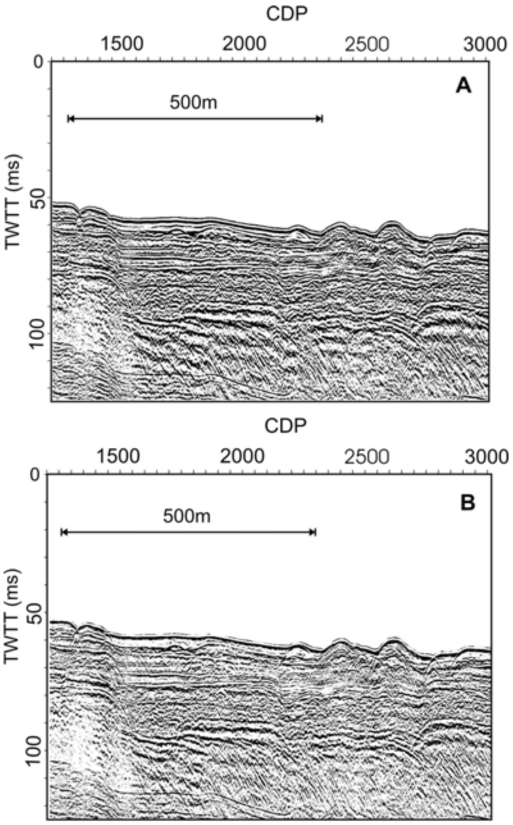

**Figure 2.9:** Examples of Boomer MCS reflection data showing the effect of a predictive deconvolution filter prior to stacking. **A)** Multichannel stacked data with no filter applied. **B)** Multichannel stacked data with 4ms operator length / 1ms predictive distance deconvolution filter applied. Data is enhanced at depth due to a reduction in noise, but is compromised higher in the section due to increased diffraction. Vertical Exaggeration ~6.

### Velocity Analysis

An accurate velocity model is required in order to place the same reflector at the same two way travel time (TWTT) at all offsets within the CDP gather. This ensures that when the Normal Moveout Correction (NMO) is applied using the optimum RMS velocity model calculated for each profile, the traces stack coherently together, increasing the signal to noise ratio, and so improving data quality. In addition, the velocity profile through the sediments is required in order to accurately convert the TWTT profiles into depth profiles.

The RMS velocity models were calculated using NMO corrected CDP gathers and semblance analysis plots (Figure 2.10). Velocity analyses were conducted every 50 CDP's (25 m) along the Boomer pseudo 3D survey lines, resulting in between 35-80 analyses per line, and every 500 CDP's on the regional Sparker lines, decreasing to every 100 CDP's where the lines entered the pseudo 3D survey area. This ensured continuity between the pseudo 3D survey and the regional survey lines. The RMS velocity profile for each line was then incorporated into the stacking and migration flows within ProMAX.

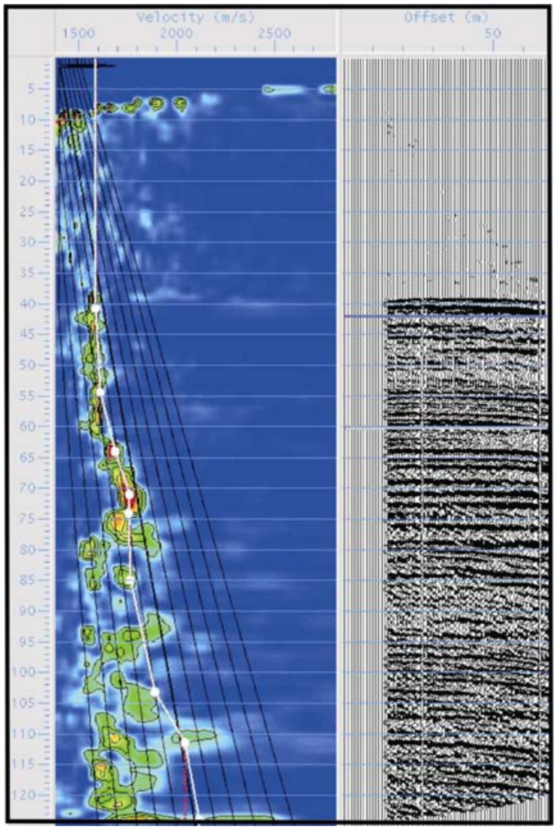

**Figure 2.10:** Example of a semblance velocity profile from the MCS Boomer reflection data. Normal Moveout Correction (NMO) has been applied to the right-hand panel to check velocity picks. Velocity profile created was unique to each line.

The Boomer MCS reflection profiles produced consistent velocities ranging from 1490 m $s^{-1}$ to 2200 m $s^{-1}$, whilst the regional Sparker profiles produced velocities ranging from 1440 m $s^{-1}$ to 2800 m $s^{-1}$. In order to check the velocities picked, they were compared to average log velocities gained from both the Marion Dufresne piston core, and the Aigion AIG10 borehole onshore (Hicks, 2004; Moretti et al., 2004), and found to be commensurate.

Following the velocity analysis, the seismic data were stacked, to increase the signal to noise ratio, and so the resolution and detail visible within each profile (as shown in Figure 2.11).

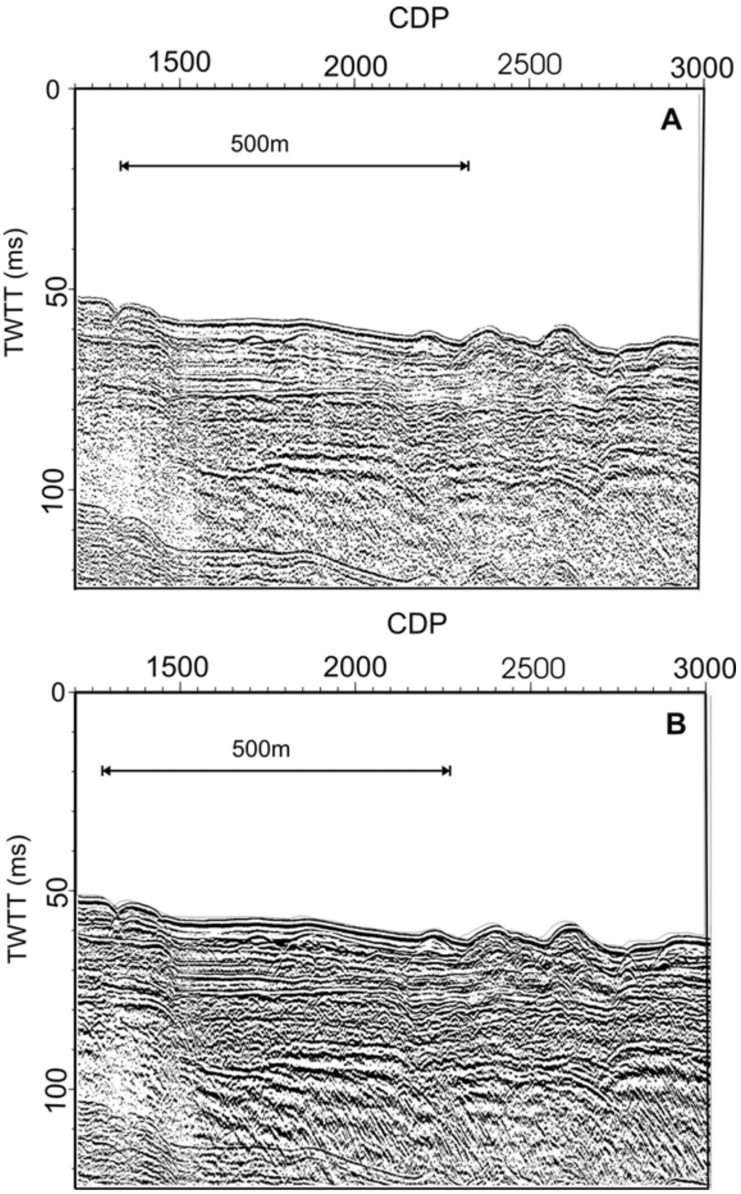

**Figure 2.11:** Example of Boomer MCS reflection data illustrating the improvement in data quality obtained through stacking. **A**) Best single channel data that has undergone Bandpass Filtering, True Amplitude Recovery (t*2) and NMO Correction (Forward, 20, using RMS velocity model from velocity analysis of Line 406).

**B**) Stacked data from the same area, which has undergone the same processing as in A, plus trace kill of channels 13, 15 & 53. Vertical Exaggeration ~6.

## Post-stack Time Migration

This was done in order to remove any diffraction effects from the stacked data caused by faulted beds or point reflectors. Migration also improved the resolution of the section by focusing the spread of energy in the Fresnel zone. A Stoltz F-K Migration (in the time domain) was applied. The Stoltz stretching algorithm used in this migration helped account for lateral and vertical velocity variations.

Initial processing applied a single seawater velocity of 1500 m $s^{-1}$ to the migrated stack, although using 105% of the RMS stacking velocity was found to produce a slightly clearer image at greater depths (Figure 2.12), as it applied a profile unique to each seismic line. However, the velocity models used did not take into account abrupt changes in overburden velocities across fault planes, and so migration artefacts may have been introduced. This influences the geometry and dip of the fault planes displayed in the final migrated section, with one example having a possible $30^o$ range in possible fault dips. Therefore fault dips used in later analysis were taken from published dips on the onshore Aigion Fault (e.g. De Martini et al., 2004; Rettenmaier et al., 2004).

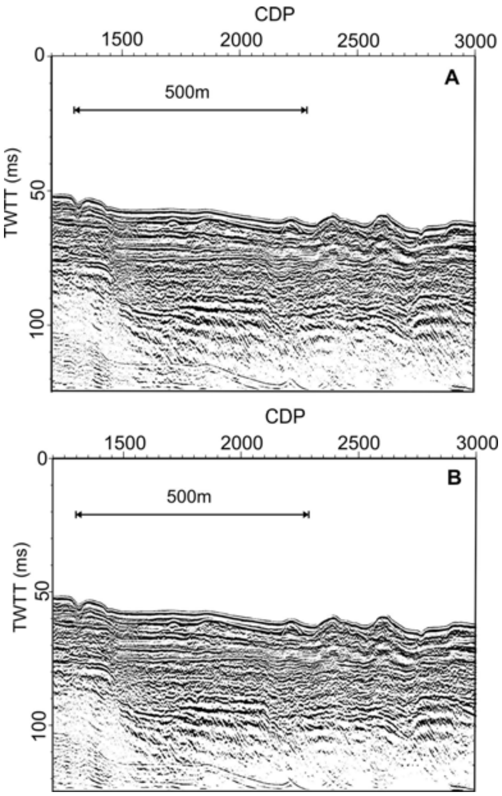

**Figure 2.12:** Example of MCS Boomer reflection data illustrating the subtle improvement in the multichannel migrated dataset when using a velocity model unique to each line as opposed to a basic seawater velocity model. **A)** Multichannel stacked data migrated using a basic water velocity of 1500 $ms^{-1}$. **B)** Multichannel stacked data using the velocity model generated through the semblance velocity analysis. The plots indicate a slight improvement in lateral continuity of the reflectors at depth in B. Vertical Exaggeration ~6.

### 2.4.3 Data Quality

The MCS reflection Boomer profiles provided high-quality sub-surface detail of the stratigraphy down to a maximum depth of ~100 m below the seafloor. Beneath this, loss of acoustic impedance due to a highly reflective deeper horizon, combined with geometric spreading of the energy, prevented further detail being imaged. A prominent seabed multiple in both the Boomer and Sparker profiles from the detailed survey area also inhibited accurate interpretation of detail below this depth.

Three channels, (13,15, and 53), of the hydrophone streamer either did not work or recorded very poor quality data, and so were omitted from the processing and final seismic SEG-Y output of both Boomer and Sparker records.

Although stacking the Boomer data reduced the effect of the seabed multiple, some lines were found to still suffer from associated migration artefacts. Where possible, a bottom mute was applied. However, on many occasions the multiple cut across true data and so could not be muted without destroying useful data. Therefore lines most affected were run through an F-K analysis and subsequent filter in order to remove the effects of noise where possible, and improve the data quality at depth. However, many of the artefacts had steep dips similar to those of the fault planes and dipping stratigraphic reflectors, and so could not be removed without affecting and removing real data from shallower in the MCS section.

It was also observed that upon stacking the data, some of the surface detail in the uppermost few metres was lost due to amplification of the initial seabed return (see Figure 2.11). Therefore analysis of any detail in the upper Holocene section had to be undertaken using pre-stacked seismic sections. No visible improvement of data quality was seen from applying post migration predictive deconvolution and bandpass filtering, so these steps were not included in the final processing flow.

The Boomer records proved to be susceptible to swell, due to the hydrophone being surface towed. The noise generated by the swell (due to snatching of the streamer), when combined with the signal generated by the true bathymetry, can create a false representation of the seafloor, and degrade general data quality. However, the swell only picked up to a level that affected smooth towing of the streamer and source catamaran by mid afternoon. Therefore the survey day was begun earlier in order to avoid adversely corrupting the seismic records, so negating the need for static corrections to be applied during the processing of the seismic data.

Tidal influence is another possible reason static shifts need to be introduced into the processing of seismic data. Over the course of the survey period, the maximum recorded tidal range was <50 cm at Patras, Greece. Implementing static shifts would correct for any inaccuracies in the calculated depth of the seafloor due to the presence of tidal variability over the course of the survey period. However, when the tidal range was considered against the other possible sources of error, such as potential error in calculating seafloor depth of $\pm 1.9$ m due to inaccuracies in the velocity profiles applied (see Chapter 4, section 4.2), and navigational errors of up to $\pm 4$ m, combined with the range of depths (10 - >800 m) being surveyed, it was decided that the tidal influence was minimal. Therefore no static corrections were made for the tidal influence in this survey. This proved to be a valid approach, as it was subsequently found that any mis-ties between lines, when the data was taken into a 3D seismic interpretation workstation, were less than 2 ms (~1.5 m).

## 2.5 MULTIBEAM BATHYMETRY DATA

This section will detail the acquisition and processing techniques used, for the Reson Seabat 8160 swath bathymetry dataset collected.

### 2.5.1 Data Collection

A Reson Seabat 8160 50 kHz multibeam echosounder was used to collect bathymetric data across the western and central Gulf of Corinth (Figure 2.13). A central computer received information from the sonar array, using a $150^{o}$ swath across track, $1.5^{o}$ swath along track, and 126 beams. This was combined with data from the pitch-stabilised transmitter and a roll compensated receiving unit (IMU), which was located at the survey vessel’s centre of gravity.

The Applanix POS MV provided heading, heave, and positioning information taken from the GPS and DGPS antennas, resulting in 6-degrees-of-freedom positioning capability. Figure 2.14 is a system diagram for the Reson 8160 system.

During surveying, the above information was combined with incoming bathymetric data and a master database that had been set-up prior to commencing the survey. This master database comprised of navigational offsets gained from running two patch tests, roll, pitch, heading and systems information (Appendix B).

The bathymetric data collected were recorded as database files (.db) and not processing files (.qpd) to save space. The database was set up to begin a new .db file at 100MB, so that file size and operational capacity would not become compromised by overly large file sizes. Each day began a new root file, carrying a template database file from the previous day forward, thereby carrying line and grid information forward from data already collected, in addition to the data contained in the master database file. Figure 2.15 illustrates the root and sub-file layout and contents.

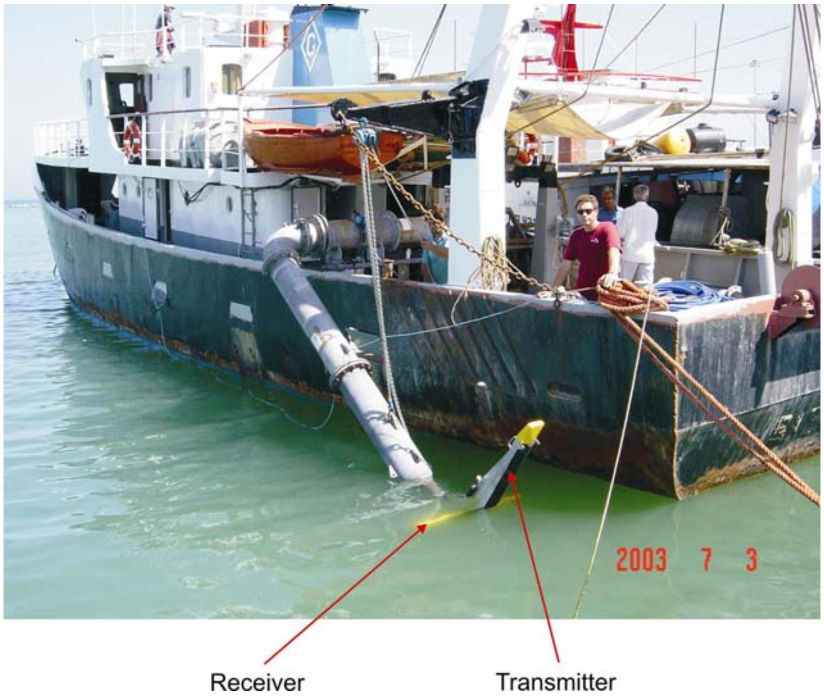

**Figure 2.13:** Photograph showing the side-mounted Reson 8160 swath bathymetry head. When deployed, the unit swung down so that the support pole was vertical in the water. The pole was supported by a bracket and metal stays to ensure that vibration in the pole, that could degrade the data being recorded by the receiver, was minimised. Photograph courtesy of A. Stefatos.

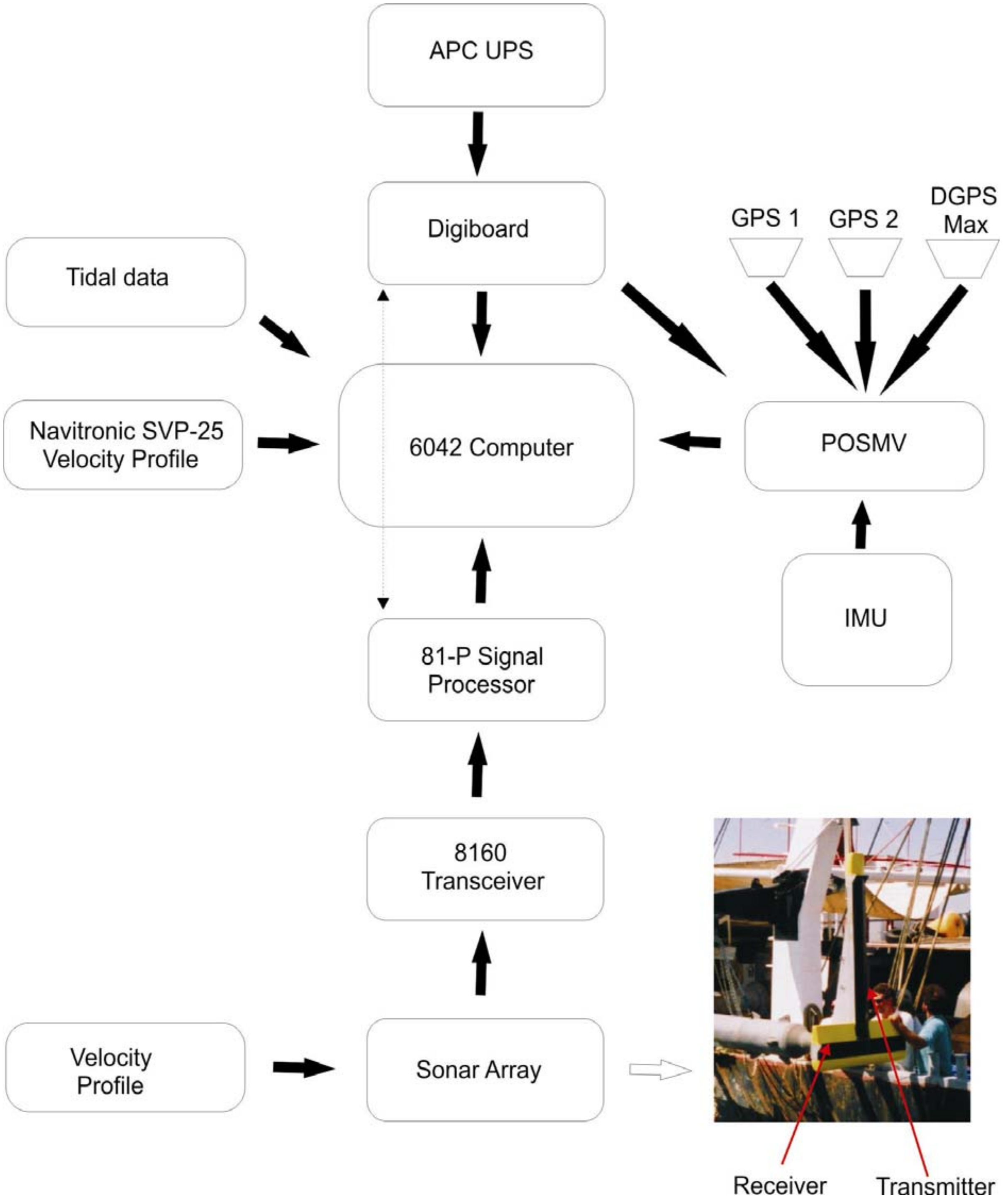

**Figure 2.14:** System diagram of the Reson Seabat 8160 Multibeam, showing equipment set-up during acquisition.

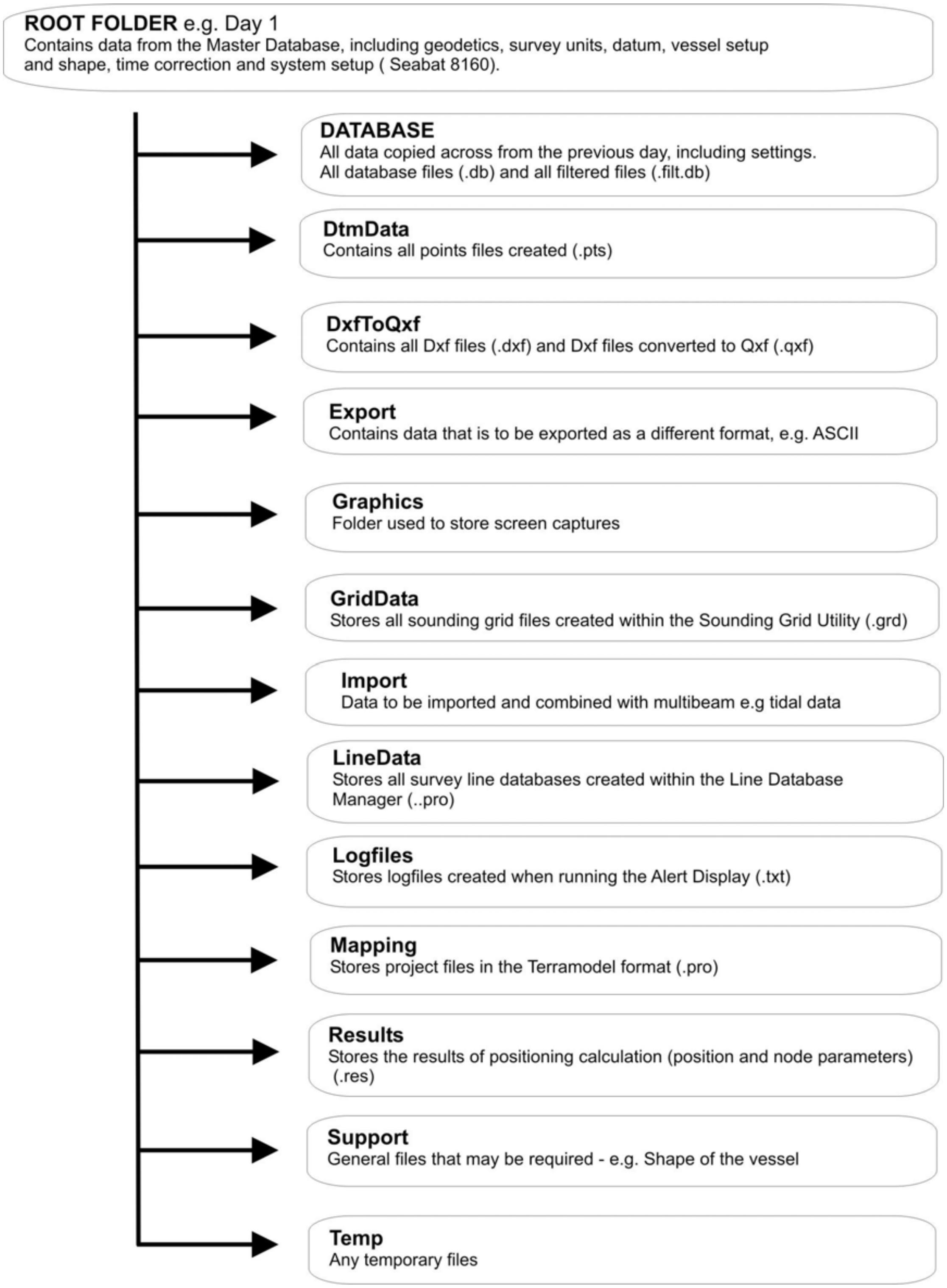

**Figure 2.15:** Schematic showing the folder and sub-folder system for storing data associated with the multibeam survey. Each survey day's data was stored within a unique Root Folder, carrying forward all survey line information from previous days surveying.

On three occasions the Navitronic SVP-25 self-logging probe was deployed, and a water velocity profile through the water column recorded. The locations chosen to take the profiles were located at the eastern and western most points of the regional survey area, in the deepest water depth for that area. The profiles were taken on two different days to note any changes in the water column over time.

### 2.5.2 Data Processing

The data files collected during the cruise were transformed to QINsy processing format for processing within the RESON 6042 Validator software. Prior to converting the data, a sound velocity profile (SVP) from the Navitronic SVP-25 self-logging probe was applied to all the data collected.

The speed of sound through water is directly related to the temperature, salinity and depth of the water column, as shown by equation 2.1;

$$\mathbf{V=1449.2 + 4.6T - 0.55T^2 + 0.00029T^3 + (1.34 - 0.01T)(S - 35) + 0.016D} \qquad \mathbf{2.1}$$

Where T is the temperature in degrees centigrade, S is the salinity in ${}^{0}/_{000}$ and D is the depth in metres (Jenson et al., 1994). Therefore in order to be able to obtain an accurate multibeam depth sounding, the data required input from a velocity profile relevant for the survey area. The velocity profile would also ensure that when the data was compiled as a mosaic, any static shifts between survey lines would be compensated for.

The three Navitronic water velocity profiles taken were virtually identical, and so one was chosen to apply to all the multibeam data collected (Figure 4.16). The velocity profile recorded a maximum depth of 758 m, whereas the survey region had a maximum depth of 858 m. Therefore the profile was extrapolated an additional 100 m before being applied. Velocities ranged from a surface reading of 1532.9 m $s^{-1}$ decreasing to 1507.8 m $s^{-1}$ at 72 m before increasing linearly to 1518.1 m $s^{-1}$ at 858 m (Figure 2.16). Readings were taken every metre.

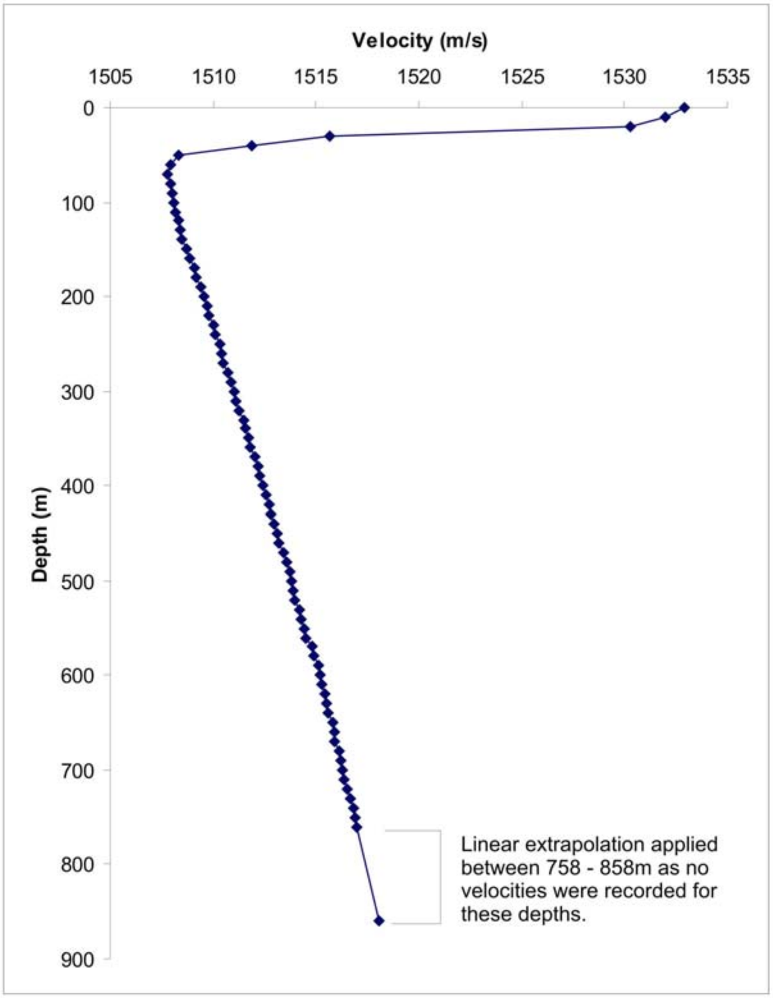

**Figure 2.16:** Water column velocity profile applied to all the multibeam swath bathymetry data collected. Velocities were recorded every 1 m, however only 1 in every 10 points is shown here. Depths where the linear extrapolation was applied are indicated.

Six additional filters were selected to apply to the raw data. These would not remove any data, but would flag the raw data points identified by these filters, for later removal within the Validator software. The filters chosen were Brightness, Colinearity, Depth, Single Spike set to 0.5 m, Range and Excluded (see Appendix C).

Each survey line was replayed within the Project Manager software, creating a QINsy file. All new files created were stored within sub-folders of the relevant root (day) folder. One of the initial survey lines collected using incorrect offsets, was also replayed using the correct offsets gained from a second patch test.

The qpd files were opened within the Processing Manager software, utilising Validator. This displayed the survey lines either singly or en-mass, as plan views, cross sections and longitudinal profiles, enabling detailed manual editing down to individual pings where required.

Initially two final sounding grids were created: one encompassing all the data, gridded at a 10 x 10 m cell size, and the second concentrating on the offshore eastern Aigion Fault tip, gridded at a 1.5 x 1.5 m cell size. These grids were then exported as points files. Other grids were created at later stages to enhance detail in certain areas. The points files were plotted using Unix and GMT, and displayed using Ghostscript.

### 2.5.3 Data Quality

Due to problems with starboard outer beams interfering with the keel of the survey vessel, and mis-match between swaths due to steep topographic gradient changes, manual editing of all data was completed six times to remove anomalous pings and spikes. However the data, when compiled in its entirety, still showed evidence of bad data points and mismatch between certain lines despite manual filtering. It is thought that the SVP used did not show the true complexity of the velocity changes in the upper shallow water layers, causing some disparity between swath overlaps at the break of slope. Therefore, two Butterworth filters were also applied (see Appendix C), one to the whole dataset, in the z plane (depth), at medium – low level. The second was only applied to the line initially collected with the incorrect offsets, in the x,y planes (Lat/Long) at high level.

Despite some bad data points remaining, the overall data quality was excellent. Numerous features were revealed in great detail, horizontally resolving structures of only a few metres in size in the detailed survey area. The resolution of the dataset, and 100% coverage in many areas, meant that the cell sizes of any grids created were very flexible, ranging from large (10 m x 10 m) giving an overview of an area, to much smaller (1.5 m x 1.5 m) enabling detailed analysis of features within any one area. Spike filtering of the regional dataset was later undertaken to further improve the data quality for the regional multibeam bathymetry dataset (Hicks, 2004).

As with the MCS dataset, no corrections were made to the multibeam data with respect to tidal influences over the course of the survey period. The tidal range during surveying was <0.5 m whereas the depths being surveyed were predominantly >400 m during the regional survey. See section 2.4.3 for further details regarding the possible need for static corrections to be applied to the datasets, and why it was decided not to apply these corrections in this survey.

## 2.6 Strike Projection

The MCS reflection profiles and multibeam bathymetry data were collected in order to quantify fault activity and variability in displacement through time. It is important therefore to ascertain the strike projection used, onto which the fault – horizon contact points identified in Chapter 4 will be projected. Figure 2.17 shows the main faults identified, and their orientation to North. The dominant fault orientation is east –west, with the survey lines running perpendicular to this in a north-south orientation. Therefore the simplest strike projection to use is east-west, running parallel to the dominant fault orientation. The local origin chosen, which will be used in all further quantitative analysis (Chapter 6), is 599700 / 4233500 UTM (Zone 34N).

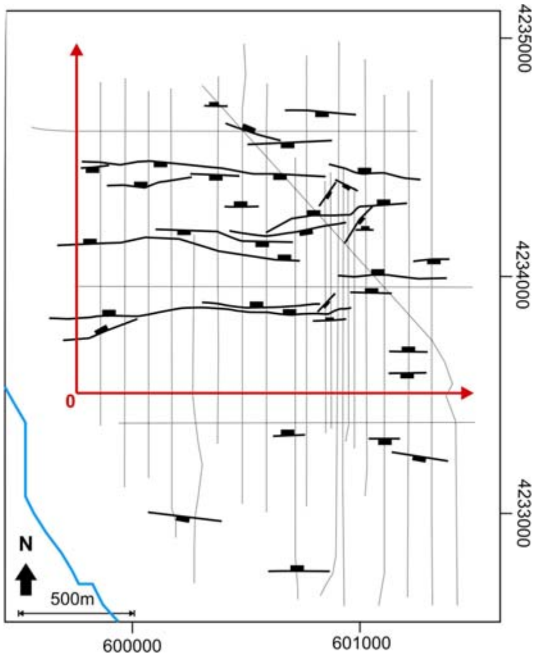

**Figure 2.17:** Map showing the faults identified from the MCS reflection profiles and multibeam bathymetry datasets (Chapters 4 and 5), and their positioning relative to the MCS lines and north. The red lines show the strike projection used, with “0” representing the local origin chosen.

# Chapter 3

## Active Faulting within the Offshore Western Gulf of Corinth, Greece: Implications for Models of Continental Rift Deformation [1]

Discrimination between different lithospheric extension models focusing on the roles of low-angle vs. high-angle faulting, and how strain is distributed, requires high-fidelity imaging of brittle deformation. High-resolution seismic reflection and multibeam bathymetric data in the western Gulf of Corinth continental rift were collected to establish the contribution of offshore faults to extension. Onshore fault slip here is significantly less than expected from geodetic strain rates. The rift at this location is a half-graben tilted to the north by S-dipping faults within the uppermost crust. A basement horst on the northern margin is uplifted by the North and South Eratini faults, and the axial channel is fault controlled. Subsided lowstand shorelines in the hanging wall of the North Eratini and the well-studied Aigion fault suggest that the faults have similar displacements. Summed extension from the four major faults across this part of the rift (Eliki, Subchannel, South Eratini, North Eratini) is ~8–16 mm/yr, thereby reconciling geologic and geodetic data sets. Distributed deformation across isolated multiple faults can model this part of the rift without recourse to, and potentially incompatible with, an underlying low-angle detachment.

### 3.1 INTRODUCTION

The Gulf of Corinth is an active continental rift (Figure 3.1) with high levels of seismicity and rapid extension. Rifting began in the Pliocene–Pleistocene, and southern margin fault systems stepped north with time, uplifting formerly subsiding hanging-wall deposits. The rift has been described as a half-graben with rift-controlling faults on the southern margin. Until recently the offshore gulf has not been explored systematically, although the presence and significance of offshore faults have been discussed (e.g., Stefatos et al., 2002).

Models of continental extensional deformation have distinguished between (1) strain focused on a few discrete structures between rigid blocks, and (2) broadly distributed strain over a number of faults or within fault blocks. Non brittle deformation may also be partially accommodated by the lower crust. Low-angle normal faulting and subhorizontal detachments have been identified or inferred in many rift settings, including the Corinth rift (e.g. Rigo et al., 1996).

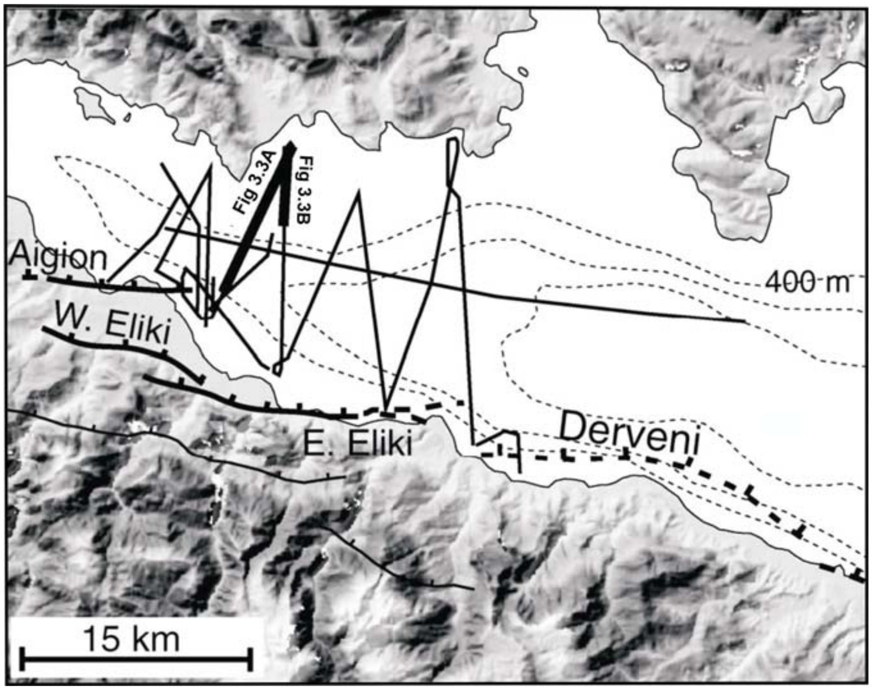

**Figure 3.1:** Map illustrating known onshore faults and multichannel Sparker seismic tracklines. Locations of Figures 3.3A and B are indicated to provide a contextual setting for these figures. Bathymetric contours are every 200 m. (After McNeill et al., 2005a).

Geodetic measurements indicate an increase in total N-S rift extension from 0 to 5 mm/yr in the east of the Corinth rift to 10–15 mm/yr in the west (Clarke et al., 1998; Briole et al., 2000). Onshore geomorphic and paleoseismological studies of southern margin faults provide estimates of slip rates. In the eastern gulf, individual faults may accommodate the majority of extension (e.g., Armijo et al., 1996). In the western gulf, slip rates of the major onshore faults are significantly less than those predicted by geodesy.

Quaternary deposits in the footwalls of the Eliki and Aigion Faults are uplifted at ~1 mm/yr, and potentially contribute 2–7 mm/yr of extension (McNeill and Collier, 2004; De Martini et al., 2004). These results suggest that major offshore faults may accommodate extension within the western gulf if deformation rates over different time scales ($10^1$–$10^2$ vs. $10^3$ – $10^5$ yr) are compared (Stefatos et al., 2002; Moretti et al., 2003; McNeill and Collier, 2004). Until now, the geometry and contribution of active faults on the northern margin have remained unquantified.

To test models of rift deformation, a high-resolution geophysical survey was conducted in the western-central gulf to constrain fault geometry and to quantify strain across these structures using lowstand shoreline markers.

## 3.2 METHODOLOGY

High-resolution seismic reflection and multibeam bathymetry data were collected in July 2003 under the direction of the Universities of Patras and Southampton. Seismic acquisition involved a sparker source and 60 channel streamer, with N-S across-rift profiles (Fig. 1). Processing applied to multichannel seismic data included deconvolution, stacking, bandpass filtering, and time migration. A Reson Seabat 8160 50 kHz multibeam echosounder was used to collect bathymetric data, with a $150^0$ swath across track with 126 beams. Sonar positioning was calculated by differential global positioning system and an inertial navigation system. Multibeam data are gridded with a 10 m cell size (Figure 3.2).

## 3.3 ANALYSIS

### 3.3.1 Seafloor Geomorphology and Sediment Transport

The morphology of the west-central Gulf of Corinth is dominated by slope canyon systems feeding an axial channel which is only present within this part of the gulf (Figure 3.2). Canyons dominate the southern margin but are rare on the northern margin. Where fault traces are positioned just offshore with a narrow shelf and steep slope, canyons are not developed, and the slope is dominated by mass wasting (Ferentinos et al., 1988).

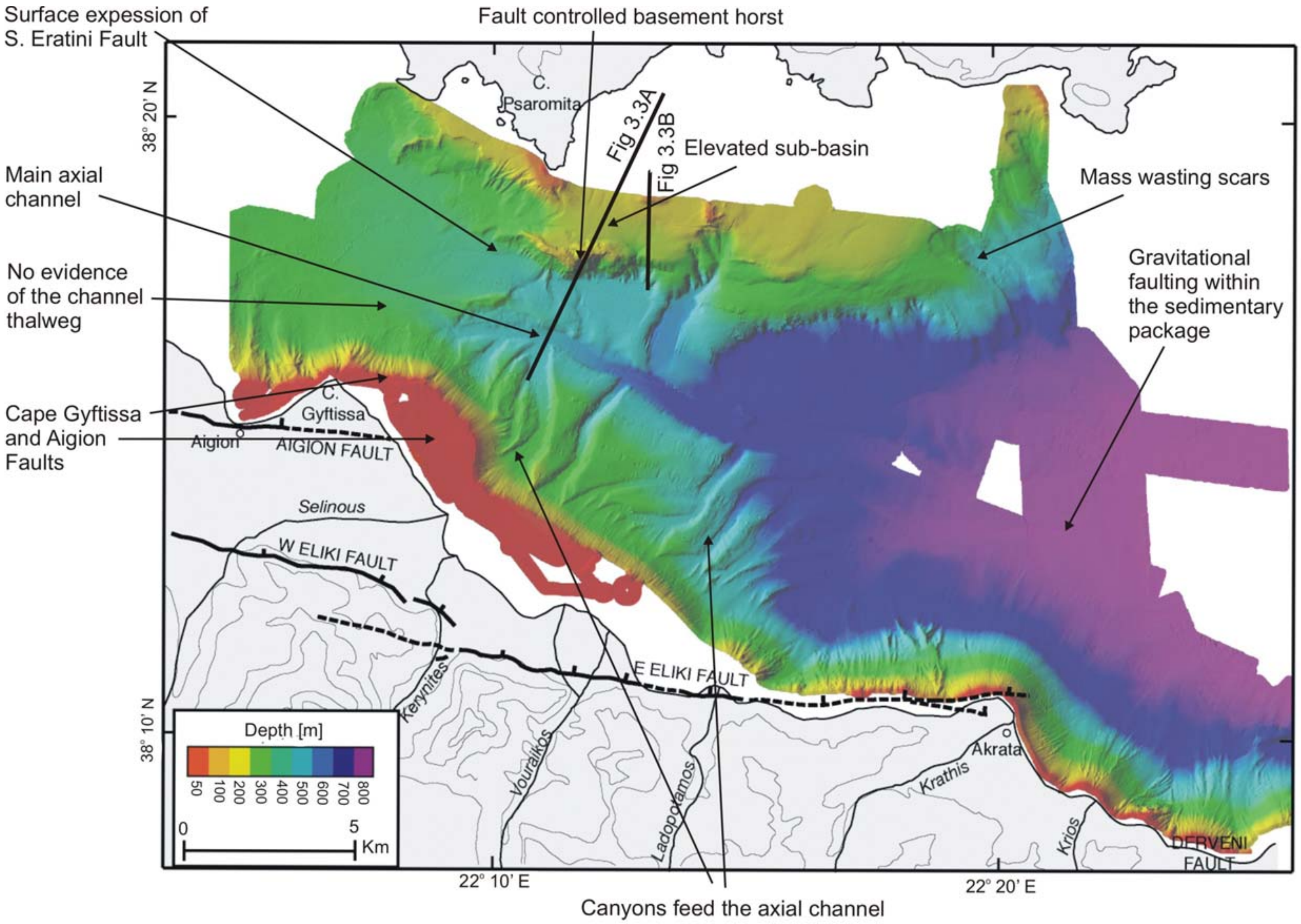

Figure 3.2: Regional 8160 Swath Bathymetry collected by the MV Vasillios G, showing locations of southern onshore faults (McNeill and Collier, 2004). Prominent features discussed in the text have been indicated.

### 3.3.2 Offshore Fault Geometry

Multibeam and seismic reflection data (Figures 3.2 and 3.3) have been used to compile an updated map of active faulting within this part of the rift (Figure 3.4). Stratigraphic markers (lowstand shorelines and deltaic clinoform sequences, Figure 3.3) from glacial Lake Corinth can be used as strain markers for fault displacement. A 60±70 m sill at the entrance to the gulf (Perissoratis et al., 2000) controls the lowstand level of Lake Corinth and a change from lacustrine to marine conditions (Collier et al., 2000). The timing of this transition is determined from eustatic sea-level curves (e.g., Siddall et al., 2003) and by dated core samples.

The offshore extensions of the southern bounding faults and intervening transfer zones are imaged in multibeam and seismic data (Figures 3.2 and 3.4). The Aigion Fault tip extends several kilometers eastward onto the shelf and slope, with no clear deformation in the zone between it and the Eliki fault to the south. The overlapping Eliki and Aigion faults are contemporaneously active over at least 5 km and as much as 10 km along fault (e.g., De Martini et al., 2004), which is rare for the Corinth fault systems, but the tapering displacement profile of the Aigion Fault suggests that it is recently established. In the transfer zone between the eastern Eliki and Derveni faults (Figures 3.2 and 3.4), displacement on the East (E) Eliki fault decreases rapidly as no fault trace is observed offshore. Strain must be transferred rapidly from the Eliki to Derveni Faults, suggesting that they are linked at depth, and act as one fault system. A splay of the Derveni Fault is imaged in multibeam data supporting an offshore location (Figure 3.4).

No transfer zone faulting was imaged here, despite the identification of N-S faults onshore displacing terraces near Akrata (McNeill and Collier, 2004). The E-W Cape Gyftissa Fault, 2 km north of the Aigion Fault (Figures 3.2 and 3.4), is imaged in both bathymetric and seismic data and may continue westward across Aigion harbor. Displacement of the transgressive horizon (11 ±13 ka) following the Last Glacial Maximum (LGM) gives an approximate slip rate of 1 ±1.5 mm/yr.

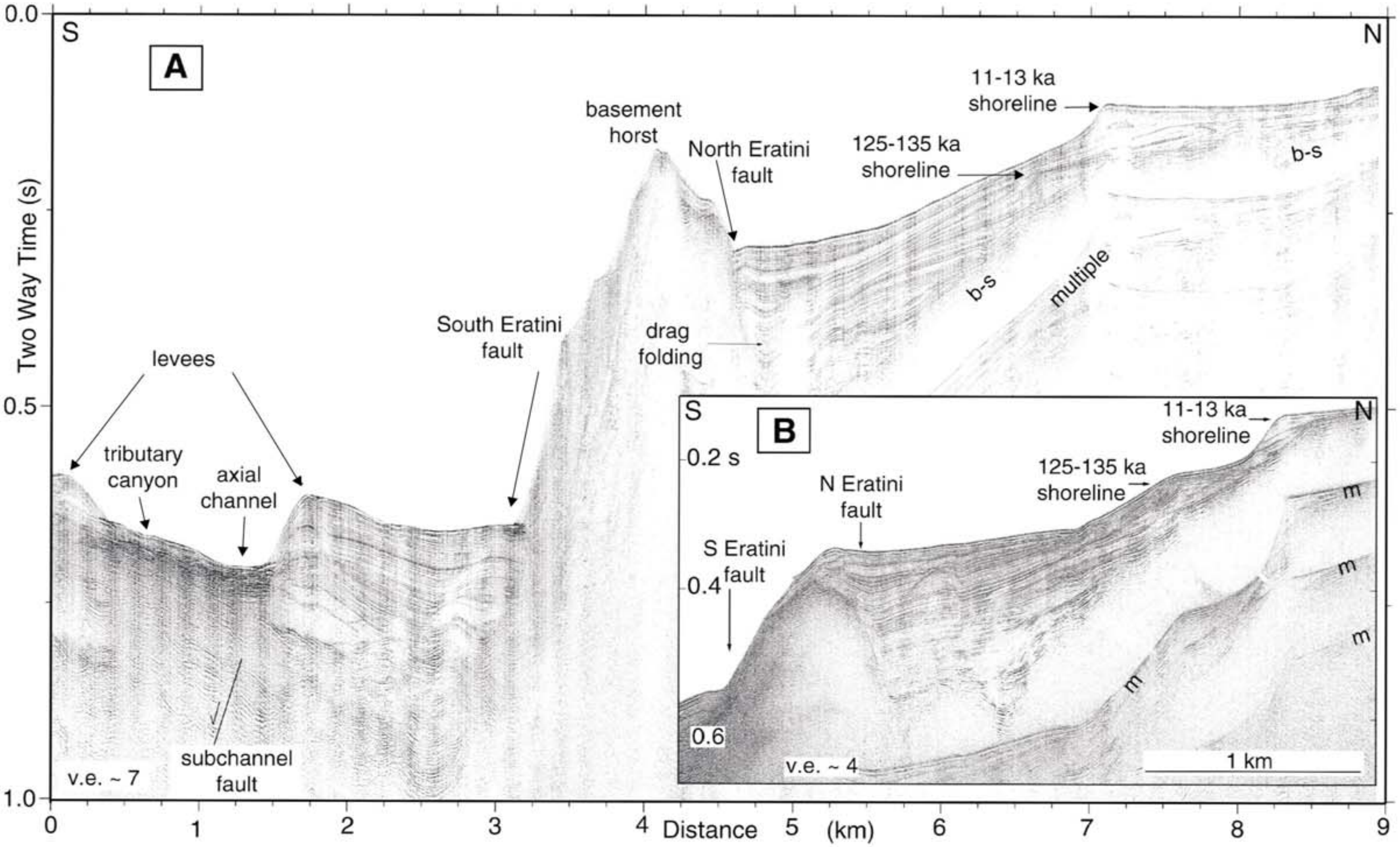

**Figure 3.3: A =** Seismic line 11 across fault-controlled axial channel and northern margin of Gulf of Corinth, showing major fault-controlled basement horst with deltaic sediments ponding behind. Sequence stratigraphic interpretation of these sediments reveals lowstand clinoform sequences and shorelines of Lake Corinth subsiding in hanging-wall of North Eratini fault. Note northward stratigraphic tilt and growth strata associated with South and North Eratini faults (b-s - basement-sediment contact; v.e. - vertical exaggeration). **B =** Inset shows northern section of seismic line 10 across elevated subbasin showing details of stratigraphy used to quantify fault displacement. Shorelines represent termination of clinoform deposition following stages 2 and 6, ca 11-13 and 125-135ka respectively (m-multiple). See Figure 1 for locations.

No major basement-offsetting faults were identified in our data between the southern bounding faults discussed here and the axial channel. Other data sets, penetrating to basement in all locations, appear to support this hypothesis (e.g., Goodliffe et al., 2003). The morphology of the margin suggests that steep slopes generated by fan morphology and mass wasting on steep slopes (Figure 3.2) may have previously been misinterpreted as multiple N dipping fault traces.

A S-dipping fault is identified beneath the axial channel, suggesting fault control (Figure 3.3A). This fault is also observed in deeper penetrating multichannel seismic data that confirm basement offset (e.g., Goodliffe et al., 2003), and in other seismic data sets (Stefatos et al., 2002).

The northern margin is dominated by a basement horst (Figures 3.2, 3.3 and 3.4) uplifted by the North (N) and South (S) Eratini faults (after the nomenclature of Stefatos et al., 2002; km 3, 5, Figure 3.3). The horst is most prominent near the Psaromita Peninsula and is progressively buried and reduced in topography to the east and west, with faults as long as 15 km. Sequence stratigraphic interpretation, hanging-wall growth strata, tilted sediment wedges, drag folding, and seafloor displacement all indicate recent and continuous activity of these faults, but the N Eratini Fault is relatively young, only active in the past ~0.4 m.y. (Figure 3.3). N-dipping strata in the hanging walls of the subchannel and S Eratini fault (km 1–3, Figure 3.3) produce a half-graben geometry (e.g., Figure 3.3A) dominated by these S-dipping faults (see also Stefatos et al., 2002; Goodliffe et al., 2003).

Late Pleistocene lowstand deltaic clinoform sequences and shorelines (also identified by Lykousis et al., 1998) have subsided in the hanging wall of the N Eratini Fault (Figures 3.3A, 3.3B). The transition from subhorizontal to dipping strata approximates past sea level, and therefore the cap of this sequence represents lake level as the Corinth sill was flooded. This occurred ca. 11–13 ka, following the LGM (stage 2), and ca. 125–135 ka, after stage 6 (Siddall et al., 2003). These two shorelines are now at ~80–95 m and 150–165 m on lines 10 and 11 (Figure 3.3; see also Lykousis et al., 1998), suggesting subsidence rates of ~1–3 mm/yr for the past 11–13 k.y. and ~0.6–0.9 mm/yr for the past 130 k.y. Subsidence takes place ~1–2 km from the surface fault trace.

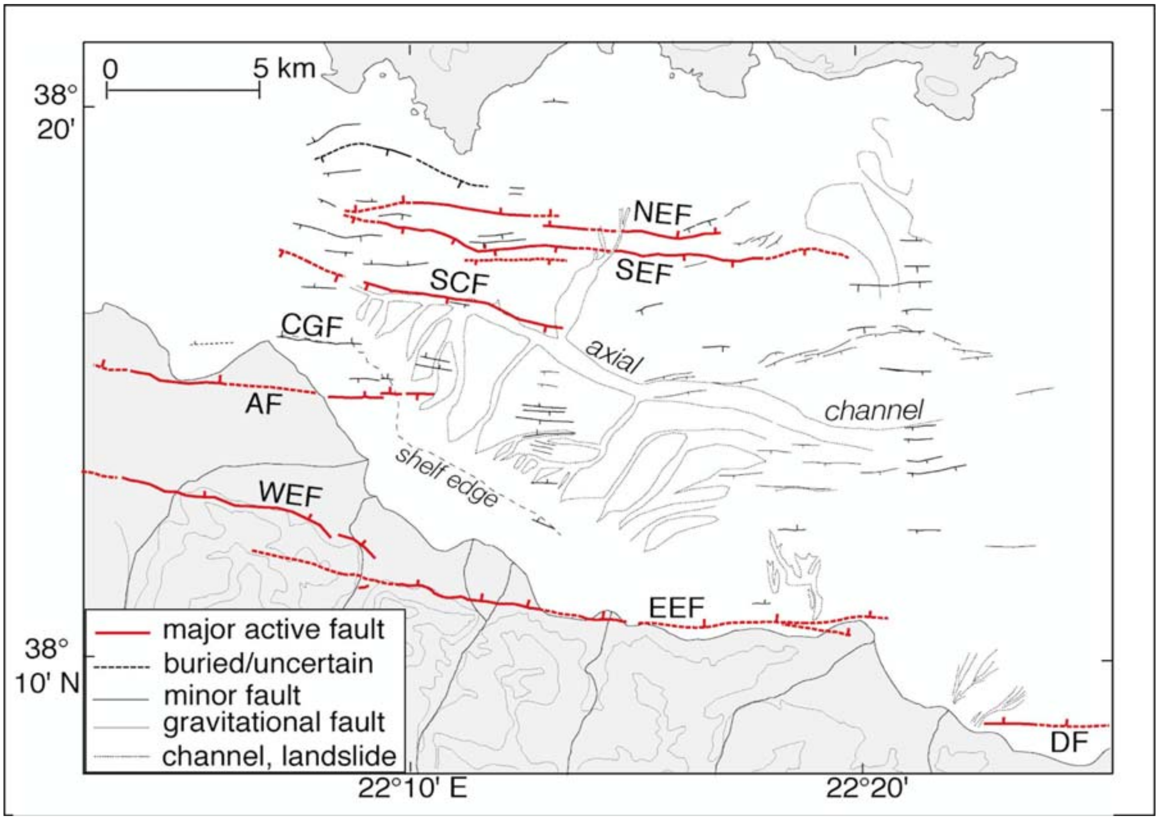

**Figure 3.4:** Interpretation of faults and other morphological features. Onshore faults are from McNeill and Collier (2004). AF = Aigion Fault, WEF = Western Eliki Fault, EEF = Eastern Eliki Fault, CGF = Cape Gyftissa Fault, SCF = Sub-channel Fault, SEF = South Eratini Fault, NEF = North Eratini Fault and DF = Derveni Fault (After McNeill et al., 2005a).

Subsidence rates in the N Eratini hanging wall are similar to those in the hanging walls of faults with constrained slip rates, e.g., the Aigion Fault. Shorelines in the Aigion hanging wall are at very similar depths to those in the N Eratini hanging wall, and a similar distance from the fault trace. Therefore, one would expect these faults to have comparable slip rates if fault geometry and mechanics are similar.

## 3.4 DISCUSSION AND CONCLUSIONS

New geophysical data suggest that northern margin faults within the western Gulf of Corinth have slip rates comparable to those of the southern bounding faults (Aigion and Eliki). Uplift rate data from the Aigion Fault (De Martini et al., 2004), comparison with the E Eliki Fault (McNeill and Collier, 2004), and reappraisal of the uplift:subsidence displacement ratio from reprocessed seismic data (e.g., Sachpazi et al., 2003) support a slip rate of ~4–6 mm/yr for the Aigion Fault and therefore for the N Eratini Fault. The recent rate of slip of the S-dipping S Eratini Fault should be similar to that of the N Eratini Fault. The slip rate of the subchannel fault is unconstrained but clearly significant. The northward tilt of basin sediments supports the dominance of the northern margin S-dipping faults in the longer term, with N-dipping faults behaving as antithetics. A combination of N- and S-dipping faults requires interaction at depth, which should be considered by future dislocation modeling.

These results confirm that strain is distributed across a number of major faults within the western rift. To determine the contribution of offshore faults to regional extension, we sum the horizontal components of slip at ~$22^{o}$ 15’ E. The four major faults are the E Eliki, N Eratini, Subchannel, and S Eratini. We assume that the last two faults have slip rates and dips similar to those of the Aigion fault, and therefore an approximate extension rate per fault of 2–4 mm/yr yields a total extension rate of ~8–16 mm/yr. This encompasses recent geodetic measurements of extension of 10–15 mm/yr and suggests that geologic and geodetic rates of deformation can be reconciled in this part of the rift.

Subsidence on the northern coast during the 1995 Aigion earthquake could have been generated by movement on the N Eratini Fault, although Bernard et al. (1997) preferred a N dipping fault plane source 2–3 km south of the axial channel. We find no evidence for a major structure at this location.

Accommodating net strain on a series of high-angle faults (>$30^{0}$) renders a low-angle detachment (e.g., Rigo et al., 1996) at depth superfluous to match extensional strain. Furthermore, if all the offshore faults cut the entire seismogenic layer, they are geometrically incompatible with a subhorizontal N-dipping detachment. A detachment is also incompatible with microseismicity data (Hatzfeld et al., 2000). Microseismicity studies show distributed seismicity across the rift with potential nodal planes compatible with both N or S dipping faults (Hatzfeld et al., 2000). Evidence for the former is stronger when examining some large events (e.g., 1995 Aigion) over the past few decades, but may not be representative of all, or longer term, seismicity. Regardless of the precise nature of the seismic activity of these offshore faults, they clearly dominate net strain across the rift.

---

1) This chapter appeared as a paper in *Geology*; April 2005; v.33; no.4; p.241-244; doi:10.1130/G21127.1. The authors are L.C. McNeill, **C. J. Cotterill**, T. J. Henstock, J. M. Bull, A. Stefatos, R. E. Ll Collier, G. Papatheodorou, G. Ferentinos and S. E. Hicks. Contribution to the paper is indicated in the listed order of the authors. Processing and preliminary interpretation of the multibeam dataset was undertaken by C. J. Cotterill.

# Chapter 4

# Stratigraphic Framework and Horizon Identification

This chapter will describe the strong, laterally extensive seismic horizons and stratigraphic units that are used in all further analysis of fault development across the Aigion Shelf. In order to accurately quantify spatial fault geometry and development (Chapter 5) and any variability in fault displacement rates (Chapter 6), it is important to define the seismic character of the units and horizons identified, how they were identified, as well as constraints in estimating the ages of each horizon and potential sources of error.

Five sub-surface horizons have been mapped, based on their clarity, lateral extent and correlation across the survey area. The MCS reflection profiles show a layered stratigraphy, separated by distinct seismic horizons. These horizons are often offset by normal faulting. Figure 4.1 and Plate 1C show the faults identified within the MCS reflection profiles overlain onto the multibeam bathymetry of the survey area. The fault numbering scheme used in Figure 4.1 will be used throughout this thesis to accurately locate the faults or fault segments discussed.

## 4.1 SEISMIC STRATIGRAPHY

The Gulf of Corinth is bounded at its western end by the Rion Sill, currently lying at a depth of 60-65 m (e.g. Perissoratis et al., 2000). The sill means that during times of eustatic sea-level fall, the Gulf periodically becomes an isolated basin, before undergoing a transition back to marine conditions when sea-level rise overtopped the sill. Interactions between the sill and sea-level, combined with a high sedimentation rate due to re-working of uplifted deltaic deposits, results in clear, seismically and stratigraphically distinct units being formed, separated by acoustically strong reflectors, hereafter known as horizons. Based on their acoustic signature, three main units have been identified in this survey area. The following sections will detail the main characteristics of these units.

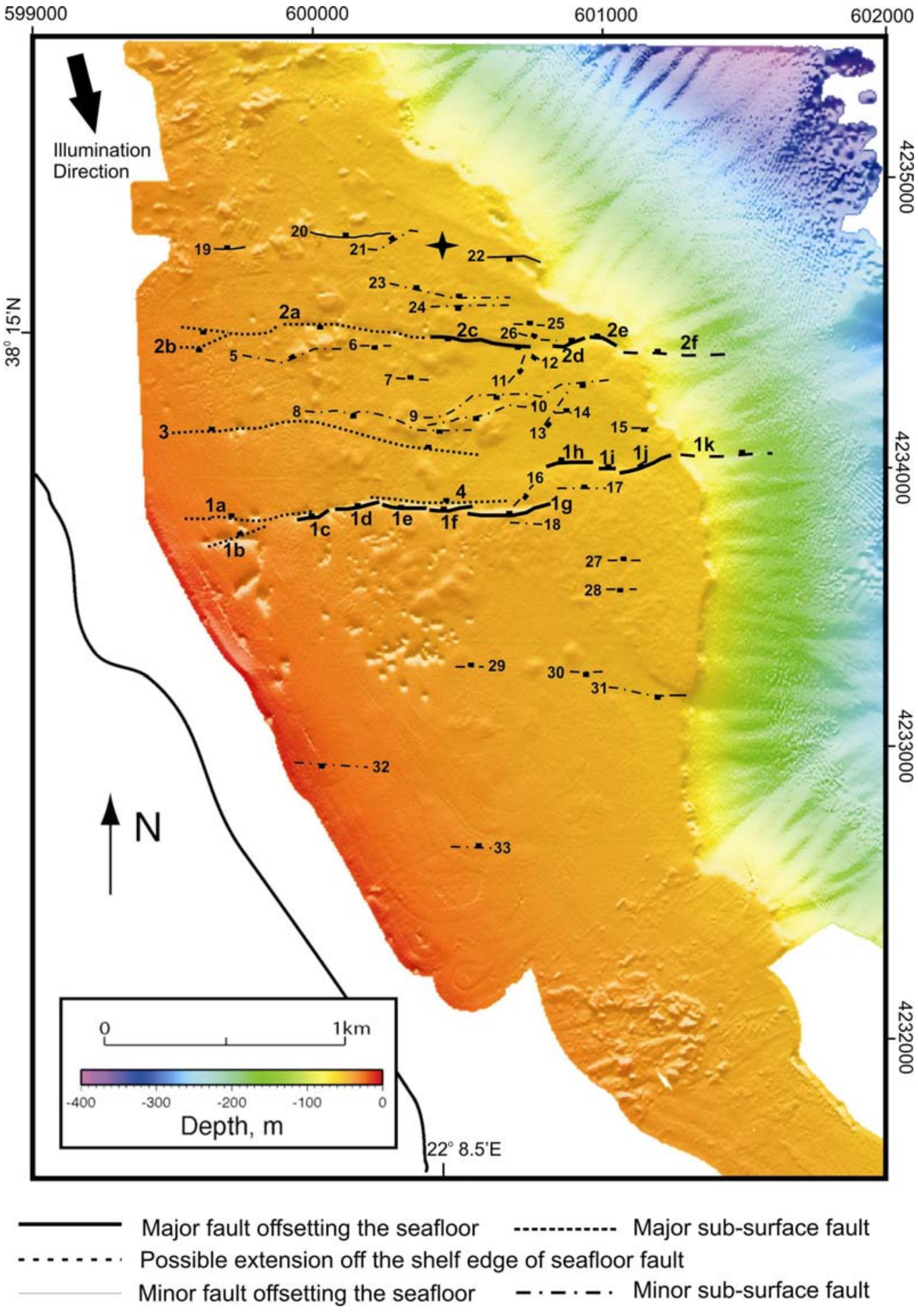

**Figure 4.1:** Sub-surface and surface faults and fault segments interpreted in IESX from the MCS reflection profiles, and overlain onto the multibeam bathmetry image. Black star indicates the location of the reference point discussed in the analysis of errors (section 4.2.4).

### Unit 3 and Horizon H5

Unit 3 (U3) is the deepest imaged package (Figure 4.2). It is characterized in its upper ~10 ms TWTT by a series of linear horizontal to sub-horizontal reflectors. Below this, the reflectors, identified as clinoforms, have a true dip of ~30$^{o}$. Variations observed in the apparent dip of these clinoforms (15$^{o}$ – 40$^{o}$) are the result of survey profiles running obliquely across the delta foresets. Beneath 110 ms TWTT, there is little primary energy returned, with data often masked by multiples. It is therefore not possible to estimate the depth to which these dipping reflectors reach, or whether the angle of dip varies with depth.

Horizon H5 forms the upper boundary to U3 (Figure 4.2). It has an overall NE trending dip direction, and in places is offset by normal faults (Figure 4.2D). However, the offset appears to be limited to the major faults imaged, including faults **1, 2** and **3** (Figure 4.1). Figure 4.2 indicates the position of these faults on Boomer line 406, located at CDP's 1400, 2800 and 2100 respectively. However, these may not be the only faults offsetting this horizon, as limited penetration and dipping internal reflectors may mask more minor fault displacements.

### Unit 2 and Horizon H4

Unit 2 (U2) is characterised by a broken, discontinuous seismic signature (Figure 4.3). There is a distinct change in seismic character at the base of this unit, where the reflectors become laterally continuous and horizontal to gently dipping, with H5 forming the base of this unit. Horizon H4 forms the upper boundary to U2 (Figure 4.3). It has a strong acoustic return, is often uneven, and is taken to be a laterally extensive ravinement surface that has been recorded across much of the Gulf of Corinth, formed during eustatic sea-level rise (e.g. Perissoratis et al., 2000; Collier et al., 2000; Lemeille et al., 2004). Horizon H4 has an overall NE trending dip direction, and shows significantly more displacement by normal S and N-dipping faults (Figure 4.3D) then horizon H5. The most prominent of these include faults **1**, **2**, **3** and **5** (Figure 4.1), located on the example MCS profile (Line 406) at CDP's 1450, 2800, 2050 & 2400 respectively (Figure 4.3A)

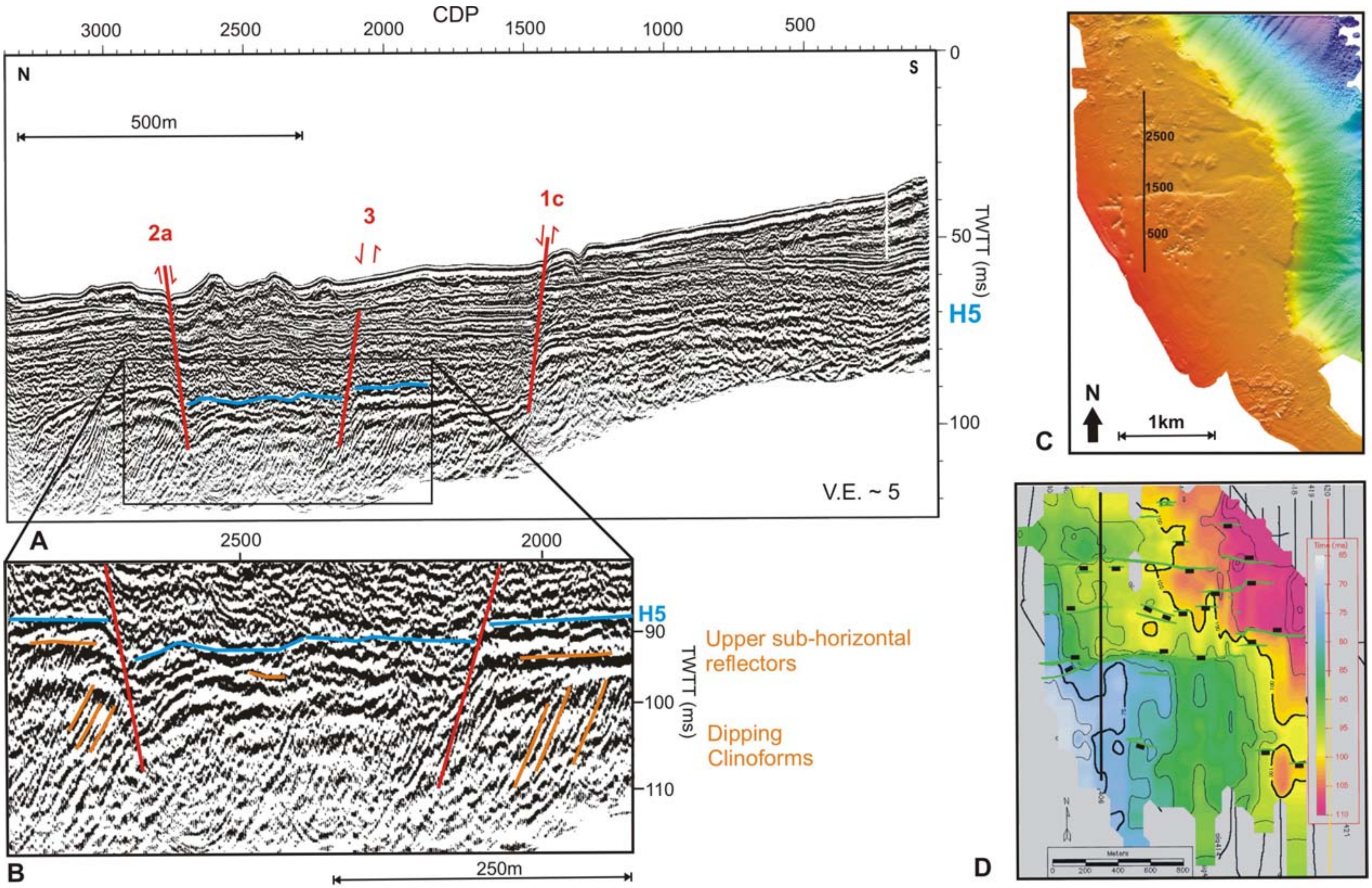

**Figure 4.2:** MCS reflection line 406 showing the location of Horizon 5, and the faulting offsetting this horizon. A**)** Annotated MCS reflection line. Numbers in red correspond to faults on Figure 4.1. B**)** Enlargement of a section of the profile, showing the seismic character of Unit 3, and how H5 bounds it at the top. C**)** Multibeam bathymetry showing the profile location. **D)**Time Structure map of H5**,** showing a NE trending dip to the horizon. The location of the MCS reflection profile is indicated.

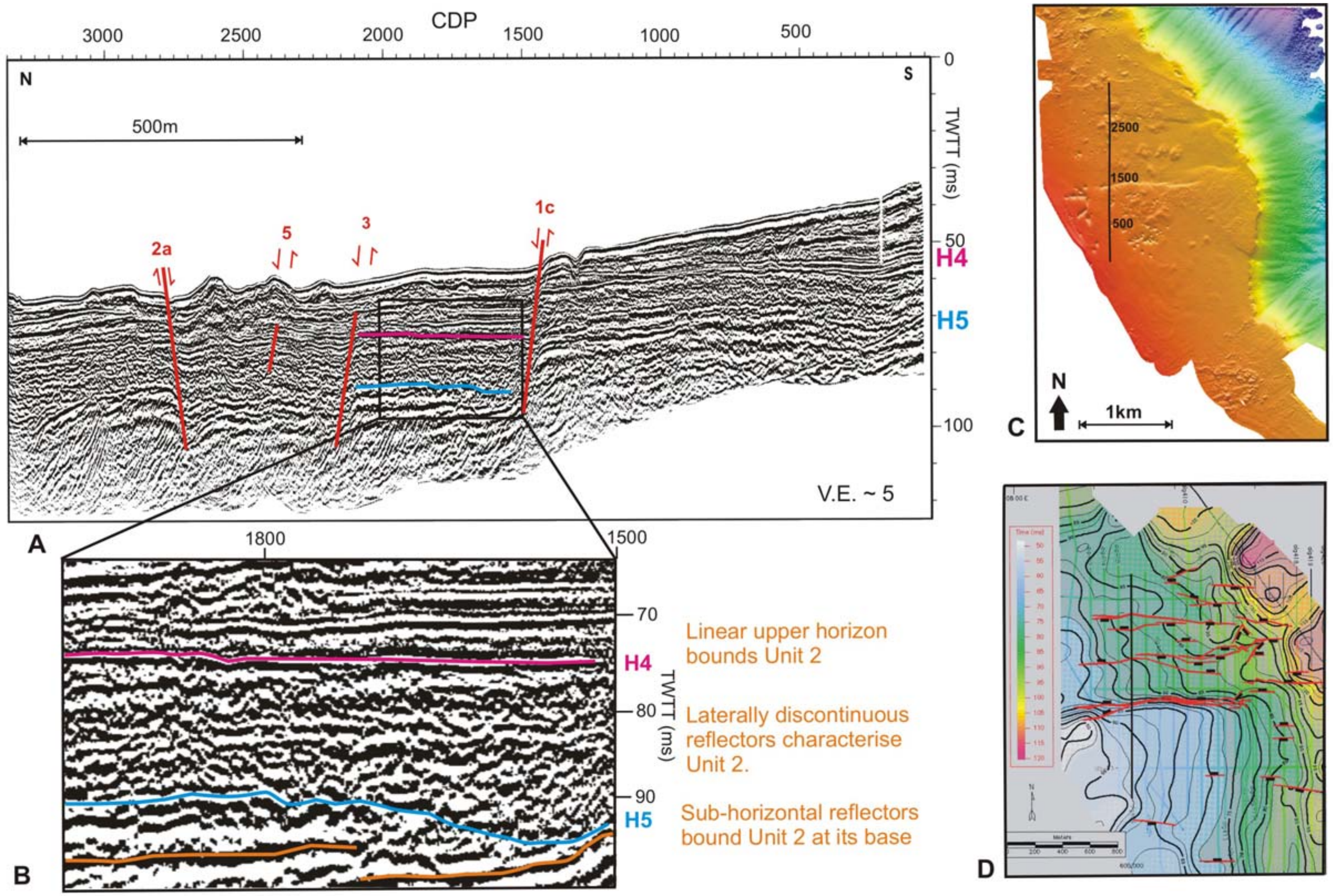

**Figure 4.3:** Boomer MCS reflection profile (line 406, Plate 1B) showing the location of Horizons 4 & 5, and the faulting offsetting this unit. A) Annotated MCS reflection line. Numbers refer to faults labelled in Figure 4.1. B) Enlargement of a section of the profile showing the seismic character of Unit 2, and how H4 and H5 bound the unit. C) Multibeam bathymetry showing the profile location. **D)** Structure map of H4 showing the NE trending dip to the horizon, and the influence of both major and minor faults. The location of the MCS reflection profile is also indicated.

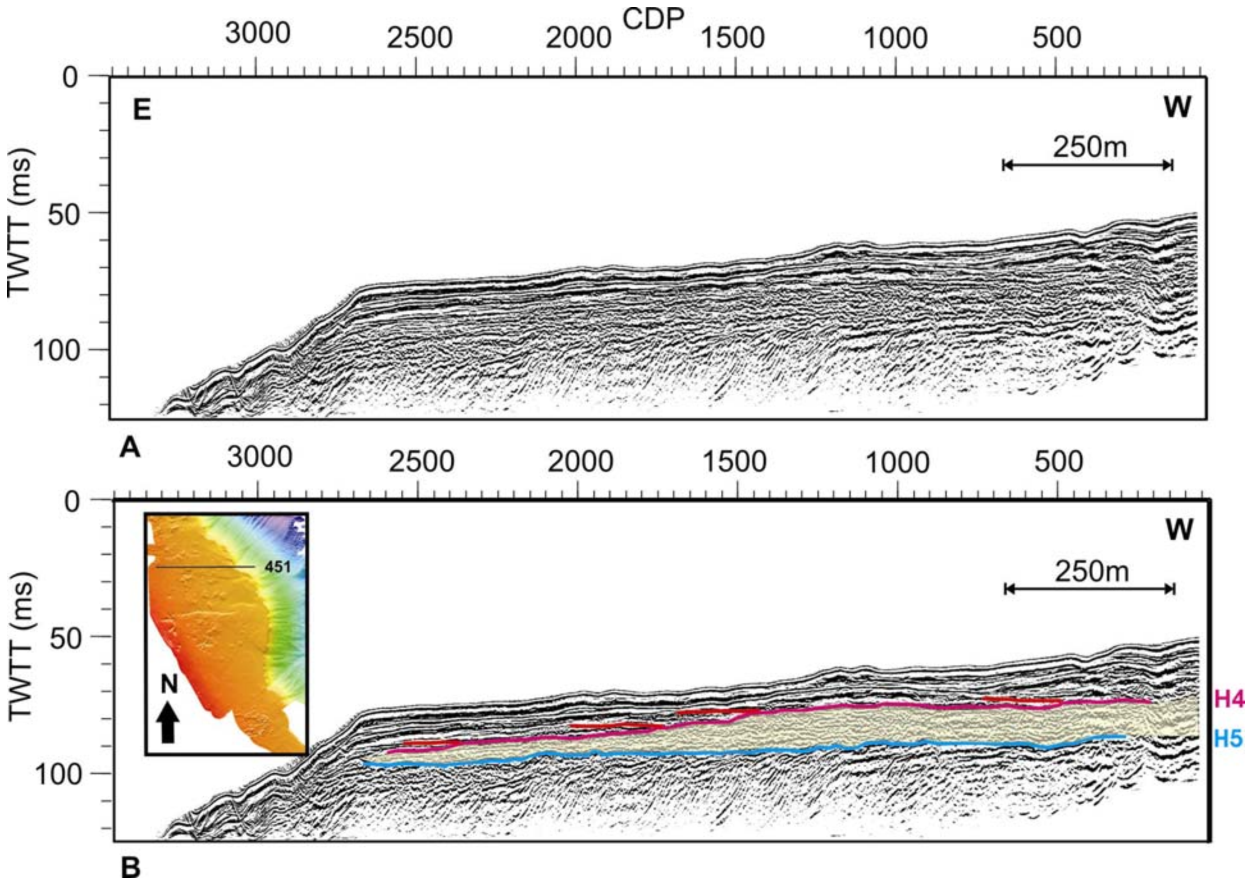

**Figure 4.4:** MCS reflection profile (Line 451) illustrating the thinning of U2 (shaded area) from west to east, nearshore to offshore, and onlap of sediments onto H4. **A)** un-interpreted profile. **B)** shows horizons H4 and H5 which bound U2 as it thins. It also indicates the reflectors from unit U1 onto H4. Profile location is indicated on the multibeam bathymetry inset.

Within the centre of a graben formed between the two major normal faults (**1** and **2**, Figure 4.1), the unit has a relatively constant N-S thickness, but it ranges in thickness from ~20 ms TWTT on the westernmost nearshore profiles, thinning eastwards to <10 ms TWTT at the shelf edge (Figure 4.4). The southernmost ends of some the MCS reflection profiles show U2 thinning in the footwall of a major N-dipping fault (**1**, Figure 4.1), before pinching out towards the shoreline (CDP's 2400-700, Figure 4.5). However, this pinching out is not evident in all the Boomer profiles, suggesting that this may be a localised feature, dependant on either sediment supply or erosion from fluvial sources during the lowstand and early trangression.

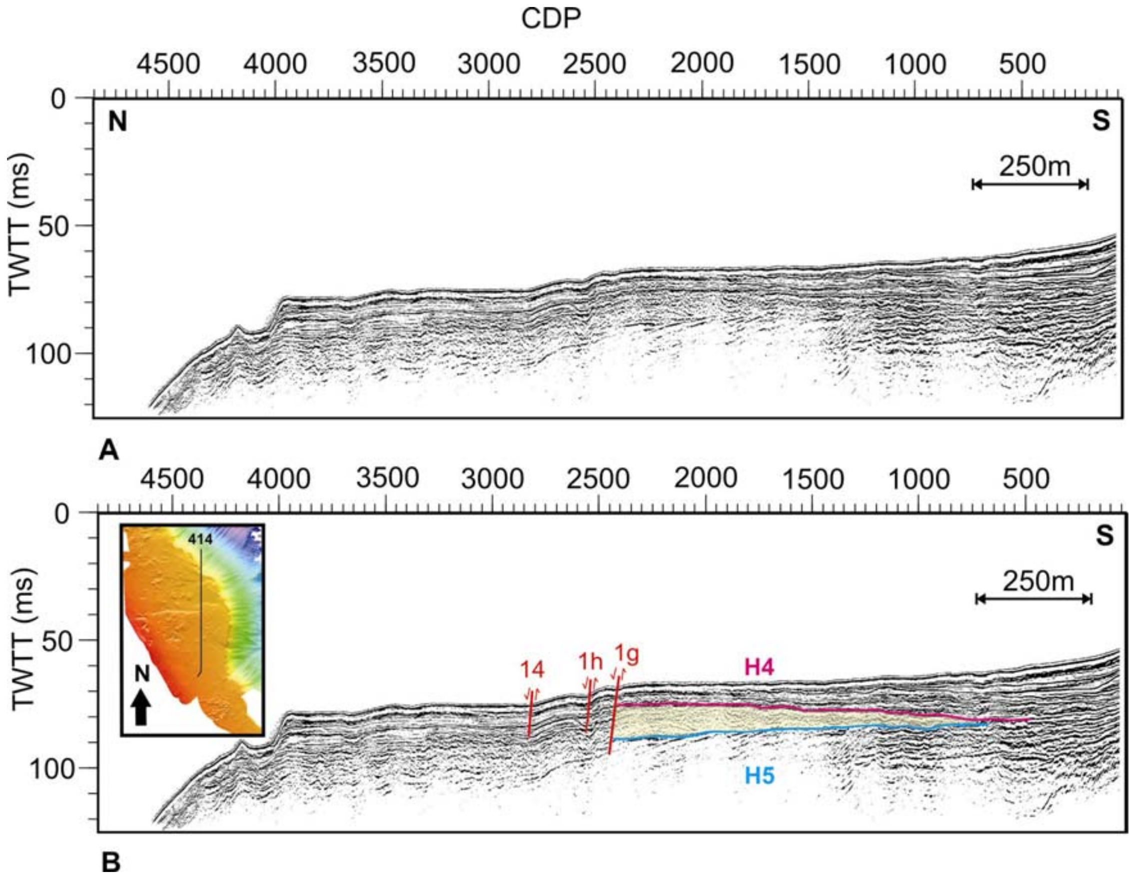

**Figure 4.5:** MCS reflection profile (Line 414, Plate 1B) illustrating the pinching out of U2 (shaded area) southwards towards the shoreline, that occurs on some of the profiles. **A)** un-interpreted profile. **B)** interpreted profile showing horizons H4 and H5 converging towards the south causing U2 to pinch out. Profile location is shown on the multibeam bathymetry inset.

### Unit 1 and Horizons H3 – H1

The youngest unit (U1) is generally characterised by linear sub-horizontal reflectors, bounding areas of acoustic transparency. Some of the inshore profiles show prograding reflectors in the footwall of the Aigion Fault (Figure 4.6). The unit has an overall trend of sediments thinning eastwards. N-S, the unit varies in thickness from 5 ms TWTT (~4 m) on the uplifted footwalls of major faults that offset the seafloor (e.g. fault **1**, Figure 4.1), to 25 ms TWTT (~20 m) within the graben formed by faults **1** and **2** (Figure 4.1).

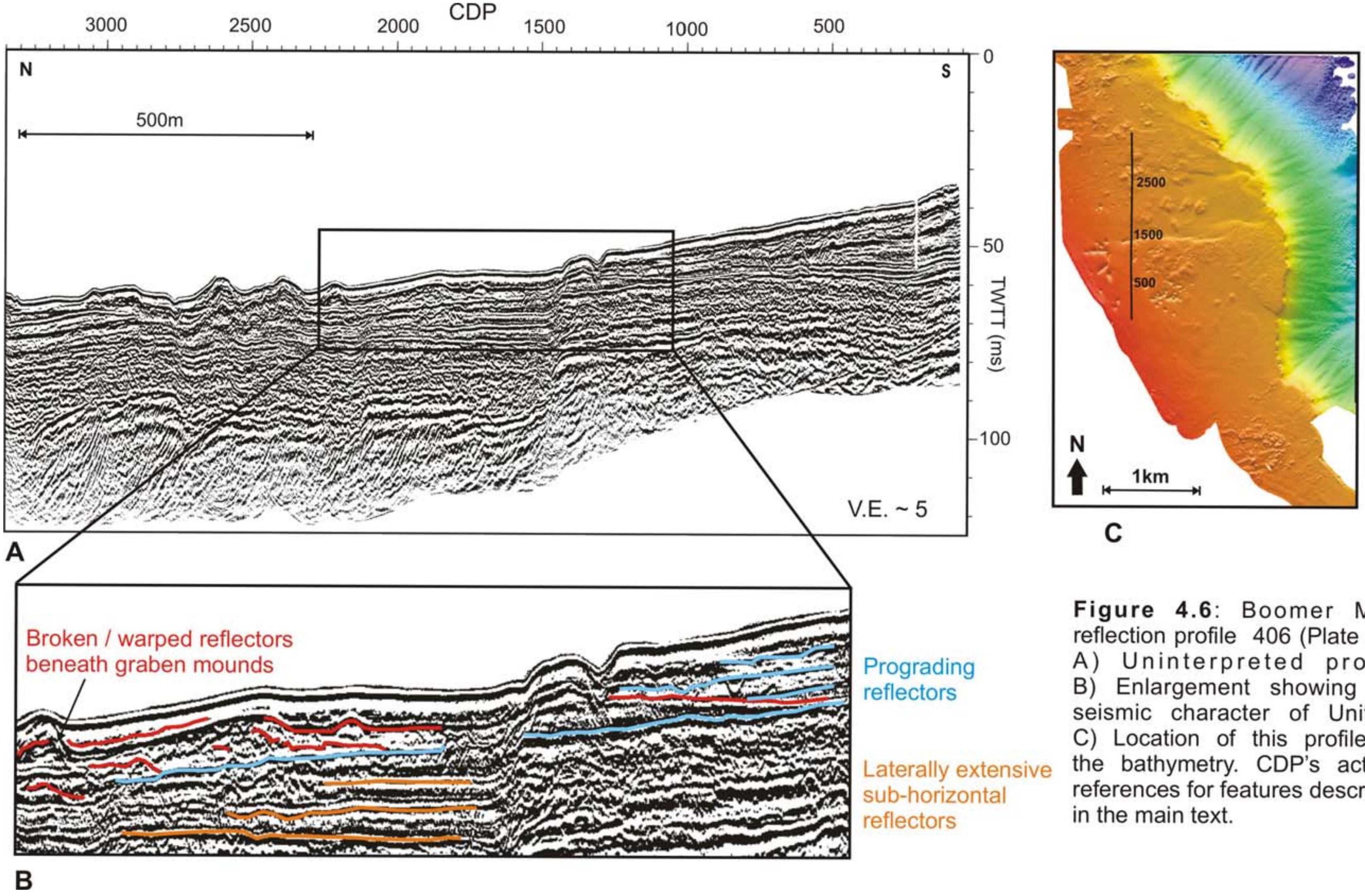

**Figure 4.6**: Boomer MCS reflection profile 406 (Plate 1B). A) Uninterpreted profile B) Enlargement showing the seismic character of Unit 1. C) Location of this profile on the bathymetry. CDP's act as references for features described in the main text.

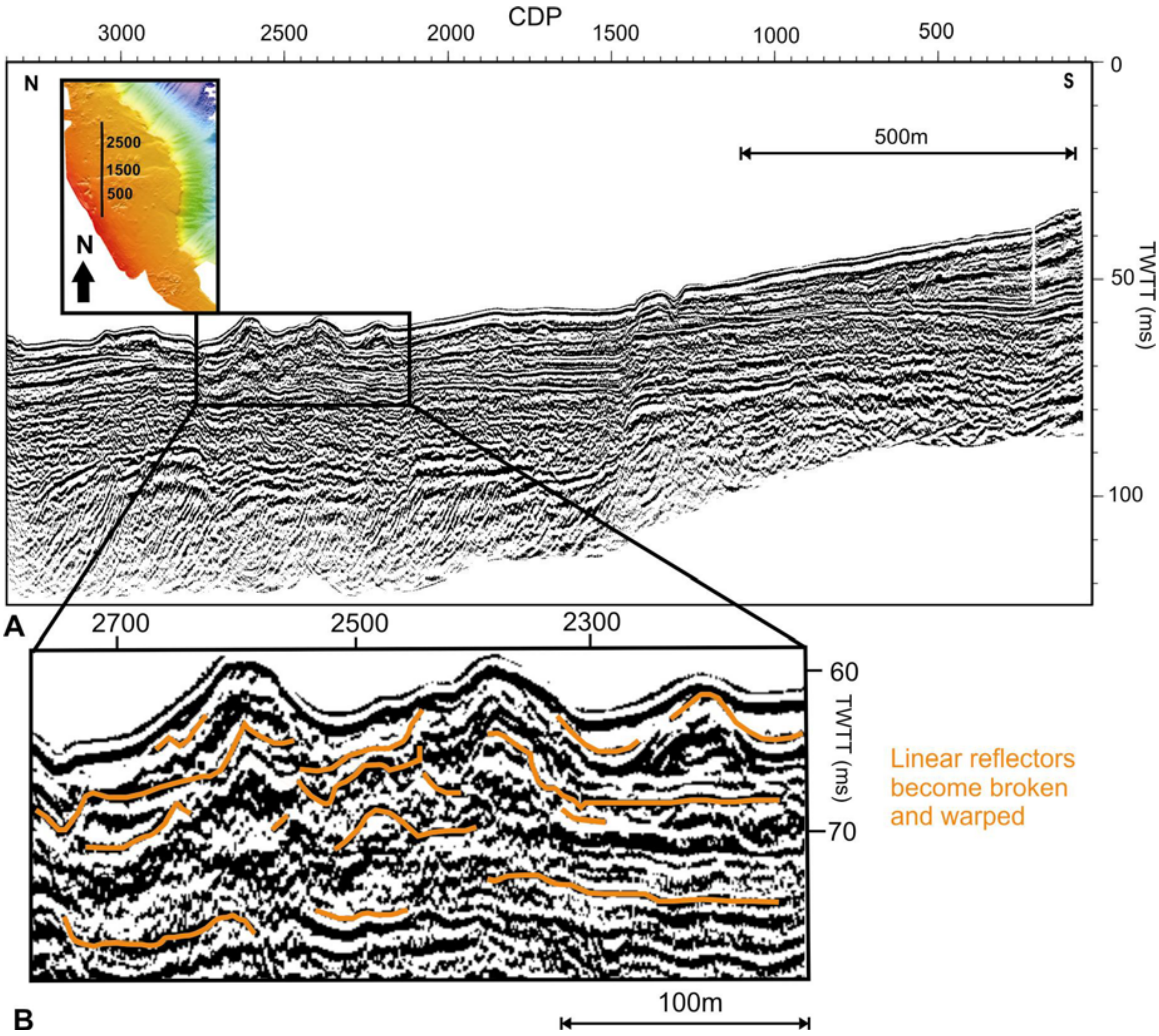

**Figure 4.7:** MCS reflection profile (Line 406, Plate 1C) showing the deformation of sediments beneath seafloor mounds. Profile location is show on the multibeam bathymetry inset in A.

Many of the youngest reflectors appear to be deformed and offset. This is especially noticeable beneath mound-like seafloor features (Figure 4.7). There is evidence of partially preserved sub-surface depressions (e.g. Line 411, CDP 225, Figure 4.8B) and mound-like features (e.g Line 411, CDP 3050, Figure 4.8C). These features are predominantly located on the younger reflectors within U1, forming laterally extensive deformation horizons. The sub-surface mounds are often onlapped by younger sediments (e.g. Line 411, CDP 3050, Figure 4.8C). These sedimentary features will be discussed in more detail in Chapter 7.

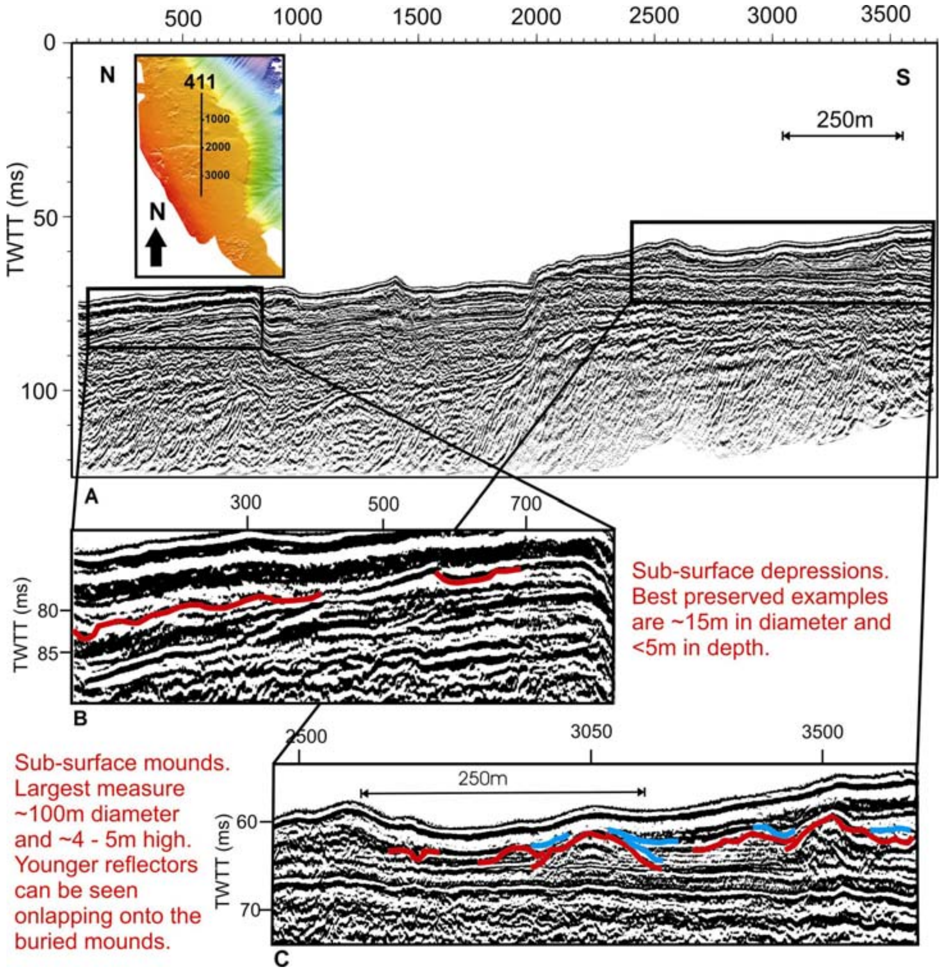

**Figure 4.8:** MCS reflection profile (Line 411, Plate 1C) showing examples of the sub-surface sedimentary features found within unit 1. **A)** uninterpreted profile showing profile location on the multibeam bathymetry inset. **B)** enlargement showing indications of preserved depressions. **C)** enlargement showing the sub-surface mounds.

Younger sediments are seen to onlap onto the ravinement surface (H4), which forms the base of this unit (e.g CDP’s 1500, Figure 4.4 & 2750, Figure 4.9). The southern ends of many of the MCS reflection profiles show thickening of unit U1 southwards, towards the shoreline (Figure 4.10). This is the exact opposite of the pinching out of U2 observed at the same locations (Figure 4.5), and may be related to sediment supply and sea-level changes. During the lowstand, when this area may have been sediment starved, this space would remain unfilled, resulting in U2 pinching out. Following marine inundation, an increase in sediment supply filled this space, due to proximity to the shoreline and terrestrial sediment sources, resulting in progradation and thickening of U1.

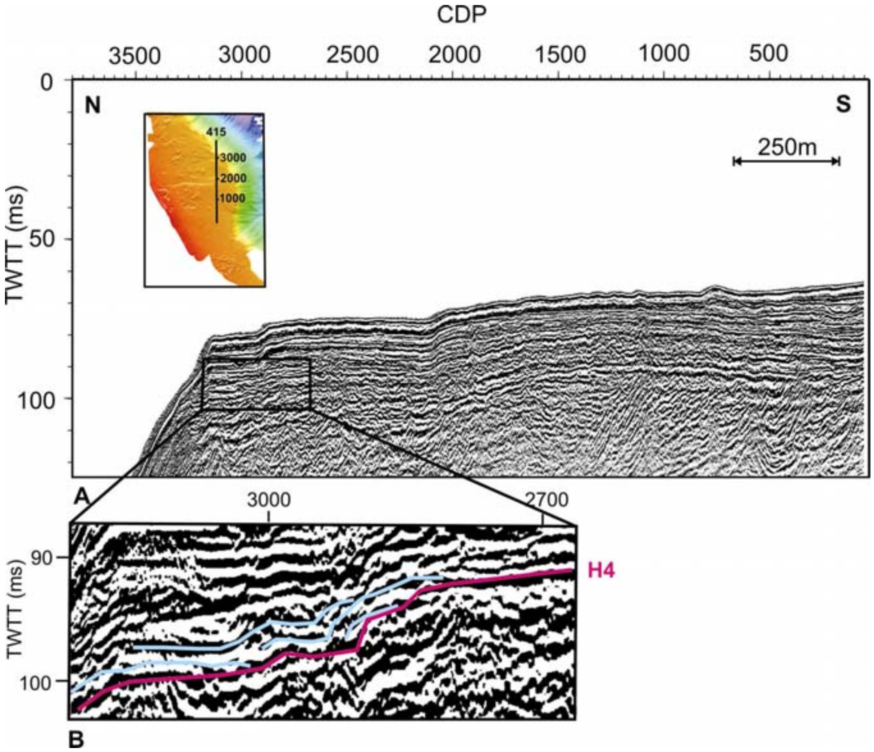

**Figure 4.9:** MCS reflection profile (Line 415, Plate 1C) showing onlap of sediments onto the ravinement surface at the shelf edge, deposited as sea-level rose and inundation of the shelf occurred. Profile location is shown on the multibeam bathymetry inset in A.

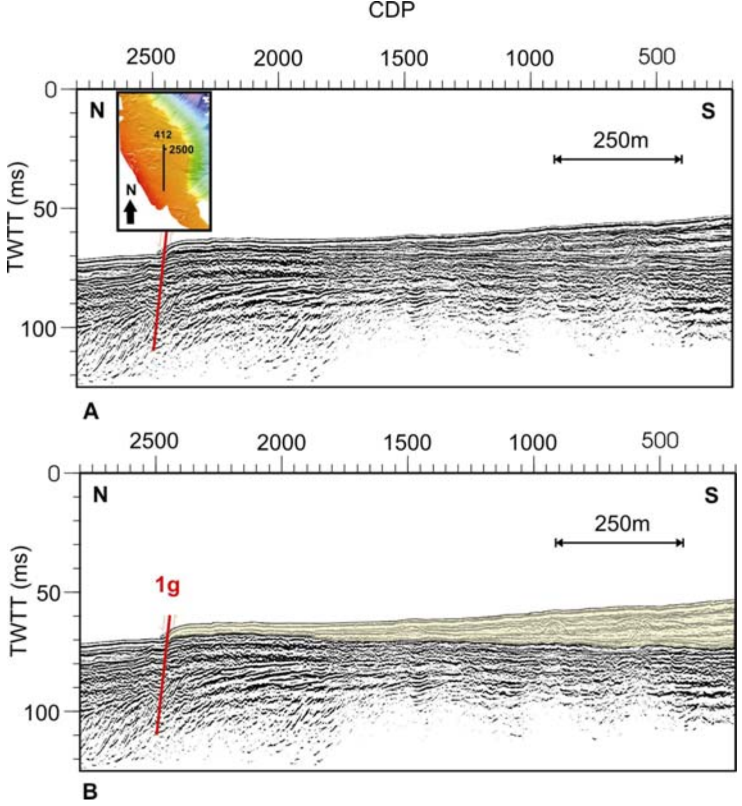

**Figure 4.10:** MCS reflection profile (Line 412, Plate 1C) showing the thickening of U1 southwards towards the present day shoreline.
Multibeam bathymetry inset shows the profile location; shaded area indicates U1; number corresponds to fault map (Figure 4.1).

Horizons H1 – H3 were identified from their strong acoustic character and lateral extent, within a unit that is often affected by deformation of horizons and areas of acoustic transparency. Figure 4.11 shows one of the MCS reflection profiles as it appears in the IESX package. The oldest horizon (H3) in this unit forms the upper boundary to a sub-unit which is characterised by a few strong laterally extensive reflectors (Figure 4.11), in a sub-unit that is otherwise transparent. H3 rapidly dies out to the south on the footwall of the Aigion Fault, onlapping onto the ravinement surface (H4). It is the horizon most affected by fault displacement within U1 (Figure 4.12C), and so the sediments beneath it are subject to localised thinning and thickening against the fault planes. Detailed analysis of sediment thicknesses on all horizons will be further discussed in Chapter 5, section 5.3.

Horizon H2 sits between two sub-units characterised by acoustically weaker reflectors (Figure 4.11), which have a laterally discontinuous, broken character. Its strong seismic return compared to the weaker returns either side of it suggest a possible change in grain size, or other physical properties including cementation.

Horizon H1 often appears to be associated with a band of “fogging”, where the reflectors situated immediately above it in U1 appear blurred. This may be related to near-surface fluids / gas in the unconsolidated upper sediments. Although laterally extensive, horizon H1 is the most difficult to trace due to deformation and warping of the horizon beneath the surface mounds (Figure 4.7). In the survey lines 411 - 419, it cannot be traced across the Aigion Fault into the footwall. However, further south from the fault plane, there is evidence of a horizon that is similar in appearance to H1, suggesting that erosion of the footwall sediments in the immediate vicinity of the fault has destroyed H1.

H1 forms the lower boundary to a sub-unit of varying thickness, which often appears transparent to semi-transparent, showing little internal structure where reflectors are visible. The exceptions to this occur beneath seafloor mounds, where although the reflectors have a stronger signature, they are broken and warped (Figure 4.7). The package between H1 and H2 is also acoustically transparent in many locations, however, there are some MCS reflection profiles where internal stratification is visible. In these areas, the reflectors are horizontal to sub-horizontal with a regular spacing of <0.5 ms TWTT (<0.5 m). This sub – unit appears relatively uniform in thickness running N-S along the

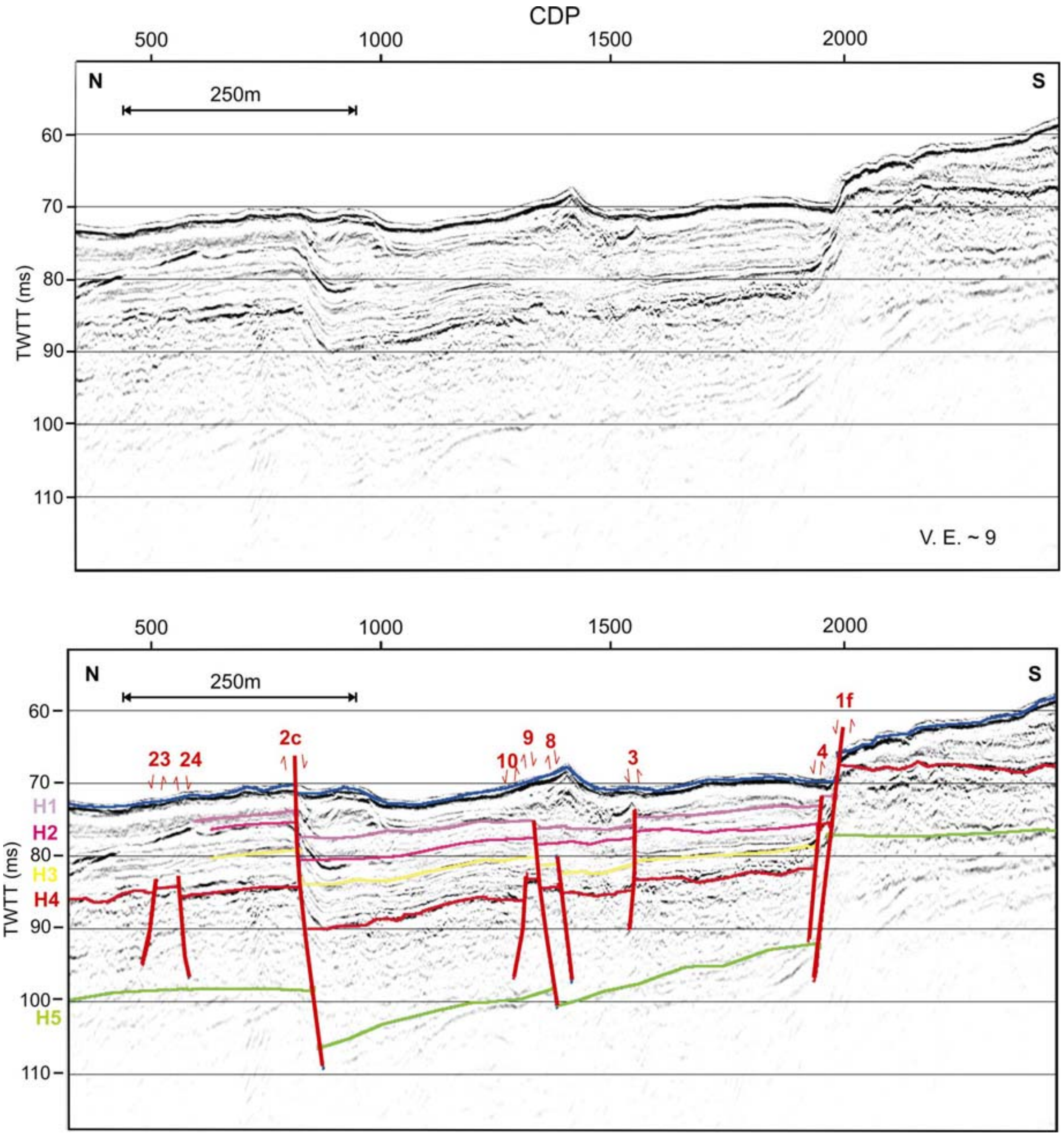

**Figure 4.11:** MCS reflection profile (Line 411, Plate 1B) showing the location of horizons H3 – H1 within U1, and relative to H4 and H5. The interpreted profile also shows the faults displacing each horizon. Fault numbers relate to Figure 4.1. An enlargement of the MCS reflection line can be found in Plate 2.

profiles, but thins W-E across the profiles. The sediments between H3 and H4 have a general W-E trend of thickening across the profiles.

Figure 4.12 shows the structure plots for horizons H3 – H1. Overlain onto the structure plots are the faults associated with each horizon. It can be seen that the oldest horizon (H3) is affected by the greatest offset from faulting. The number of faults offsetting the horizons decreases with each younger horizon. All three horizons have an overall NE trending dip. They are easily mapped across the first 11 MCS reflection lines (Lines 403 – 413, Plate 1B). Further eastwards however, with increasing distance away from the source of terrestrial sediment input, a reduction in sediment supply has resulted in significant thinning of unit U1, so that internal horizons can no longer be accurately identified.

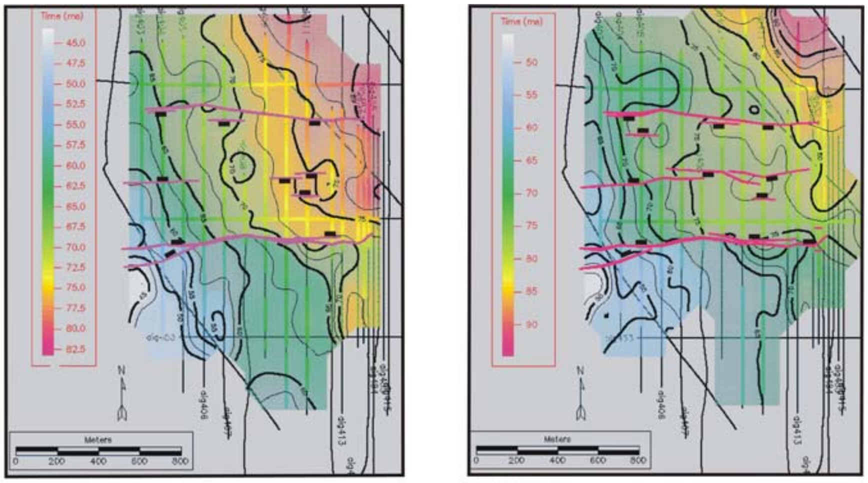

A: H1

B: H2

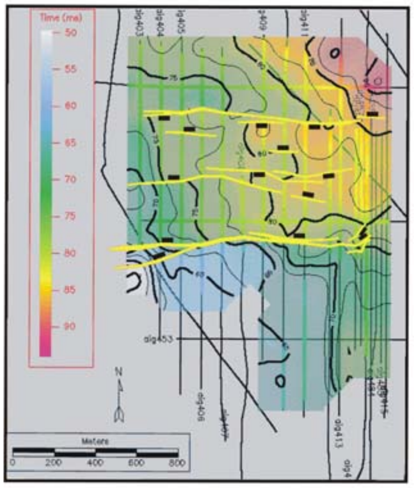

C: H3

**Figure 4.12:** Time-to-Horizon (ms) structure maps of the three youngest horizons identified within the MCS reflection profiles. Faults displacing each horizon have been overlain onto the structure plots. Sense of throw is indicated for each fault. The fault patterns are seen to be more complex for the older, deeper horizons. All three horizons show an overall NE trending dip direction.

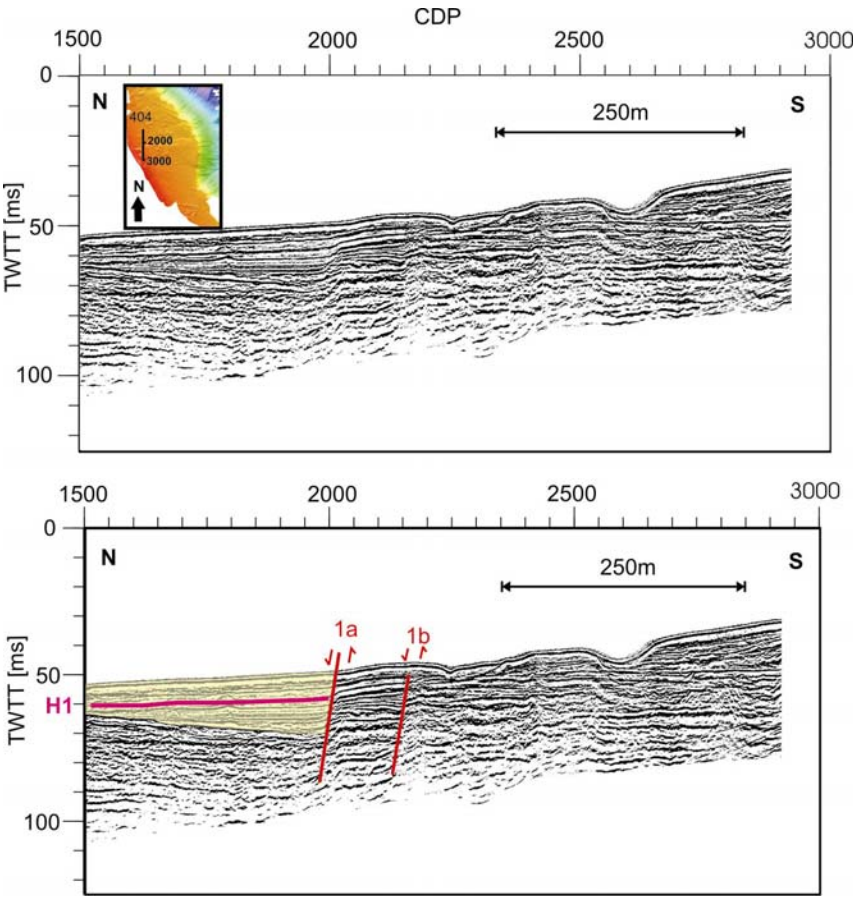

**Figure 4.13:** MCS reflection profile (Line 404, Plate 1C) showing thickening of the hanging-wall sediments into segment 1a of the offshore Aigion Fault. The multibeam bathymetry inset shows the profile location; shaded area indicates U1; numbers correspond to the fault map (Figure 4.1).

There is significant thickening of the unit U1 in the hanging-walls of the two dominant faults (**1** & **2**, Figure 4.1), caused by subsidence of the hanging-wall (Figure 4.13). The thickening occurs predominantly in the older sediments, beneath horizon H2. The reflectors above H2 are horizontal, suggesting that displacement rates on the fault had decreased during this period of deposition. The formation of these sedimentary wedges is discussed in more detail in Chapter 5, section 5.1.7.

## 4.2 ANALYSIS OF ERRORS AND AGE CONTROL

There are several possible sources of error associated with using horizons mapped within MCS reflection profiles to calculate fault displacement rates. These are due to: uncertainties in the initial picking and correlation of each horizon within the survey grid;

assigning an approximate age to each post-H4 horizon; errors associated with the interval velocity profiles used to estimate depth of each horizon; and measuring the true vertical displacement across a fault plane when localised perturbations, including erosion and sediment drag, may be affecting the horizons. In addition, the assignment of ages to each of the horizons is based upon using the age and depth of the well documented ravinement surface H4 as a benchmark, and assuming a constant sedimentation rate over the ~12kyr period being considered.

Each of the possible sources of error will be addressed in turn. As they are uncorrelated, it is possible to then estimate the cumulative effect of all the errors (e.g. velocity, picking and age assignment), using a general expression for uncorrelated errors. This is carried out for each specific horizon, and the discrete time intervals being used in the fault displacement analysis (Chapter 6). This ensures that the contribution of each quantifiable error is included, making the final fault displacement rates calculated, and associated error ranges, as accurate an indication of fault activity as possible.

### 4.2.1 Horizon Picking and Correlation

Errors in picking the horizons are derived from uncertainties due to resolution across the seismic profiles. To minimize the possible effects of mis-picking, the interpretation was performed using a pseudo 3D grid. The line spacing of 25-100 m meant it was possible to correlate each horizon between profiles, using tielines and markers at every intersection of one seismic line with another. These markers indicated where previously picked horizons should be located on the crossing line. By continually re-visiting each line and intersection, working out from a central point where confidence in the picks was highest, and using circular correlation to verify horizon assignments, it was possible to more accurately locate and refine the picking for each horizon. It is estimated that the picking of each horizon was accurate to within ± 2 ms TWTT (~1.5-2 m).

As previously indicated there are areas of transparency and fogging of the data, which makes accurate picking of horizons H1 – H3 in the most seaward lines difficult. Interpretation of horizons H1 – H3 across the whole of the survey area was therefore not possible, preventing a full analysis of variability in fault displacement rates over 1000's years timescales being carried out for all the faults imaged on the Aigion Shelf (Chapter 6).

### 4.2.2 Velocity Profiles

Accurate velocity profiles are required for each seismic line in order to convert the TWTT (ms) into depth. Any errors within the velocity picks will impact on the calculated depths of horizons and features. Velocity analyses were conducted on each line, every 50CDP's (25 m), using a semblance plot (See Chapter 2 for processing details), with velocities found to range from 1500 to 2300 $ms^{-1}$. An analysis of the minimum and maximum interval velocities at a reference point (Table 4.1; location shown on Figure 4.1) indicates that the error increases with depth as resolution of defined horizons decreases, ranging from 3% on H1 to 8% on H4.

### 4.2.3 Depth of Horizons

Errors within the velocity profile and horizon picking will affect the calculated depth for each horizon. The combined error can be accounted for using a general expression for uncorrelated errors. An example for one horizon is shown in equation 4.1:

$$\left(\frac{\delta d_{H1}}{d_{H1}}\right) = \sqrt{\left(\frac{\delta v_{H1}}{v_{H1}}\right)^2 + \left(\frac{\delta t_{H1}}{t_{H1}}\right)^2} \qquad \textbf{(4.1)}$$

where $d$ = estimated depth of each horizon; $v$ = interval velocity at each horizon; $t$ = TWTT (ms); $H1$ = horizon 1; $H2$ = horizon 2; $\delta$ = errors associated with each factor; $\delta_v$ is taken from Table 4.1; $\delta_t$ = 2ms TWTT as discussed in section 4.2.1. Table 4.1 shows the calculated error in depth associated with each individual horizon, both as a percentage and in metres.

| Horizon | Location (TWTT ms) | Interval Velocity (m/s) | Max. Interval Velocity (m/s) | Min. Interval Velocity (m/s) | Error ($\delta$v m/s) |
|---|---|---|---|---|---|
| **Seabed** | 73 | ***1553*** | 1580 | 1500 | ***50*** |
| **H1** | 80 | ***1590*** | 1702 | 1560 | ***110*** |
| **H2** | 82 | ***1637*** | 1748 | 1572 | ***110*** |
| **H3** | 86 | ***1715*** | 1820 | 1590 | ***125*** |
| **H4** | 90 | ***1868*** | 2015 | 1730 | ***150*** |

| Horizon | $\delta$v / v (%) | Location (TWTT ms) | Estimated Depth Beneath Seabed (m) | Error ($\delta$d m) | Depth Error (%) |
|---|---|---|---|---|---|
| **Seabed** | 3 | ***73 +/- 2ms*** | ***0*** | ***0*** | 0 |
| **H1** | 7 | ***80 +/- 2ms*** | ***4*** | ***0.3*** | 8 |
| **H2** | 7 | ***82 +/- 2ms*** | ***5.5*** | ***0.4*** | 7 |
| **H3** | 7 | ***86 +/- 2ms*** | ***9*** | ***0.7*** | 8 |
| **H4** | 8 | ***90 +/- 2ms*** | ***14*** | ***1.2*** | 8 |

| Horizon | Location (TWTT ms) | Estimated Age (ka) | Age Error ($\delta$t ka) | Cumulative Error (%) |
|---|---|---|---|---|
| **Seabed** | 73 | 0 | 0 | **4** |
| **H1** | 80 | 3.5 | 0.5 | **14** |
| **H2** | 82 | 4.5 | 0.6 | **14** |
| **H3** | 86 | 7.5 | 1.1 | **14** |
| **H4** | 90 | ***11.5*** | ***1*** | **9** |

| Horizon Intervals | Depth Between Horizons (m) | Cumulative Depth Error (%) of $H_x$ & $H_y$ | Cumulative Depth Error ($\delta$d m) of $H_x$ & $H_y$ | Total Time Interval Error (%) | Time Interval (kyr) |
|---|---|---|---|---|---|
| **H4 - Seabed** | ***14*** | 8 | ***1.2*** | **9** | 11.5 |
| **H4 - H1** | ***10*** | 11 | ***1.1*** | **16** | 8 |
| **H4 - H2** | ***8.5*** | 11 | ***0.9*** | **16** | 7 |
| **H4 - H3** | ***5*** | 12 | ***0.6*** | **17** | 4 |
| **H3 - H2** | ***3.5*** | 11 | ***0.4*** | **16** | 3 |
| **H2 - H1** | ***1.5*** | 10 | ***0.2*** | **16** | 1 |
| **H1 - Seabed** | ***4*** | 7 | ***0.3*** | **14** | 3.5 |

**Table 4.1:** Error analysis results for both specific horizons and discrete time intervals, calculated using a general expression for uncorrelated errors. The bold cumulative error column gives the percentage errors used in analysis of fault displacement rates when looking at each horizon. The bold total time interval column gives the percentage errors used when looking at changes in displacement over different time intervals. The bold cumulative error calculated represents a combined analysis of errors in horizon picking, velocity analysis, assignment of age and depth estimation of horizons. Input values used in each equation (4.1 – 4.3) are shown in bold italics.

Errors within the velocity profile will also affect the depths calculated for the fault / horizon contact points. Despite performing a velocity analysis every 25 m, the changes in velocity across the fault plane may not be accurately represented if there is a large amount of displacement accrued on the fault, causing different stratigraphic units with different interval velocities to sit opposite each other. The largest change across a fault plane was ~150 $ms^{-1}$, between U3 and U2. Therefore, a velocity analysis similar to the one detailed above was performed either side of a major N-dipping fault (**1**, Figure 4.1), on 3 MCS reflection lines. It produced similar results, suggesting that the errors calculated in Table 4.1 can account for variations across the fault planes.

### 4.2.4 Assigning Approximate Ages to Horizons

It has been suggested that the Rion Sill may not always have been at its current depth of ~60 m due to local fault activity (Chronis et al., 1991). This potentially introduces a degree of error into calculating at what times the Gulf may have become an isolated marine basin. However, recent work has suggested that the sill has not moved significantly over the past 12 ka (Hicks, 2004), the time period being considered in this survey. Therefore sill movement is not considered to be a major influencing factor when calculating the relative ages of the horizons.

As an erosional ravinement surface associated with global eustatic sea-level rise, and documented at many locations across the Gulf of Corinth, horizon H4 is the horizon with the most defined date constraints upon which to base age estimations for the other horizons. Horizons H3 – H1 are not laterally extensive, whilst H5 is considered to be diachronous (section 4.3.1). Ideally, a horizon dated using cores or boreholes situated in close proximity to the survey area would be correlated across to the H4 horizon picked within the seismic interpretation. However, lack of proximal cores, combined with the additional uncertainty caused by fault offset and problems with core locations, prevented this being the sole method used.

There have been three cores taken in the footwall of the Aigion Fault (Schwartz and Tziavos, 1979) (Figure 4.14) penetrating to a maximum depth of 20 m below the

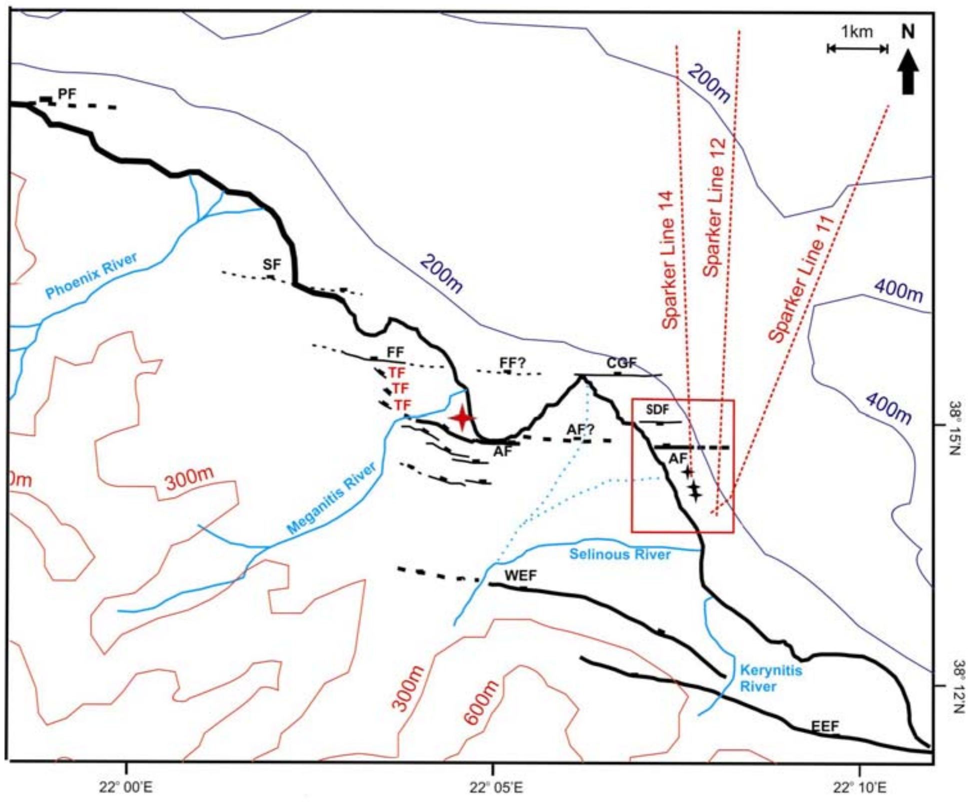

**Figure 4.14:** Map illustrating the relationship between the proposed offshore extension of the Aigion Fault, and the sites of the onshore AIG10 borehole (red star) (Lemeille et al., 2004; Rettenmaier et al., 2004) and the three offshore cores taken by Schwartz & Tziavos (1979) (black stars). The red rectangle shows the survey area in which multibeam bathymetry and MCS reflection profile were collected, with the red dashed lines indicating the location of the regional MCS reflection lines that enter the survey area. Solid lines indicate known faults while dashed lines indicate possible faults. Dashed blue lines indicate previous positions of the Selinous River. AF = Aigion Fault; EEF & WEF = Eastern and Western Eliki Faults; CGF = Cape Gyftissa Fault; FF = Fassouleika Fault; TF = transfer faults; PF = Psathopyrgos Fault. Faults from Palyvos et al., 2005; Stefatos et al. 2002; Koukouvelas, 1998; McNeill et al., 2005b.

seabed, in water depths of ~40 m. Carbon-14 dating of pelecypod and coral taken from above the transgressive horizon located in core 3 at ~58 m below present day sea level, gave an age of 10.2 ± 0.5 ka. However, it is not known at what depth, above the transgressive horizon, the dated material was located, and no exact coordinates could be found for the cores, making it impossible to accurately locate them within the survey area, and so correlate them against the MCS reflection data collected. The AIG10 borehole is located onshore, in the hanging-wall of the Aigion Fault, ~6 km west of the Aigion Shelf, across a predominantly coarse grained delta (Figure 4.14). These factors combine to make correlation difficult. However, carbon-14 dating of samples taken from a depth of ~65 m, located ~5 m above the transgressive horizon, gave an age of 11.5 ± 0.04 ka BP (Lemeille et al., 2004).

This date was extrapolated by Lemeille et al. (2004), using mean sedimentation rates, to give a date for the transgressive horizon (H4) of ~11.8 ka. Perissoratis et al. (2000) have inundation of the Gulf occurring between 10-12 ka BP, based on radiocarbon dating, whilst in the eastern Gulf, Collier et al. (2000) dated the trangressive horizon at ~12 ka, using radiometric dating.

Figure 4.15 shows that between 10 – 11.5 ka sea-level rose ~ 25 m, (Siddall et al., 2003). Taking an E-W transect across the shelf, running parallel to the main fault strike orientation, to avoid the combined effects of uplift and subsidence due to displacement of horizon H4 from faulting, the maximum lateral height variation is ~25 m. Based on this, complete inundation of the exposed shelf, forming the H4 ravinement surface, would have occurred within ~2 ± 0.5 ka, using the Siddall et al. (2003) sea-level curve. This timing assumes a constant rate of sea-level rise and takes into account the error of ± 12 m in the reconstruction of the sea-level curve, stated by Siddall et al. (2003).

However Kershaw et al. (2005) state that between 11.5 and 10 ka, sea-level in the Gulf of Corinth rose rapidly, at ~25 mm $yr^{-1}$, based on the growth of a reef, and biota zoning within that reef, at Mavra Litharia on the southern margin of the Gulf. If correct, this would mean inundation of the Aigion Shelf occurred in only 1 kyr.

The time period required for inundation of the shelf therefore lies within the error ranges and dates assigned to horizon H4 by other authors (11.5 ± 0.04 ka (Rettenmaier et al., 2004), 10.2 ± 0.5 ka (Schwartz and Tziavos, 1979) and 12 ka (Collier et al., 2000). Consequently, H4 is considered as a broadly synchronous horizon for the purpose of this study, with an assigned age of 11.5 ± 1 ka (9% error). This age is based predominantly on the AIG10 dating, but takes into account the dates calculated using other datasets.

To then estimate the ages of H1 – H3, a reference point on Boomer line 410 was chosen, based on its location away from major faults and variable terrestrial sediment inputs (Figure 4.1). This limited the potential errors associated with variability in sediment

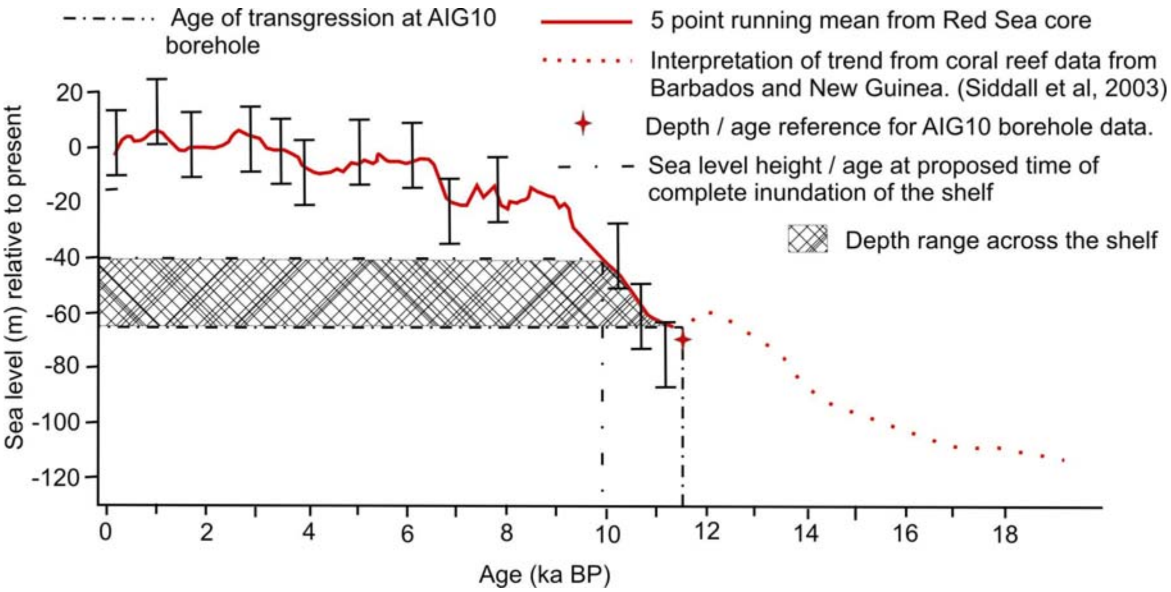

**Figure 4.15:** Sea level reconstruction after Siddall et al. (2003). Running mean is based on $\delta^{18}$O records. Error bars indicate the ± 12 m error on the reconstruction. Dot / dashed line at 11.5 ka indicates the proposed date for the start of marine inundation based on the AIG10 borehole. The second dot/dashed line at 10ka indicates the time when complete inundation of the shelf is proposed to have occurred, based on the lateral E-W height variation across the shelf on the trangressive horizon H4. This suggests a time period of ~1.5 kyr was required for full marine inundation to occur.

thicknesses, or fault displacement influencing sedimentation patterns. It does lie close to the shelf edge, which is affected by mass wasting. However it is not believed that this has significantly altered the thickness of the sediment package. The depth beneath the seabed to the trangressive horizon H4 was measured at this reference point (14 m). Horizons were then assigned estimated ages (Table 4.1), by interpolating between 11.5 ka and the present day, based on their relative positions between H4 (11.5 ka) and the seabed (0 ka), and assuming a constant sedimentation rate.

Evidence from the AIG10 borehole (Lemeille et al, 2004) supports the hypothesis that rapid climate change and increased aridity at ~5ka led to an increase in sediment supply in the Holocene. This would contradict the assumption of a constant sedimentation rate used in this analysis. However, differential increases in displacement across the two main faults (Chapter 6) suggest that changes in displacement rates observed are not solely due to changes in sediment supply rates. This fact, combined with the lack of datable material from which to obtain accurate dates for the horizons, has led to the adoption of a constant sedimentation rate for the purpose of this short-timescale study.

Errors associated with each age were calculated (δt ka), again using the equation for uncorrelated errors. An example for one horizon is shown in equation 4.2;

$$\left(\frac{\delta age_{H3}}{age_{H3}}\right) = \sqrt{\left(\frac{\delta depth_{H3}}{depth_{H3}}\right)^2 + \left(\frac{\delta age_{H4}}{age_{H4}}\right)^2 + \left(\frac{\delta depth_{H4}}{depth_{H4}}\right)^2} \qquad \textbf{(4.2)}$$

Where $\delta_{depth}$ is taken from Table 4.1 (δd m); *depth* = estimated depth (m) from Table 4.1; $\delta_{ageH4}$ is 1ka and $_{ageH4}$ = 11.5ka. Depths used in this equation were originally estimated in the analysis in section 4.2.3, where possible variations in velocity and time, and the associated impact on calculated depths, were taken into account.

The cumulative errors in Table 4.1, for each horizon, therefore account for the effects of variability within the velocity analysis, horizon picking, depth calculation and age estimation. However the fault displacement analysis (Chapter 6) also looks at discrete time periods. The combined errors relating to a specific time period encompass the uncorrelated depth errors for each of the horizons that form the upper and lower boundaries to that period, as well as the depth and age error associated with H4 (as the benchmark horizon). An example of the equation used for one time period is shown in equation 4.3. The total errors for each time interval are given in Table 4.1.

$$\left(\frac{\delta interval_{H3-H2}}{interval_{H3-H2}}\right) = \sqrt{\left(\frac{\delta depth_{(H3+H2)}}{depth_{(H3+H2)}}\right)^2 + \left(\frac{\delta age_{H4}}{age_{H4}}\right)^2 + \left(\frac{\delta depth_{H4}}{depth_{H4}}\right)^2} \qquad \textbf{4.3}$$

The errors given in Table 4.1 are considered to be representative of the potential cumulative errors that can be accounted for. However, it is acknowledged that assuming a constant sedimentation rate, and that the estimated errors are independent of each other, may introduce additional errors that cannot be compensated for.

### 4.2.5 Horizon Deformation

Movement on a fault can cause sediment drag (Figure 4.16). This is a localised effect, affecting both footwall and hanging-wall sediments either side of a fault plane. To correct for this, sub-surface horizons are projected towards the fault plane from locations where they are undisturbed (e.g. Mansfield and Cartwright, 1996). As this can be corrected for during interpretation, it is not considered to contribute to the overall error considered in later analysis of fault displacement. A similar effect can be generated at the surface through sediment re-distribution, such as erosion, destroying horizons.

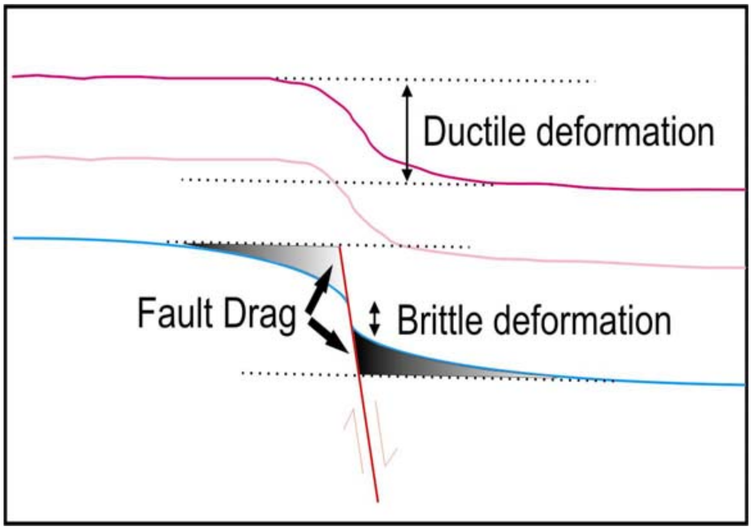

**Figure 4.16:** Cartoon illustrating the possible effects on sediments adjacent to the fault plane due to fault drag. The coloured lines represent horizons; shaded areas show the extent of possible up / downward warping of sediments prior to brittle deformation. To gauge the true displacement on a sub-surface horizon therefore, measurements have to be projected across the fault plane, indicated by the dotted lines, from areas where the horizons appear un-deformed.

## 4.3 DISCUSSION

It is noted that the horizon structure maps (Figure 4.12) show a more stylised interpretation of faulting than Figure 4.1, showing exaggerated changes in orientation. This is due to the nature of picking fault boundaries between the MCS reflection profiles within IESX. The faults shown on Figure 4.1 therefore represent the final interpretation of fault geometry gained from using both the MCS reflection and the multibeam datasets.

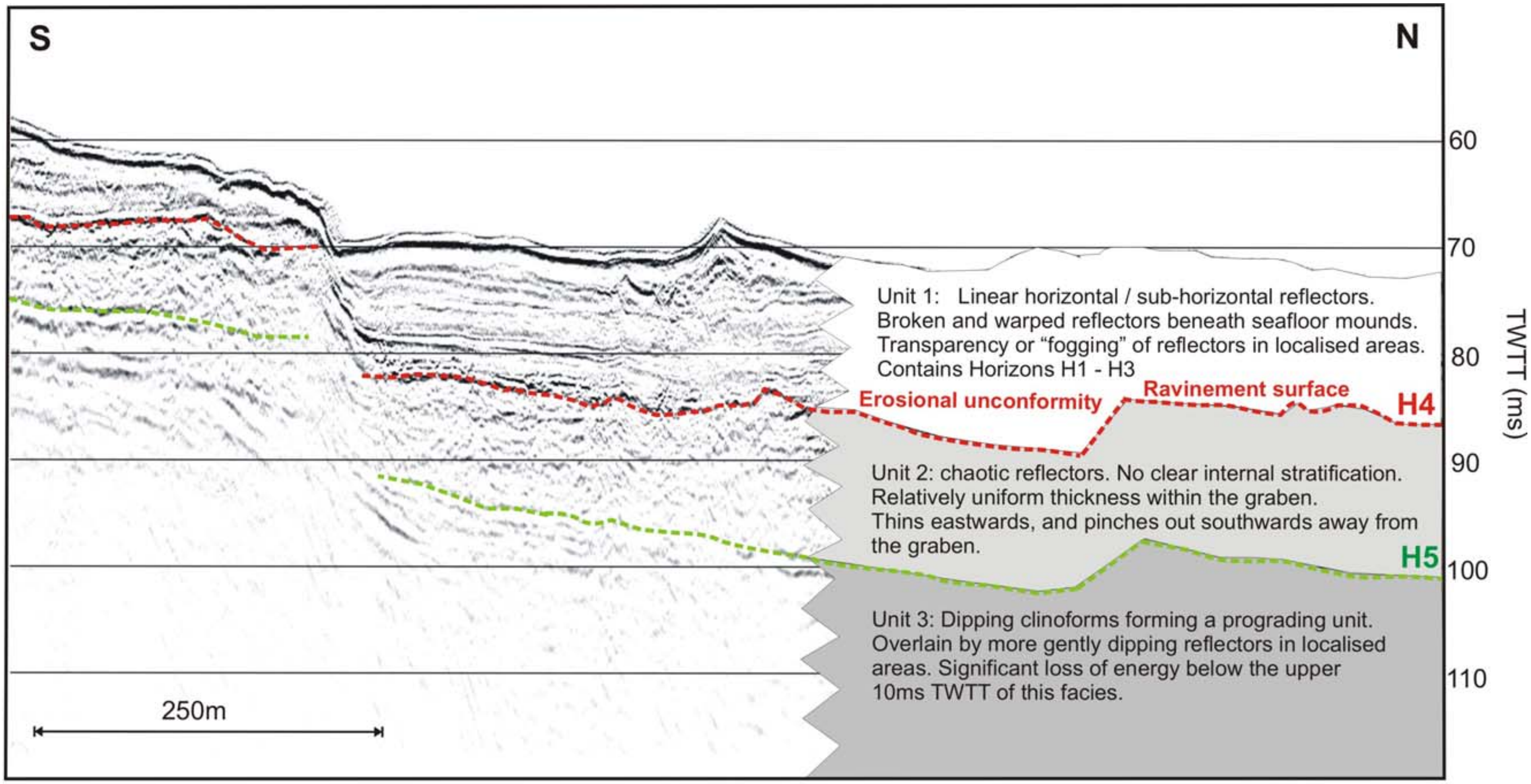

**Figure 4.17:** MCS reflection profile (Line 411, Plate 1C) illustrating the main characteristics of each unit. Two prominent horizons are indicated: the transgressive ravinement surface of ~11.5ka (H4) in red, separating the sub-aerial (below) and the marine deposits (above); and the green lowstand horizon (H5), separating the marine (below) from the sub-aerial deposits of the late lowstand and early transgression (above).

### 4.3.1 Depositional Environment

The main features of each seismically distinct unit identified, and the locations of the horizons discussed are summarized in Figure 4.17. The link between these units and their internal structure and sea-level behaviour / systems tract formation is shown in Figure 4.18.

The systems tracts identified in Figure 4.18 form through a dynamic inter-play between eustatic sea-level, sedimentation and tectonic controls. Figure 4.19 shows a generic model of systems tract architecture (A) and compares to the model proposed for the Aigion Shelf, formed from the interpretation of the MCS reflection profiles. Using the model of sequence stratigraphy (Figures 4.18 and 4.19), it is interpreted that the oldest unit (U3) was deposited during the last lowstand. Clinoforms formed as the fan delta prograded, during sea-level fall (Dart et al., 1994; Perissoratis et al., 2000). The calculated dip of the clinoforms at the current delta front (~30$^o$) is in agreement with the angle of repose for sand deposits (32-34$^o$) (Bagnold, 1941), and the approximate angle of internal friction for coarse - grained deltaic clinoforms, which Lekkas et al. (1996) have documented as ranging between 10 - 40$^o$ in this region. Dart et al. (1994) document foreset dips of between 8 – 40$^o$ for the Keranitis fan, which has been uplifted in the Aigion Fault footwall. As the closest fan delta, it is likely that the Keranitis clinoform dips are a good proxy for the clinoforms imaged offshore.

Horizon H5 formed during the last sea-level lowstand. Due to the unknown time period over which it formed, its lateral extent and the lack of material to use as an age control, it is not possible to assign ages to any specific points along the horizon. The horizon is therefore considered to be diachronous, and so could not be used in any quantitative evaluation of changes in fault displacement rates with time.

The beach topsets are overlain by sub-aerial (including fluvial) topset deposits (U2), laid down as the shelf became fully exposed, when sea-level fell below the level of the Rion Sill, leaving the Gulf of Corinth as an isolated basin. Perissoratis et al. (2000) suggest that exposed shelf areas may have undergone periods of erosion during this time,

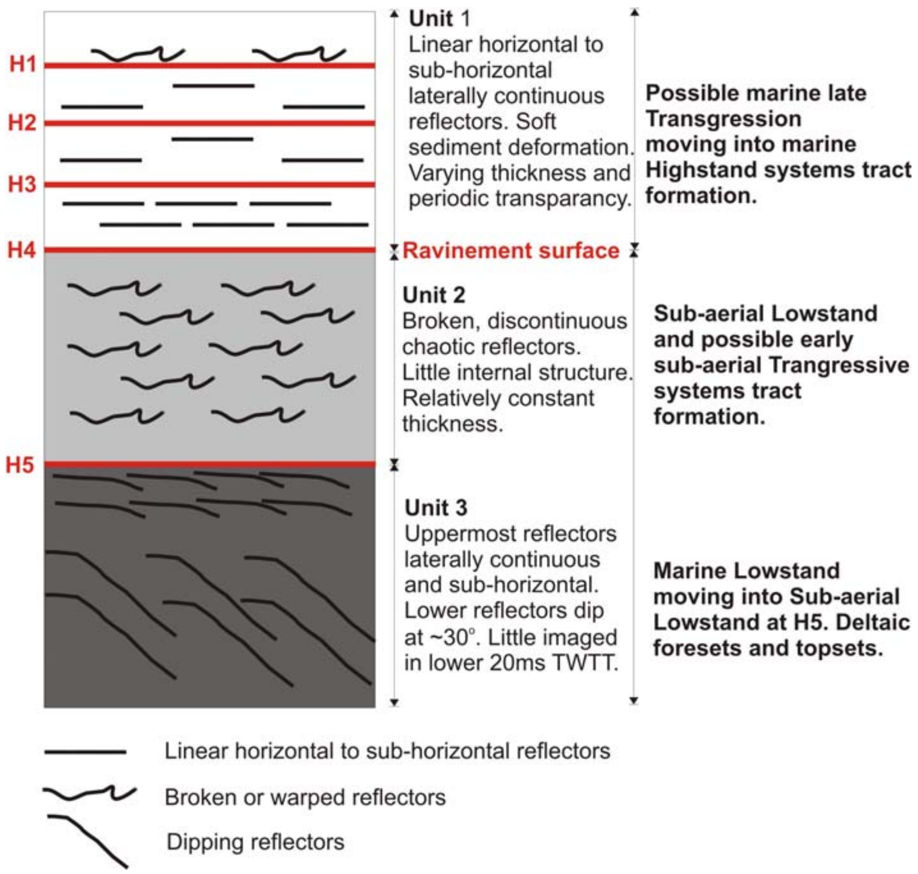

**Figure 4.18:** Relationship between the seismic units identified and their correlation to Lowstand, Transgressive and Highstand Systems Tracts.

leading to the formation of a unit with little internal structure, as observed in U2. The youngest sediments in U2 may have been deposited during the early stages of subsequent global sea-level transgression, prior to over-topping of the Rion Sill.

Thinning of U2 to the south (Figure 4.6) may have been caused by reworking of the deltaic sequences by rivers flowing across the shelf during the lowstand period. If there was no fluvial source in close proximity supplying sediments from re-worked fan deltas onshore, sub-aerial deposits may have been limited or absent. The mouth of the river systems would have been located close to the present day break in slope / shelf edge, and so areas inshore of this may have become sediment starved, causing pinching out of U2 in the present day inshore areas. In addition, marine transgression following overtopping of the Rion Sill may have caused erosion of unconsolidated sub-aerial deposits, and so thin sediment veneers may have been stripped away and re-worked.

The sub-aerial topsets are overlain by an erosional ravinement surface (H4) formed during marine inundation linked to post-lowstand global sea-level rise. Unit 1, lying above the ravinement surface, therefore represents late stage transgression, moving into a Holocene highstand depositional sequence laid down following complete inundation of the shelf.

With a rise in eustatic sea-level it would be usual to see the formation of a transgressive systems tract, recognizable as either a condensed succession or retrogradational succession of shelf deposits (Miall, 1999). However, in this survey area the transgressive deposits cannot be distinguished as a discrete unit across the whole of the Aigion Shelf, separate from the sub-aerial lowstand tract and the highstand tract now forming. The early stage deposits are not identifiable within the aeolian/fluvial deposits of U2. Following overtopping of the Rion Sill, they can be partially traced across the shelf, however the vertical resolution of the survey, combined with the oblique angle that sediments were deposited due to shelf topography, make it difficult to identify transgressive deposits over the whole shelf. In addition, deformation from faulting may have distorted the onlapping sediments. Figure 4.19 therefore summarises the stratigraphy based on evidence from selected survey lines.

Onlap of sediments onto the ravinement surface can be seen in some locations (Figure 4.4), predominantly on the E-W orientated tielines, where fault offset has not resulted in warping or deformation of the sediments. However, even on these tie-lines, there is no distinct unit that can be traced laterally across the shelf.

The trend of sediment thickness increasing W – E between H3 and H4, the deepest sub-unit within U1, opposes the general trend of U1 thinning W – E. It may reflect the transition between sub-aerial deposition, when sediments were initially laid down at the shelf edge whilst the mid-inner shelf was sediment starved, and the later transgression into marine deposition across the whole shelf.

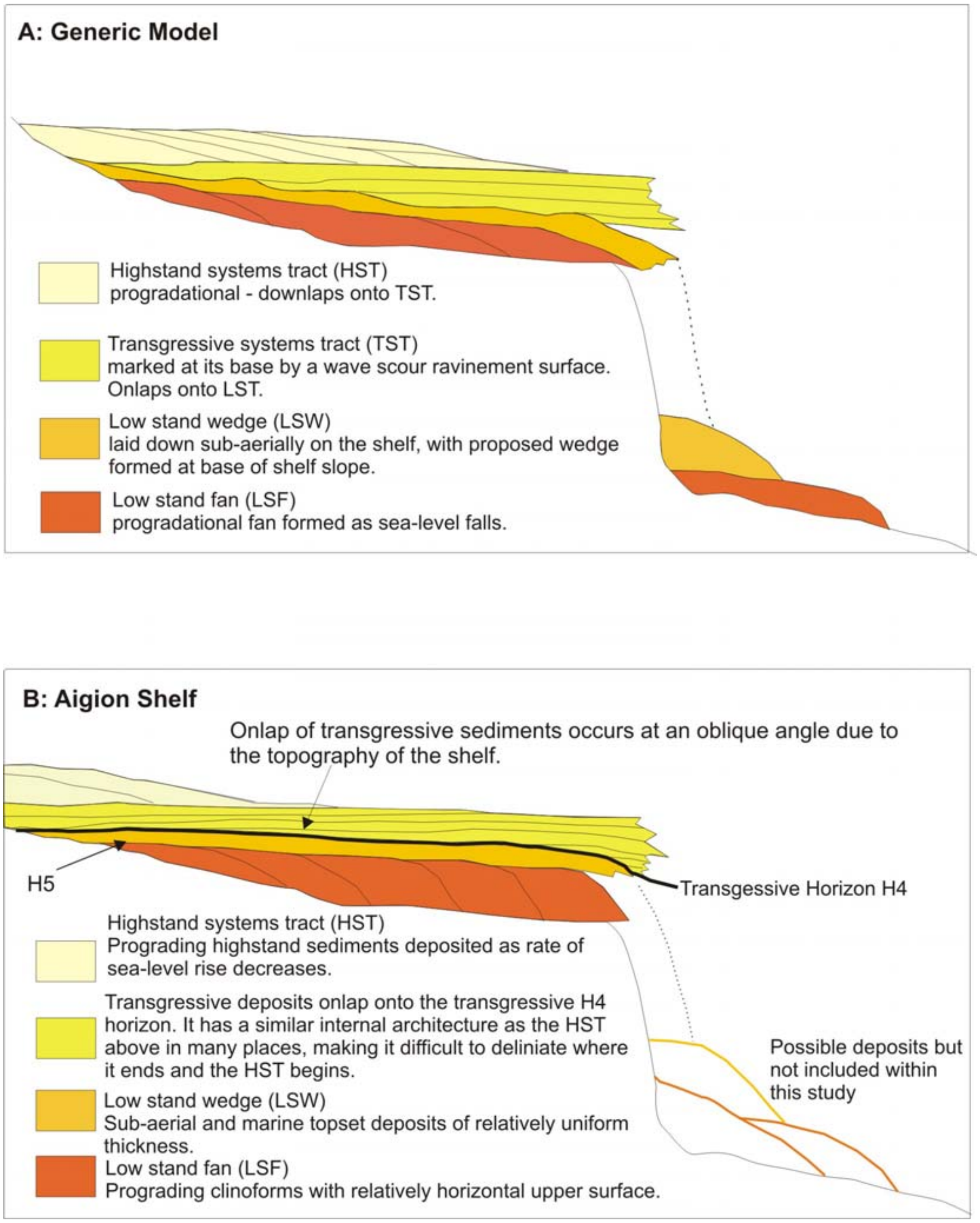

**Figure 4.19:** Cartoon illustrating the architecture of systems tracts formed through changes in eustatic sea-level. **A)** Generic diagram of system tract architecture. Deposits shown at the base of slope are presumed to form as fluvial inputs reach the shelf edge during the lowstand, and deposit sediments into the deep basin (After Miall, 1999). **B)** Architecture proposed for the Aigion Shelf following interpretation of the MCS reflection profiles. It shows a very similar architecture to the generic model, supporting the interpretations made concerning the formation of the primary reflector, interpreted as being a erosional ravinement surface associated with sea-level rise and marine transgression.

There is little evidence of the oldest highstand deposits in U1 downlapping onto the ravinement surface, which would bound the top of a transgressive tract. However, the lines closest to the present day fluvial sources of terrestrial sediments do show progradation and downlap of the most recent highstand deposits. Dating of material from the AIG10 borehole indicates that following the transgression, sedimentation rates were in the order of 6 mm $yr^{-1}$. However, this increased dramatically to 12 mm $yr^{-1}$ between 6 – 4 ka BP (Rettenmaier et al., 2004). At approximately the same time sea-level rise stabilised (Figure 4.17), so reducing the creation of accommodation space available for sediment deposition. These factors combined could help explain the progradation of the younger sediments observed in U1.

### 4.3.2 Sedimentology and Seismic Stratigraphy

Lemeille et al. (2004) describe the Holocene unit above the transgressive horizon in the AIG10 borehole as being alternating layers of coarser sediments (fine to coarse sand, gravels and pebbles), interpreted as re-worked beach deposits, and black plastic clay. Rettenmaier et al. (2004) also state that the clay is a silty clay with marls intercalated with coarser beds. This description of intercalating deposits of different sediment types is supported by Lekkas et al. (1996). Cores from the onshore delta also show this layered structure, with grain sizes ranging from pebbles to clay and silts (Soter et al., 2001). It is this intercalation of materials with different grain sizes and properties that cause the strong returns from the near horizontal reflectors in U1, due to differences in acoustic impedance between the contrasting layers.

The areas of transparency imaged in U1 may represent periods when sedimentation was predominantly hemipelagic, with little fluvial input of coarser grain sizes. These transparent layers are an average of 2ms TWTT (~1.5 m) in thickness, representing a period of ~1.5 ka deposition. The layered nature of the transparent packages imaged in U1 suggests a cyclical deposition process is responsible for the construction of the present fan.

The Aigion fan delta has been primarily constructed through deposition of alluvial sediments, eroded from older, now uplifted fan deltas (Perissoratis et al., 2000; Soter et al., 2001). The primary rivers feeding into this area at the present day are the Selinous and the Kerynitis rivers. It is known that the seaward end of the Selinous River has migrated to many positions through the dating of abandoned bridges and historical archives (Soter and Katasonapoulou, 1998) (Figure 4.14), although only the last ~2 kyr of migratory activity can be accounted for by these methods.

River migration due to back-tilting of a fault block should be uni-directional, resulting (when considering the Selinous River) in a southerly trending pattern of deposition, as propagation of the Aigion Fault eastwards causes uplift, resulting in migration of the river from north to south. However this pattern is not observed, as the layered stratigraphy described occurs across the whole shelf throughout the upper Holocene U1 unit.

There may be alternative processes that contribute to the seismic stratigraphy imaged, including: shallow gas / fluid seepage (Papatheodorou et al., 1993; Christodoulou et al., 2003); or specific distribution patterns of fines due to seasonal water circulation patterns and coastal upwelling within the Gulf of Corinth (Lascaratos et al., 1989). Anti-clockwise circulation moving fines from south to north across the Aigion Shelf may counter the north to south pattern resulting from river avulsion due to footwall uplift.

Piper et al. (1990) state that the general fan delta morphology observed along the southern Gulf of Corinth coastline shows deposition of flood transported pebbles at river mouths and onto the nearshore fan, whilst distal regions mainly show fine grained sediments that appear acoustically transparent. Therefore the layered structure observed on the Aigion Shelf may represent a combination of fan growth and progradation of the coastline, combined with localised variability in sediment supply and deposition, as opposed to resulting purely from episodic phases of river avulsion.

### 4.3.3 Depositional Structure and Mass Wasting

At the shelf edge the angle of the lower slope appears to mirror the dip of the internal clinoforms in unit U3. This may suggest that there is a link between the depositional architecture of this unit and susceptibility of the slope to mass wasting along suitably orientated planes of weakness.

Coarse-grained Gilbert type deltas often have slumped slopes associated with gravitational failure due to the unstable nature of the steep slope (Ferentinos et al., 1988). Papatheodorou and Ferentinos (1997) and Hasiotis et al. (2002) have both documented substantial failure of these Holocene deposits following the 1995 Ms 6.1 Aigion earthquake. Rotational slides, gravity flows and sand / water ejections were identified, and failure was common along bedding planes (Papatheodorou and Ferentinos, 1997). They suggested that the sub-horizontal reflectors imaged in U3 provided failure planes, and that cyclic loading due to earthquakes increased pore - water pressure, resulting in liquefaction and failure. It is possible that clay layers found in the AIG10 borehole by Lemeille et al. (2004) act as impermeable barriers in this locality. This may result in a build-up of pore water pressure in the layers in between, potentially causing these layers to act as failure planes.

### 4.4.1 CONCLUSIONS

- Three distinct seismic units can be identified in the MCS profiles. Through analysis of the controls governing sea-level in the Gulf of Corinth, it can be seen that the three acoustically distinct units correspond to two systems tracts formed during sea-level extremes. Unit U3 relates to lowstand marine deposition, with U2 representing sub-aerial lowstand and early transgressive deposits. U1 corresponds to late transgression and highstand marine deposition.

- Transgressive deposits occur in both the later stages of U2 and early stages of U1 deposition. However, no distinct transgressive unit can be identified in the MCS reflection profiles.

- Five laterally continuous horizons have been identified in the MCS reflection profiles. However, dating constraints mean that only four (H1-H4) can be considered synchronous, and assigned estimated ages. Based on an age of 11.5 ± 1 ka for the transgressive horizon H4, horizons H1, H2 and H3 are assigned approximate ages of 3.5 ± 0.5 ka, 4.5 ± 0.6 ka and 7.5 ± 1.1 ka respectively. There is no age control on horizon H5.

- The horizons mapped are laterally extensive across most of the Aigion Shelf, and so can be used as the basis for more detailed evaluation of fault displacement rates and fault growth (Chapter 6).

- There are maximum possible vertical displacement errors of ± 14% on horizons H1, H2 and H3, and ± 9% on H4, based on interpretation of the MCS reflection profiles. These errors represent a cumulative analysis of potential variability linked to: horizon correlation and picking; velocity analysis; estimation of horizon ages and depths; and sediment drag against the fault planes, and will be used in the quantitative analysis of fault displacement (Chapter 6). The errors relating to the time periods considered in later fault analysis (Chapter 6) range from 9% to 17% (Table 4.1).

- The seismic character of the MCS profiles suggests that the depositional style reflects a significant influence from tectonic activity, including localised deformation horizons, thickening of sedimentary packages against fault planes, and evidence of a link between internal architecture and mass wasting.

# Chapter 5

# Fault Geometry and Syn-Tectonic Sedimentation

This chapter will overview the main features observed across the Aigion shelf, both surface and sub-surface, recorded in new bathymetric and seismic reflection datasets. The sedimentation history across the shelf will be analysed within the context of both tectonic and sea-level controls. Fault geometry and activity over the last 11.5kyr will be explored, addressing the fault geometry and distribution, segmentation and length of the major faults, and the distribution of faults within assigned arrays. The observations will be discussed with reference to pre-existing bathymetric and geological data. This will provide a detailed framework prior to a more quantitative analysis of fault behaviour and displacement rates, using a 3D seismic interpretation package, in Chapter 6.

## 5.1 FAULT GEOMETRY AND ASSOCIATED FEATURES

The location of the onshore Aigion Fault system is well documented, although its precise geometry and the nature of segmentation is debated (e.g. Koukouvelas & Doutsos, 1996; Lekkas et al., 1998; Pantosti et al., 2004; Palyvos et al., 2005). Koukouvelas (1998), Pantosti et al. (2004) and Palyvos et al. (2005) describe it as having three segments, although Palyvos et al. (2005) also believe that it is linked to the Fassouleika and Selianitika Faults, forming the larger Aigion-Neos fault system.

The main onshore Aigion Fault sits to the north of the Western Eliki Fault, overlapping this fault by ~4 km, and south-east of the Psathapyrgos Fault (Figure 5.1). Koukouvelas (1998) and Pantosti et al. (2004) state that the Aigion Fault has an onshore segment (indicated by a dashed line on Figure 5.1) that crosses the Aigion delta, located east of the clear, topographically defined, main segment. Koukouvelas (1998) uses surface cracking following the 1995 Aigion earthquake to define this segment, although the exact location / existence of the segment is not clear due to a lack of topographical expression. However, the presence of a sub-surface segment crossing the delta leads to the

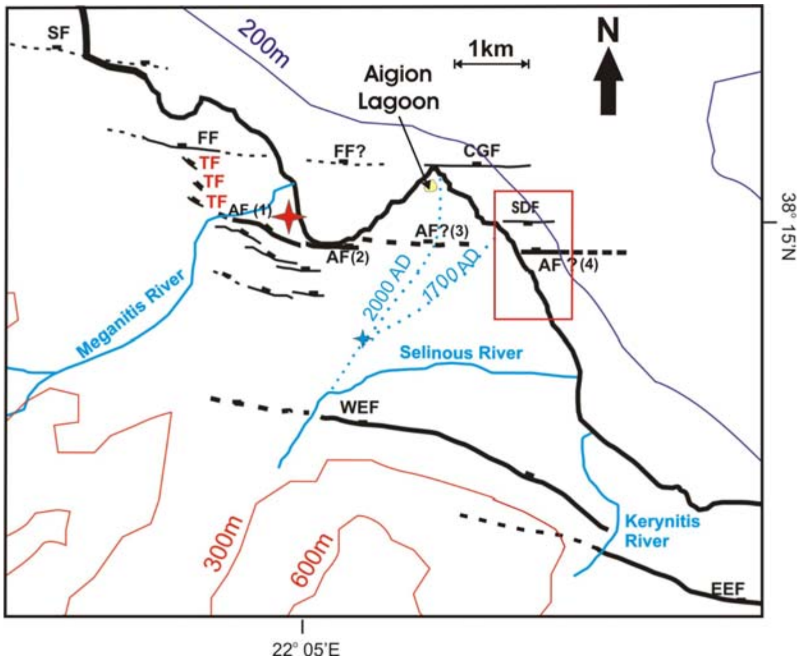

**Figure 5.1:** Map illustrating the relationship between the Aigion Fault (AF) and neighbouring faults. Solid lines indicate known faults, dashed lines indicate inferred extensions of faults. Red box indicates the area surveyed for this thesis. SF = Selianitika Fault; FF = Fassoulieka Fault; TF = transfer fault zone; WEF and EEF = Western and Eastern Eliki Fault; CGF = Cape Gyftissa Fault; SDF = south dipping graben bounding fault. Fault locations taken from McNeill and Collier (2004); Palyvos et al. (2005); Koukouvelas (1998). Dotted blue lines and blue star indicate the approximate positions of the Selinous River and an abandoned Roman Bridge (Soter and Katsonopoulou, 1998).

supposition that there may be a link to an offshore extension to this fault system. This thesis and authors including Soter and Katsonopoulou (1998) and Stefatos et al. (2002) present data that shows a defined offshore fault zone. If the location of the well-defined onshore segment of the Aigion Fault is projected eastwards, it crosses the Aigion Shelf <0.5 km north of this N-dipping normal fault zone (Figure 5.1). Therefore it is proposed that the offshore fault may be part of the onshore Aigion Fault system, connected by a possible sub-surface segment. Based on this assumption, the onshore and offshore segments combine to total ~15 km, which is comparable with other fault systems in the Gulf of Corinth (Armijo et al., 1996; McNeill and Collier, 2004).

### Overview of Surface Features

Figure 5.2 shows the multibeam bathymetry image, gridded with a 1.5 x 1.5 m cell size and illuminated from the NNW (enlargement Plate 1A), highlighting specific features.

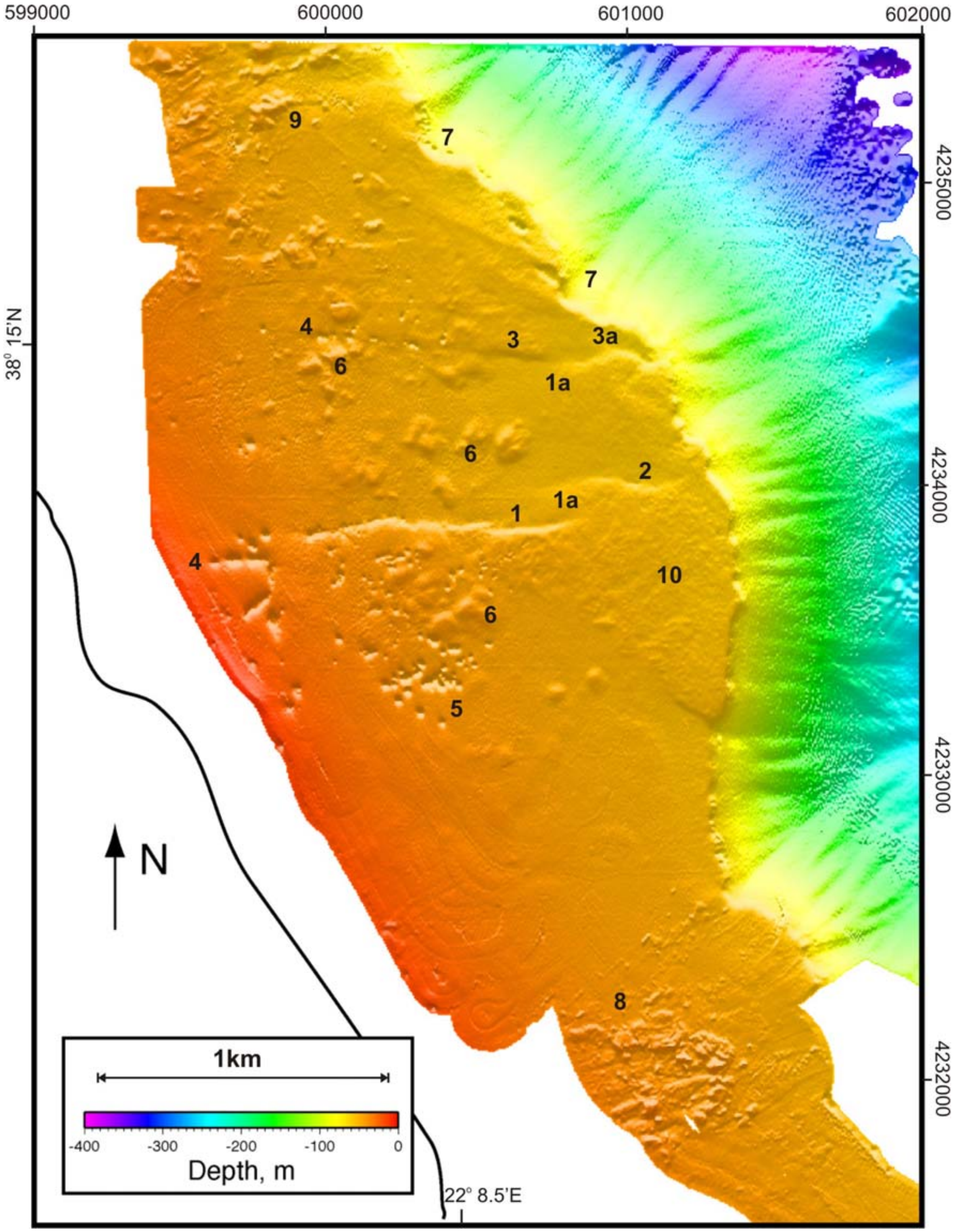

**Figure 5.2:** Annotated swath bathymetry of the offshore Aigion Shelf, indicating the main structural and sedimentary features; 1-3 = faults; 4-5 = pockmarks; 6 = mounds; 7 = mass wasting; 8-10 = other morphological features. Each feature is discussed fully in section 5.1.1. Multibeam image is gridded with a 1.5m x 1.5m cell size. Illumination is from the NNW. An enlargement of the multibeam image, without annotation, can be found in Appendices, Plate 1A.

### Faults

Numbers **1 – 3**, Figure 5.2, show three major normal, E-W orientated faults offsetting the seafloor. **1** is proposed to be the offshore extension of the N-dipping Aigion Fault, with **2** being a northward stepping segment of the same fault system. **3** represents a major S-dipping fault. The faults **1** and **3** form a graben, which narrows gradually eastwards (Figure 5.3), as individual segments of the Aigion Fault step northwards.

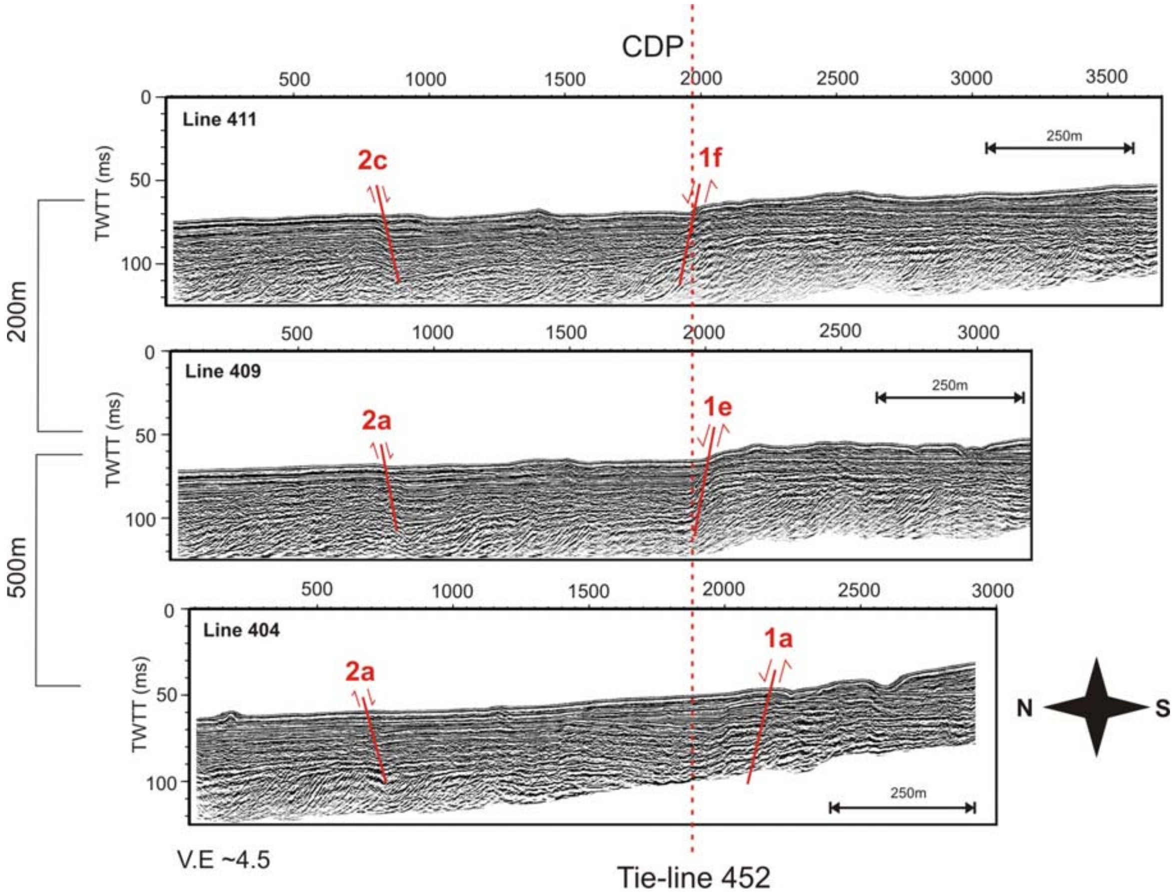

**Figure 5.3:** Examples of three of the MCS reflection profiles that illustrate the narrowing of the graben geometry eastwards. Fault numbers refer to scheme shown in Plate 1C. Over ~700 m, the graben narrows by ~150m. The narrowing is principally due to the northward stepping of segments 1e and 1f relative to 1a (Plate 1C).

### Fault Related Features

**4** (Figure 5.2) are linear strings of pockmarks located west of faults **1** and **3**, delineating sub-surface fault location. **6** are mound-like features, predominantly occuring within the graben. Some lie in close proximity to a line of pockmarks, whilst the three largest ones form an E-W line down the centre of the graben. Analysis of the MCS reflection profiles shows them to be predominantly located above sub-surface faults (Figure 5.4). The close proximity of many of the mounds and pockmarks to faults suggests a link between the formation of these features (Chapter 7).

### Sedimentological Features

**5** (Figure 5.2) is a cluster of near circular pockmarks located in the footwall of the N-dipping Aigion Fault, covering an area of ~6km$^2$. They appear to be unrelated to any surface or sub-surface faulting, and have a different surface expression to the linear pockmark strings.

Numbers **8** and **9** (Figure 5.2) are mound like features, however they are much more irregular and jagged in appearance than those at **6**. **8** has an arcuate shape to the overall deposition, with evidence of channels being incised through the deposits. Due to the proximity of **8** to the present day outflow of the Selinous River, it is believed that these are fluvial deposits that have been eroded by episodic events, possibly from mass flow / storm events. **9** also appears to have channels running SW-NE through the feature, suggesting that these may also be fluvial deposits, laid down during an earlier discharge position of the Selinous River.

Number **10** highlights an area of textural “dimpling” of the seafloor. It is believed that this is caused by an interplay between sedimentation and water circulation at the shelf edge. This hypothesis will be addressed in more detail in section 5.1.5.

### 5.1.1 Overview of Fault Distribution

The distribution of faults visible on the seafloor compared to those mapped on the transgressive horizon (H4, ~11.5 ± 1 ka), indicates that the seafloor has undergone significantly less displacement by minor faulting than the ~11.5 ± 1 ka horizon (Figure 5.5).

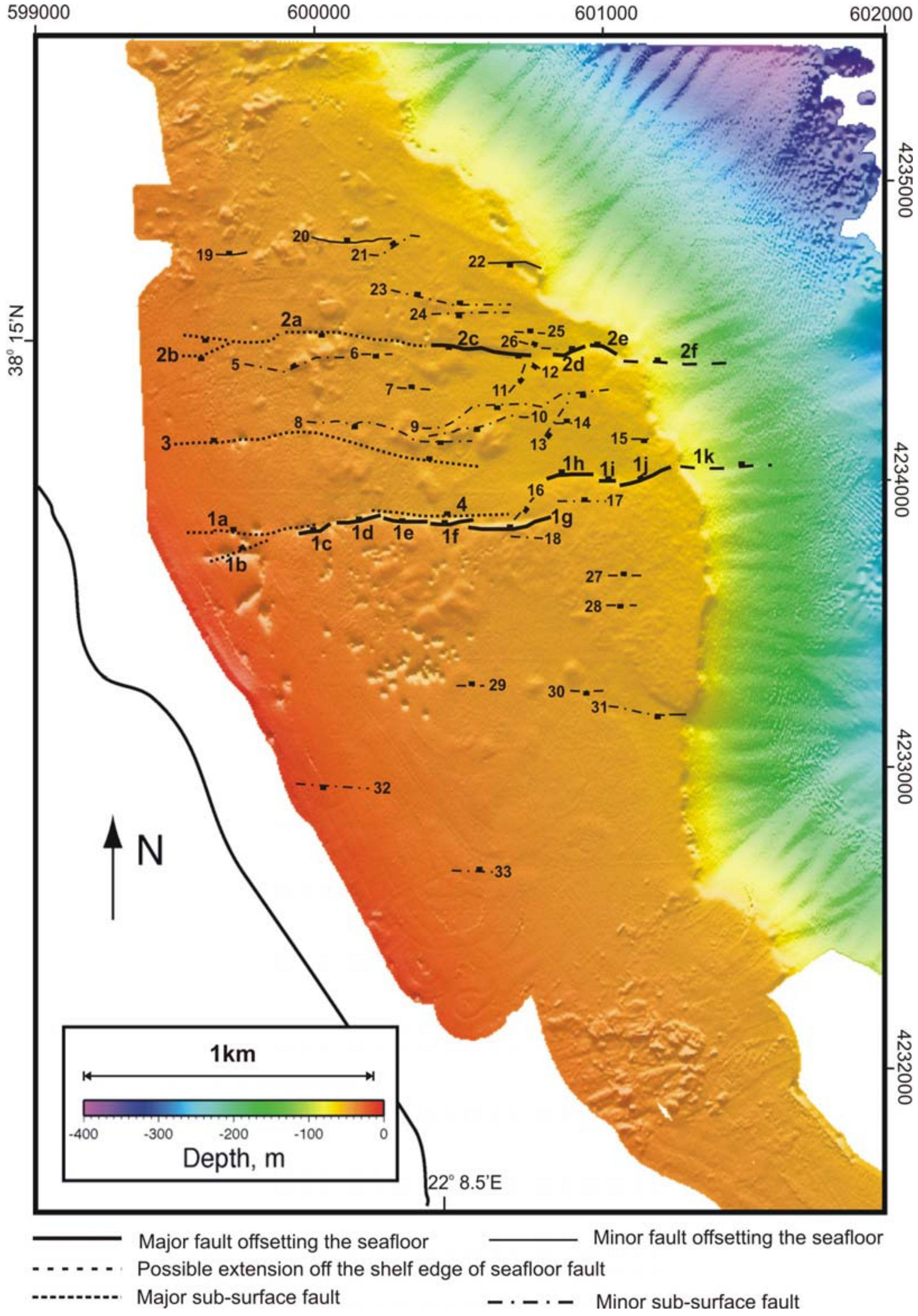

**Figure 5.4:** Surface and sub-surface faults interpreted from the MCS reflection profiles and the multibeam bathymetry, overlain onto the bathymetry image. An enlargement of this plot can be found in Plate 1C. Numbering scheme used in this figure will be referred to throughout this thesis.

Most of the minor sub-surface faults are located within the graben (**3 – 17**, Figure 5.4), although some are located in the footwalls of both the Aigion Fault and the major S-dipping graben bounding fault (N and S of the graben). They are predominantly orientated E-W, mirroring the orientation of the major faults (**1** & **2**, Figure 5.4), although within the step-over zone the faulting becomes more complex. This zone is where both the main faults change geometry, with the Aigion Fault stepping northwards (**1g** to **1h**, Figure 5.4), whilst the S-dipping fault reverses polarity (**2c** to **2d**, Figure 5.4). Within this step-over zone, three faults display a change in orientation, having a SW-NE trend (**11,13** & **16**, Figure 5.4), before terminating against faults that have the predominant E-W trend.

In cross-section, all the faults appear planar. With the limited penetration due to the high-resolution nature of this survey, and the reduction in primary energy return below 110 ms TWTT, it is not possible to determine fault geometry below this depth, or whether the faults merge onto one main detachment plane. However due to the close proximity and interaction between many of the faults, it is hypothesised that faults **1 – 18** (Figure 5.4) connect at depth at <1 km. This will be addressed further in Chapter 8.

Due to the number of faults mapped, it was decided to divide them into three main arrays (Figure 5.6). Division was based on proximity to, and so interaction between faults, sense of fault dip, lateral coherence of each fault, and size – both in fault length and vertical displacement. The two main arrays are centred around the main Aigion Fault, comprising **1**, **4**, **15-18** (Figure 5.4), and the main S-dipping fault, comprising **2**, **3**, **5-14** (Figure 5.4). The third array consists of small faults, both N and S-dipping, that are <300 m in length, and are located within the footwalls of the two graben forming faults (**19-33**, Figure 5.4).

In order to accurately locate features discussed later in this chapter, Figure 5.7 shows the locations of the MCS reflection survey lines overlain onto the multibeam bathymetry image (enlargement Plate 1B). CDP numbers (Figure 5.7) and fault numbers (Figure 5.4) will be used to link features identified in both datasets.

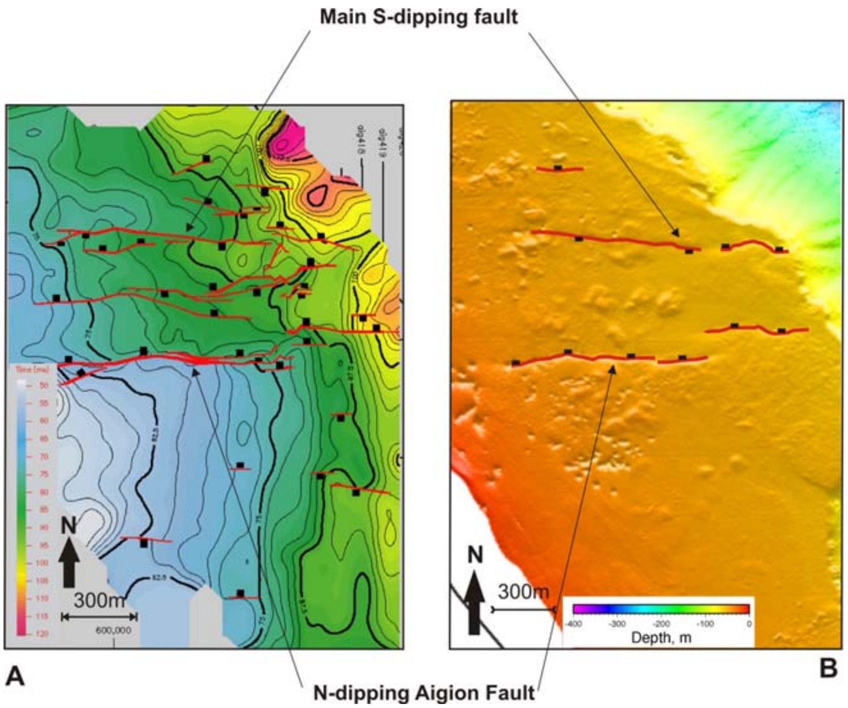

**Figure 5.5:** Illustration of the distribution of mapped faults offsetting the transgressive horizon (H4) and the present day seafloor. **A)** Faults offsetting horizon H4 (~11.5ka). Colour scale is in TWTT (ms), representing depth to the horizon from the seafloor. **B)** Faults offsetting the seafloor. There is a significant decrease in the number of faults deforming the seafloor as compared to H4. Reasons for this are addressed initially in section 5.1.2, and more fully in Chapter 6.

**Figure 5.6:** Plot illustrating the division of faulting into the three arrays. Red = Array centred around the N-dipping Aigion Fault; Blue = Array centred around the S-dipping graben bounding fault; Green = Array comprising all the minor footwall faults. Polygons indicate the sense of dip.

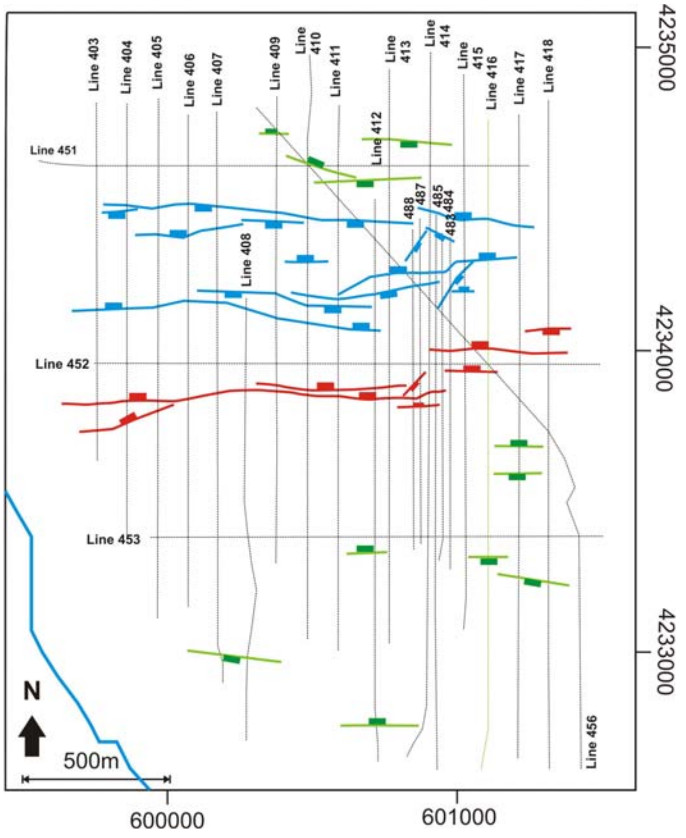

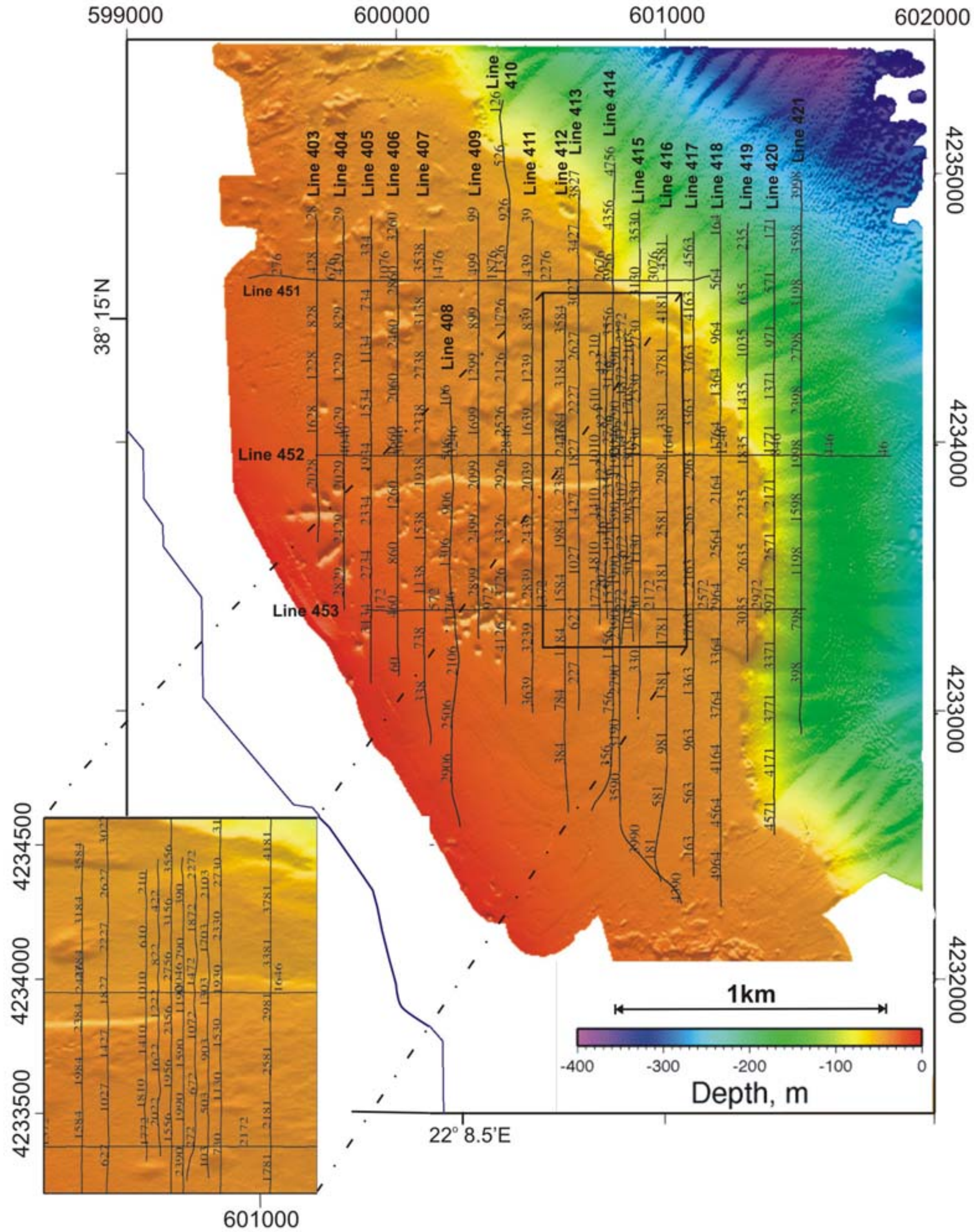

**Figure 5.7:** Multibeam bathymetry plot with the location of the MCS reflection survey lines run overlain. Every 400th CDP is shown (200 m spacing) for each profile. Enlargement shows the area where the survey lines were run at 25 m spacings. An enlargement of this figure can be found in the Appendices, Plate 1B.

### 5.1.2 Aigion Fault and Associated Array

The offshore Aigion Fault is the most significant fault imaged in terms of vertical displacement, showing a present-day maximum displacement at the seafloor of ~3 m and ~14 m at horizon H4. The multibeam image indicates that the main Aigion Fault trace is segmented at the seafloor (**1a – 1k**, Figure 5.4, Plate 1C), with segments ranging in length from ~100 - 400m. Six of these appear to closely interact (**1a – 1g**, Figure 5.4), forming a seafloor trace that is >1km in length.

At the eastern end of the offshore Aigion Fault, ~500m west of the shelf edge, there is a northward step (**1h – 1k**, Figure 5.4). This area is defined as a step-over zone (see also 5.1.3). The multibeam bathymetry data from the Aigion Shelf indicates that this fault trace may continue beyond the shelf edge, however, the surface trace of this continuation is not visible in the regional multibeam dataset. It is possible that debris from the shelf edge has eroded any surface expression of this fault. Therefore it is not known how far beyond the shelf edge this fault system may continue.

The minor graben faults **4** and **15 – 18** (Figure 5.4) are believed to interact with the offshore Aigion Fault, based on dip direction / angle, and proximity. They have therefore been combined with the offshore Aigion Fault to form the Aigion array (red, Figure 5.6). None of these faults appear to be segmented, and they range in length from 100 – 500 m. All of them are sub-surface. The most significant one (**4**, figure 5.4) has a maximum vertical displacement of 4m on horizon H4.

### 5.1.3 Dominant S-dipping Fault and Associated Array

The prominent S-dipping fault bordering the north of the graben **(2a – 2c**, Figure 5.4) is located between 300 – 800 m north of the Aigion Fault. Approximately 1500 m along strike (from W – E), this S-dipping fault changes polarity, becoming N-dipping (**2d** & **2e**, Figure 5.4). This occurs at the same E-W position along strike as the prominent northward step on the Aigion Fault (**1g** to **1h,** Figure 5.4**)** , in what is termed as a step-over zone in this study.

The S-dipping fault (**2**, Figure 5.4) is also segmented, comprising six segments ranging in length from ~100 – 650 m. It has a shorter seafloor trace than the offshore Aigion Fault (**1**, Figure 5.4). However, a number of pockmarks forming a linear trace ~750m long immediately west of the fault (**4**, Figure 5.2), delineate its sub-surface location, indicating that at depth the two faults are probably of a similar length.

The graben faults **3** and **5 – 14** (Figure 5.4) are believed to interact with this S-dipping fault, based on proximity and dip, and so have been combined with it to form the graben array (blue, Figure 5.6). They range in length from 100 m – 1 km, with the most significant fault (**3**, Figure 5.4) showing a maximum vertical displacement on horizon H4 of 6 m.

### 5.1.4 Footwall Array

Minor faults occur north and south of the graben, in the footwalls of the two major faults. They are not regularly spaced, do not appear to converge within the upper 100 m, and are only laterally traceable for <300 m. North of the graben, three are visible at the seafloor (**19, 20** & **22**, Figure 5.4). However faults **21** and **23 – 33** (Figure 5.4) only displace the trangressive horizon (H4).

It is proposed that the minor faults are a response to gravitational stresses resulting from differential uplift associated with the Cape Gyftissa, Aigion and Eliki faults. They formed to accommodate strain between these fault systems. If mass wasting of the shelf edge had been the driving process in their formation, it is believed that they would mirror the orientation of the shelf edge, and not the E-W orientation of the main faults.

### 5.1.5 Textural Variation across the Shelf

An area of seafloor that appears texturally different to its surroundings is coincident with the step-over zone (Figure 5.8). Continuity of the upper reflectors in U1 indicate that this feature is not caused by fluids / sediments migrating up from deeper in the section, although there is slight doming on H4 which results in a thinner drape of sediments above H4. Figure 5.4 shows that segments **1h – 1j** bound this area to the north. However, no faults follow the southern limits of this area, although fault **31** (Figure 5.4) does bound this area at the shelf edge. A channel-like feature can be traced for ~200 m along the southern edge of this area, although no source for this is visible. Therefore, whilst uplift on segments **1h - 1j** and fault **31** may be driving the thinning of the sedimentary drape, and controlling the southern limit of this area, it cannot explain the textural change. One possibility is that upwelling of deeper waters, and anti-cliockwise circulation patterns across the shelf, documented by Lascaratos et al. (1989) are causing re-mobilisation of the exposed fine grained sediments deposited on the uplifted block along the shelf edge. This would result in an erosive surface forming, which may have a rougher surface texture, so causing the dimpled morphology.

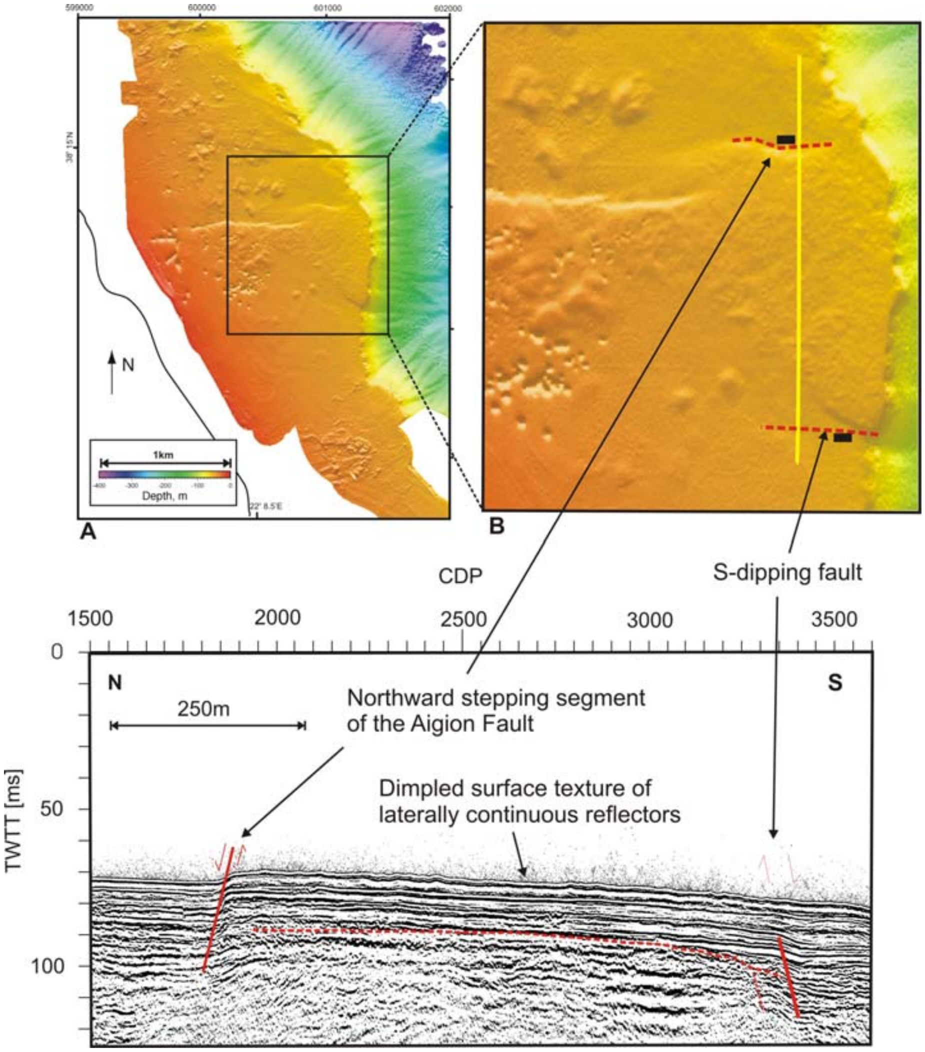

**Figure 5.8:** Mulitbeam bathymetry image, and example MCS reflection profile from the area of dimpled topography and thinning of sediments over horizon H4, in the footwall of the Aigion Fault. The MCS profile used is Line 417 (Enlargement in Plate 3). Horizon H4 is indicated by a dashed red line in the seismic profile.

### 5.1.6 Syn-tectonic Sedimentation

The two dominant faults that have seafloor expression (**1** and **2**, Figure 5.4) cause significant tilting of the strata and the formation of sedimentary growth wedges into the hangingwalls. The sediments deposited between H4 (~11.5 ka) and the present show tilting to the south, forming a significant sedimentary wedge in the hangingwall of the Aigion Fault. It is most obvious on lines 403 – 405, with a slight expression of thickening on line 406, before all horizons become horizontal (in the east) by line 407 (Figure 5.9).

This thickened wedge covers an along strike distance of ~350 m, corresponding to segment **1a** (Figure 5.4). It suggests that this segment initially experienced a greater degree of displacement than those to the east (**1c – 1g**). The thickening of sediments does not continue in the youngest sediments, occurring primarily between horizons H4 (~11.5 ka) and H3 (~7.5 ka). If the location of maximum displacement had moved eastwards onto segments 1c – 1g, thickening of the sediments above horizon H3 would be expected in MCS reflection profiles 407 – 414. However, this is not observed. It is likely that this change in the attitude of the reflectors deposited is a result of a change in the style of deformation, from a half-graben to graben.

Some of the sediments deposited in the graben between H4 (~11.5 ka) and H3 (~7.5 ka) show tilting to the north, forming a slightly thickened wedge in the hangingwall of the S-dipping fault, indicating dominance of this fault. It occurs on lines 410 – 413 (Figure 5.10), corresponding to segment **2c** (Figure 5.4). West of line 410 (line 409, Figure 5.7, Plate 2), corresponding to segment **2a**, H4 is horizontal with no obvious sedimentary wedge forming above it. This indicates that there was less movement on segment 2a during this time, and that the two graben bounding faults had similar displacement rates. East of line 413, the S-dipping fault reverses polarity, with no evidence of a wedge being preserved. After ~7.5 ka the reflectors in lines 410 – 413 become more horizontal, suggesting that the displacement on the relevant segments of the two graben bounding faults (**2c** and **1f/1g**, Figure 5.4) was becoming more comparable.

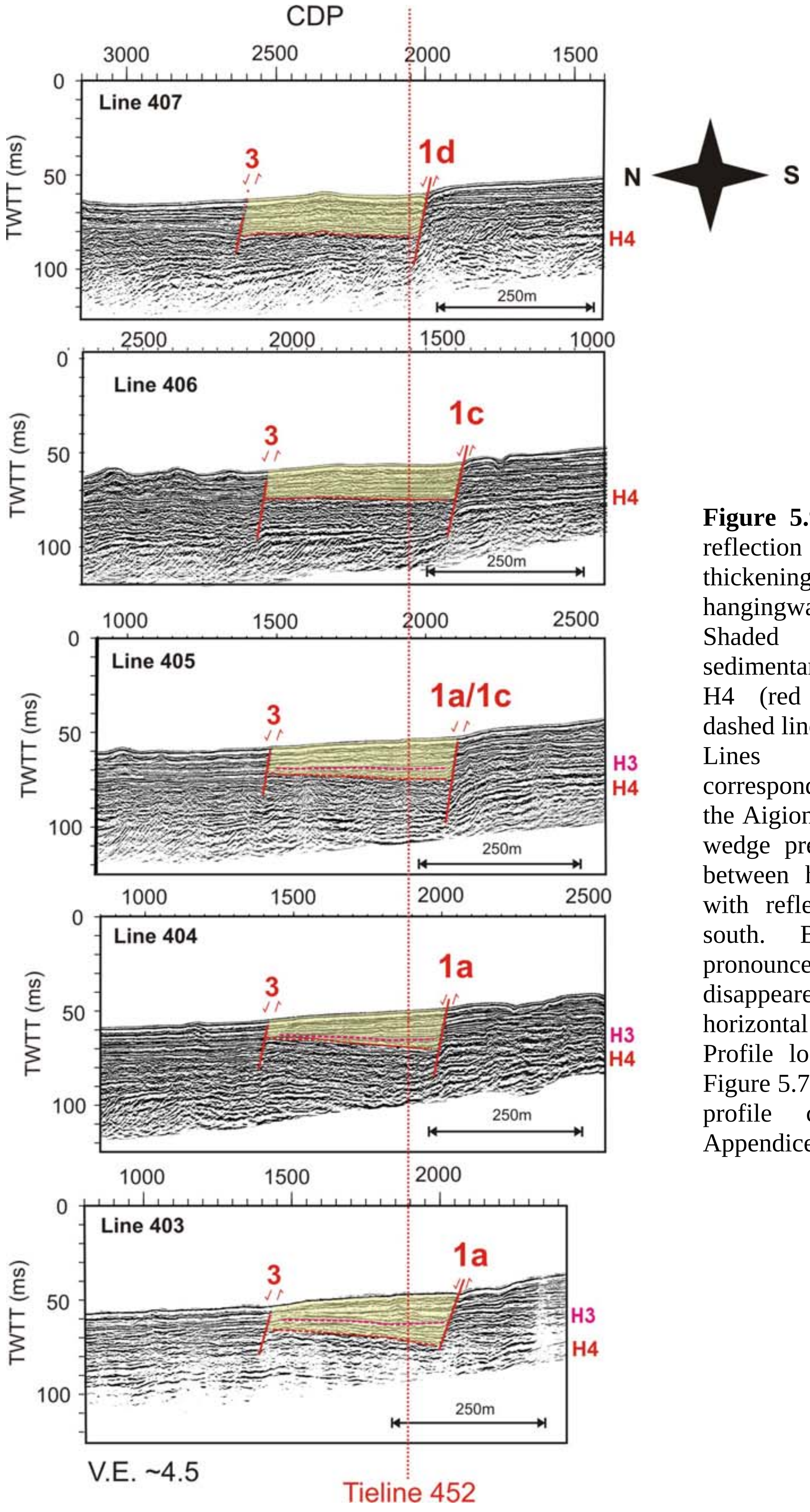

**Figure 5.9:** Examples of MCS reflection profiles illustrating the thickening of sediments in the hangingwall of the Aigion Fault. Shaded area highlights the sedimentary wedge to horizon H4 (red dashed line). Pink dashed line is H3.

Lines 403 and 404, corresponding to segment 1a of the Aigion Fault, show a defined wedge predominantly occurring between horizons H4 and H3, with reflectors inclined to the south. By line 407 this pronounced wedge has disappeared and all reflectors are horizontal to sub-horizontal.

Profile locations are shown in Figure 5.7. Enlargements of each profile can be found in Appendices, Plate 2.

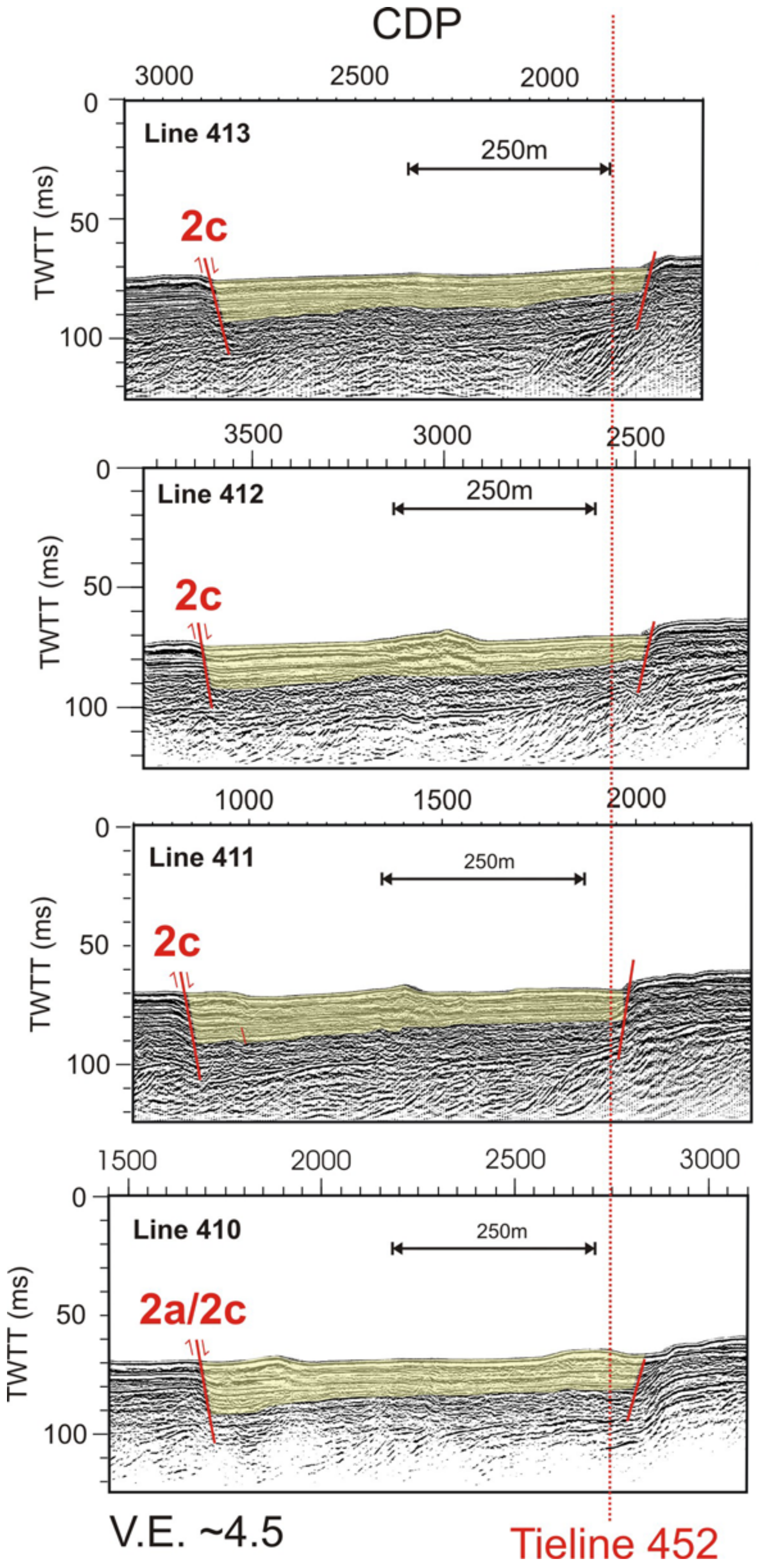

**Figure 5.10:** Examples of MCS reflection profiles illustrating the thickening of sediments above horizon H4 in the hangingwall of the S-dipping fault. The thickening predominantly corresponds to segment 2c. However it is not as defined as the sedimentary wedge in the hangingwall of the Aigion Fault. Profile locations are shown in Figure 5.7. Enlargements of each profile can be found in Plate 2.

There is evidence of recent progradation (Figure 5.11), from the present day shoreline north-easterly, which is most obvious on the nearshore seismic profiles (403 – 410, Plate 2). Reflectors beneath horizon H3 appear sub-parallel to horizon H4. However, reflectors deposited after horizon H2 (~4.5ka) dip north, downlapping onto older reflectors. This is a result of the interplay between the rate of sea-level rise, which Siddall et al. (2003) predict slowing at ~6ka, combined with an increase in sediments supplied into the area, that Lemeille et al. (2004) document from analysis on the AIG10 borehole.

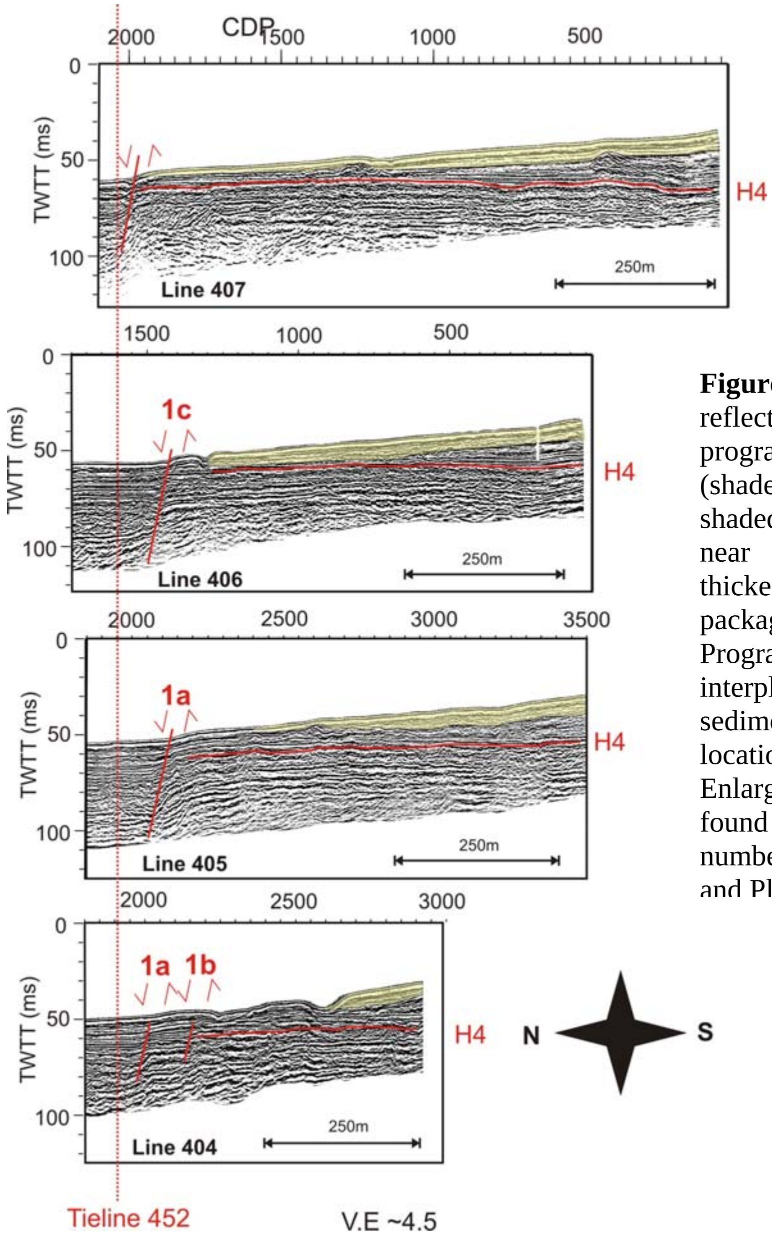

**Figure 5.11:** Examples of MCS reflection profiles illustrating the progradation of the sediments (shaded) above horizon H2, (base of shaded area). Horizon H4 appears near horizontal, indicating that thickening of the sedimentary package is not due to back-tilting. Progradation occurs due to the interplay between sea-level and sediment supply rates. Profile locations are shown in Figure 5.7. Enlargements of the profiles can be found in Appendices, Plate 2. Fault numbers correspond to Figure 5.4 and Plate 1C.

## 5.2 HORIZON STRUCTURE AND DEFORMATION

Using the horizons identified in Chapter 4, it is possible to analyse how the fault displacement and fault geometry has changed with time. Figure 5.12 shows the structure plots for each of the horizons, measuring the depth to the horizon in TWTT (ms). The faults displacing each horizon are indicated. The thickness of each fault trace in the structure plots indicates the amount of displacement of that horizon.

An easterly to north-easterly dip of 1.5 – $2^{o}$ was calculated for each of the depth-to-horizon plots shown in Figure 5.12. This is consistent with the dip of $2^{o}$ and an easterly trend proposed by Stefatos (2005). The dip is steeper on horizon H4 than on the other horizons, possibly due to a change in depositional style. Horizon H4 formed during sea-level rise, associated with wave base erosion, whilst horizons H3 – H1 were formed during submarine conditions, allowing a more even distribution of the available sediments.

Figure 5.12D shows that there are a number of fault segments that range in length from 100 – 1220 m offsetting horizon H4 (11.5 ± 1 ka). However by H1 (3.5 ± 0.5 ka) (Figure 5.12A), most of the minor faults are no longer visible or have reduced in length to <500 m and the Aigion and the S-dipping faults have become dominant (**1** & **2** respectively, Figure 5.4; Plate 1C).

Three of the minor faults within the graben (**3, 8** & **10**, Figure 5.4; Plate 1C) displace all four horizons, although their lateral extent reduces with decreasing age. By H3 (7.5 ± 1.1 ka, Figure 5.14C) fault **3** shows a small gap of ~100 m in its lateral continuity, circled in red. The size of this break increases in H2 (4.5 ± 0.6 ka, Figure 5.14B) to 200 m and again in H1 to 500 m. Faults **8** and **10** (Figure 5.4; Plate 1C) do not show any breaks in their lateral continuity, but do show significant reductions in their length with each successive horizon from 500 m to 100 m.

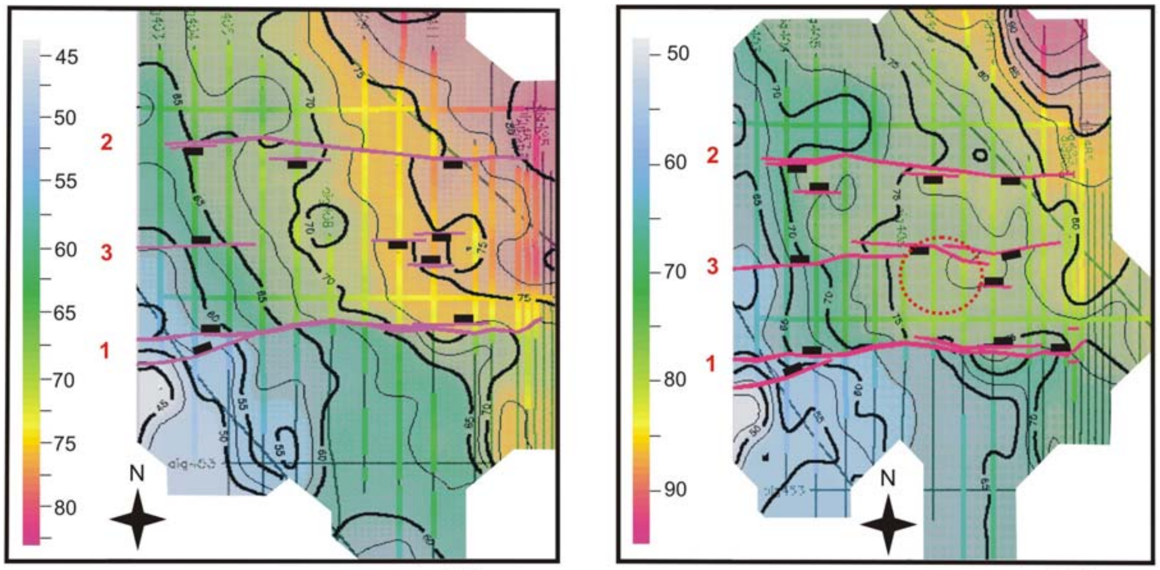

**A: H1 - 3.5 +/-0.5ka**

**B: H2 - 4.5 +/-0.6ka**

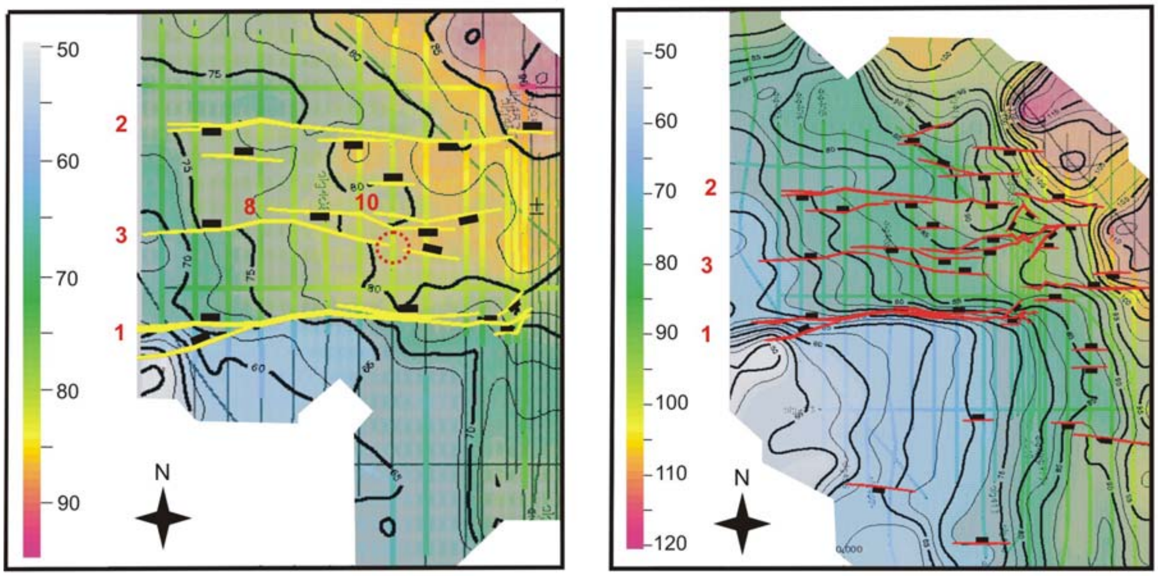

**C: H3 - 7.5 +/- 1.1ka**

**D: H4 - 11.5 +/- 1ka**

**Figure 5.12:** Horizon and structure plots for the four horizons identified in the MCS reflection profiles. Measurement of the depth to each horizon is in TWTT (ms). Contours plotted every 2.5 ms; red numbers relate to fault numbers (Figure 5.4 and Plate 1C). The footwall array faults disappear by H3, and by H2 many of the graben faults have either disappeared or reduced in lateral extent.

Apparent burial of fault tips, as with faults 8 and 10, can be caused by a decrease in the displacement rate towards the tip (to below the sedimentation rate), causing only the central part of a segment to be visible. Burial of central sections of a fault may indicate that the fault is segmented, and that the segments are accruing displacement differentially, causing some to be covered whilst others are still visible.

## 5.3 SEDIMENTATION HISTORY OF THE AIGION SHELF

Isopach plots (generated within the 3D interpretation software), can be used to determine the sedimentation history for discrete time periods during the last 11.5 kyr. Variations in sedimentation patterns can be used to make observations about fault activity and assess potential fault growth.

### 5.3.1 ~11.5 – 0 ka (H4 to Seabed)

Figure 5.13 shows the total sediment thickness accumulated since 11.5 ka. There is a defined deposition minimum (pale blue, 0-2.5 ms TWTT) in the footwall of the Aigion Fault (**A**, Figure 5.13), where seafloor offset is greatest, and uplift of the footwall reduces available accommodation space. This corresponds to fault segments **1e-1g** (Figure 5.4). A less defined minimum (green blue, **B**, Figure 5.13) can be seen on the footwall of a S-dipping fault (**2a**, Figure 5.4), again related to where seafloor offset is greatest. Proximity of both these deposition minimas to major faults that offset the seafloor, suggest they are tectonically controlled as opposed to being driven by sediment supply rates.

The thick sediments to the south (deep pink, 25-30 ms TWTT) (**C**, Figure 5.13) correspond to the location of present day fluvial inputs from the Selinous and Kerynitis Rivers. This depocentre corresponds to where progradation of sediments above H2 was observed in the MCS reflection profiles (Figure 5.11). Reflectors below H2 (~4.5 ka) appear sub-horizontal to H4, indicating that back tilting of the footwall is not sufficient to explain this thickening of sediments.

There is another deposition maximum located at the north of the survey area (**D**, Figure 5.13). This corresponds to an area where Venetian historical archives suggest the mouth of the Selinous River has been located (during periods of avulsion), prior to

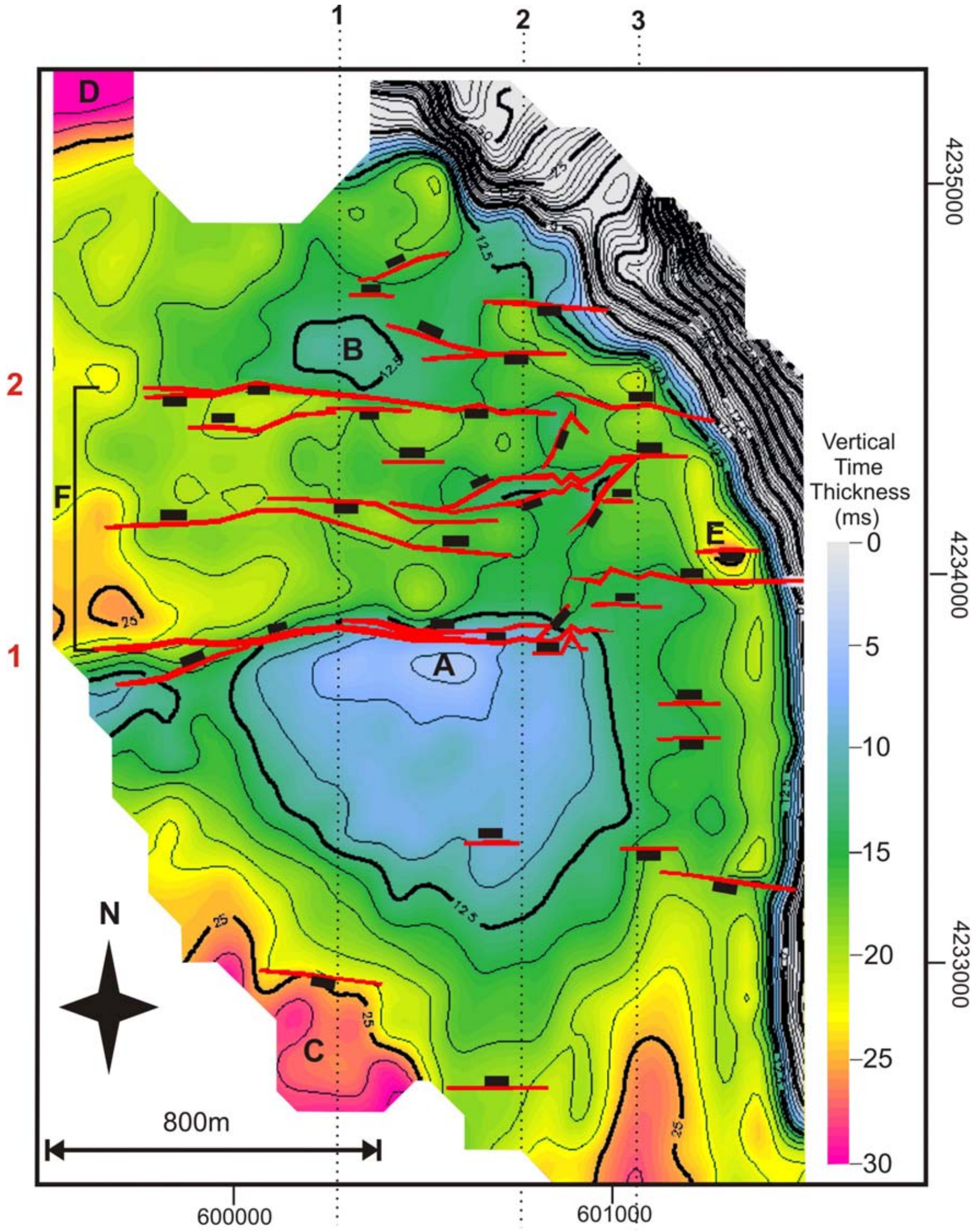

**Figure 5.13:** Isopach map showing the thickness of sediments deposited post ~11.5 ka (in TWTT ms). Upper boundary to the isopach is the present day seafloor; lower boundary is the trangressive horizon H4. Faults offsetting H4 are shown. Polygons indicate the downthrown hangingwalls; red numbers indicate fault numbers (Figure 5.4 and Plate 1C). Dotted lines correspond to locations of markers used in the fault displacement analysis (Chapter 6). Letters correspond to features discussed in the main text.

containment within a man-made channel (Soter and Katsonopoulou, 1998) (see Figure 5.1). Surface indications of this fluvial deposition (**D**, Figure 5.13) can be seen in the multibeam data (**9**, Figure 5.2).

A localised maximum (**E**, Figure 5.13) can be seen centred around a small S-dipping fault at the shelf edge (**15**, Figure 5.4), located on MCS reflection line 417 (Appendices, Plate 3). Contours closing against this fault indicate that there is a localised topographic low forming as a result of fault activity.

The graben (**F**, Figure 5.13) shows a general trend of sediments thinning eastwards towards the shelf edge (25 – 12.5 ms). There is a band of slightly offset sediments orientated NE-SW at the step-over zone, between lines 2-3 (Figure 5.13), which mirrors the orientation of minor graben faults that are orientated ~040$^0$ NE (**11,13** & **16**, Figure 5.4). This band of sediments terminates to the south against a major N-dipping fault (**4**, Figure 5.4). It suggests that the complex faulting pattern at the step-over zone is over-riding the sedimentation patterns caused by subsidence and creation of accommodation space associated with the major N-dipping fault and S-dipping faults (**1a-g** & **2a-2c**, Figure 5.4).

This isopach can be further broken down into four discrete time periods based on the horizons H4 – H1 (Figure 5.14) defined in Chapter 4.

### 5.3.2 ~11.5 – ~7.5 ka (H4 – H3)

The isopach for the ~4 kyr period between horizons H4 and H3 (Figure 5.14A) indicates relatively little deposition was occurring on the shelf (0 – 4 ms). There is a deposition minimum (**A**, Figure 5.14A) on the footwall of the Aigion Fault (**1f** & **1g**, Figure 5.4), where no deposition has occurred. There is also an isolated minimum occurring close to the shelf edge (B, Figure 5.14A) associated with the footwall of a small S-dipping fault (**22**, Figure 5.4). The thickest sediments occur at the shelf edge and in the eastern graben (**C** & **D** respectively, Figure 5.14A), in direct contrast to the pattern shown in Figure 5.13 for the ~11.5kyr period.

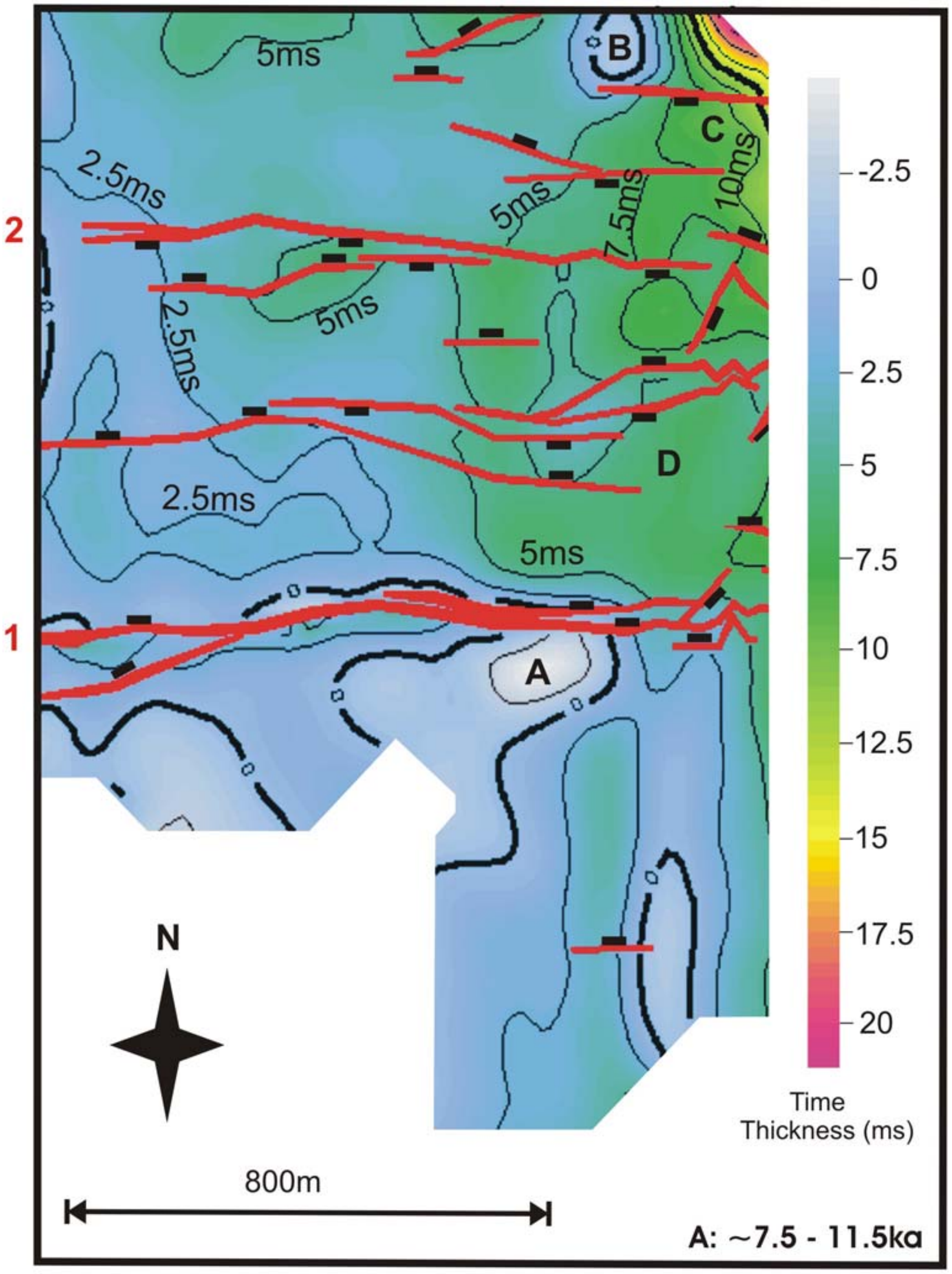

**Figure 5.14:** Fault and isopach plots of the four time periods that combine to form the isopach shown in Figure 5.14. Scale bars are initially used that are specific to each time period, to enhance the detail. Figure 5.15 shows the same plots using a common scale. Numbers in red correspond to the fault numbering shown in Figure 5.4 and Plate 1C.

**5.14A)** Isopach plot representing the time period from ~7.5 ka - ~11.5 ka (Horizon H3 – Horizon H4). The thickness of the sediments deposited are measured in TWTT (ms), contoured every 1 ms.

### 5.3.3 ~7.5 – ~4.5 ka (H3 – H2)

The isopach for the ~3 kyr period between horizons H3 and H2 (Figure 5.14B) indicates that deposition was occurring predominantly along the western nearshore edge of the survey area (**A**, Figure 5.14B), suggesting that progradation was rapid following the stabilisation of sea-level. This area of high deposition terminates southward against the Aigion Fault (**1a**, Figure 5.4), suggesting that the fault controls the position of the depocentre. The dominant synthetic fault within the graben (**3**, Figure 5.4) and the western end of the S-dipping fault (**2**, Figure 5.4) have no impact on sediment deposition, with little variation between the thickness of sediments in their respective footwalls and hangingwalls.

There is one localised deposition maximum (**B**, Figure 5.14B) located in the hanging-wall at the eastern end of the main S-dipping fault (**2c**, Figure 5.4). The localisation of this maximum may indicate that there has been differential displacement occurring on the segments comprising this fault, with **2c** accruing more than those adjacent to it, so creating a localised depocentre. There are also deposition minimums located on the Aigion Fault footwall (**C**, Figure 5.14B), and at the shelf edge (**D**, Figure 5.14B). The first is likely to be tectonically controlled, relating to segments **1c** & **1d**, (Figure 5.4) where increasing displacement has reduced accommodation space. The second, at the shelf edge, is more likely to be the result of a reduction in sediment supply due to distance away from a coastal source, as it does not appear to be related to any specific faults that offset horizon H3. A third localised minima (**E**, Figure 5,14B) in the eastern footwall of the Aigion Fault is also believed to be a result of distance from coastal terrestrial inputs.

### 5.3.4 ~4.5 – 3.5 ka (H2 – H1)

The isopach for the ~1 kyr period between horizons H2 and H1 (Figure 5.14C) shows a depocentre developing within the graben (**A**, Figure 5.14C), indicating that the N-dipping Aigion Fault and the main S-dipping fault bordering the graben are the dominant controls on deposition (**1** & **2** respectively, Figure 5.4).

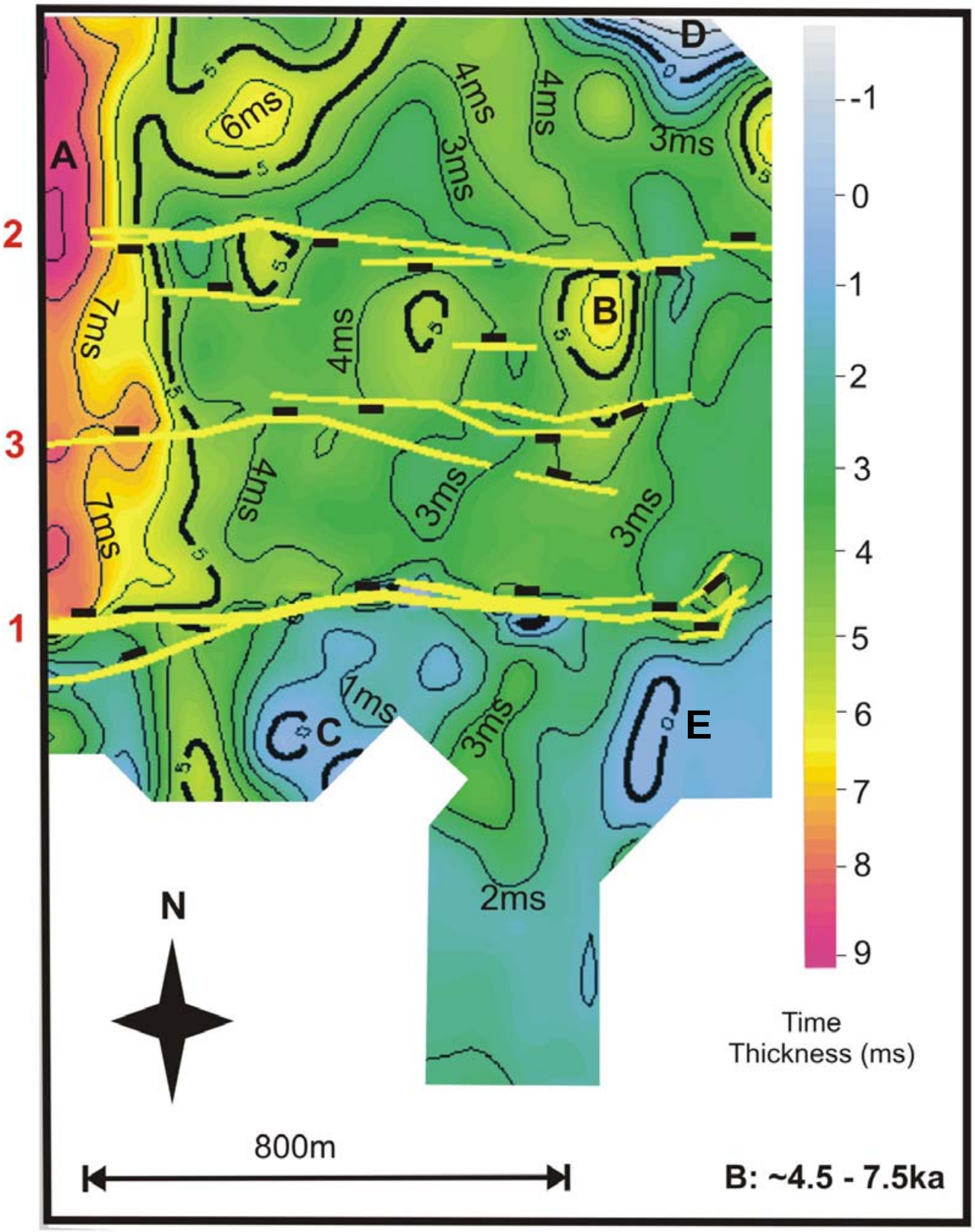

**Figure 5.14B:** Isopach plot representing the time period from ~4.5 ka - ~7.5 ka (Horizon H2 – Horizon H3). The thickness of the sediments deposited are measured in TWTT (ms), contoured every 1 ms.

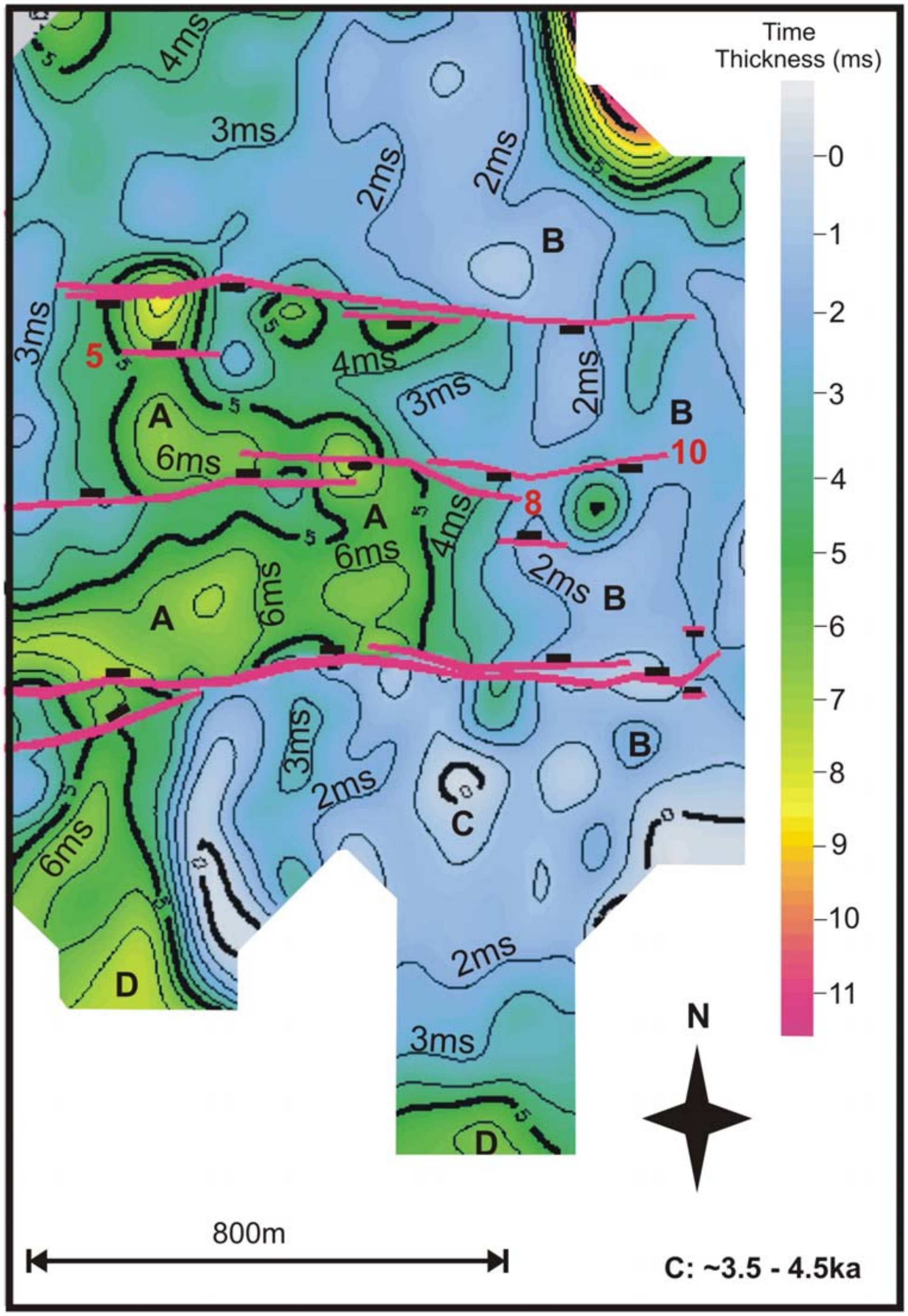

**Figure 5.14C:** Isopach plot representing the time period from ~3.5 ka - ~4.5 ka (Horizon H1 – Horizon H2). The thickness of the sediments deposited are measured in TWTT (ms), contoured every 1 ms.

Changes in isopach thickness across minor faults (**3, 5, 8** & **10**, Figure 5.4) indicate that they were active during this period of deposition. However as the surface expression of faulting within the graben dies off to the east, so the thickness of the sediment package remains constant across both the major and minor faults (**B**, Figure 5.14C). This is likely to be an effect of decreasing displacement on faults **1**, **2** & **10** (Figure 5.4), causing minimal offset between the footwalls and hangingwalls.

There is a clear deposition minimum (**C**, Figure 5.14C) on the Aigion Fault footwall (**1e** & **1f**, Figure 5.4), although it appears to have moved eastwards by ~400m when compared to the previous isopach (Figure 5.14B). The southernmost ends of the seismic profiles show an increase in the thickness of sediments (**D**, Figure 5.14C). This may be due to a change in the source and quantity of sediments being deposited in this area. It is possible that the Selinous and Kerynitis rivers are supplying fluvial sediments into the area. An alternative hypothesis is that increased displacement on the Aigion Fault (**1a – g**, Figure 5.4) has caused backtilting of the footwall, however the reflectors deposited during this period appear horizontal, arguing against this idea. Activity on the fault during this period will be examined in more detail in Chapter 6 to try and explain this feature.

### 5.3.5 ~3.5 – 0 ka (H1 – Seabed)

The isopach for the ~3.5 kyr time period between horizon H1 and the seabed (Figure 5.14D) indicates that the maximum deposition (deep pink, 15 ms TWTT) is now located at the southern end of the nearshore survey lines (**A**, Figure 5.14D). The MCS reflection profiles show evidence of sediment progradation in this area.

The depocentre minimum (**B**, Figure 5.14D) on the footwall of the Aigion Fault (**1d-g**, Figure 5.4) is no longer as pronounced as in the previous isopach. An increase in fluvial / nearshore sedimentation rate may be exceeding the effects of fault displacement.

The graben depocentre identified in the previous isopach is still clear, and has increased laterally eastwards (**C**, Figure 5.14D). The variability of sediment thicknesses seen within the graben in the previous isopach (Figure 5.14C), especially within the nearshore 600 m of the area, appears to have reduced. The number of minor faults

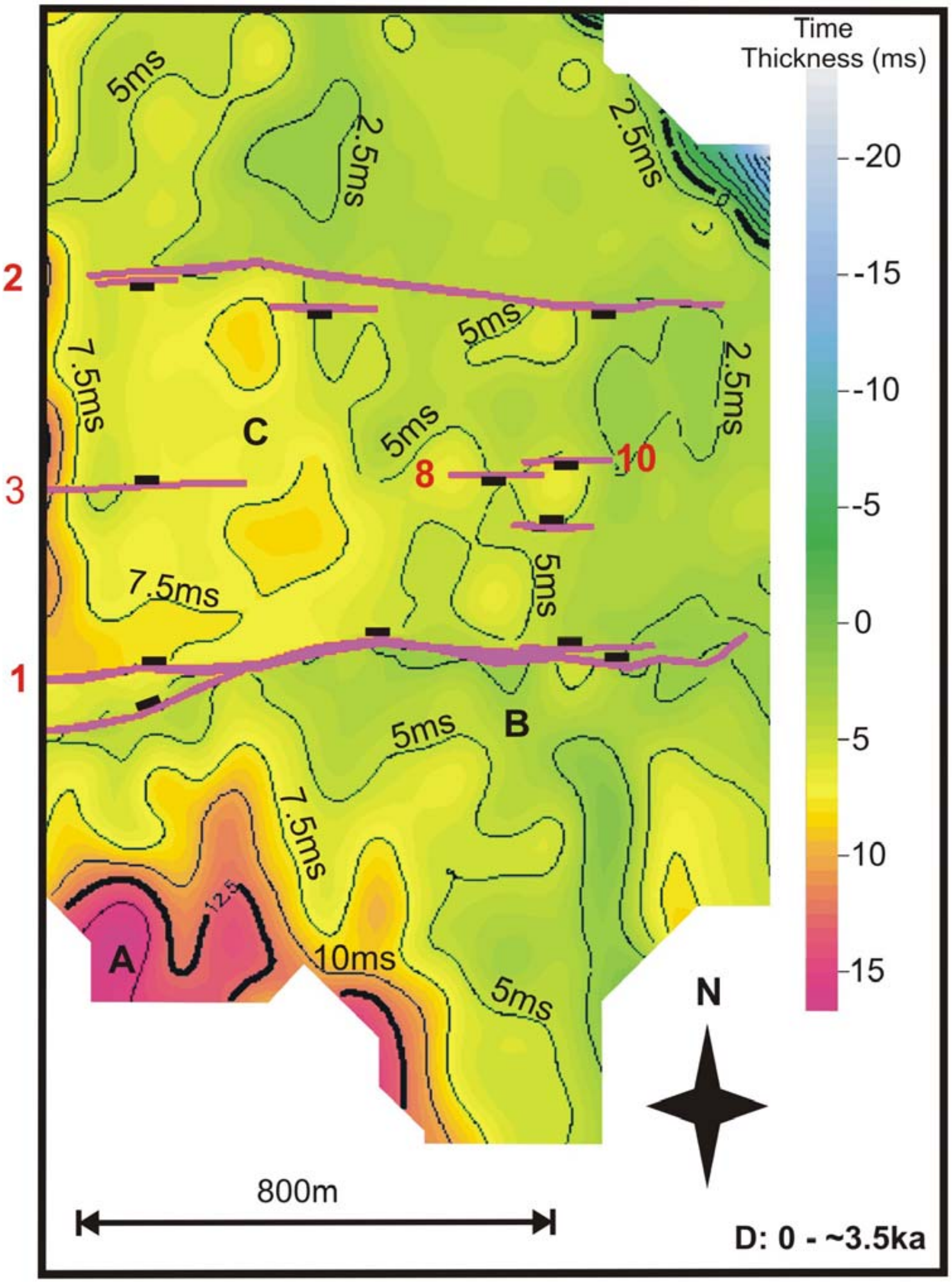

**Figure 5.14D:** Isopach plot representing the time period from the present day to ~3.5 ka (Horizon H1). The thickness of the sediments deposited are measured in TWTT (ms), contoured every 2.5 ms.

offsetting the oldest horizon from this isopach period has also reduced, with only sections of faults **3, 8** and **10** (Figure 5.4) visible, indicating that there has been a decrease in the impact of tectonic activity on the sediment deposition patterns within the graben.

## 5.4 DISCUSSION

### 5.4.1 Influences of Faulting and Sediment Deposition on Stratigraphy

Sedimentation rates that are equal to, or higher than the displacement rates of syn-sedimentary faults, result in a detailed record of fault activity and growth (e.g. Hardy and Gawthorpe, 1998; Cowie et al., 2000; Childs et al., 2003; Taylor et al., 2004; Bernal et al., 2004). Syn-tectonic sediments record the interplay between sedimentation rates and the changes in distribution of accommodation space due to the displacement and / or growth of faults (Poulimenos et al., 1993; Schlische and Anders, 1996; Cowie et al., 2000).

Figure 5.15 shows the same isopach plots described in sections 5.3.2 - 5.3.5, bit with the colour scales adjusted so that they can be directly compared. They indicate that over the time intervals considered in plots A – D, sedimentation rates range from 6.5 to 0 mm yr$^{-1}$ (Table 5.1), with an average rate of 1.2 mm yr$^{-1}$ over the 11.5 kyr time period.

| **Age Range (ka)** | **Isopach Period (kyr)** | **Maximum Isopach Thickness (TWTT / m)** | | **~Maximum Sedimentation Rate (mm yr$^{-1}$)** | **Minimum Sedimentation Rate (mm yr$^{-1}$)** | **Average Rate (mm yr$^{-1}$)** |
|---|---|---|---|---|---|---|
| **0 – 11.5** | 11.5 ± 1 | 30ms | 25m | 2.2 ± 0.2 | 0.3 ± 0.03 | 1.2 ± 0.1 |
| **7.5 – 11.5** | 4 ± 1.5 | 8.5ms | 7m | 1.8 ± 0.3 | 0 | 0.5 ± 0.09 |
| **4.5 – 7.5** | 3 ± 1.3 | 9ms | 7.5m | 2.5 ± 0.4 | 0 | 1 ± 0.2 |
| **3.5 – 4.5** | 1 ± 0.8 | 9ms | 7m | 6.5 ± 1 | 0 | 1.5 ± 0.2 |
| **0 – 3.5** | 3.5 ± 0.5 | 15ms | 12m | 3.5 ± 0.5 | 0.5 ± 0.07 | 1.5 ± 0.2 |

**Table 5.1:** Summary of approximate sedimentation rates calculated from the isopach plots of the five time periods.

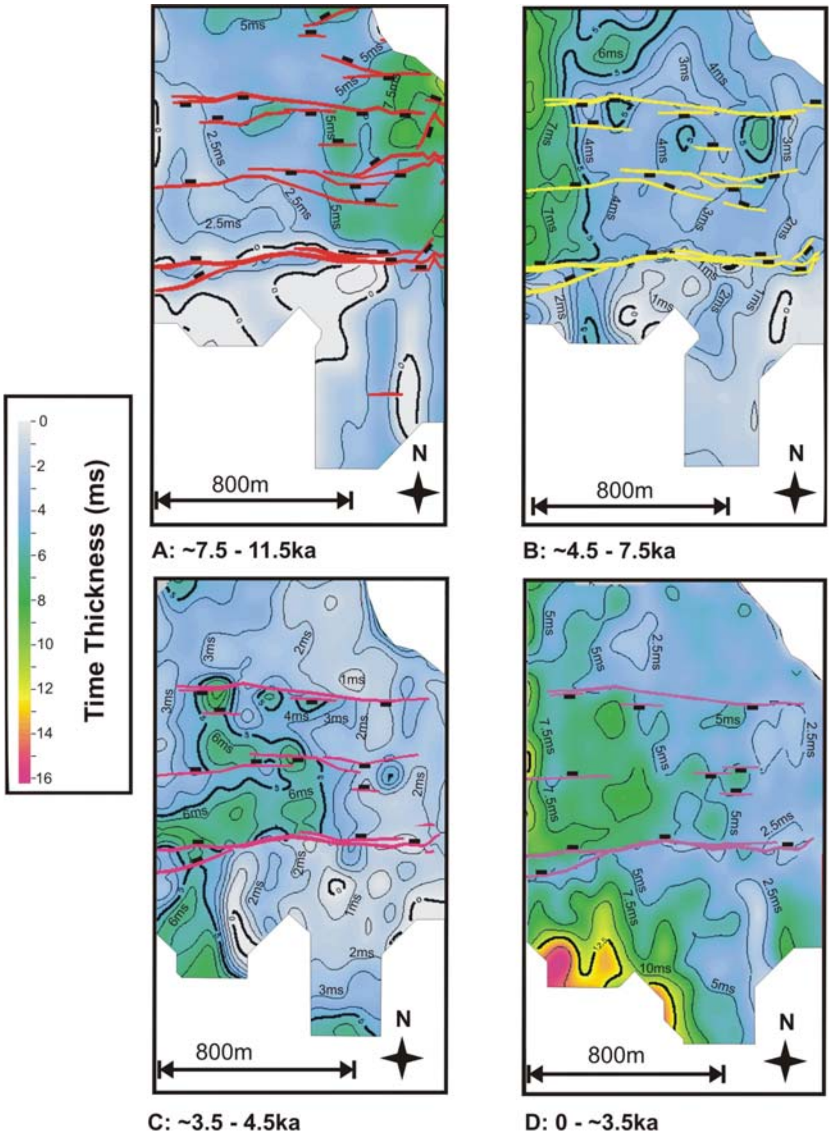

A: ~7.5 - 11.5ka
B: ~4.5 - 7.5ka
C: ~3.5 - 4.5ka
D: 0 - ~3.5ka

**Figure 5.15:** Isopach plots showing the thickness of each sedimentary unit. Thicknesses are shown in ms. The faults displacing the lower boundary to each unit are shown. The colour scale corresponds to all four plots.

Figure 5.16 illustrates how the locations of the main depocentres have varied, and their relationship to major faults. Between 11.5 - 7.5 ka (Figure 5.16A) deposition was at its greatest at the shelf edge. There is little evidence for the formation of isolated depocentres, although the two graben bounding faults (highlighted in red) do control pooling of the sediments within the eastern graben. This period corresponds to a period between the subaerial deposition related to the end of the lowstand, and transition into marine conditions as sea-level rose and flooded the shelf. Analysis of sea-level rise (chapter 4) suggests that this occurred rapidly, within ~ 1-2 kyr. However, the depocentre pattern suggests that deposition was primarily concentrated at the shelf edge, where fluvial inputs would have initially dispersed into Lake Corinth. This suggests that little deposition was accumulated immediately following sea level rise, when it would be expected to see depocentres forming in the western part of the survey area.

However, between ~7.5 – 4.5 ka (Figure 5.17B) deposition was primarily located in the western most graben, in close proximity to the nearshore sediment sources. The sediment source is localised, with shelf topography and faulting controlling deposition patterns. During the 3kyr period following transgression (7.5 – 4.5 ka), the primary sediment source is believed to have been located north of the Aigion Fault. Research by Lascaratos et al. (1989) and Piper et al. (1990) have shown that an anticlockwise gyre in the central Gulf dominates oceanic circulation patterns, with clockwise eddies occurring across the Aigion Shelf, causing upwelling during the Summer months. This combined process results in south to north water circulation patterns across the shelf, inhibiting the movement of sediment southwards onto the uplifted Aigion Fault footwall.

From ~4.5 – 3.5 ka (Figure 5.16C) continued subsidence of the Aigion and S-dipping fault’s hangingwalls result in an increase in accommodation space within the graben. There is a small lateral movement eastwards of the deposition minimum on the footwall of the Aigion Fault, suggesting that the location of maximum displacement on this fault was also propagating eastwards. The minor faults within the graben have begun to have an impact on deposition patterns. Deposition has moved further eastwards in the graben, when compared to the Figure 5.16B, suggesting that maximum displacement on the graben forming faults may also have moved eastwards. A significant depocentre has also formed south of the Aigion Fault. The curved shape of this depocentre is indicative of differential uplift along the footwall of the Aigion Fault, combined with proximity to coastal sediment sources, resulting in ponding of sediments against the tilted region.

Between ~3.5 – 0 ka (Figure 5.16D) the number of faults offsetting the sediments within the graben has appeared to decrease. This may reflect an actual reduction in the number of active faults, although it may also indicate that the displacement rate of the minor faults is lower than sedimentation rates, resulting in burial. The later is supported by

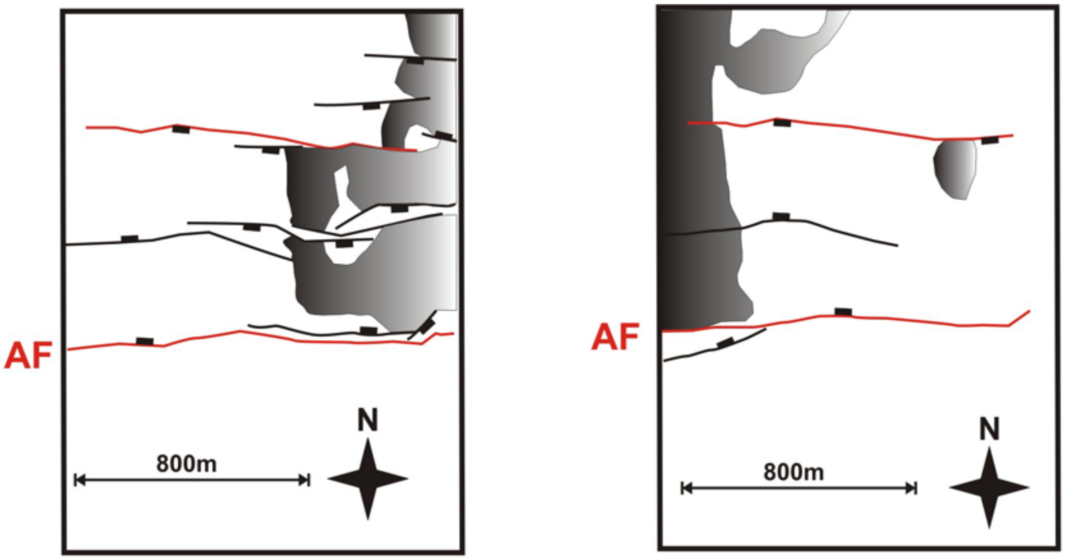

A: ~7.5 - ~11.5ka

B: ~4.5 - ~7.5ka

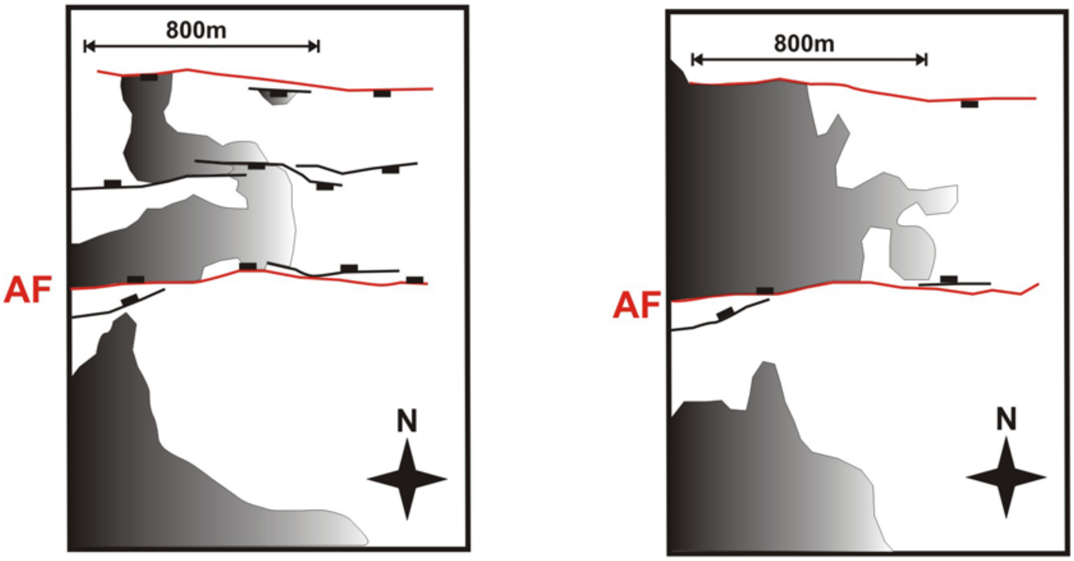

C: ~3:5 - ~4.5ka

D: ~0 - ~3.5ka

**Figure 5.16:** Cartoon illustrating the change in size and locations of the dominant depocentre over four time periods. The N-dipping Aigion Fault (AF) and the graben bounding S-dipping faults are highlighted in red. Other significant faults are shown in black.

the apparent lateral growth of the graben depocentre from Figure 5.16C to D. The uniform appearance of this graben depo-centre suggests that the differential burial observed along fault **3** (section 5.2) is due to fault segmentation rather than the development of isolated deposition maximums. The depocentre south of the Aigion Fault is still clearly defined, but its northward extent has been slightly reduced, as uplift on the footwall continues to increase.

Changes in depo-centre location may also be connected to migration cycles of the Selinous River, as it is known to have had an anastomising and avulsive history prior to containment within a concrete channel (Soter and Katsonopoulou, 1998; Collier, pers. comm, 2005). Historical records document the river discharging north, in close proximity to the Aigion lagoon, during Roman times (Figure 5.1), with a Venetian map from ~1700AD showing that the mouth had moved southwards (Soter and Katsonopoulou, 1998). Migration of the Selinous River appears to be rapid, and therefore not resolvable using the sedimentary units identified in this study. Each unit covers multiple cycles of avulsion, and so does not show specific fluctuations within each time period. It is therefore impossible within the time periods of this study to link the formation of specific depocentres to the movements of the Selinous and Kerynitis Rivers.

Throughout the past 11.5 kyr, it would appear that tectonic activity has dominated the formation of depocentres. Initially between ~11.5 – 7.5 ka, the main factor in the development of deposition loci was sea-level change. However, this rapidly evolved into being fault controlled. During subsequent marine conditions, increasing displacement on the two major normal faults (**1** & **2**, Figure 5.4), highlighted in red on Figure 5.16, appears to dominate stratigraphic patterns.

It is not possible to extract an analysis of longer-term fault behaviour and evolution using the isopachs generated in this study, due to the length of the observation period (~11.5 kyr). However, it has been shown that sediment deposition patterns do respond to tectonic activity on short timescales, which can be recognised over intervals of 1 kyr or more.

### 5.4.2 Faulting and Related Deformation Features

Figure 5.17A highlights the main morphological features identified on the Aigion shelf, and the location of the two major faults that have seafloor expression. Figure 5.17B shows the same plot, but now includes all the sub-surface faults mapped on the oldest horizon H4. It is apparent that the areas of elevated topography and dimpled seafloor texture are bounded to the north by the Aigion and S-dipping fault (**1** and **2**, Figure 5.4), and to the east by the shelf edge. As no other areas of similar textural morphology are observed associated with faulting, it is proposed that proximity to the shelf edge is the unique factor which, when combined with faulting, has resulted in their formation.

Many of the mound features, particularly those contained within the graben, are underlain by sub-surface faults, suggesting there is a link between these features and the fault arrays. However, it is also apparent that the mounds and pockmarks observed on the Aigion Fault footwall are not underlain by faults, despite their similarity in size and appearance to those mounds within the graben and the pockmarks de-lineating sub-surface faults. This would suggest that although they may be forming from the same source, possibly gas or fluid expulsion, some other factor is enabling percolation to the seafloor in the footwall rather than venting via fault structures. The relationship between faulting and mound / pockmark formation will be discussed in more detail in Chapter 7.

### 5.4.3 Fault Geometry and Interaction Between Fault Structures

Back-tilting of fault blocks relating to the Aigion Fault and main S-dipping graben bounding fault coincides with stratigraphic thickness variations, supporting the hypothesis that fault activity is the dominant influence on sedimentation patterns. However fault systems external to the survey area may also have an impact on the stratigraphy imaged.

The Western Eliki Fault lies to the south of the Aigion Fault, and is believed to be active concurrently with the Aigion Fault (Stewart and Vita-Finzi, 1996; De Martini et al., 2004). De Martini et al. (2004) document a similar displacement rate occurring on both the Western Eliki and Eastern Eliki Faults, suggesting that unless the net strain across the region is higher where the Western Eliki and Aigion faults overlap, there is no strain being transferred from the Western Eliki Fault onto the Aigion Fault. However, Micarelli et al.

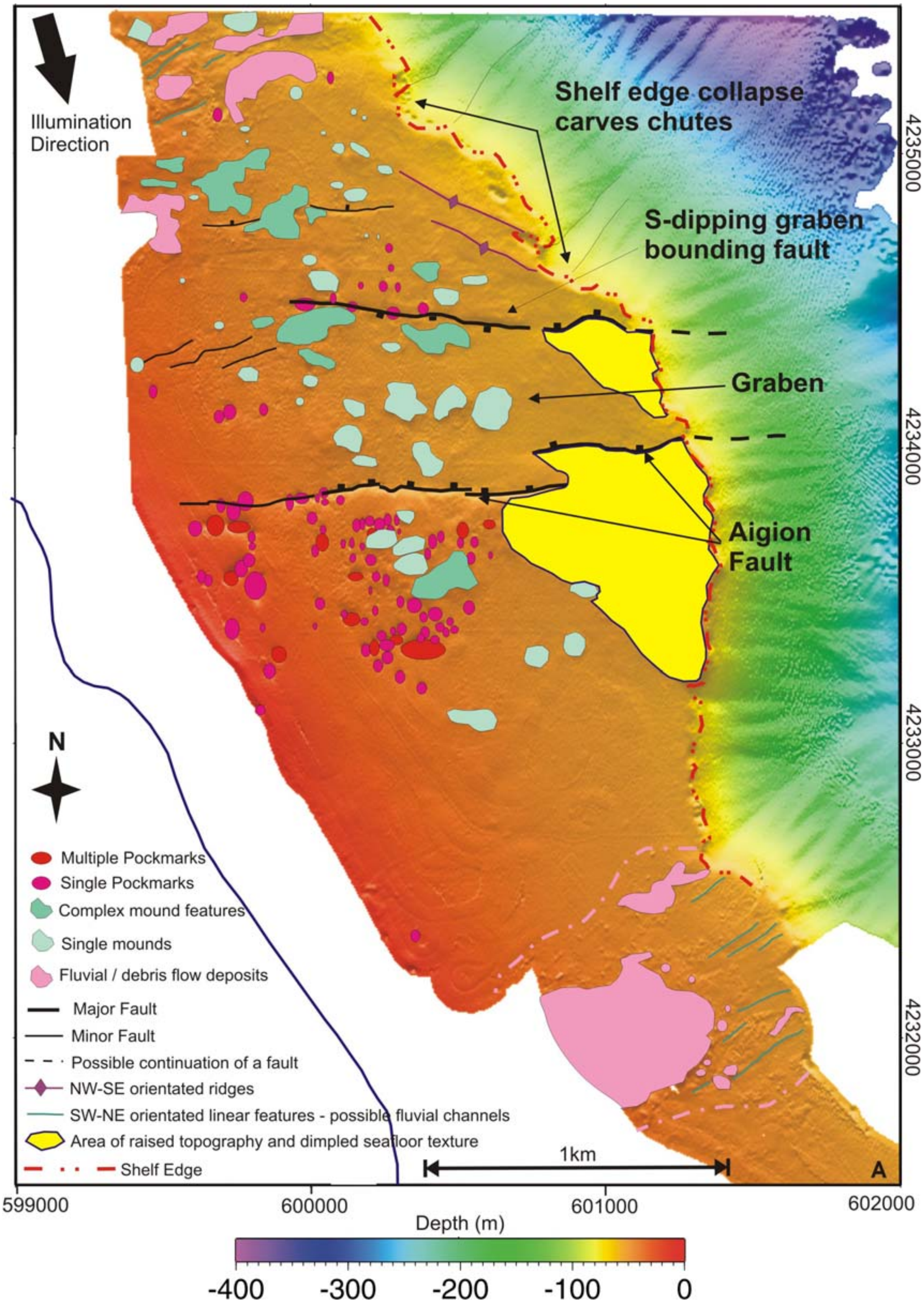

**Figure 5.17A:** Plot illustrating the morphological features identified with respect to their locations on the multibeam bathymetry image, and the surface faulting identified from the bathymetry.

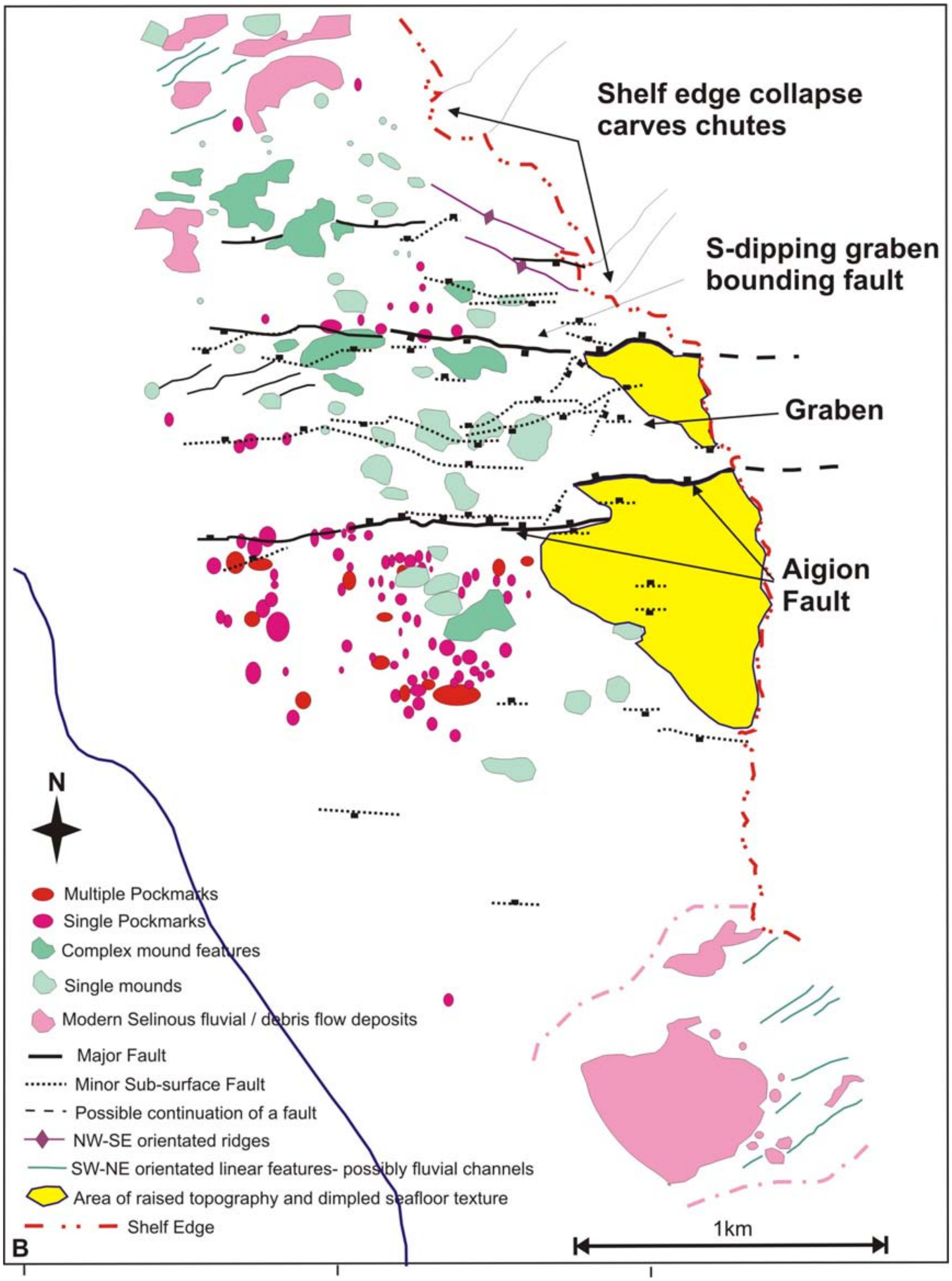

**Figure 5.17B:** Morphological features taken from Figure 5.23A shown with respect to both surface and sub-surface faulting.

(2003) show a topographic profile along the Western Eliki Fault that suggests displacement does drop gradually, from the point of overlap between the two faults to the western tip of the Western Eliki Fault. This suggests that the strain could be being transferred onto the Aigion Fault, causing an along strike decrease in displacement rates on the Western Eliki Fault. The apparent contradiction between both these studies is proposed to arise from the methods used. De Martini et al. (2004) use dating of bivalve and coral samples to correlate marine terrace uplift to sea-level curves, providing uplift rates over the past 200-300kyr. However they acknowledge that there are few samples upon which to base their datasets, which may bias their results. Micarelli et al. (2003) however, use the topographic offset between the footwall and hangingwall to produce a displacement profile along the Eliki Fault system. Although providing an along strike profile rather than one uplift rate for each of the Eliki segments, the method is more liable to biasing due to erosion and anthropogenic activity modifying the fault scarp. However, this method may give a more recent indication as to changes in displacement towards the western tip of the Western Eliki Fault, due to interaction with the growing Aigion Fault. This will be discussed further in Chapter 8.

The dynamic interplay between these two fault systems, as strain may have been re-distributed, would have affected sediment deposition, with uplift and subsidence on both faults causing variations in accommodation space. Micarelli et al. (2003) do not give a timescale for activity on the Aigion Fault affecting subsidence on the Western Eliki Fault, and so the stratigraphic patterns resulting from this process can only be generalised (Figure 5.18).

The Eliki Fault is a more established fault system, which would have initially been accommodating all the strain across this delta region, resulting in the older sediments, which were not imaged in this study, being back-tilted towards the Eliki Fault (Figure 5.18A). With activation of the Aigion Fault (Figure 5.18B), strain begins to transfer between the two systems. Sediments thicken in the hangingwall of the Aigion Fault, whilst deposits on the footwall of the Aigion Fault thin towards the Aigion Fault, due to the combined effects of uplift on the Aigion Fault footwall and subsidence on the Western Eliki Fault hangingwall.

As the Aigion Fault begins to dominate the N-S profile across the Aigion delta, and subsidence potentially slows on the Western Eliki Fault, sediments begin to prograde across the Aigion Fault footwall (Figure 5.18C), coinciding with the stabilisation of sea-level rise. This pattern of progradation continues in Figure 5.18D. Sediments also accumulate in the hangingwall of the Aigion Fault, although activity on the S-dipping fault means that they are being predominantly deposited horizontally as opposed to thickening in towards the Aigion Fault plane as observed earlier.

This is a generalised picture of deposition resulting from fault interaction, and does not take into account eastwards propagation of the Aigion Fault with time, or differential activity between the eastern and western parts of the Western Eliki Fault. Chapter 8 will discuss this further, following quantitative analysis of displacement behaviour along the Aigion Fault (Chapter 6).

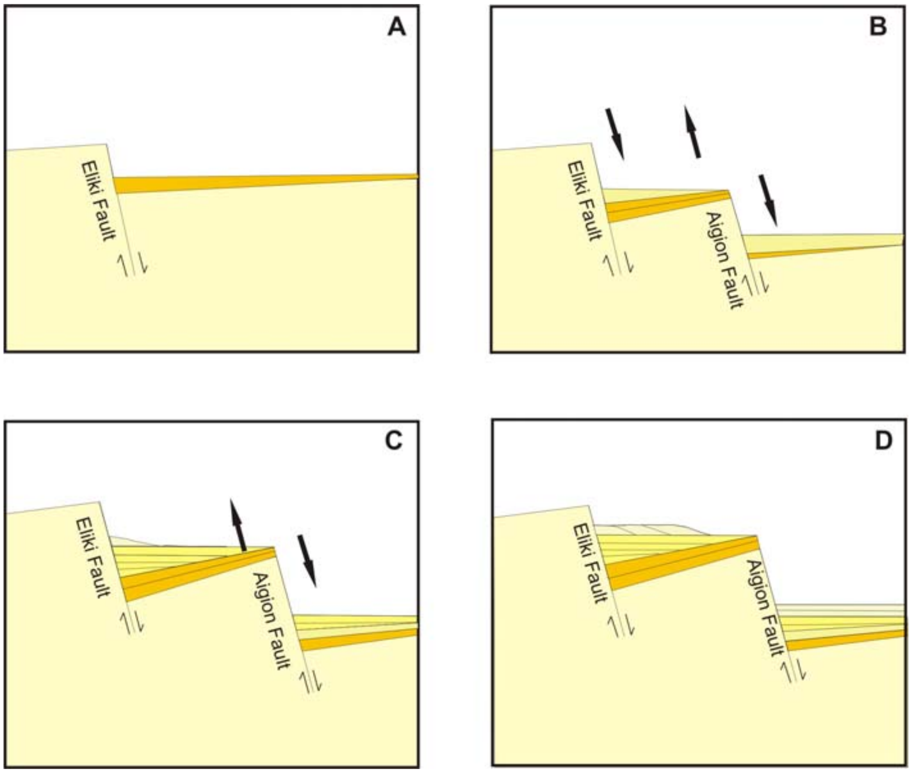

**Figure 5.18:** Cartoon illustrating the stratigraphic architecture predicted as a result of the interaction between activity on the Western Eliki Fault and the younger Aigion Fault. As there is no evidence for if / when partitioning of strain between these two faults began to cause a decrease in activity on the Western Eliki Fault, the sediments deposited cannot be linked to any particular timeframe.

It would be expected that a similar pattern of increasing accommodation space with distance north from the major S-dipping graben bounding fault would be seen. However no defined increase in sediment thickness is observed. The N-dipping Cape Gyftissa Fault, ~1 km to the north (Figure 5.1), may counteract northward tilting of the S-dipping fault's footwall, causing the area between to act as a horst block.

### Surface Rupture Length

The fault maps for each horizon (Figure 5.12) show that on each successively younger horizon, the fault lengths of the minor graben and footwall faults reduce, with many disappearing completely by horizon H1. Two main factors could result in the visible trace lengths of faults decreasing; strain localisation and the interaction between sedimentation rate and the time period of observation chosen.

It has been documented that with time, there can be a change in the nature of a fault population, with strain becoming progressively concentrated onto fewer, more major and interconnected faults (e.g. Walsh et al., 2001; Meyer et al., 2002; Walsh et al., 2003a), whilst maintaining the strain regime across the area. This shows itself as an initial decrease in fault trace length on successively younger horizons and subsequent death of smaller faults. Modelling has shown that strain localisation is a characteristic of fault system growth (Mansfield and Cartwright, 2001; Ackermann et al., 2001; Walsh et al., 2001), with numerous small faults populating an area prior to the evolution of a through - going major fault segment. Once this has occurred, the smaller faults suffer high mortality rates, with the through going system taking over the accommodation of any fault deformation and extension. Therefore the fault geometry observed on the Aigion shelf may represent the ongoing coalescence of deformation onto the more prominent faults following propagation of the fault tip through this area and off the shelf edge into the main rift basin sometime pre ~12 ka. However the timescales for this evolutionary behaviour are normally investigated over much longer periods (>1 Ma), and so it is unlikely that strain localisation is the main factor behind the changes in fault geometry observed over this 11.5 kyr time period.

If displacement rates are minimal towards the tips of minor faults, prograding sediments can lead to progressive burial of all but the major fault traces. Progradation of the sediments within unit U1 begins at ~6 – 5 ka. This date is consistent with the slowing of sea-level rise documented by Siddall et al. (2003), and an increase in sedimentation rates documented by Lemeille et al. (2004), using radiocarbon dating from the AIG10 borehole. These factors may well have resulted in the burial of the minor faults in the more recent Holocene. Therefore the minor faults may appear to have de-activated, when they are actually still active, only not accruing the degree of displacement necessary to rupture the increased sedimentary thickness accumulating above them. The result is a time lag between the horizons being deposited, and being offset by the now blind minor faults, as they continue to slowly propagate upwards.

## Segmentation and Fault Length

Segmentation of normal faults has been documented by numerous authors (e.g. Peacock and Sanderson, 1991; Trudgill and Cartwright, 1994; Cartwright et al., 1996; Walsh et al., 2003b). Segments may initially nucleate as discrete faults (Cowie et al., 2000), but with increasing displacement and lateral growth they may begin to interact (Peacock and Sanderson, 1991; Cartwright et al., 1995). Relay ramps can develop between interacting segments, with transverse faults hard linking the segments, transferring displacement from one segment to the next, until eventually they behave as one continuous fault trace. Therefore the fault trace may combine all smaller scales of segmentation within it (Trudgill and Cartwright, 1994), ranging from tens of meters to >10 km.

There has been much debate on what the term “segment” describes. Machette et al. (1991) use the term to identify the fault trace that ruptures as a consistent unit, whereas Trudgill and Cartwright (1994) identify an order of segmentation that relates to the joint surfaces and spacings in faults. In this study we have identified segments lengths, based on their surface expression imaged in the multibeam bathymetry, ranging from ~100 m – 500 m, with apparent linkage between them forming longer surface traces of >1 km. It is not known whether these are representative scales of segmentation for the onshore Aigion Fault as previous published studies only document larger scale segmentation of 2 – 8 km lengths (e.g. Koukouvelas and Doutsos, 1996; Pantosti et al., 2004; Palyvos et al., 2005), based on their lateral coherence. It is possible that the high-resolution nature of this survey is describing fault segmentation at scales not discussed onshore (due to lack of sub-surface data, and apparent lateral continuity along the fault).

Fault / segment lengths in the Gulf of Corinth have been documented on many scales, with typical basin bounding fault systems ranging between 10–40 km length (e.g. Doutsos and Piper, 1990; Roberts and Koukouvelas, 1996; McNeill and Collier, 2004). In proximity to the Aigion area, McNeill and Collier (2004) and De Martini et al. (2004) measure the surface traces of the Eastern and Western Eliki Faults as being 10-15 km in length, combining to form the 30 km long Eliki Fault system, whilst Poulimenos et al. (1993) indicate that the four main faults south of the Aigion Fault (Eliki, Kerynia, Melissia and Pyrgaki Faults) are all >12 km in length. Nearshore, between Aigion and the eastern tip of the Eliki Fault system, Stefatos et al. (2002) document four right-stepping faults of between 3.3 and 5 km length, whilst McNeill et al. (2005a), although limited by profile spacing, interpret offshore faults of ~2 – 15 km length.

The proposed onshore and offshore Aigion Fault system is therefore ~15 km in length, which fits well with fault length data from other locations in the Gulf of Corinth for a basin bounding fault. However, the offshore high-resolution multibeam and MCS reflection images have clearly shown that the total fault length is comprised of many scales of segmentation, supporting the findings of Trudgill and Cartwright (1994), Contreras et al. (2000) and Taylor et al. (2004) (amongst others), that fault growth occurs through ongoing linkage of fault segments.

## 5.5 CONCLUSIONS

- There are multiple surface and sub-surface faults on the Aigion Shelf (Figure 5.4). A proposed offshore extension of the onshore Aigion Fault has been identified (**1a – 1k**, Figure 5.4; Plate 1C), along with a major S-dipping fault (**2a – 2f**, Figure 5.4) and other associated fault splays. The two major faults form a graben that is deformed by minor faults (Figure 5.4). The graben deformation may reflect fault splays formed due to interaction between the two main faults (**1** and **2**, Figure 5.4). The two main arrays represent the splays associated with each of the main faults (Figure 5.6).

- Segmentation of the major faults, on scales from 100 m – 1 km, suggest that many are growing, in the near surface, through linkage of discrete faults (**1a – 1k** and **2a – 2f**, Figure 5.4). Chapter 6 will address the existence and nature of fault propagation in more detail.

- There is a change in fault geometry at a step-over zone where both of the major E-W orientated graben bounding faults alter either their position by stepping north (**1g** to **1h**, Figure 5.4), or reverse polarity (**2c** to **2d,** Figure 5.4). This is accompanied by three smaller SW-NE orientated faults developing within the graben at this step-over zone (**11, 13** and **16**, Figure 5.4), possibly representing accommodation faulting as the strain across the step-over zone becomes distributed.

- There is a significant reduction in the lateral extent, and number, of minor faults, from the deepest horizon (H4, 11.5 ± 1 ka) to the shallowest (H1, 3.5 ± 0.5 ka) (Figure 5.14). This may be due to changes in sediment deposition rates and fluvial discharge locations causing minor faults to become buried; fault segmentation and differential displacement on adjacent segments; or, less likely, strain partitioning occurring at depth across fault splays causing fault mortality in faults <500 m in length.

- There are a number of morphological features of interest on the Aigion Shelf (Figure 5.2), including fault related mounds and depressions. Analysis of the MCS reflection profiles combined with the multibeam bathymetry, indicates that many of these features are underlain by faulting (Figure 5.17B). This suggests that the fault arrays may be acting as pathways for migration of gases or fluids, the expulsion of which form the soft sediment deformation features mapped, as discussed in Chapter 7.

- The sedimentation pattern on the Aigion shelf reveals interplay between sediment sources and rates, fault activity and sea-level fluctuations. The graben depocentre is obviously controlled by faulting (Figure 5.14 B – D), with contours closing against fault planes showing the creation of localised topographic highs and lows (e.g. Figure 5.15C). However other areas, such as the oldest sediments at the shelf edge (Figure 5.14A) and the youngest sediments at the south of the MCS reflection profiles (Figure 5.14D), may be dominated by fluvial and shoreface deposition / progradation, during changes in sea level.

- Sedimentation patterns suggest that faulting dominates the formation of depocentres across the shelf. Whilst the isopachs generated cannot identify single migration events for either the Selinous or Kerynitis Rivers, the time periods discussed of $\geq 1$ kyr can distinguish multiple avulsive cycles and changes in coastal sediment sources.

# Chapter 6

# Fault Development and Activity

This chapter will investigate the evolution of faulting across the Aigion shelf over the past 11.5kyr. It uses quantitative analysis of fault displacement behaviour to support and build on observations made in chapter 5 regarding fault geometry and displacement.

Three factors are needed to interpret a history of fault activity: 1) the sedimentation rate must be commensurate with the fault slip rate; 2) the sedimentary sequence imaged must contain laterally extensive horizons that can be dated to within acceptable error ranges; 3) these horizons must be traceable from the footwall to the hangingwall of the faults (Taylor et al., 2004). High sedimentation rates across the survey area over the period of observation in this study has meant that there is a high-fidelity record of fault activity. Having constrained the approximate ages and stratigraphy of the horizons being used (Chapter 4), it is possible to quantify fault behaviour and activity through time.

The behaviour of the two dominant faults, and associated fault arrays, was examined over the ten discrete time periods defined by our data (Figure 6.1), allowing a unique insight into the short-term behaviour of a developing fault system. Initially the distribution of displacement between the fault arrays identified in Chapter 5 is addressed. The analysis then concentrates on the main offshore Aigion and S-dipping faults, before addressing temporal and spatial changes in displacement rates and profiles.

Assessment of the variability in displacement rates, both spatially along faults and across arrays, combined with temporal variations, will help identify changes in interactions between fault segments. Normalising the displacement data, and conducting a variance analysis, will help identify the time period of observation required to determine long-term stable fault behaviour. This analysis will also help identify structural changes to the fault population, including evidence for fault growth and linkage of segments, and analysis of strain localisation across the shelf.

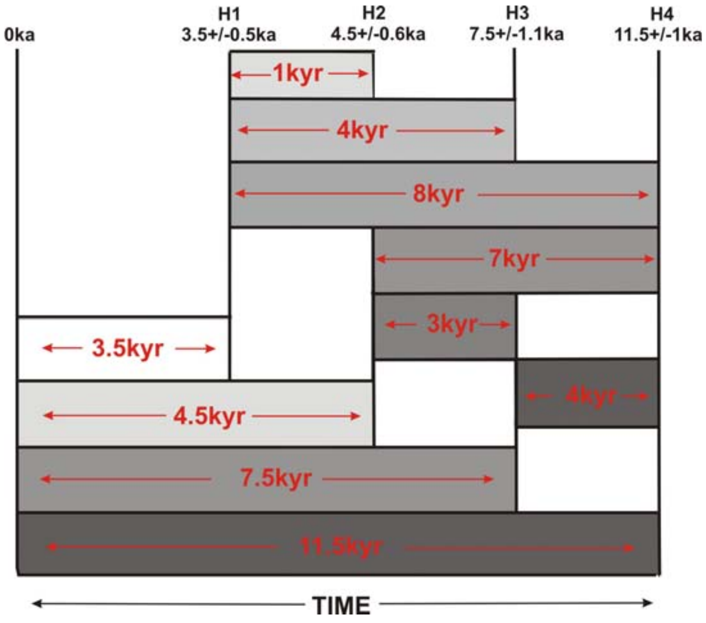

**Figure 6.1:** Cartoon illustrating the ten time periods over which fault displacement can be analysed on the Aigion Shelf. Horizons H1 – H4 are identified in the Boomer seismic reflection data

Figure 6.2 illustrates the multibeam bathymetry, surface and sub-surface faults mapped, and the strike projection (discussed in Chapter 2), used in all displacement analysis, which runs parallel to the average E-W strike of the major offshore faults. In total, 33 normal major and minor faults were identified. The N-dipping offshore extension of the Aigion Fault (1a-1k, Figure 6.2) and a major S-dipping fault (2a-2f, Figure 6.2) are the most active faults, identified by the amount of vertical displacement accrued on the oldest horizon (H4, ~11.5 ± 1 ka) of ~13 m and ~7 m respectively.

Segmentation of normal faults has been documented by numerous authors (e.g. Peacock and Sanderson, 1991; Trudgill and Cartwright, 1994; Cartwright et al., 1996; Walsh et al., 2003b). Machette et al. (1991) describe fault segments as being a unit that ruptures as one. Peacock (2002) however, describe a segment as being an “individual slip plane that is part of a set of sub-parallel faults”. Therefore, the Machette et al. (1991) “segment” can consist of a number of already linked smaller segments. In this study of the offshore Aigion Fault, a segment is defined as a discrete plane on any horizon. Therefore the offshore Aigion Fault is composed of 11 segments, whilst the S-dipping fault has 6. These segments link in the sub-surface to form longer sections of the fault system, that behave in a coherent manner, thereby fitting the Machette et al. (1991) definition.

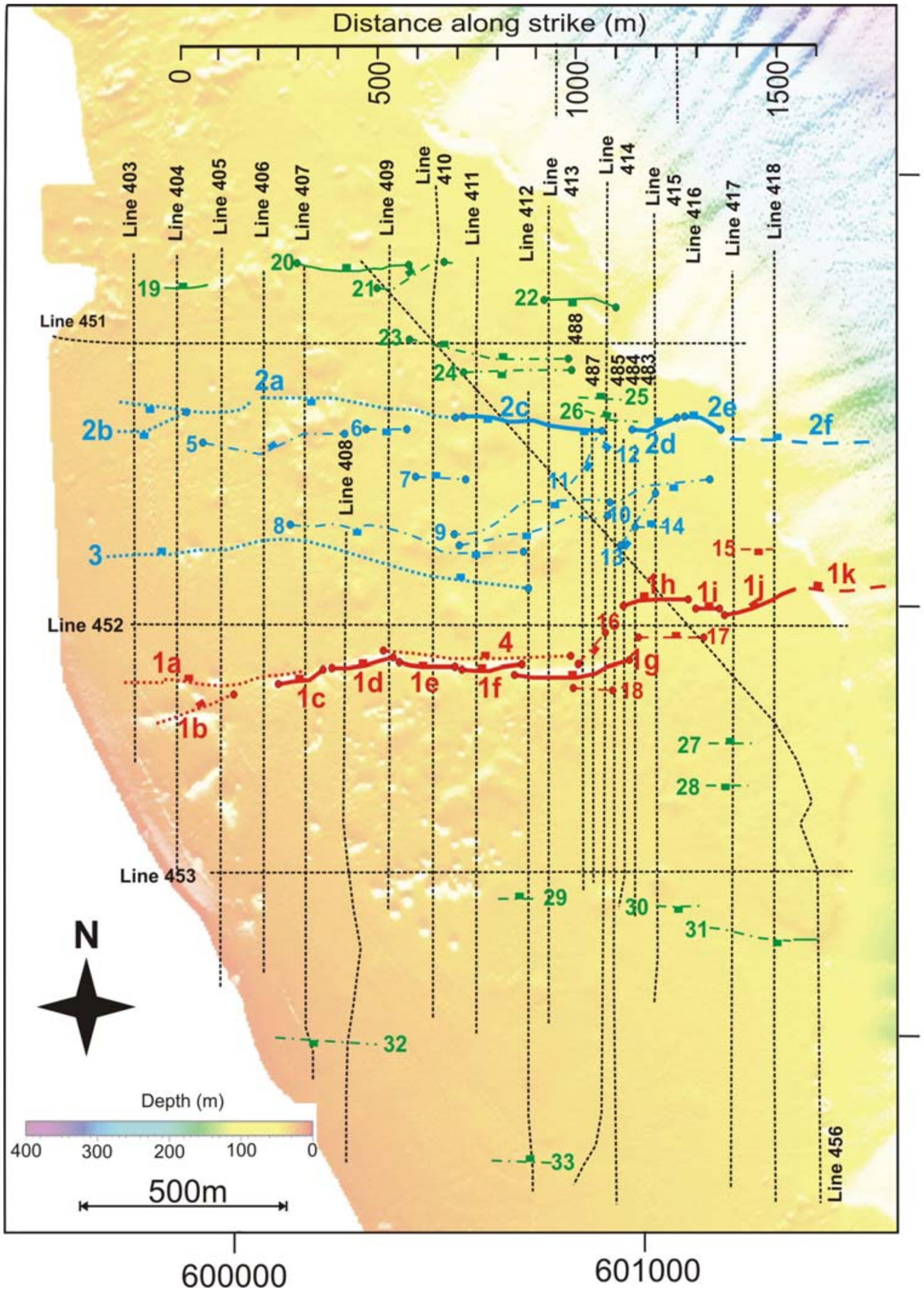

**Figure 6.2:** Surface (solid) and sub-surface (dashed) fault and multibeam bathymetry plot. The distance along strike used for the analysis in this chapter is indicated, along with the location of the step-over zone (~950 – 1250 m). MCS reflection profile lines used in the displacement analysis are labelled. Fault interpretations to the west of the origin point were gained from the Sparker profile Line 805 (Figure 2.3). Fault colours correspond to the different fault arrays; red-Aigion array; blue-S-dipping array; green-footwall array. Known terminations to segment/fault tips are indicated by dots.

## 6.1 DISTRIBUTION OF DISPLACEMENT ACROSS FAULT ARRAYS

Figure 6.3 illustrates the distribution of total displacement across the H4 horizon based on the three arrays, identified in Chapter 5. The maximum displacement observed on horizon (H4) occurs in the step-over zone (~950-1250 m along strike), where it reaches 40 ms TWTT (~34 m), corresponding to a maximum vertical displacement rate of ~3 $\pm 0.3$ mm $yr^{-1}$ over the past 11.5 kyr. Spatially averaged displacement across the shelf on H4 is ~21 $\pm 2$ m, equating to ~2 $\pm 0.2$ mm $yr^{-1}$ vertical displacement over 11.5 kyr.

The Aigion array (red) dominates overall displacement in the first 800 m along strike (Figure 6.3A), reaching a maximum vertical displacement of ~22 ms TWTT, compared to 14 ms TWTT on the S-dipping array. However, in the step-over zone there is a sharp rise in displacement on the S-dipping array, where it reaches a peak vertical displacement of 23 ms TWTT, coinciding with a decrease on the Aigion array to 11ms TWTT. Displacement on the Aigion array (red, Figure 6.3A) decreases gradually eastwards, whilst displacement on the S-dipping array (blue, Figure 6.3A) remains relatively uniform across the shelf, prior to a significant peak in displacement in the step-over zone, and a rapid decrease east of that.

Figure 6.3A shows that there is a discrepancy between the total displacement, and the aggregate from the two main arrays, indicated by the shaded area. This discrepancy is accounted for by the minor faults located in the footwalls of both the Aigion and the graben bounding S-dipping faults comprising the footwall array (Figure 6.3B). West of, and within, the step-over zone the footwall array accounts for <15% of the total displacement, however east of the step-over zone this increases to ~ 35%, due to an increase in the number of minor faults, combined with a general decrease in activity on the two main arrays.

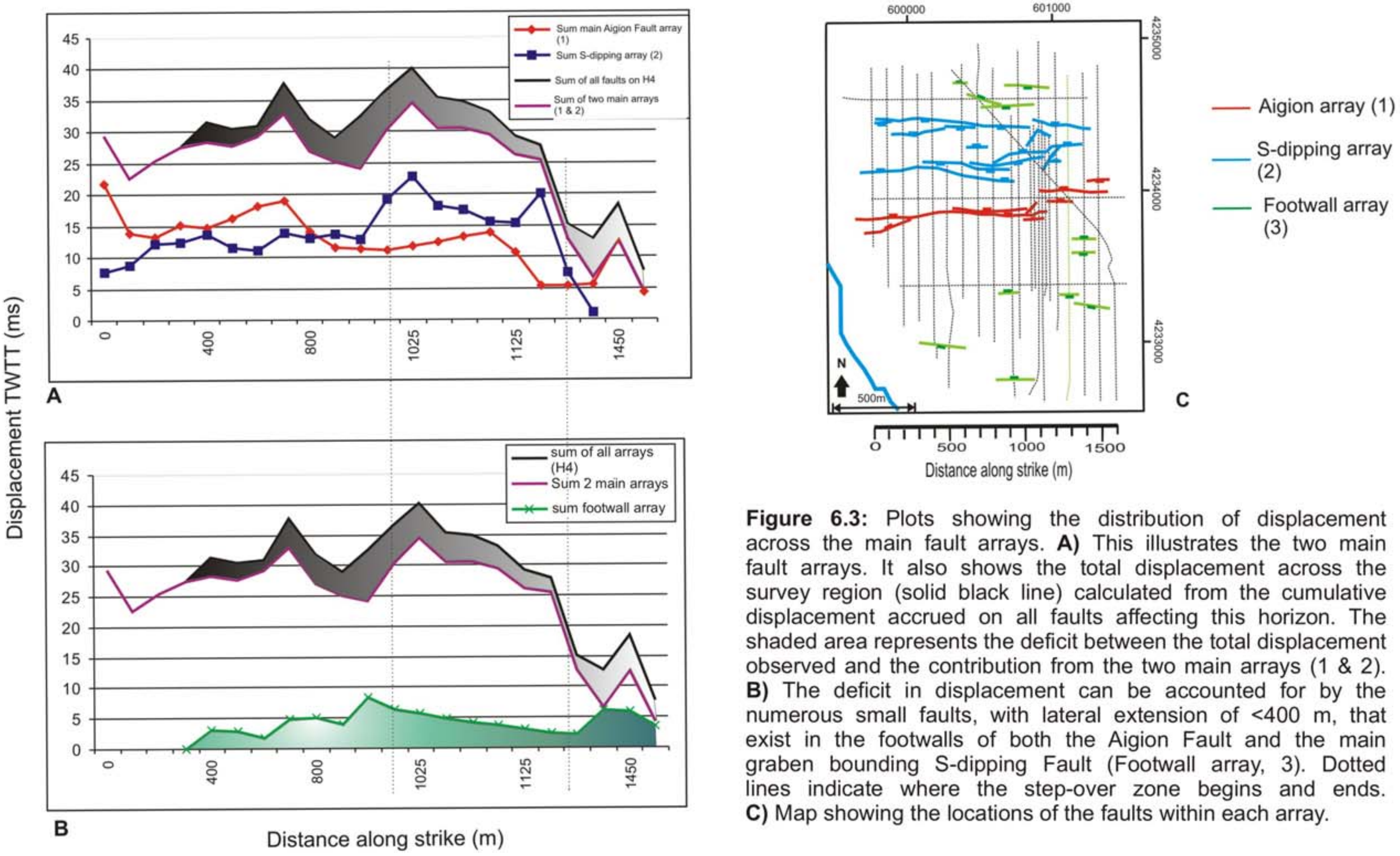

**Figure 6.3:** Plots showing the distribution of displacement across the main fault arrays. **A)** This illustrates the two main fault arrays. It also shows the total displacement across the survey region (solid black line) calculated from the cumulative displacement accrued on all faults affecting this horizon. The shaded area represents the deficit between the total displacement observed and the contribution from the two main arrays (1 & 2). **B)** The deficit in displacement can be accounted for by the numerous small faults, with lateral extension of <400 m, that exist in the footwalls of both the Aigion Fault and the main graben bounding S-dipping Fault (Footwall array, 3). Dotted lines indicate where the step-over zone begins and ends. **C)** Map showing the locations of the faults within each array.

### 6.1.1 Cumulative Displacement Across the Fault Arrays

Figure 6.4 shows three N-S profiles across the Aigion shelf, perpendicular to the fault strike. Vertical displacement on horizon H4 is plotted to show the opposing fault dips and the distribution of displacement across the shelf. Starting from zero displacement, a S-dipping fault has a negative sense of displacement, whereas a N-dipping fault has a positive sense of displacement. This method shows the geometry and sense of throw for the faults that make up the overall profile, and the distribution of displacement between each array / fault.

The Aigion array (fault numbers in red) dominates the N-S displacement profile in plots B and C. However, in the most easterly profile (plot A), which runs through the step-over zone, the displacement contributions from the footwall array (green) and the S-dipping array (blue) dominate. Plot B shows that displacement is concentrated in a narrow zone, within the graben structure, in the area where seafloor mounds are visible, coinciding with the narrowest point of the graben. In Plots A and C, displacement is more evenly distributed over a wider area.

### 6.1.2 Displacement Patterns on Mapped Horizons.

Figure 6.5 illustrates the variation in the displacement profiles of the two main arrays over the four mapped horizons, and the relative contribution of the main faults within each array. No seafloor plot is presented as it is believed to be sensitive to erosion, causing displacement on the faults to become compromised. For horizons H1 – H3, it must be noted that although displacement appears to cease ~1000 m along strike, poor resolution of these horizons due to decreasing sedimentation rates with increasing distance offshore, has meant it is not possible to correlate H3 – H1 across the faults, and so record displacement.

The relative contributions and profiles of the major faults within each array do not appear to change between horizons. The S-dipping array maintains a relatively uniform aggregate profile along strike over all the horizons, dominated by faults 2 and 3, until ~1000 m along strike, where horizon H4 shows a dramatic peak that rapidly falls to zero

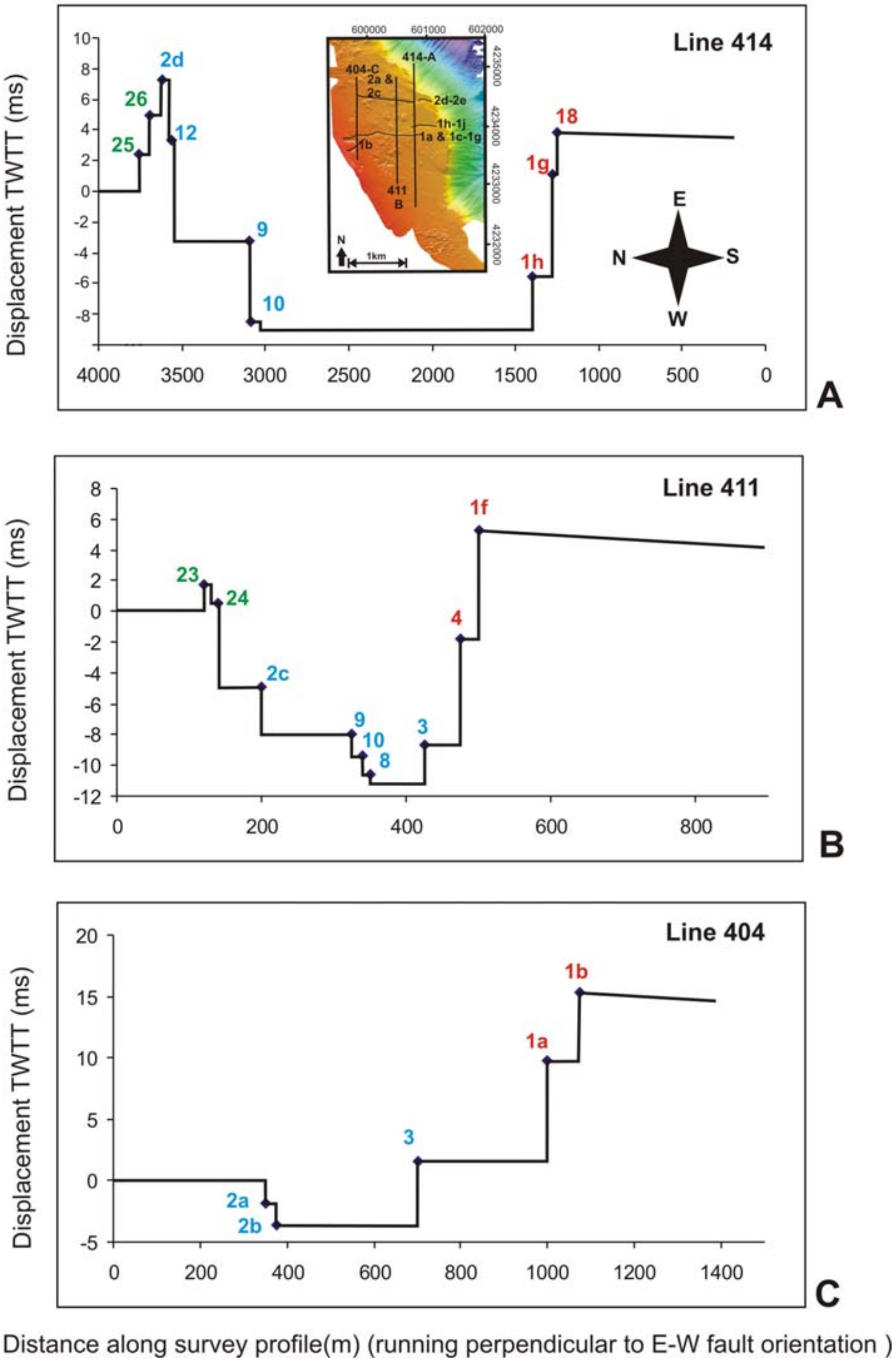

**Figure 6.4:** Examples of the displacement profiles across the Aigion Shelf of 3 survey lines running perpendicular to the main fault strike projection. Line locations are illustrated on the multibeam bathymetry inset in plot A. **A)** Line 414; **B)** Line 411; **C)** Line 404. Fault numbers correspond to the scheme shown in Figure 6.2. Red numbers indicate the Aigion array faults, blue numbers the S-dipping array and green numbers the footwall array faults. Displacement on north dipping faults is indicated by a positive sense of movement, whilst south dipping faults have a negative sense of movement.

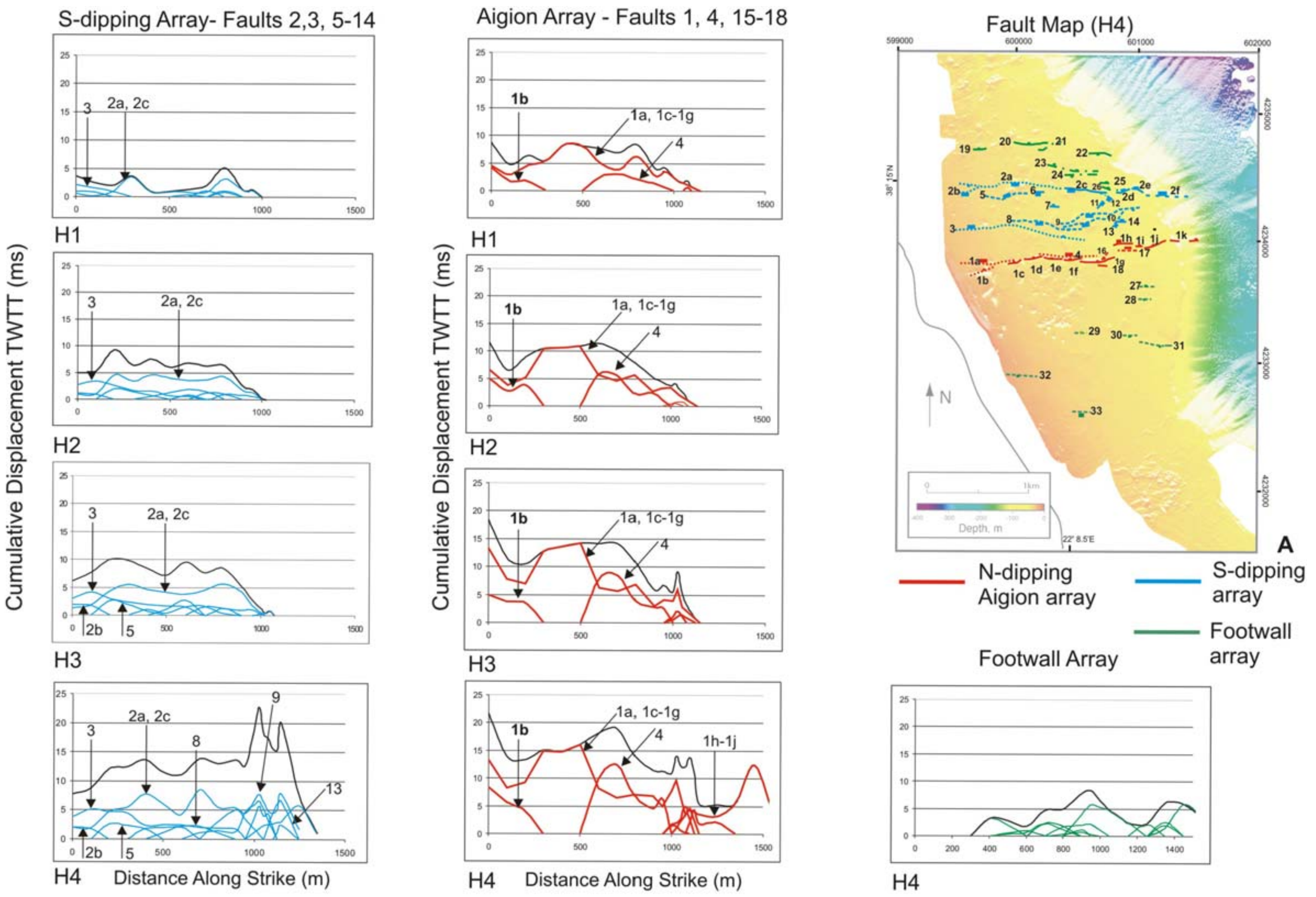

**Figure 6.5;** Profiles of total displacement over the three fault arrays, on each of the four horizons mapped. Fault map indicates the grouping of the individual faults within each array. Solid black line in each plot indicates the aggregate displacement on the horizon; contributions from the faults showing the greatest displacement on each horizon are indicated. Fault numbering refers to the scheme in Figure 6.2.

displacement ~1400 m along strike. This peak corresponds to activity on multiple minor faults located within the step-over zone.

The Aigion array predominantly shows displacement on all horizons tapering off eastwards along strike, with faults 1 and 4 dominating. On horizon H4, where there is more information on fault activity, displacement decreases to a low at ~1200 m before rapidly increasing again at ~1400 m. The displacement low (1200 m) coincides with the northward step of the Aigion Fault, from segment 1g to 1h (Figure 6.5A), with the increase (1400 m) occurring east of the step-over zone, on segments 1i and1j (Figure 6.5A). An immediate increase in displacement at the northward step of segment 1h is not observed as strain is distributed across the minor graben faults within the step-over zone.

### 6.1.3 Temporal Variations in the Distribution of Displacement

Figure 6.6 shows six of the ten possible time periods (Figure 6.1), which are most representative of the range of variability in the distribution of displacement between the two main arrays. Regardless of the amount of displacement accrued, the distribution of displacement appears to be relatively evenly spread between the Aigion and S-dipping arrays, with the exceptions of displacement at 0m along strike, where the Aigion array is consistently higher, within the step-over zone, where the S-dipping array dominates, and between 3.5 ka to present (Figure 6.6E).

In plot E, the Aigion array uniformly dominates displacement, showing at least 50% higher displacement than that accrued on the S-dipping fault. This plot represents the most recent time period being considered (0 – 3.5 ka), suggesting that there may have been a relative change in distribution of displacement across the two main arrays post ~3.5 ka.

There is a significant discrepancy between the 8 and 7 kyr profiles (Figure 6.6 B and C respectively). Between 200 – 800 m along strike, there is a 50% increase in the aggregate displacement from ~10 ms TWTT to ~20 ms TWTT over only 1 kyr (~4.5 – ~3.5 ka). This increase is also apparent on both the Aigion and S-dipping faults (section 6.4) during the same 1 kyr period, and may represent a period of earthquake clustering.

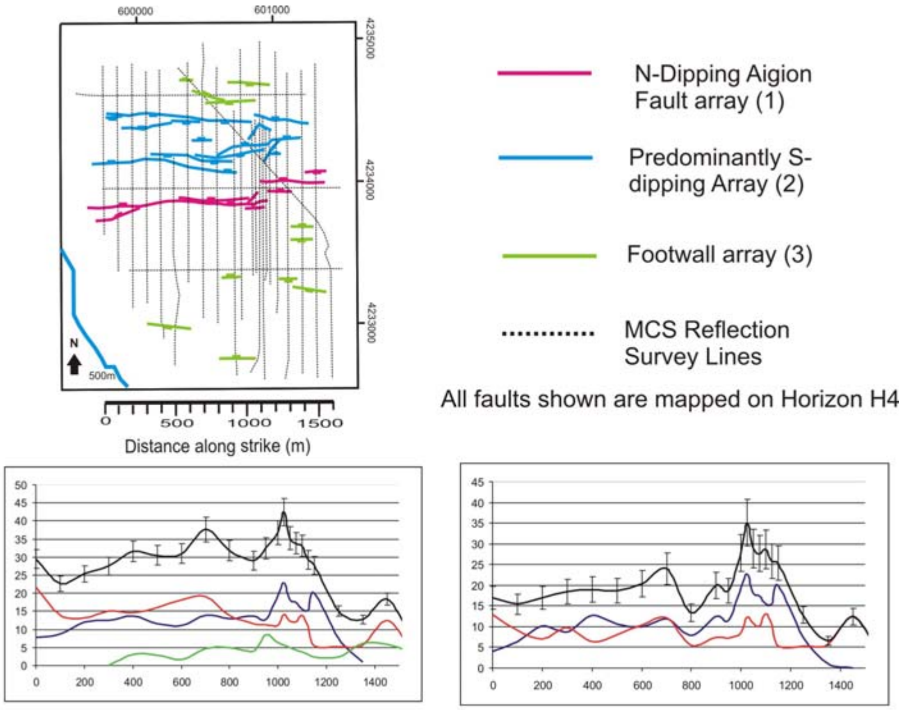

**A:** 11.5kyr Time Interval (~11.5ka - present) **B:** 8kyr Time Interval (~11.5ka - ~3.5ka)

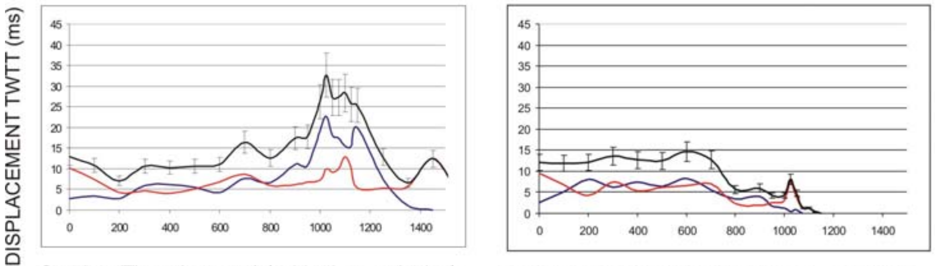

**C:** 7kyr Time Interval (~11.5ka - ~4.5ka) **D:** 4kyr Time Interval (~7.5ka - ~3.5ka)

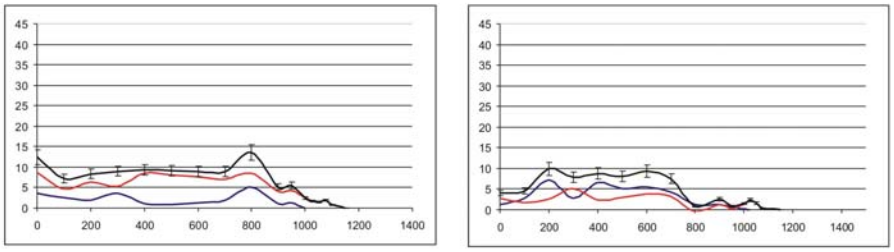

**E:** 3.5kyr Time Interval (~3.5ka - present) **F:** 1kyr Time Interval (~4.5ka - ~3.5ka)

**Figure 6.6:** Graphs illustrating the variation in the displacement profiles of the two main arrays over selected time intervals. Plots D – F have no information on displacement from ~1000 m along strike, due to poor lateral resolution of the youngest horizon (H1, ~3.5 ka). The fault map indicates the distribution of faults within each array; the aggregate total displacement from both arrays for each time interval is indicated by a solid black line, showing associated errors.

However, uncertainties associated with interpretation of the 3.5 and 4.5 ka horizons may lead to errors in displacement rates and so explain variability.

The displacement profile for each array over the three longest time periods (Figures 6.6 A – C) all have a similar shape, with displacement lows and highs occurring at the same points along strike. The shorter time periods (Figure 6.6 D-F) show more diversity in profile shape. This suggests that periods ≥7 kyr are more representative of long-term displacement, whilst the shorter time periods (D-F) show more random variability.

In the three longest time periods being considered (Figure 6.6 A – C) there is a displacement high occurring at the step-over zone, between 1000-1200 m along strike, which does not appear in plots D-F. However, biasing of the short term results due to problems with accurate resolution and correlation of horizons H3 – H1 cannot be discounted.

## 6.2 SEGMENTATION AND FAULT PARTITIONING

### 6.2.1 Aigion Array

It is possible to analyse fault interactions within each array using the displacement profiles. Figure 6.7 shows the 7 faults that make up the Aigion array. At the seafloor, segmentation of fault 1 (Figure 6.2) into its component parts of 1a and 1c – 1g is obvious, however at depth, the displacement profile of these segments suggests that they are behaving as one coherent unit (Figure 6.7C) on all of the horizons. They are therefore considered as a linked system within this analysis. Faults 1b, 4, and 16-18 are considered as separate parallel splays to the main fault strand in this array. (This will be discussed further in section 6.7).

Where segments 1a and 1b overlap, displacement on segment 1a decreases, reaching a low on all horizons ~100 m along strike (Figures 6.4B and 6.7C). The displacement rapidly increases as segment 1b dies off, reaching a maximum on segment 1d, (~500 m along strike), of 16 ms TWTT. At this point fault 4 begins, and the rapid increase in its displacement to 12 ms TWTT ~ 600 – 700 m along strike coincides with a

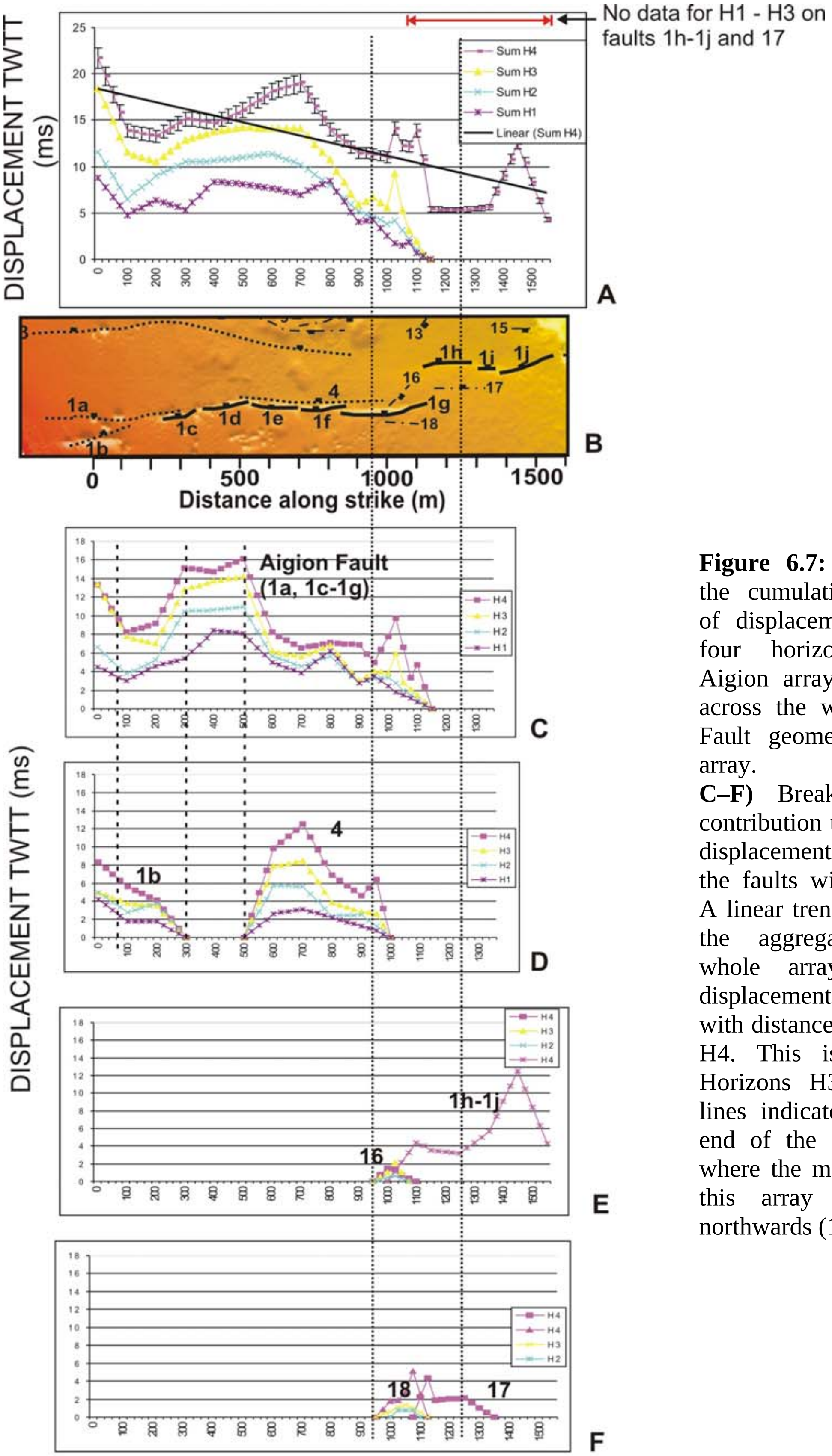

**Figure 6.7:** Plots showing the cumulative distribution of displacement across the four horizons with the Aigion array. **A)** aggregate across the whole array. **B)** Fault geometry within the array.

**C–F)** Breakdown of the contribution to the aggregate displacement from each of the faults within this array. A linear trendline applied to the aggregate from the whole array (A) shows displacement decreasing with distance along strike on H4. This is mirrored on Horizons H3 –H1. Dotted lines indicate the start and end of the step-over zone, where the main fault within this array (1, B) steps northwards (1g to 1h, B).

decrease in displacement to ~6 ms TWTT on the main Aigion Fault, corresponding to segments 1e and 1f.

The transference of displacement between segments 1e and 1f to fault 4 is rapid, with a displacement gradient of 0.06 across the overlap between the western tip of fault 4 and eastern tip of segment 1e. The displacement gradient is calculated by taking the total displacement in TWTT, measured from the zero point at a segment tip to the maximum observed on the segment, and dividing by the distance along strike that this displacement is accrued over. Fault 4 rapidly dies out ~1000 m along strike, terminating against fault 16.

The north stepping strand of the Aigion Fault (segments 1h-1j, Figure 6.7E) has ~100 m overlap with segment 1g. Interaction between these two segments, and the influence of the minor faults located within the step-over zone, prevents segments 1h-1j reaching their maximum displacement (13 ms TWTT) until they pass out of the step-over zone, ~1400 m along strike.

### 6.2.2 S-Dipping Array

Figure 6.8 shows the 12 faults that make up the S-dipping array. The main S-dipping fault (segment 2a, Figure 6.2) has a displacement low centred at ~600 m along strike (Figure 6.8C). This coincides with displacement highs on faults 6 and 8 (Figure 6.8D & E). Fault 6 is the closest to segment 2a, and shows the most rapid change in displacement, with tip gradients of 0.03 as opposed to 0.01 on fault 8. Fault 8 also displays a more symmetrical, bell-shaped profile, suggestive of an isolated fault. Therefore it is possible that the displacement low on segment 2a is predominantly linked to displacement behaviour on fault 6.

There is also a displacement low on segment 2a for the first 100 m along strike (Figure 6.8C), which coincides with displacement highs on faults 2b and 3 (Figures 6.8D and F respectively). As displacement on segment 2b begins to decrease 100 m along strike, segment 2a rapidly increases to a displacement high, showing a displacement gradient of 0.02.

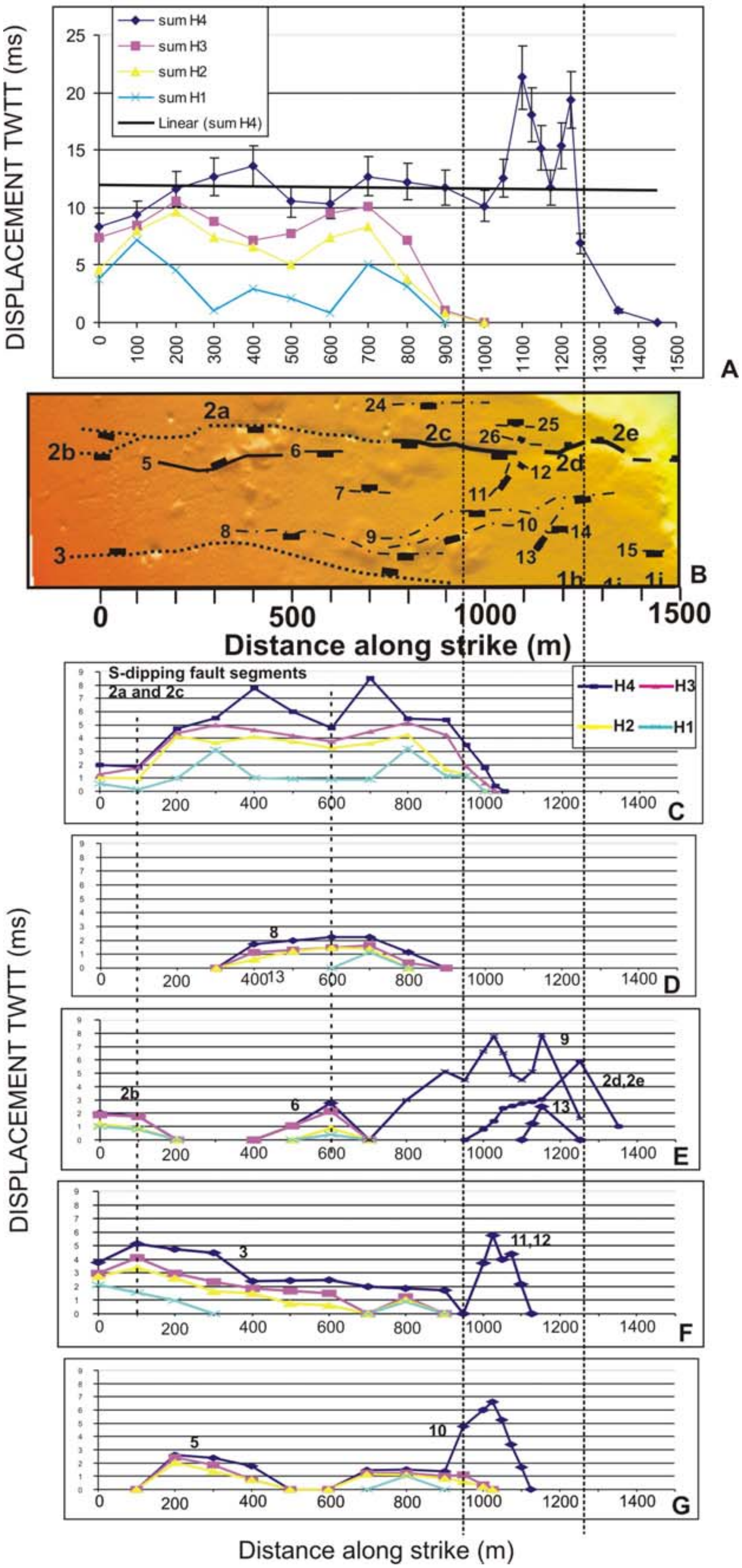

**Figure 6.8:** Plots showing the distribution of cumulative displacement across the four horizons with the S-dipping graben bounding array. **A)** aggregate across the whole array. **B)** Fault geometry within the array.

**C–G)** Breakdown of the contribution to the aggregate displacement from each of the faults within this array. A linear trendline applied to the aggregate from the whole array (A) shows uniform displacement with distance along strike on H4. Horizons H3 – H1 show a more bell-shaped profile, although this could be influenced by lack of lateral resolution of these horizons after ~1 km along strike. Dotted lines indicate the start and end of the step-over zone, where the main fault within this array (2, B) reverses polarity (2d & 2e, B).

Plots C – F are not shown at the same vertical scale as A. This is so they can be shown relative to each other so that fault interactions can be clearly seen.

The main S-dipping fault (segment 2c, Figure 6.8B) dies off rapidly 1050 m along strike as it enters the step-over zone (Figure 6.8C). This coincides with a displacement high occurring on faults 9 – 12 (Figures 6.8D, F and G), suggesting that strain is being distributed across numerous faults while the change in polarity between segments 2c and 2d is occurring.

Fault 10 shows an unusual high in displacement on H4 at the western end of the step-over zone (Figure 6.8G). The younger horizons H3 – H1 however, appear to show a more symmetrical distribution of displacement on fault 10, about a central high ~800 m along strike. Resolution limitations associated with H3 – H1 for faults 9 - 12 make interpretation of this pattern of apparently increased displacement on H4 inconclusive. However, it does appear to suggest that there may have been an early phase of activity in the step-over zone. All the faults in the step-over zone show very sharp tip gradients of between 0.07 – 0.03.

It is obvious that the segments within each array have a significant effect on the displacement profiles. The interaction between faults within each array supports the hypothesis that the faults are connected at depth, and that the minor faults observed interacting with the main S-dipping fault and the N-dipping Aigion Fault are splays, across which strain is being partitioned.

## 6.3 DISPLACEMENT PROFILES ON INDIVIDUAL FAULTS

### 6.3.1 Aigion Fault

The total vertical displacement accrued on each horizon, (TWTTms), on the main Aigion Fault, segments 1a – 1g (Figure 6.2) is illustrated in Figure 6.9. On all the horizons, there is a general trend of displacement decreasing with distance along strike from W to E. The similarity in the shape of the displacement profiles for all the horizons, suggests that the segments are already linked and behaving in a coherent and stable manner throughout this time period.

Displacement highs on H4 are observed on segments 1a (~13 ms TWTT, 0m along strike), 1c and 1d (~16 ms TWTT, 500 m along strike), except where 1b cross-cuts 1a

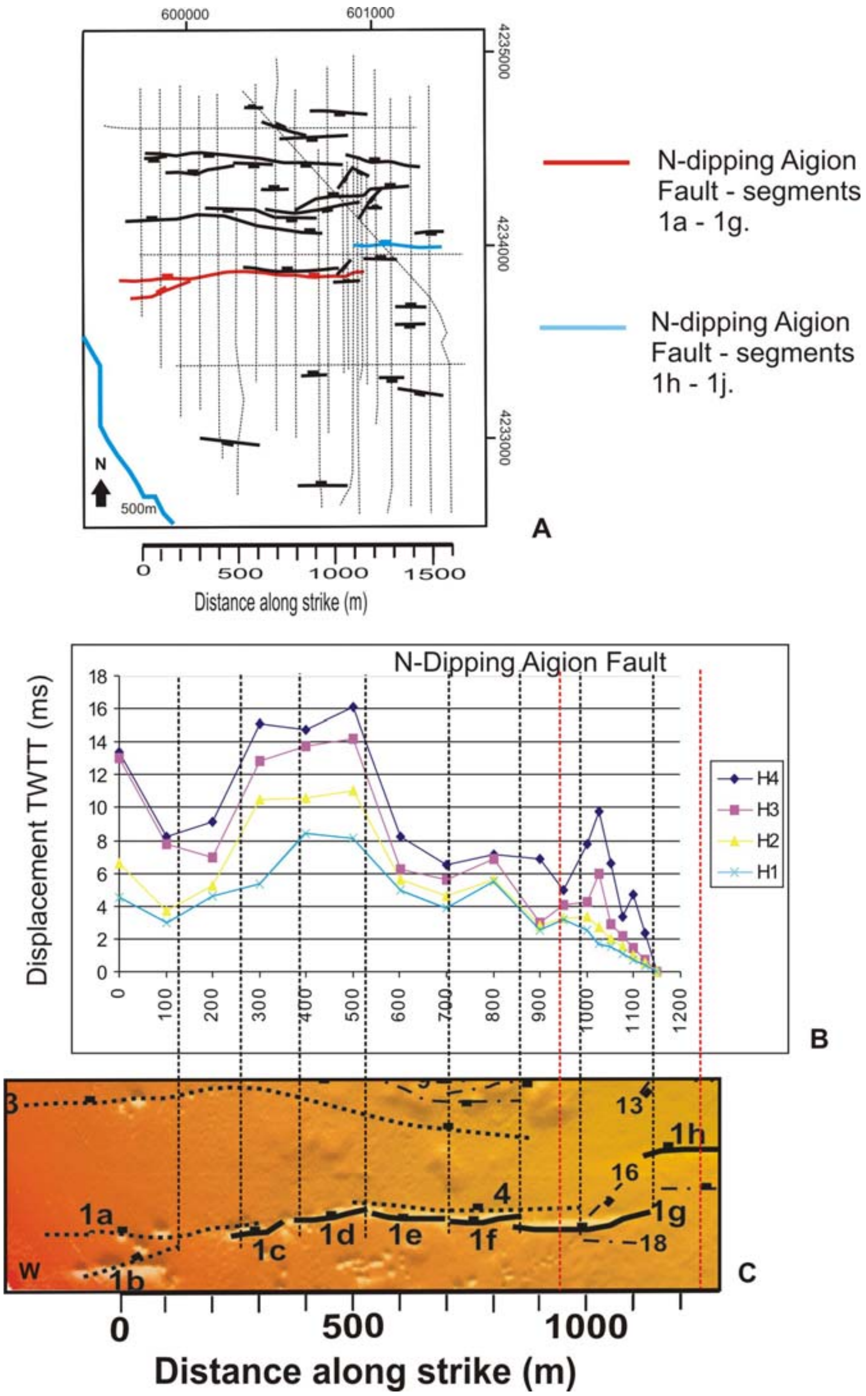

**Figure 6.9:** Total cumulative displacement profile for segments 1a+1b-1g of the main N-dipping Aigion Fault (1, Figure 6.2), over the four mapped horizons. The fault map (A) shows the lateral extent of faulting on the oldest horizon (H4 ~11.5ka). No displacement data for horizons H3 – H1 exists for the north stepping segments (1h – 1j, B) due to lack of resolution. Multibeam image (C) shows the nature of segmentation and fault interaction at the seabed. Red dashed lines indicate the extent of the step-over zone.

causing a displacement low (~ 8 ms TWTT, ~ 100 m along strike). There is also a peak in displacement at the step-over zone on horizons H4 and H3 (10 and 6 ms TWTT respectively, ~1000 m along strike), corresponding to segment 1g. On horizons H2 and H1 this peak disappears, and displacement decreases through this point in a more linear fashion.

On all horizons, regardless of the amount of displacement accrued, the locations of displacement lows remain relatively constant along strike, suggesting that there are static relic segment boundaries controlling their position (e.g. 700 m along strike = boundary between segments 1e and 1f). On H4 there are two additional lows that are not observed on any of the other horizons ~950 and 1175 m along strike. These relate to the eastern tip of fault 4/ western tip of fault 18, and the eastern tip of the obliquely orientated fault 16 (Figure 6.9C) respectively.

### 6.3.2 Graben Bounding S-Dipping Fault

The total vertical displacement accrued on each horizon, (TWTTms), on the major S-dipping graben bounding fault, segments 2a – 2c (Figure 6.2) is illustrated in Figure 6.10. The displacement profiles show more variation over the horizons than observed on the Aigion Fault, however the general displacement trend is still similar on all the horizons.

H4 shows a generally symmetrical bell-shaped profile with a significant displacement low at the centre, ~600m along strike. Horizons H3 and H2 show a flatter profile, 200 to 800 m along strike, with displacement gradually tapering off at either end. Horizon H1 is again relatively uniform along most of its length, but with two peaks at ~300 m and 800 m along strike. The tapering of displacement from ~900 m to 1050 m, observed on all horizons, coincides with the eastern tip of segment 2c. The relatively static zero displacement point for all the horizons suggests that this segment tip has not propagated during the past ~11.5 kyr. However, identification of lateral fault growth is dependant on survey line spacing and propagation rates, and so propagation may be unresolvable if the rates were slow. This will be discussed further in section 6.7.3.

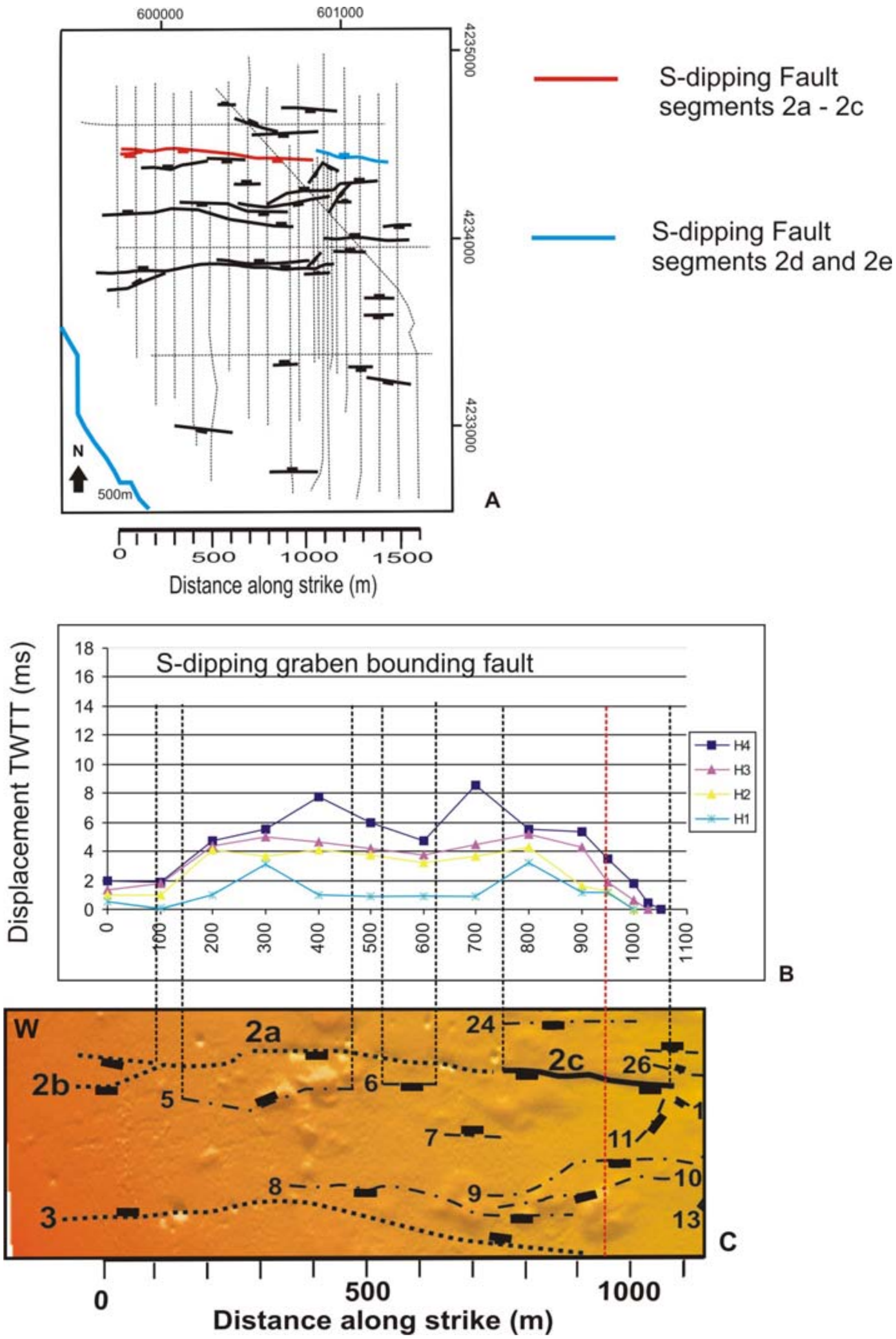

**Figure 6.10:** Total cumulative displacement profile for segments 2a + 2c of the main S-dipping graben bounding fault (2, Figure 6.2), over the four mapped horizons. The fault map (A) shows the lateral extent of faulting on the oldest horizon (H4 ~11.5 ka). No displacement data for horizons H3 – H1 exists for the segments that reverse polarity (2d and 2e, B) due to lack of resolution. Multibeam image (C) shows the nature of segmentation and fault interaction, and illustrates the possible links into displacement variation along the fault, which will be discussed in the main text. Red dashed line indicates the start of the step-over zone.

The displacement low observed on horizons H4 and H1 centred at ~600 m along strike does not appear to coincide with a segment boundary along fault 2. However it does lie opposite fault 6 (Plot C), suggesting that interaction with nearby minor faults may also be affecting the displacement profile. The displacement profiles for the S-dipping fault suggest less continuity between horizons than observed on the Aigion Fault, implying that the system is more open to differential movement on discrete segments through time.

## 6.4 DISPLACEMENT RATES

### 6.4.1 Sedimentary Backstripping and True Displacement Rates

Segments 1a-1g of the Aigion Fault and 2a–2c of the graben bounding S-dipping fault are both well sampled across the survey area on all four horizons. “Sedimentary backstripping” removes the influence of displacement accrued on each successively younger horizon. Through this method, it is possible to constrain the displacement that accumulated over a specific time period. Due to the relatively young age of the stratigraphic units and the shallow depths involved, and following comparisons with the analysis used by Taylor (2003), it was decided that decompaction corrections were not necessary.

Spatially averaged displacement rates were calculated by dividing the total vertical offset accrued across the oldest horizon of each stratigraphic unit (taking into account the effects of fault drag), and dividing by the number of observations made along that horizon. The maximum and minimum rates observed on each horizon were included to highlight the variability in displacement with distance along strike over each time period. Errors on displacement rates and time periods were calculated using the percentage errors determined in Chapter 4, section 4.2.4.

Tables 6.1 and 6.2, summarising these vertical displacement rates, indicate that there has been significant variation in the rates over the different time periods, on both major faults. The spatially averaged rate on both faults saw a significant increase at ~4.5 ka, with a two-fold increase on the Aigion Fault and >six-fold on the S-dipping fault. Post ~3.5 ka, the spatially averaged vertical displacement rate on the Aigion Fault remained constant at 0.8 mm yr$^{-1}$, however the high rate observed on the S-dipping fault was short-lived, reverting from 1.4 mm yr$^{-1}$ back to 0.3mm yr$^{-1}$ sometime after 3.5 ka.

It is possible that the jump in displacement rates is a simple short-term fluctuation, possibly linked to clustering of earthquakes and a period of enhanced rupture on the main faults. It may also be a response to resolution and correlation limitations. However, the increase was maintained after the 1 kyr period by the Aigion Fault and not the S-dipping fault. It may be that whatever caused the higher rates initially, initiated coalescence of activity onto the dominant Aigion Fault, resulting in the higher displacement rate being maintained by this fault after the 1 kyr period of enhanced activity.

The range of displacement rates observed over the four time periods suggests that both faults experience variable displacement along their lengths, with some segments accruing more vertical displacement than others. This may be caused by localised rupturing along the fault length, with segment boundaries or cross-cutting faults inhibiting displacement. However, the maximum rates are not seen to change consistently in one direction, which would indicate the lateral propagation of the fault. Instead the maximas are randomly located along strike.

| Horizons | Ages (ka) | Time Period (kyr) | Spatially Averaged Rate (mm yr$^{-1}$) | Maximum Rate (mm yr$^{-1}$) | Minimum Rate (mm yr$^{-1}$) |
|---|---|---|---|---|---|
| H4-H3 | 11.5 - 7.5 | 4 ± 0.7 | 0.4 ± 0.1 | 0.8 ± 0.1 | 0.1 ± 0.02 |
| H3-H2 | 7.5 – 4.5 | 3 ± 0.5 | 0.5 ± 0.1 | 1.8 ± 0.3 | 0.1 ± 0.02 |
| H2–H1 | 4.5 – 3.5 | 1 ± 0.2 | 0.9 ± 0.1 | 4.3 ± 0.7 | 0.1 ± 0.02 |
| H1–seabed | 3.5 - 0 | 3.5 ± 0.5 | 0.8 ± 0.1 | 2.0 ± 0.3 | 0.03 ± 0.01 |

**Table 6.1:** Approximate displacement rates for the Aigion Fault

| Horizons | Ages (ka) | Time Period (kyr) | Spatially Averaged Rate (mm yr$^{-1}$) | Maximum Rate (mm yr$^{-1}$) | Minimum Rate (mm yr$^{-1}$) |
|---|---|---|---|---|---|
| H4-H3 | 11.5 - 7.5 | 4 ± 0.7 | 0.3 ± 0.1 | 0.9 ± 0.2 | 0.1 ± 0.02 |
| H3-H2 | 7.5 – 4.5 | 3 ± 0.5 | 0.2 ± 0.03 | 0.7 ± 0.1 | 0.1 ± 0.02 |
| H2–H1 | 4.5 – 3.5 | 1 ± 0.2 | 1.4 ± 0.2 | 2.7 ± 0.4 | 0.4 ± 0.06 |
| H1–seabed | 3.5 - 0 | 3.5 ± 0.5 | 0.3 ± 0.1 | 0.8 ± 0.1 | 0.00 ± 0 |

**Table 6.2:** Approximate displacement rates for the major S-dipping graben bounding fault

### 6.4.2 Total Displacement Rates

Displacement rates on the two main faults can also be analysed over longer periods using the total displacement accrued on each horizon between the time it formed and the present day (Tables 6.3 and 6.4). This method averages out the short-term fluctuations, such as that observed between 4.5 and 3.5 ka (Tables 6.1 and 6.2), and so is useful for identifying the longer-term displacement trends, if any. However, it lacks the resolution that backstripping the data can give.

Tables 6.3 and 6.4 show the spatially averaged vertical displacement rates across the two main arrays (Aigion Fault array and the S-dipping array), and the average displacement rate for the primary faults within each array (Aigion Fault (1) and S-dipping fault (2), Figure 6.2).

| **Horizons** | **Horizon Age (ka)** | **Time Period (kyr)** | **Spatial Average Aigion array (1) (mm yr$^{-1}$)** | **Spatial Average Aigion Fault (mm yr$^{-1}$)** | **Contribution of Aigion Fault to the total displacement across the array** |
|---|---|---|---|---|---|
| H4-seabed | 11.5 ± 1 - 0 | ~11.5 | 0.9 ± 0.1 | 0.6 ± 0.1 | ~65% |
| H3-seabed | 7.5 ± 1.1–0 | ~7.5 | 1.1 ± 0.2 | 0.8 ± 0.1 | ~70% |
| H2–seabed | 4.5 ± 0.6–0 | ~4.5 | 1.3 ± 0.2 | 0.9 ± 0.1 | ~70% |
| H1–seabed | 3.5 ± 0.5-0 | ~3.5 | 1.2 ± 0.2 | 0.9 ± 0.1 | ~75% |

**Table 6.3:** Cumulative displacement rates for the Aigion array and Aigion Fault. Errors for the array and fault are taken from Chapter 4, section 4.2.4. Array geometry is shown in Figure 6.3C.

| **Horizons** | **Horizon Age (ka)** | **Time Period (kyr)** | **Spatial Average S-dipping array (2) (mm yr$^{-1}$)** | **Spatial Average S-dipping fault (mm yr$^{-1}$)** | **Contribution of S-dipping fault to the total displacement across the array** |
|---|---|---|---|---|---|
| H4-seabed | 11.5 ± (1)–0 | ~11.5 | 0.99 ± 0.1 | 0.33 ± 0.03 | ~35% |
| H3-seabed | 7.5 ± (1.1)–0 | ~7.5 | 0.69 ± 0.1 | 0.39 ± 0.1 | ~55% |
| H2–seabed | 4.5 ± (0.6)–0 | ~4.5 | 1.00 ± 0.1 | 0.54 ± 0.1 | ~55% |
| H1–seabed | 3.5 ± (0.5)-0 | ~3.5 | 0.54 ± 0.1 | 0.31 ± 0.04 | ~60% |

**Table 6.4:** Total displacement rates for the S-dipping array and S-dipping graben bounding fault. Errors for the array and fault are taken from Chapter 4, section 4.2.4.

The displacement data can also be viewed in terms of percentage contribution from each of the primary faults to their array (i.e. Aigion Fault to the Aigion array) (Tables 6.3 and 6.4). The percentage contribution of the Aigion Fault to the total displacement on the Aigion array is relatively constant over all the time periods. However, the contribution from the S-dipping fault to its array increases from ~35% over the longest time period (11.5 kyr) to ~60% over the most recent 3.5 kyr period.

Growth wedges seen in the seismic data support an increase in displacement on the S-dipping fault. It is possible that the increase in contribution from the S-dipping fault is a result of mortality of the minor faults within this array. However, it may also be an aliasing effect due to the poor lateral resolution of the younger horizons H3 – H1 across the minor faults in this array, causing an under-estimation of their contribution to displacement over the more recent time periods of observation.

## 6.5 TEMPORAL AND SPATIAL DISPLACEMENT PROFILES

Temporal variations in fault displacement can give an indication of periodic lows in displacement on individual segments. Where these locations coincide with segment boundaries or fault tips, it can be said that the boundary is “locking”. Temporary variations can also indicate where there has been migration of displacement along segments, possibly associated with surface-rupturing, segment linkage or fault growth through lateral propagation.

Horizon H4 is the most reliably constrained horizon, and so was chosen as the benchmark from which to compare variability in the displacement profiles at each horizon along the two main faults (1 and 2, Figure 6.2). Figure 6.11 shows that for each fault, small fluctuations in displacement over one time period are often balanced over another time period. However, there are three main exceptions to this.

Figure 6.11A shows two locations (~950 m and 1100 m along strike), circled in red, where displacement was minimal over all four time periods of observation. These locations coincide with where fault 16 cross-cuts segment 1g (~950 m along strike), and the overlap between 1g and the north stepping segment 1h (~1100 m along strike) (Figure 6.11B). Minimal displacement occurring at the same location along strike on all four

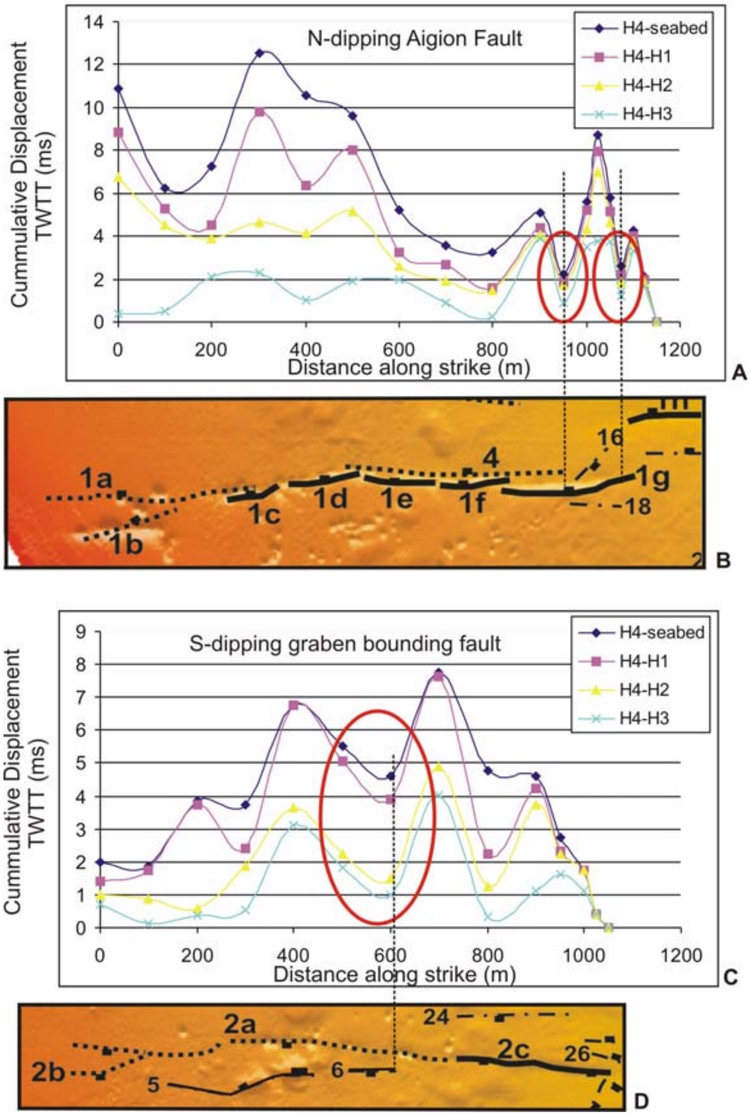

**Figure 6.11:** Plots of the net displacement over different time periods, relative to H4, observed on the two main faults. **A)** Aigion Fault (1) with **B)** showing the relationship between the displacement profile and fault segments; **C)** Main S-dipping fault (2) with **D)** showing the relationship between the displacement profile and fault segments. Areas indicated in red represent locations of possible segment locking or minimal displacement on all time scales, due to fault or segment interaction. Time periods considered:
H4–seabed = ~11.5kyr
H4–H1 = ~8kyr
H4–H2 = ~7kyr
H4–H3 = ~4kyr.

horizons, suggests that full rupture may be inhibited, resulting in a zone of minimal strain accumulation.

On the S-dipping fault (Figure 6.11C) there is only one location, ~600m along strike, which shows a significant displacement low on all four horizons. This coincides with the eastern tip of fault 6, suggesting that displacement on segment 2a of the S-dipping fault is being inhibited by the stress field around this tip (Figure 6.11D). However, the horizons are not as tightly clustered at this point as for the two locations described on the Aigion Fault, indicating that although this is a displacement minima on all timescales, vertical displacement is still accumulating, particularly in the time period between horizon H2 and H1 (4.3–3.5 ka). This coincides with the period where displacement rates saw a significant, albeit temporary, increase (Tables 6.2 and 6.4).

The following two sections use the 10 discrete time periods identified in our data (Figure 6.1) to address whether or not there has been significant variability in the along strike displacement profiles of the two main faults over time. Displacements of <3 ms TWTT will not be discussed due to the vertical resolution constraints of the horizons picked in the MCS reflection profiles of ~2 ms TWTT either side of a fault plane, giving a combined error of ~3 ms TWTT (~2.5 m). However, due to the good correlation between the MCS reflection profiles, and the significant grid of data acquired, it is believed variations of $\geq 3$ ms TWTT are real, reflecting true variations in displacement.

### 6.5.1 Displacement Variations along the Aigion Fault

Section 6.4, Table 6.1 discussed the displacement rate variability for the Aigion Fault over several specific time periods of observation. Whilst analysing the average, minimum and maximum displacement rates can give an overall indication of variation in activity, it is impossible to make along strike comparisons between different time periods. Therefore profiles of the 7 time periods that are most representative of the displacement variability were plotted, to analyse temporal along strike variations (Figure 6.12).

Plots A, C, E and G represent the displacement profiles for the four horizons ($11.5 \pm 1$ ka, $7.5 \pm 1.1$ ka, $4.5 \pm 0.6$ ka and $3.5 \pm 0.5$ ka respectively) to present, previously discussed. All the profiles have very similar shapes, indicating a stable profile has been established prior to ~11.5 ka, and that the fault has maintained a self-similar displacement profile over the time period being considered in this thesis despite localised interactions between segments and splays. This supports the displacement data from section 6.4, indicating that the percentage contribution of this fault to activity of its array has remained constant over all the time periods of observation. However, it is notable that it is during the most recent 3.5 kyr period that up to 50% of the total displacement appears to have been accrued.

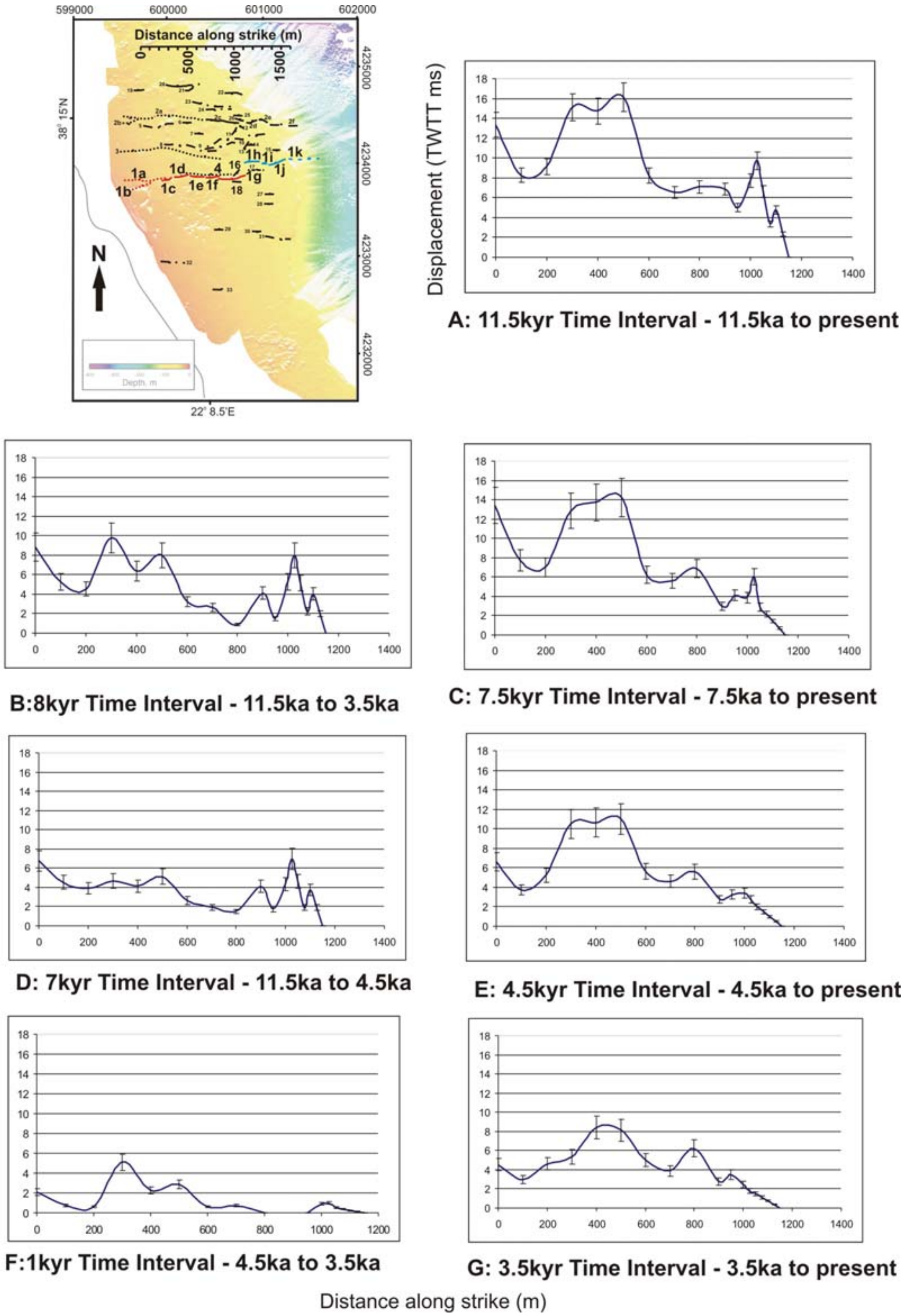

A: 11.5kyr Time Interval - 11.5ka to present

B:8kyr Time Interval - 11.5ka to 3.5ka

C: 7.5kyr Time Interval - 7.5ka to present

D: 7kyr Time Interval - 11.5ka to 4.5ka

E: 4.5kyr Time Interval - 4.5ka to present

F:1kyr Time Interval - 4.5ka to 3.5ka

G: 3.5kyr Time Interval - 3.5ka to present

**Figure 6.12:** Graphs illustrating the variation in displacement profiles over selected time intervals for the N-dipping Aigion Fault (1, Figure 6.2). The fault location map indicates the segments being discussed (1a – 1g, Figure 6.2). It is not possible to quantify variability in movement on segments 1h – 1j (Figure 6.2), shown in blue on the location map, due to poor lateral resolution of horizons H3 – H1.

All the profiles generally show a similar trend of displacement decreasing with distance along strike. There are two displacement peaks, occurring 200-600 m and ~1000 m along strike, corresponding to segments 1c/1d and 1g respectively. In profiles 6.12A-E there is a dip in the displacement high at ~400 m, which corresponds to the boundary between segments 1c and 1d (Figure 6.2). However in 6.12G there is a high 400 m along strike, suggesting there has been rupture of this boundary over the last 3.5 kyr.

All profiles show a displacement low between 0 and 200 m along strike, again related to fault interaction, corresponding to where segment 1b terminates against segment 1a (Figure 6.2). There is also a displacement low over all the time periods occurring at ~950 m along strike, especially in 6.12F where displacement is zero, corresponding to midway along segment 1g. The location indicates that the low is not caused by a segment boundary. However, it does correspond to where fault 16 terminates against segment 1g (Figure 6.2), suggesting that interaction between the two faults is affecting displacement, causing complete locking over the shortest time period of observation.

Profiles 6.12B and D cover the periods from ~11.5 ka - ~3.5 ka and ~11.5 ka - ~4.5 ka respectively. They show similar displacement shapes except between 200-600 m along strike. In 6.12D there is an average of ~4 ms TWTT displacement between 200-600 m along strike, however with only a 1 kyr increase in the period of observation, this average displacement increases by >50% to ~9 ms TWTT displacement in 6.12B. This would suggest that in the 1kyr period between 4.5 and 3.5 ka there was rapid movement at this location, corresponding to segments 1c and 1d (Figure 6.2). This matches data from the displacement analysis in section 6.4, which showed a significant increase in rates occurred during this period.

### 6.5.3 Displacement Variations along the Dominant S-Dipping Fault

Figure 6.13 shows the displacement profile for the major S-dipping fault over the same 7 time periods as shown for the Aigion Fault. As with the Aigion Fault, the profiles show substantial variation in the amount of displacement accrued over different periods of observation, although unlike the Aigion Fault there is also substantial variation in the shape of the displacement profiles over all the time periods.

In all profiles, there is a displacement low, or dip in displacement occurring ~100-200 m and ~600 m along strike. These lows are the only ones that are present on all seven displacement profiles, and correspond to where segment 2b terminates against 2a, and the eastern tip of the S-dipping fault 6 affecting segment 2a respectively. The low at ~200 m along strike is particularly noticeable in 6.13D, where displacement reaches zero. This suggests that this part of the fault had “locked” and was accumulating strain. However, Figure 6.13B shows that over the next 1kyr, from ~4.5 ka - ~3.5 ka, displacement changes from zero to a high of almost 4 ms TWTT. The location coincides with a sharp bend in segment 2a (Figure 6.2), suggesting that this bend may represent a barrier that was subject to a rapid release of the accumulated strain over this 1 kyr period.

At ~300 m along strike there is a displacement high in profiles 6.13C and G but a displacement low in 6.13B and zero displacement in 6.13F at the same location along strike. This location corresponds to both a “bend” in fault 5, where it moves closer to segment 2a, and the start of fault 8 (Figure 6.2). These two faults may therefore be splays of the main S-dipping fault, with differential movement on them causing a displacement response on segment 2a.

The variability of displacement over different time periods, associated with changes in segment orientation, or proximity to fault or segment tips, suggests that the S-dipping fault was more susceptible to bypassing of strain onto sub-parallel faults, resulting in more random behaviour, as displacement switched between faults. The variability over all timescales suggests that no one time period dominates net displacement, as observed with the most recent time period on the Aigion Fault.

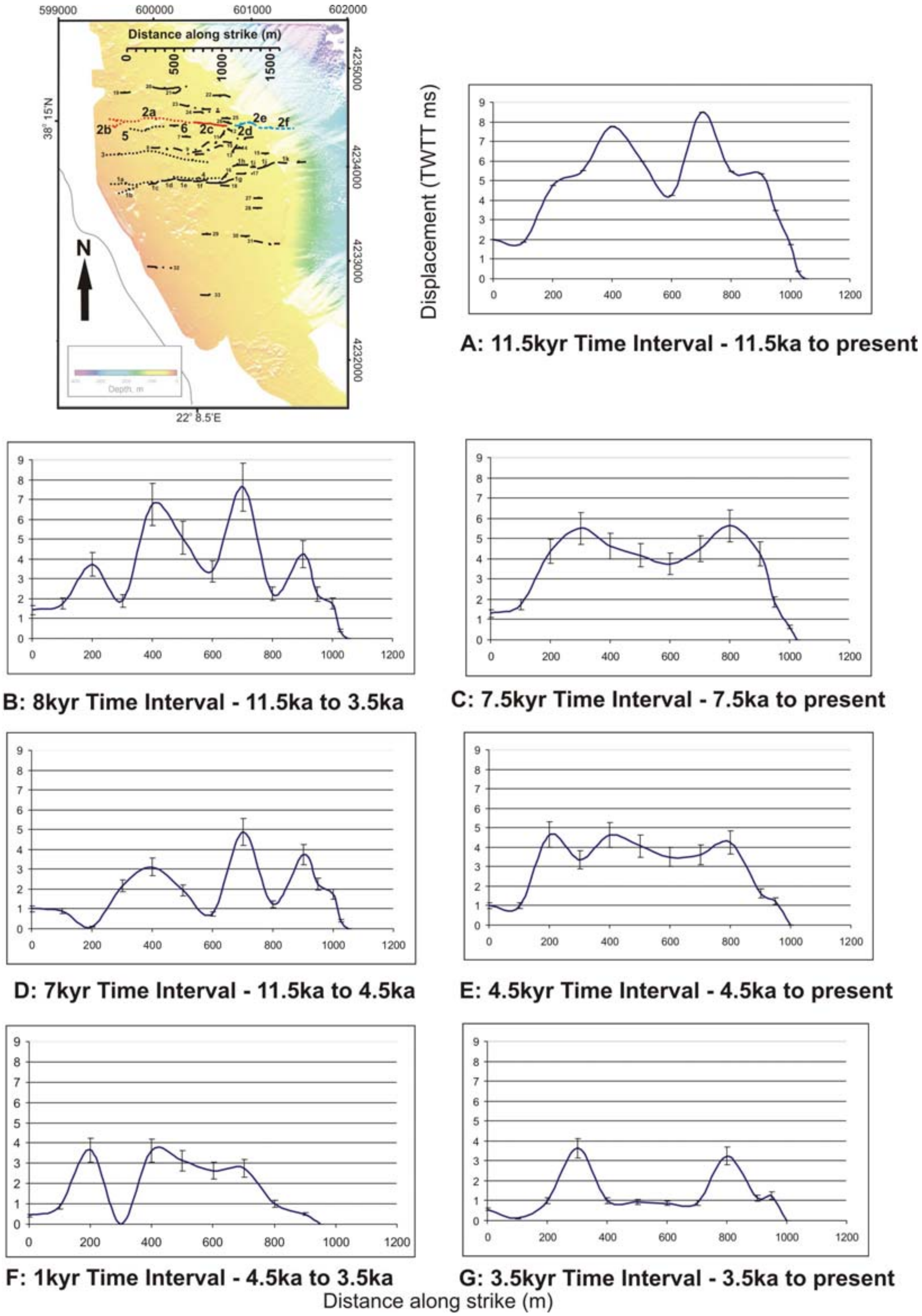

A: 11.5kyr Time Interval - 11.5ka to present

B: 8kyr Time Interval - 11.5ka to 3.5ka

C: 7.5kyr Time Interval - 7.5ka to present

D: 7kyr Time Interval - 11.5ka to 4.5ka

E: 4.5kyr Time Interval - 4.5ka to present

F: 1kyr Time Interval - 4.5ka to 3.5ka

G: 3.5kyr Time Interval - 3.5ka to present

**Figure 6.13:** Graphs illustrating the variation in displacement profiles over selected time intervals for the S-dipping graben bounding fault (2, Figure 6.2). The fault location map indicates the segments being discussed (2a – 2c, Figure 6.2). It is not possible to quantify variability in movement on segments 2d and 2e (Figure 6.2), shown in blue on the location map, due to poor lateral resolution of horizons H3 – H1.

### Summary

The longest period of observation for both faults (Figures 6.12A and 6.13A) indicates significant variations in displacement behaviour between the two faults. Displacement on the S-dipping fault generally appears to tapers off towards both ends of the fault, reaching a maximum towards the centre (Figure 6.13A). This shape is more suggestive of the behaviour of an isolated fault, as opposed to the Aigion Fault (Figure 6.12A), where displacement decreases gradually to the east. This profile shape is indicative of interactions with other segments located further west (onshore), suggesting it is part of a larger fault system. To test this, a second order polynomial curve was fitted to both of the above displacement profiles (Figure 6.14), and it appears to confirm the hypotheses above.

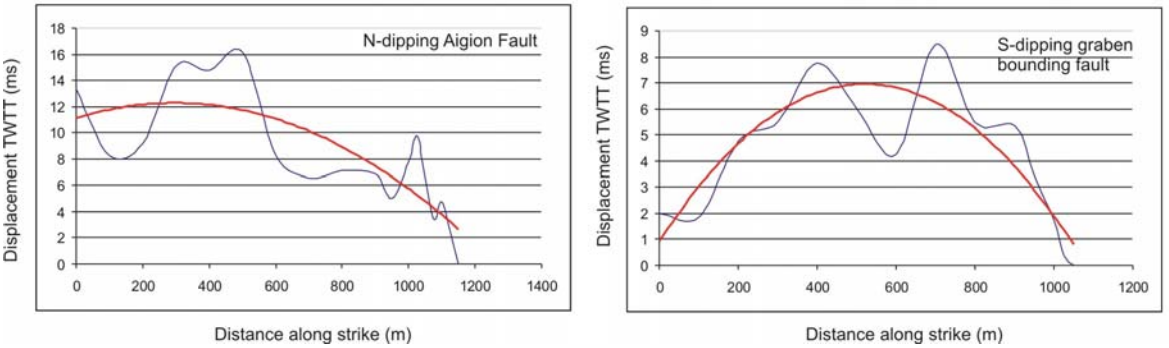

**Figure 6.14:** Plots of the ~11.5 kyr – 0 displacement profile of the two main faults with a second order polynomial curve fitted. It indicates that the N-dipping Aigion Fault may extend further eastwards (onshore), whilst the S-dipping fault behaves as an isolated fault, showing a bell-shaped curve.

## 6.6 VARIANCE ANALYSIS

In this section, the variability of fault displacement profiles will be discussed, using the 10 different length time periods identified in our data (Figure 6.1), and following the method used by Bull et al., (in press). Figures 6.12 and 6.13 indicate that shorter time periods of observation show high displacement variability and irregularity. Mansfield and Cartwright (2001) showed that in the short-term, linked fault segments often behave independently, showing a more variable displacement profile than that presented by the longer-term pattern of strain accumulation across a fault system. This suggests that short term estimations of slip rates gathered from single event surface rupture or paleoseismology may not be representative of the longer-term evolution and behaviour of a specific fault system. If so, it is important to determine over what time periods activity on a fault should be observed to reliably represent long-term behaviour.

The analysis of time period dependency when assessing displacement is undertaken by normalising the displacement data and assessing the variances of each displacement profile for a time period compared to the profile for the longest period of observation, which is 11.5 ± 1 ka in this survey.

### 6.6.1 Normalising Data

The displacement accrued on both the N-dipping Aigion Fault and the S-dipping graben bounding fault for each of the ten possible time periods of observation was normalised i.e. displacement on each survey line divided by the mean displacement rate for that time period. Normalising displacement using the mean for each period makes the profiles more representative of the overall activity during a particular time period, whilst still recognising the contribution of variable displacement on segments.

The mean of all ten normalised profiles was then calculated i.e. sum of normalised observation points from each time period divided by the number of observations in that time period. Observations are regularly spaced along the fault strike, therefore spatial bias should be minimal.

The results were plotted against the normalised distance along strike for each of the faults i.e. distance along strike for each observation point divided by the total length of the fault (Figures 6.15 & 6.16). For both faults the mean profile of the normalised activity over the ten discrete time intervals best matches the profile of the longest period of observation, i.e. 11.5 – 0 ka (Figures 6.12A & 6.13A).

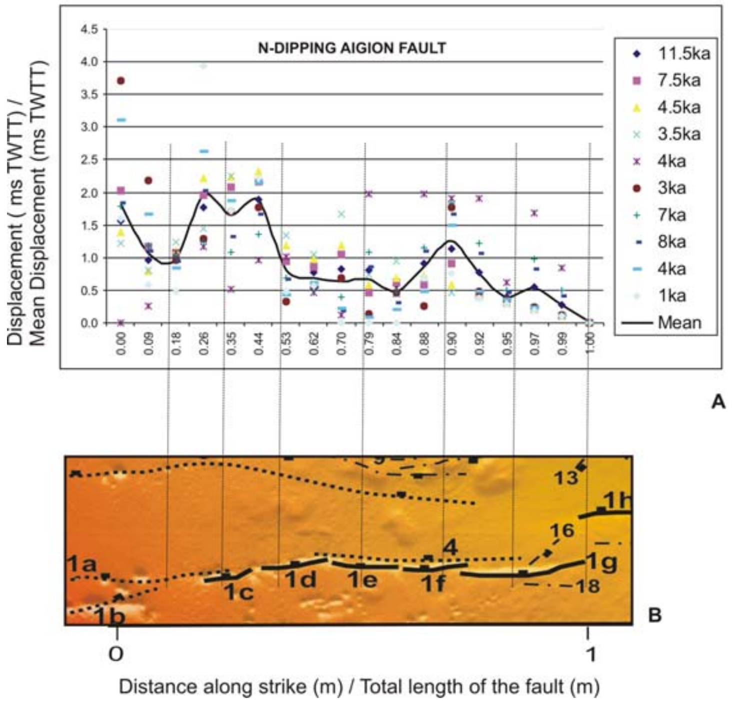

**Figure 6.15:** Plot showing the normalised displacement profile (indicated by symbols) for the ten discrete time periods of observation for the Aigion Fault. **A)** Solid line indicates the normalised mean of all the time periods. **B)** Enlargement of the fault map (Figure 6.2) showing the segmentation of the Aigion Fault, scaled so that the length of segments 1a – 1g corresponds to the normalised fault length shown in A.

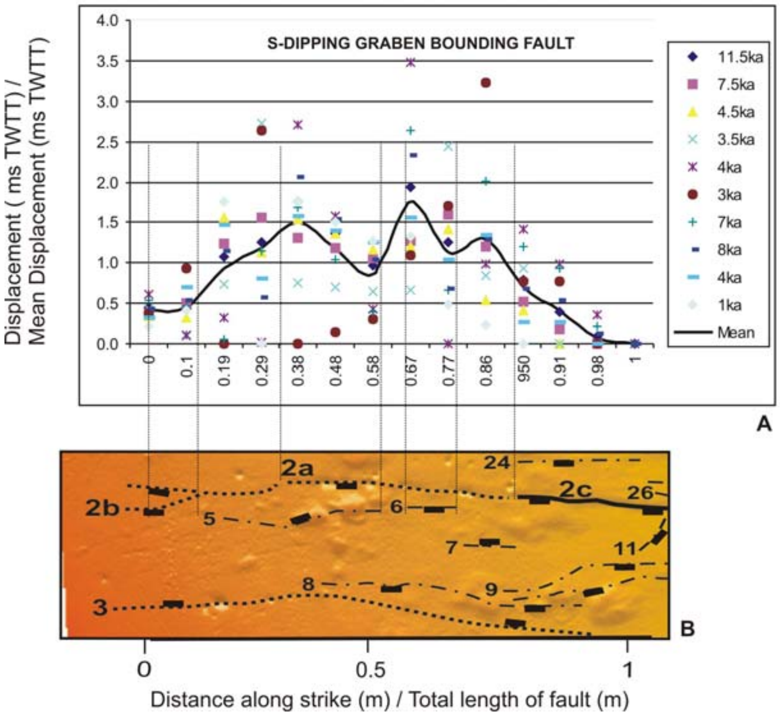

**Figure 6.16:** Plot showing the normalised displacement profile (indicated by symbols) for the ten discrete time periods of observation for the major S-dipping fault. **A)** Solid line indicates the normalised mean of all the time periods. **B)** Enlargement of the fault map (Figure 6.2) showing the segmentation of the S-dipping fault, scaled so that the length of segments 2a – 2c corresponds to the normalised fault length shown in A.

### 6.6.2 Variance Analysis

The normalised mean from each of the time periods of observation was then taken away from the normalised mean of the longest period of observation (~11.5 ± 1 kyr), giving a set of nine residuals for each fault. The variances of these residuals were then plotted against the time period of observation (Figure 6.17). The variance shown between the calculated residuals gives an indication of the temporal variability of displacement exhibited by the fault. If the residuals are high or widely spread, this suggests significant displacement variability over that length of time. This results in there being little indication of longer-term fault behaviour.

Figure 6.17 shows an overall trend of variance decrease with time. The plots indicate that for observation periods >4-6 kyr, the variance rapidly decreases, suggesting displacement patterns become more indicative of long-term displacement behaviour on that fault, regardless of the amount of displacement accrued. It is notable that the plots show very similar trends. This could be due to a change in sedimentation rate, where apparent rapid movement on the fault is actually due to low sedimentation across the area. However, both faults show differential changes in displacement suggesting that the similarity in the plots is not a response solely to variability in sedimentation, but may be due to the faults being linked. However, it is acknowledged that there are a limited number of datapoints from which to draw conclusions.

The relatively low initial variance, at ~1.5 kyr, may indicate that there are periods within the short-term, where faults exhibit more stable patterns, indicative of the longer-term displacement profiles. It is hypothesised that the cumulative effect of clustered earthquake cycles may periodically restore, in the short-term, the overall displacement profile back to one resembling the longer-term norm, even though in general, the displacement profiles for periods of observation <~4 kyr are not representative of the long-term displacement behaviour. However, the 1.5 kyr datapoint could also represent an anomaly.

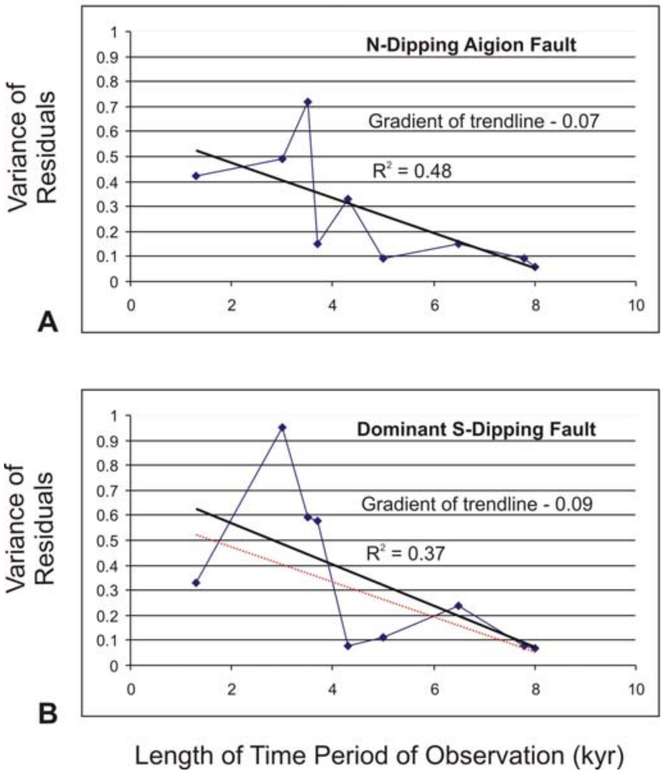

**Figure 6.17:** Plots illustrating the variance of the residuals between the normalised displacement profiles against the period of observation (kyr) for the Aigion Fault (**A**) and the major S-dipping fault (**B**). Time periods calculated against the baseline 11.5 ka horizon (H4) e.g. 8 kyr period represents 3.5 ka – 11.5 ka.
Linear trendlines and the $R^2$ value indicate the data fit. The dotted red line in plot B indicates the position of the trendline from plot A, relative to B.

It is suggested that the length of time taken for a fault system to establish a true representation of long-term displacement behaviour is linked to the slip rate. The faster a fault slips, the shorter the time period required before the length / displacement relationship has been fully established (Figure 6.18). The gradient for the Aigion Fault is slightly steeper than the S-dipping fault's, suggesting that it has a faster slip rate. Displacement rates support this hypothesis, with average displacement on the Aigion Fault being 40 – 50% higher (with the exception of the 1 kyr period between 4.5 and 3.5 ka) (Tables 6.4 & 6.5). However the variance plots (Figure 6.17) suggest that both faults begin to resemble the long-term profile after approximately the same time period (>4 kyr). This suggests that despite the difference in slip rates, indicating distributed deformation, possible linkage of the faults at depth may be resulting in similar results from the variance analysis, as the faults behave as a coherent system over the long-term.

The variance analysis indicates that with a high-resolution, short timescale survey, it is possible to get a detailed picture of fault behaviour, resolving the period of observation required to establish a longer-term more stable displacement profile, and recognising the time periods over which significant variability can occur. Short-term

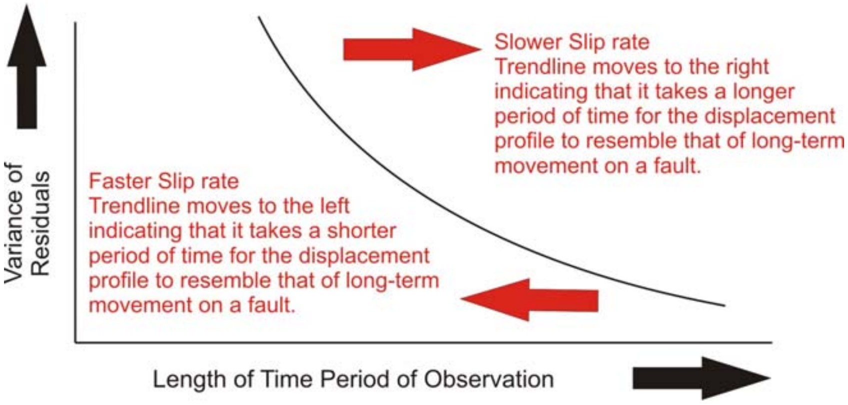

**Figure 6.18:** Cartoon showing the relationship between the variance trendline and slip rates. It enables a qualitative comparison between expected slip rates on the N-dipping Aigion Fault and the major S-dipping graben bounding fault, based on the trendlines applied in Figure 6.17.

variability can therefore be identified on faults in regions where geodetic surveys cannot resolve fault activity due to array spacing.

## 6.7 DISCUSSION

The detailed analysis of the seismic reflection profiles has identified five main areas to be addressed when considering the development of the Aigion Fault and faulting across the Aigion Shelf: 1) the nature of fault segmentation, and whether shallow structures observed are being driven by deeper processes; 2) the variability of displacement rates in space and time for individual faults and the overall fault system; 3) fault growth and propagation history of the Aigion Fault over the past ~12kyr; 4) the nature of fault interaction and pinning of fault segment tips; 5) the validity of using different time periods of observation when addressing fault displacement. Each of these issues will be discussed separately before summarising the Holocene evolution of the offshore Aigion Fault in Chapter 8.

### 6.7.1 Segmentation

Segments can nucleate as discrete faults (e.g. Cowie et al., 2000) on many scales. However, with increasing displacement and lateral growth they begin to interact (Peacock and Sanderson, 1991; Cartwright et al., 1995; Childs et al., 1995). Linkage and transfer of displacement occurs between segments, until eventually they behave as one continuous fault trace (Chapter 1, Figure 1.7), with displacement lows indicating the positions of relic segment boundaries. Therefore the largest fault trace may combine multiple smaller scales of segmentation within it (Trudgill and Cartwright, 1994).

Using the classification adopted in this study, whereby a segment is defined by its discrete plane, the multibeam bathymetry indicates that segments of <500 m length form the offshore extension of the N-dipping Aigion Fault. Displacement profiles indicate that hard linkage may have occurred between some of these segments, forming larger fault sections of >1 km in length that are behaving in a coherent manner.

Koukouvelas and Doutsos (1996) indicate that onshore segmentation of the Aigion Fault ranges between 2 – 8 km. Doutsos and Poulimenos (1992) describe trace lengths of >1.5 km in the NW Peleponnesos, whilst Roberts and Jackson (1991), Goldsworthy and Jackson (2001) and McNeill and Collier (2004) document segment lengths of 10 – 25 km in the Gulf of Corinth.

The difference between the Corinth segment lengths suggests that in many previous studies, the smaller scales of segmentation have not been documented. It is almost certain that the lack of offshore sub-surface data with closely spaced survey lines has prevented smaller segments being identified, whilst vegetation cover and anthropogenic activities onshore has masked smaller segments onshore. It is also possible that the Machette et al. (1991) definition has been adopted, using surface rupture during earthquakes as a means of identifying larger segment lengths. This study suggests that the Aigion Fault, and probably other Gulf of Corinth faults, are composed of a number of orders of segmentation.

Table 6.5 gives examples of the various scales of segmentation described in studies from fault zones in several extensional provinces. The range of segment lengths on the Aigion Fault appears consistent with the majority of the examples given, with the main exception being the Wasatch Fault zone (Machette et al., 1991). It is proposed that this discrepancy arises from how segments are defined, as discussed in the introduction to this chapter.

| Location | Segment Lengths | Maximum Total Fault Length (km) |
|---|---|---|
| **Thingvallavatn, Iceland**<br>(Bull et al., (in press) | 800m – 3.5km | 11km |
| **Volcanic Tableland, California**<br>(Dawers et al., 1993) | <50m – 2.2km | 2.2km |
| **Canyonlands, Utah**<br>(Trudgill and Cartwright, 1994) | 10’sm - >10km | >10km |
| **Rangitaiki, New Zealand**<br>(Taylor et al., 2004) | 4 - 5km | 19km |
| **Aigion, Gulf of Corinth** | <500m – 8km | ~15km |
| **Sofiko Range, Gulf of Corinth**<br>(Koukouvelas et al., 1999() | 15m – 9.5km | 9.5km |
| **Wasatch Fault, Utah**<br>(Machette et al., 1991) | 11 – 70km | 343km |

**Table 6.5:** Summary of segment lengths documented in extensional provinces, and the maximum fault length that they combine to form.

It is believed that the multiple sub-surface, sub-parallel faults imaged on the Aigion shelf are splays of a major fault at depth, formed through upward bifurcation of deformation, supported by coherant fault modelling (Walsh et al., 2003b). Meyer et al. (2002) and Childs et al. (2003) believe that these connected fault splays develop “early” in the fault system’s evolution, and that geologically instantaneous linkage of segments results in a stratigraphic pattern resembling that of a single fault. However, as each extensional regime is unique, it is not known what is meant by “early”. In the Meyer et al. (2002) study, “early” was described as being within the first 1 – 2 Myr of fault initiation, with Nicol et al. (2005b) suggesting this may occur in <0.5 Myr. Taylor et al. (2004) found that linkage occurred after ~1 Ma of fault interaction. Therefore, it is unlikely that the whole Aigion Fault system has reached this stage of instantaneous linkage. Chapter 8 will discuss age constraints for the development of the Aigion Fault, in order to determine whether or not linkage on this timescale is feasible, with regards to the calculated slip rate.

Linkage of the two splays at depth supports the findings from section 6.2.1, which indicate significant interaction between the faults of the Aigion array. It also explains why the isopach data from Chapter 5 shows no evidence of isolated sub-basins forming against each specific segment of the offshore Aigion Fault.

### 6.7.2 Displacement and Slip Rate on the Offshore Aigion Fault

#### Changes in Displacement and Segment Length

The spatially averaged displacement rates obtained for the Aigion Fault ranged between 0.4 ± 0.1 mm $yr^{-1}$ and 0.9 ± 0.1 mm $yr^{-1}$, although the minimum and maximum rates obtained (0.03 ± 0.01 mm $yr^{-1}$ and 4.3 ± 0.7 mm $yr^{-1}$ respectively) showed that there was significant temporal and spatial variability.

There was a two-fold increase in displacement rates between ~4.5-3.5 ka, which was maintained on the Aigion Fault for the remainder of the observation period (~3.5 kyr). Taylor et al. (2004) conducted a similar analysis of short-term displacement behaviour on the Rangitaiki Fault, New Zealand. They observed a three-fold increase in displacement upon segment linkage. However, analysis of the stratigraphy (chapter 5) does not indicate isolated depo-centres forming against segments of the Aigion Fault, that later evolved into larger basins as linkage occurred. Likewise, displacement data for the Aigion Fault suggests that the segments identified from the multibeam are behaving as a coherent unit at depth (Figure 6.9). Therefore it is not believed that the increase in displacement rates is due to a rapid increase in fault length as a result of segment linkage.

Various authors have estimated displacement rates from the Aigion Fault and surrounding basin bounding systems. These are summarised in Table 6.6. The displacement data obtained from this study of the offshore extension of the Aigion Fault best fits with the short timescales analysed by Pantosti et al. (2004), for the western section of the onshore Aigion Fault. However, the offshore short-term displacement rates are also consistent with the longer term rates (1.8 Myr) of Doutsos and Poulimenos (1992) for the inactive relic basin bounding faults. This suggests that although the Aigion Fault is recognised as a young fault, the observation period of ~11.5 kyr is long enough to obtain a reliable record of long-term behaviour, as supported by the variance analysis.

The maximum vertical displacement observed on horizon H4 for each segment imaged plotted against segment length is shown in Figure 6.19. It also shows the spatial average for the whole of the offshore extension of the Aigion Fault, the offshore major S-dipping fault, the onshore Aigion Fault, and the Eastern and Western Eliki Faults, in order

| Location | Vertical Displacement Rate (mm $yr^{-1}$) | Time Period of Observation | Technique Used | Author |
|---|---|---|---|---|
| Offshore Aigion Fault extension | 0.39-0.88 ± 0.1-0.3 (1:2 u:s ratio) | 12kyr | Stratigraphic Analysis | This study |
| Westernmost onshore segment of Aigion Fault | 0.3 - 2.5 | 1kyr | Radiocarbon dating (Paleoseismology) | Pantosti et al. (2004) |
| Central onshore segment of Aigion Fault | 2.6 – 3.6 | 200-300kyr | Uplifted Marine Terraces | De Martini et al. (2004) |
| Western Eliki Fault | 3.15 – 4.4 | 200-300kyr | Uplifted Marine Terraces | De Martini et al. (2004) |
| Eastern Eliki Fault | 2.4 – 3.4 | 200-300kyr | Uplifted Marine Terraces | De Martini et al. (2004) |
| Aigion-Neos system | 1.9-2.7 | 2kyr | Radiocarbon dating (Paleoseismology) | Palyvos et al. (2005) |
| Eliki Fault system | 3 – 6.3 | ~200kyr | Uplifted Marine Terraces | McNeill and Collier (2004) |
| Kerynia, Mellissia and Pyrgaki Faults | 0.16 - 0.76 | 1.8Ma | Biostratigraphy | Doutsos and Poulimenos (1992) |

**Table 6.6:** Table of displacement rates across the Aigion Fault and other systems, obtained from different techniques and over different periods. The Aigion-Neos system includes the Fassouleika and Selianitika Faults (Chapter 4). The Kerynia, Mellissia and Pyrgaki Fault are included as examples of established, now inactive, basin bounding faults found to the south of the Aigion Fault. The Eliki Fault is included as the closest major active fault system. 1:2-3.2 uplift to subsidence ratio was used (McNeill and Collier, 2004).

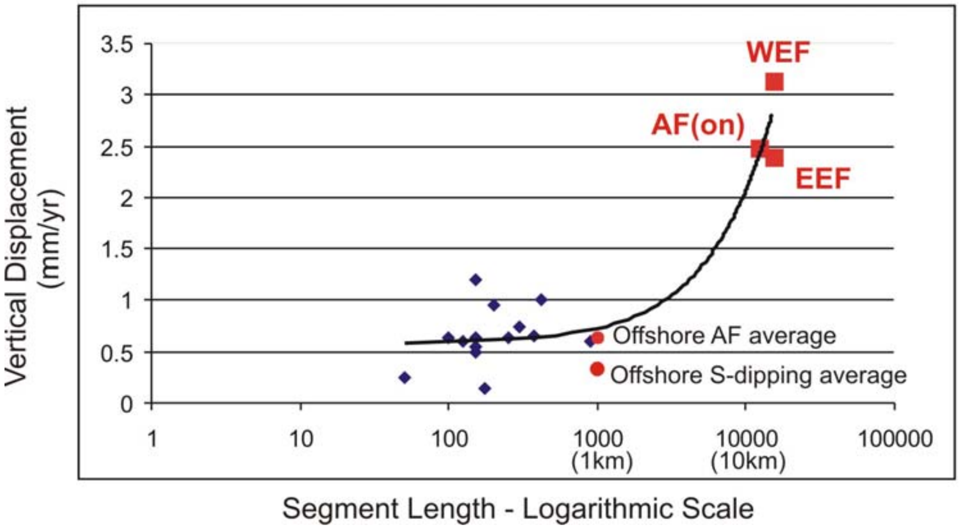

**Figure 6.19:** Illustration of displacement against segment length observed on the Aigion Fault and the neighbouring Eliki Fault system, with a linear trendline applied. Blue diamonds indicate segment lengths and displacement on horizon H4 (11.5 kyr time period). The red circles indicate the average displacement from all the mapped offshore segments on both the Aigion Fault and the S-dipping graben bounding fault. The red squares indicate the displacement when observing both longer fault lengths, and longer time periods of observation (>100 kyr). WEF and EEF are the Western and Eastern Eliki Faults, AF(on) is the onshore Aigion Fault. WEF, EEF and onshore AF rates calculated from uplift rates of De Martini et al. (2004), using 1:2 uplift:subsidence ratio.

to compare the displacement data from this short term study, with longer term fault displacement rates from studies encompassing >100 kyr.

In order to display all orders of segment length clearly, a logarithmic scale was used. A linear trendline was then applied to the data to illustrate the scatter of points around an idealised length / displacement relationship. (The trendline appears curved due to the logarithmic segment length scale). The scatter is greatest amongst the shorter segment lengths, suggesting that there is higher variability where segments still have a degree of independent movement, prior to full linkage and establishment of a stable displacement profile. The data points that relate to the onshore Aigion and Eliki systems are taken from a much longer period of observation (> 100 kyr as opposed to ~10 kyr for the offshore values). These points lie closer to the trendline, suggesting that the length / displacement profile becomes more stable when viewed over longer timescales.

## Displacement and Segment Interaction

Mansfield and Cartwright (2001) and Childs et al. (2003) suggested that fault evolution is a combined result of fault tip propagation, and overlap and linkage between segments. They proposed that even when linked, segments remained kinematically independent, with previous fault segment boundaries sometimes acting as asperities, preventing full rupture along a now linked fault system. Over various timescales, each segment was observed to display individual displacement behaviour, although when the profile of the whole fault was considered, the displacement profile of the linked system indicated a single fault.

The similarity between the profiles of vertical displacement on the Aigion Fault over the four horizons (Figure 6.9) indicates that the segments are linked to some degree, and behaving as a coherent system overall. However the range of displacement rates in Tables 6.1 and 6.2, from $0.03 \pm 0.01$ mm $y^{-1}$ to $4.3 \pm 0.7$ mm $y^{-1}$, indicate that there is significant variability over short timescales. An example of how interacting fault segments can have distinct displacement profiles, and yet when combined into an aggregate across a system, indicate one coherent fault system, is shown in Figure 6.20.

The data from Walsh and Watterson (1990) (Figure 6.20, **1**) show two distinct features of fault interaction. Where fault tips are close to overlapping, the aggregate profile retains a displacement minimum (black arrow, Figure 6.9, 1c). However where there is significant overlap, there is a displacement high, due to the combined contribution from multiple faults (red arrow, 1c). The overall displacement profile is one of an isolated fault.

The data from the Aigion Shelf (Figure 6.20, **2**) appears more complex, due to the numerous points of overlap and tip interaction. However, it does follow similar displacement principles. There are four main displacement minimums, indicated by the black arrows in Figure 6.20, 2b. When the vertical displacement of segments is summed (2c), two displacement lows remain in the aggregate, however two of the previous lows become displacement highs associated with segment overlap. Trudgill and Cartwright (1994) found evidence of displacement highs at points of segment interaction, caused by

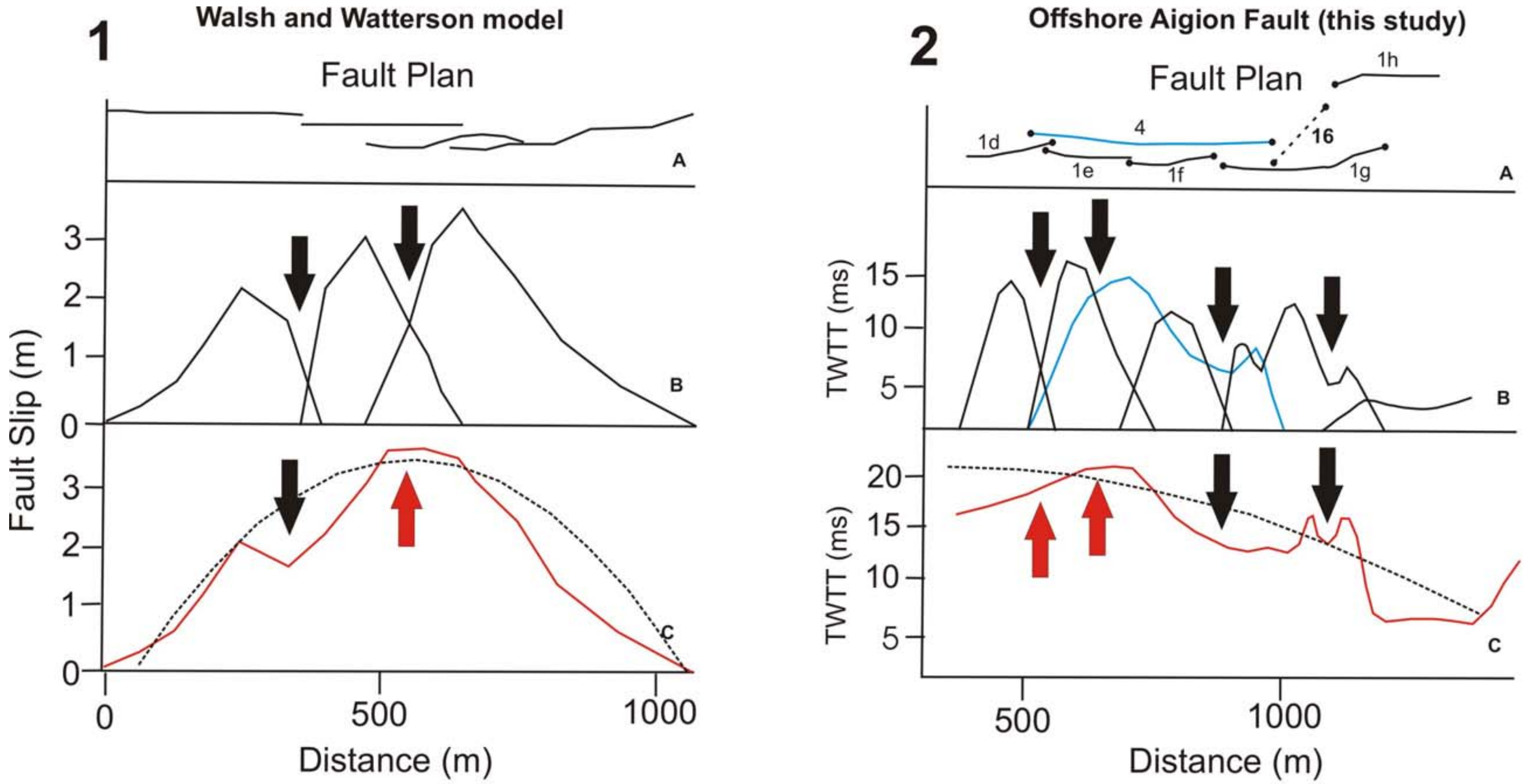

**Figure 6.20:** Cartoon illustrating the displacement profile resulting from interacting fault segments. Scheme 1 comes from Walsh and Watterson (1990) whilst scheme 2 illustrates data from a section of the offshore Aigion Fault. Black arrows indicate displacement lows, whilst red arrows indicate where cumulative displacement from overlapping faults has resulted in a displacement highs. Dashed line in plot 2c indicates the aggregate displacement profile, suggesting that the offshore fault system is one part of a larger system. Fault 4 is included in scheme 2 as it interacts so closely with the Aigion Fault, and is believed to take up a significant component of the displacement. A) Plan view of fault geometry; B) Individual segment displacement profiles; C) Aggregate displacement profile.

transference of strain onto sub-parallel faults. The inter-graben faults may therefore be acting as bypass structures, particularly in the step-over zone.

What is unusual in the Aigion dataset is that the two displacement lows coincide with significant segment overlap, where one might expect to see a high. The only factor that appears different between the example in Figure 6.20, 1, and the Aigion Fault, is the orientation of fault 16 (Figure 6.2). This fault deviates from the predominantly E-W orientation, and therefore does not just overlap with segments 1g and 1h and fault 4, but cross-cuts them, possibly preventing rupture. Effects of a fault that does not become incorporated into a later through-going system, may therefore result in longer-term indications of past interaction. The dashed line in Figure 6.20, **2**, suggests that the offshore Aigion Fault does not have the profile of an isolated fault system, instead resembling one component of a larger system which extends further westwards.

## Displacement and Slip Rate

Fault slip rates can be calculated using vertical displacement rates from this study, and a fault dip of 55$^{o}$ established from the AIG10 borehole (Rettenmaier et al., 2004; Table 6.7). If displacement accrued on the single fault at depth is distributed across a number of faults at shallower depths, the displacement on all the mapped faults needs to be considered in the final analysis of extension across the Aigion Shelf. The average slip rates over the 11.5 kyr period of observation for the Aigion Fault, main S-dipping fault, and the aggregate from all faults mapped on horizon H4 were 0.8, 0.4 and 2.6 mm yr$^{-1}$ respectively. It is believed that these slip rates are under-estimated, as up to 40% of the strain, accommodated on small faults that are below seismic resolution, is often unaccounted for (Bull, Pers. Comm).

Despite the potential for under-estimation, all the above rates are consistently lower than the long-term rate of 9-11 mm yr$^{-1}$ documented by De Martini et al. (2004) for periods of 200-300 kyr. However, De Martini et al. (2004) use a forward dislocation model that relies on a number of unknown assumptions, with regards to input parameters. The resulting subsidence for the observed topographic uplift is unrealistic, therefore the slip rates are not considered to be comparable.

| Fault | Period of Observation (kyr) | Fault Dip | Average Slip Rate (mm yr$^{-1}$) | Minimum Slip Rate (mm yr$^{-1}$) | Maximum Slip rate (mm yr$^{-1}$) |
|---|---|---|---|---|---|
| **Aigion Fault** | ~11.5 | 55$^o$ | 0.8 ± 0.07 | 0.3 ± 0.03 | 1.5 ± 0.1 |
| **S-dipping fault** | ~11.5 | 55$^o$ | 0.4 ± 0.04 | 0.2 ± 0.02 | 0.8 ± 0.07 |
| **All faults** | ~11.5 | 55$^o$ | 2.6 ± 0.2 | 0.7 ± 0.06 | 3.5 ± 0.3 |

**Table 6.7:** Slip rates for the N-dipping Aigion Fault; major S-dipping graben bounding fault; and total rate taking into account the contributions from all faults mapped on the oldest horizon (H4, ~11.5 ka). Fault dip based on onshore dip of Rettenmaier et al. (2004).

### 6.7.3 Fault Growth

There are two types of fault growth proposed by past studies – radial tip propagation of a single isolated fault (e.g. Walsh and Watterson, 1987 and Cowie and Scholtz, 1992) and segment linkage (e.g. Segall and Pollard, 1980; Peacock and Sanderson, 1991 and Cartwright et al., 1995).

Determining whether fault growth due to lateral propagation has occurred here depends on resolving the present day fault tip, and previous tip locations on older horizons. With a minimum survey line spacing of 25 m, the lateral propagation rates would have to be >3 mm yr$^{-1}$ if fault propagation was to be resolved between horizons (line spacing / time period). The structure plots for each horizon, shown in Chapter 5, Figure 5.14 suggest that the segments of the two main faults (**1** and **2**, Figure 6.2) have not increased in length during the time period of observation, and that the majority of minor faults apparently disappear over the 8 kyr period between H4 and H1.

Three explanations could possibly be drawn from this study: 1) Prior to 11.5 ka, the fault tips of both the Aigion Fault and major S-dipping graben bounding fault were already located beyond the shelf edge, and so no lateral propagation would be imaged in this survey. Nicol et al. (2005b) and Meyer et al. (2002) presented evidence from fault systems where the length of the fault was rapidly established at depth very early in the development stages (<0.5 Ma). If this behaviour holds true for faults within the western Gulf, it supports this first hypothesis; 2) Propagation rates on the minor faults may be below the resolution limit of 3 mm yr$^{-1}$, and so no lateral extension of any of the minor fault segments has been recorded; 3) Progressive burial by prograding beach deltaics during the latest Holocene is masking activity on the minor (blind) faults. With variables including interactions with other faults; the earthquake recurrence interval and the nature of fault segmentation, it is impossible to categorically state why we did not resolve lateral fault propagation.

Growth through linkage may also occur as a result of repeat fracturing in the pre-weakened rock structure, caused by interaction between the stress fields of opposing fault tips (D'Alessio and Martel, 2004). These fractures link to form splays that flank the main fault system (Twiss and Moore, 2001; D'Alessio and Martel, 2004), causing an increase in the vertical displacement across a wider area of deformation, but without apparent lateral growth. It is believed that the Aigion and S-dipping arrays bound a damage zone associated with the growth of the dominant Aigion Fault. Segment linkage and radial propagation of the fault tip through this survey area at some point in the past may have caused the fracturing and formation of sub-parallel splays that flank the main fault. Therefore the changes in displacement observed may indicate a change in the distribution of displacement between the multiple faults as the fault system matures, rather than lateral fault growth. It is not clear when this damage zone formed.

### 6.7.4 Fault Interaction and Pinning

The displacement gradients at fault tips discussed in section 6.2.1 of between 0.01 and 0.06, suggest that there is significant segment interaction occurring across the Aigion Shelf. The interaction and resulting steep gradients are more obvious in the Aigion array (Figure 6.7), especially between segments 1a and 1b, and 1d with fault 4, than in the S-dipping array (Figure 6.8), where faults such as 6 and 8 have a bell-shaped profile indicative of an isolated fault. The gradients observed in the Aigion Shelf data were compared with a schematic representation of fault tip displacement gradients proposed by Nicol et al. (1996b) (Figure 6.21). The figure shows similarities between the schematic data and the field data, supporting the hypothesis that faults on the Aigion Shelf are interacting.

This finding is supported by other field data (Cowie and Shipton 1998). They suggest that displacement at the fault tip does not taper to zero, but is associated with steep displacement gradients. This type of displacement behaviour is especially noticeable where fault segment tips are restricted or pinned due to interaction with neighbouring segments, preventing lateral propagation and effectively fixing the fault length (Nicol et al. 1996a ; Peacock, 2002; Walsh et al., 2003a).

However, McNeill and Collier (2004) state that the displacement profile of the Eliki Fault is relatively uniform across the segment boundary between the Western and Eastern Eliki segments, with no major gradient associated with the overlapping segment tips. There is therefore a behavioural difference between segment interactions and the effects of pinning observed on the younger Aigion Fault, and the older Eliki system. The lack of quantitative information published on fault tip displacement gradients with which to compare geological data to modeled predictions makes it difficult to infer if this difference in the observed gradients is due to maturity of the fault system, or some other factor, such as scales of observation.

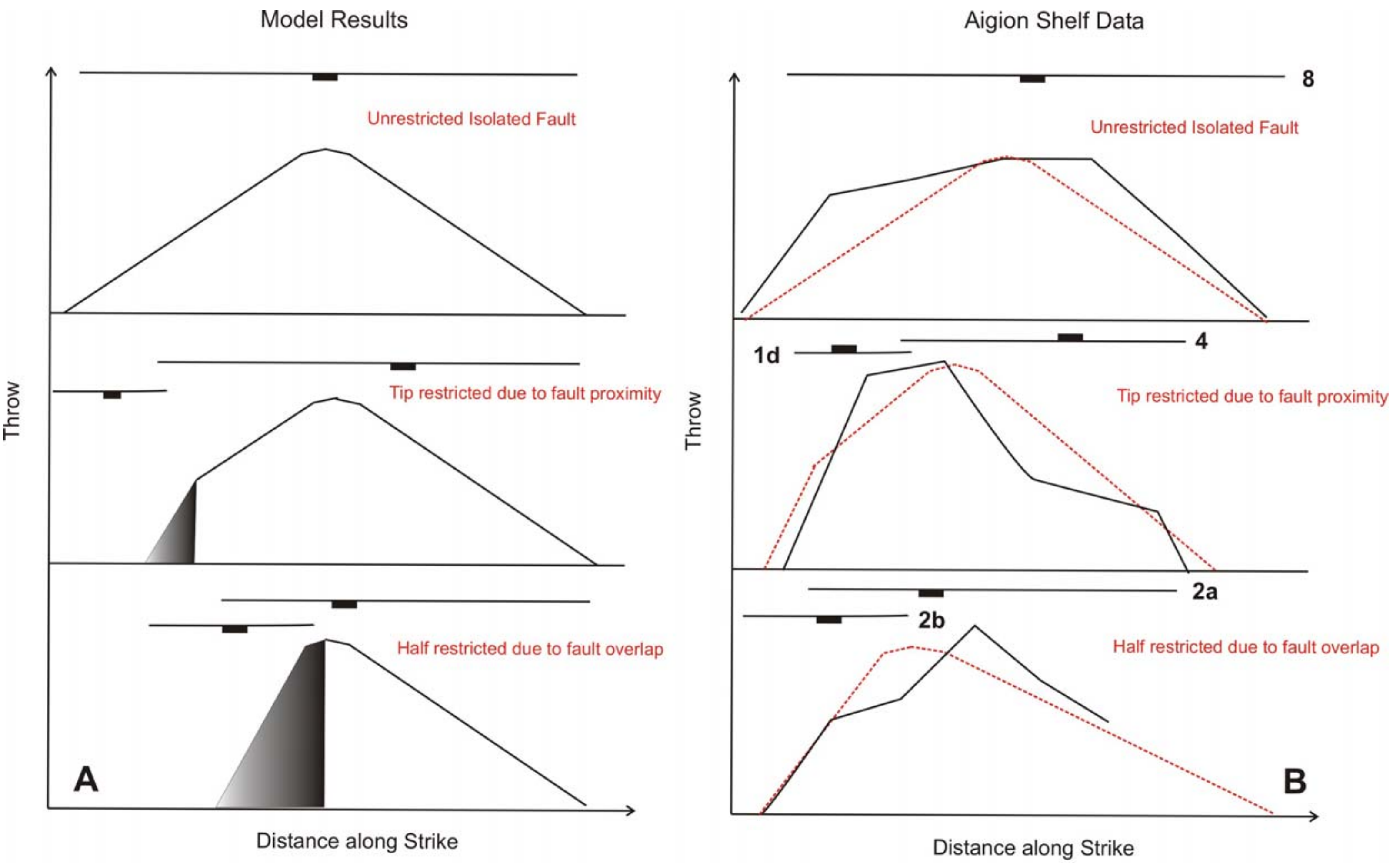

**Figure 6.21:** Cartoon illustrating the effects on fault tip displacement from proximity to, and overlap with neighbouring fault segments. **A)** Model results after Nicol et al (1996). Shaded areas indicate the restricted areas of the fault. Fault tips that are restricted have higher displacement gradients than the unrestricted tips. The displacement maximum appears to move off centre and towards the point of interaction. **B)** Solid black lines indicate the displacement profiles of fault segments from the Aigion Shelf. The dashed red lines indicate the model predictions (Nicol et al., 1996b). Fault numbers relate to Figure 6.2. It shows a clear similarity between the predictions of tip restriction, and that observed in this study.

### 6.7.5 Validity of Short-Term Observation Periods

Traditionally, analysis of fault displacement, fault growth and changes in geometry using seismic reflection profiles has been conducted over timescales of c. $10^5$ – $10^6$ years. Shorter timescale observations ($10^2$ -$10^5$ years) have used paleoseismology and high-resolution seismic reflection data (e.g. Taylor et al., 2004; Palyvos et al., 2005; Nicol et al., 2005b; Bull et al., in press). Whilst the longer timescale offers an insight into the final geometry of a fault system, evidence of ephemeral growth stages, such as development of relay ramps, segment linkage, and earthquake activity are usually unresolvable. Lamarche et al. (in press) and Bull et al. (in press) both investigate the temporal variability of fault behaviour on much shorter timescales from 2.5 to 20 kyr, and reveal substantial displacement changes during these periods. Palyvos et al. (2005) suggest they have identified changes in displacement rates on the onshore Aigion Fault resulting from a few earthquake cycles (c. $10^3$ years). However, these occur over very short timescales, and have been documented at only a few locations on the fault. Therefore it is suggested that they are more likely to represent surface slip during single earthquakes as opposed to real changes in displacement rates.

Previous long-term studies conducted in the Gulf of Corinth, and specifically on the Aigion Fault, encompass a range of time periods of 100-500 kyr (Armijo et al., 1996; McNeill and Collier 2004; Micarelli et al., 2004; De Martini et al., 2004). Whilst these studies give a reliable indication of the long term behaviour of the fault system, they cannot distinguish between discrete periods of fault development when displacement rates may vary considerably. Published work by Stewart and Vita-Finzi (1996) suggest an average Holocene uplift rate on the Eliki Fault of 1.5 mm $yr^{-1}$. However, the dated samples yield uplift ranges from 0.8 – 2.2 mm $yr^{-1}$, indicating significant temporal and spatial variability occurs within the Holocene average. Likewise Pirazzoli et al. (1994) use marine notches to identify short-term pulses of accelerated uplift occurring over intervals of ~1.5 kyr in the eastern Gulf. This suggests that short-term variability occurring in the Gulf of Corinth can be recognised from within longer-term trends if the stratigraphy is well-constrained.

The Aigion Fault provides both an onshore and an offshore component that can be used in fault analysis. Whilst marine terraces uplifted in the onshore footwall can give an indication of the longer-term displacement behaviour (e.g. De Martini et al., 2004), the limited datable material associated with sea-level highstands often prevents a more detailed analysis of behaviour. In the offshore environment, detailed seismic stratigraphy has meant that a much shorter timescale analysis can be conducted.

This study indicates significant variability in displacement rates over short timescales, especially in the 1 kyr period between 4.5 and 3.5 ka. This jump, if real, is indicative of periods of enhanced activity on the fault, and would not have been resolvable over longer time periods. Therefore episodic activity can be distinguished if the time periods of observation are short enough, revealing evidence of localised pinning and intermittent rupturing through segment boundaries.

Normalising the displacement data from the different time intervals, and calculating the variance residuals, showed the time periods over which the data provided a long-term, stable profile of fault behaviour. The similarity between the mean normalised profile and the profile from the longest period of observation (11.5 ± 1 kyr) indicates that normalising the dataset has not destroyed the overall picture observed on the long term,

The analysis revealed that a time period of >4-6 kyr would provide a realistic idea of long-term behaviour on the Aigion Fault system. This is similar to the period of >6 kyr established by Bull et al. (in press), following analysis of a normal fault system in New Zealand. Shorter timescale observations may not give representative profiles, although they offer a valuable insight into short-term displacement behaviour of the Aigion Fault.

## 6.8 CONCLUSIONS

- Displacement profiles of >7 kyr are similar to profiles from the longest period of observation (11.5 kyr). Analysis of the variance residuals suggests periods of >4-6 kyr will show the long-term, stable displacement profile of the offshore Aigion Fault. In contrast, profiles from shorter time periods of observation (1 – 3 kyr) are much more irregular, and indicate temporal and spatial variability, and the potential short-term influence of earthquake clustering.

- The displacement profile for the offshore Aigion Fault is very similar on all mapped horizons. This suggests that although the seafloor expression of the fault is segmented, at depth the segments are linked and moving as a coherent unit. In addition, there is significant interaction between the dominant faults within each fault array, and between the Aigion and S-dipping arrays themselves. This suggests that not only are the segments of the main faults linked at depth, but that the faults themselves are the surface expression of splays propagating upwards from a single structure at depth.

- The high-resolution seismic reflection profiles and multibeam bathymetry indicate no resolvable lateral propagation of the two main faults, and a reduction in the number of minor faults, over the ~11.5 kyr period of observation. Three hypotheses are proposed to explain this: 1) the combined effect of slowing sea-level rise and progradation across the shelf has caused burial of the still active minor faults; 2) lateral propagation has been below the survey resolution of 3 mm $yr^{-1}$; 3) there has been no lateral progradation during this time period.

- There were significant increases in displacement rates, and evidence of rupture through previously inhibited segment boundaries, in the 1 kyr period between ~4.3 and 3.5 ka. Spatially averaged displacement on the Aigion Fault increased almost two-fold during this time from 0.5 to 0.9 $\pm 0.1$ mm $yr^{-1}$, whilst the S-dipping fault saw > six-fold increase from 0.2 to 1.4 $\pm 0.2$ mm $yr^{-1}$over the same period. After 3.5 ka, rates were maintained on the Aigion Fault, but dropped back to previous levels on the S-dipping fault. Total displacement rates across the Aigion Shelf remained relatively constant both during and after this 1 kyr period of enhanced activity, suggesting that the displacement rate of the system did not increase, but was beginning to localise onto the main offshore Aigion Fault.

- Analysis of the displacement profiles from the longest period (~11.5 kyr) indicates that the S-dipping fault is behaving as an isolated fault structure, with a bell shaped displacement profile. The offshore Aigion Fault however, has displacement increasing westwards, suggesting that it continues onshore. The gradual decrease of displacement eastwards along this offshore fault system supports the hypothesis that it represents the eastern tip of the Aigion Fault system.

# Chapter 7

# Surface and Near-Surface Fault Related Deformation Features

This chapter will discuss the pockmarks and mound-like deformation features that are observed occurring across the Aigion Shelf, often in close proximity to the normal faults discussed in Chapters 4 – 6. It will also address the mass wasting occurring at the shelf edge, and investigate whether there is any relationship between this and the fault deformation occurring across the shelf.

## 7.1 POCKMARKS

There are numerous surface depressions, believed to be pockmarks, imaged in both the MCS reflection profiles and the multibeam bathymetry data. Some form linear strings up to 750 m long (Figure 7.1), and are located directly above, or within ~100 m of both N and S-dipping sub-surface normal faults. Others form clusters covering areas of up to 6 $km^2$ (Figure 7.1). The clustered pockmarks appear to be predominantly unfilled, ranging in depth from c.1.5 to 5 m and in diameter from c.15 to 60 m. They have no obvious sub-surface faults beneath them, and their proximity to the Aigion Fault ranges in distance from <10 m to ~650 m south of the fault trace. Both the diameter and depth of the depressions in this cluster increase with distance away from the Aigion Fault trace. This coincides with a gradual downward sloping of the trangressive (H4) horizon to the south (Figure 7.2).

Transparency in the upper sediments, combined with migration artefacts due to the steep sided nature of the pockmarks, make it difficult to fully analyse the extent of sub-surface deformation beneath them. However, it would appear that the sub-surface disturbance beneath the largest pockmark penetrates 5-10 m below the seabed. Preservation of pockmarks in the sub-surface following burial appears to be limited.

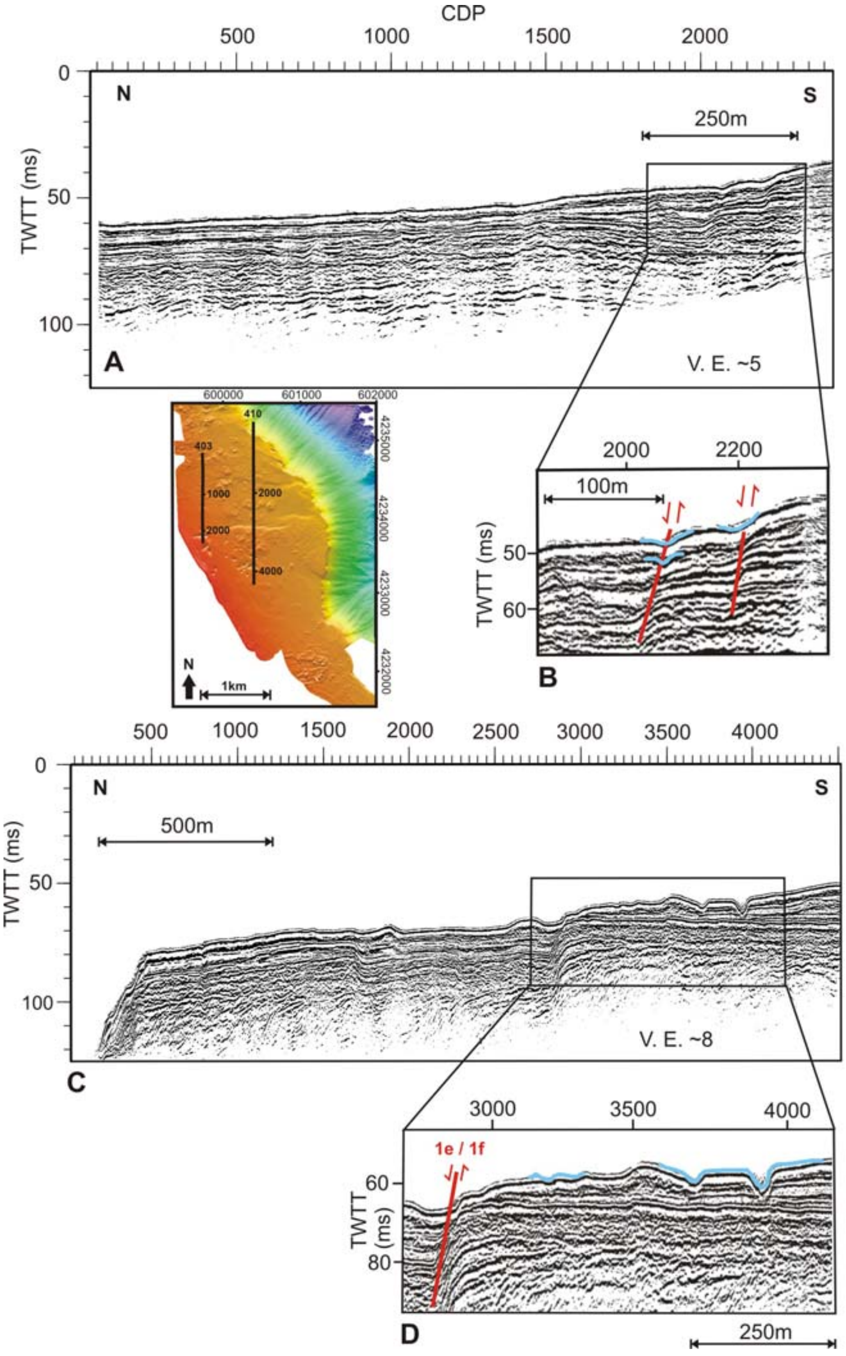

**Figure 7.1**: Boomer MCS reflection profile of Lines 403 and 410 (Plate 1B). A) Uninterpreted profile of line 403. B) Examples of two pockmarks (blue) lying above normal faults (red). This line crosses the edge of the two pockmarks, as shown in the multibeam image inset, and so does not reflect their true depth or diameter. Unfortunately no MCS reflection profile crossed directly over one of the linear pockmarks. C) Uninterpreted profile of line 410. D) Enlargement showing examples from the pockmark cluster located in the footwall of the Aigion Fault. Fault numbers refer to numbering scheme shown in Plate 1C. Line location is shown on the multibeam inset. Enlargements of both profiles are shown in Plate 2.

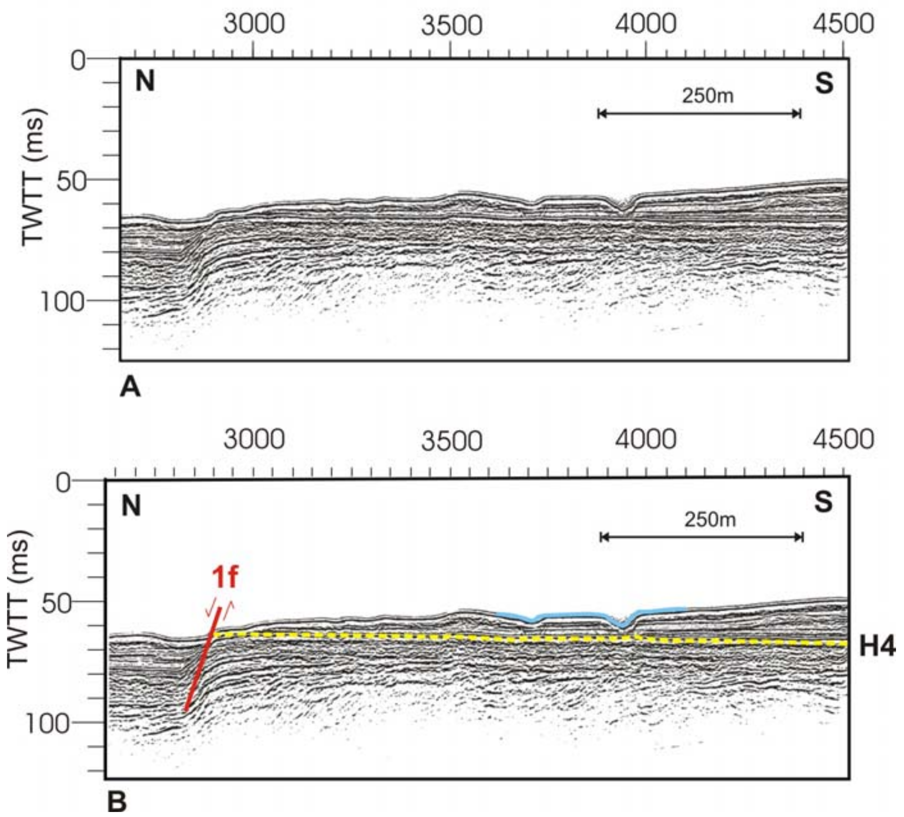

**Figure 7.2:** Section of Boomer MCS reflection line 410 showing the gradual sloping of the transgressive horizon H4 towards the south. In this profile, there is a deepening of H4 of ~6 m occuring over ~750 m, from CDP3000 to 4500.
The pockmarks shown in Figure 7.1C/D are again highlighted in blue in this figure. Figure 7.1 and Plate 2 show the MCS reflection profile in its entirety, and the location of the line on the multibeam dataset.

## 7.2 MOUNDS

The MCS reflection profiles and multibeam data image a number of mound-like features. Seafloor examples have an average height above the seabed of 4 m, and diameter of 150 m (Figure 7.3). Some of the sub-surface mounds are an equivalent size, however the majority appear to be less than half that size (Figure 7.4). Many of the sub-surface mounds have younger reflectors onlapping onto them, indicating progressive burial over time (Figure 7.4). All the mounds show sediment disturbance beneath them (Figure 7.3C), with linear horizontal reflectors becoming broken and warped. Disturbance is predominantly limited to the youngest sediments above H4 (<11.5 ± 1 ka), however, some of the larger mounds within the graben show pronounced upward warping of H4, with possible effects reaching down to H5 (~28 m below the seafloor).

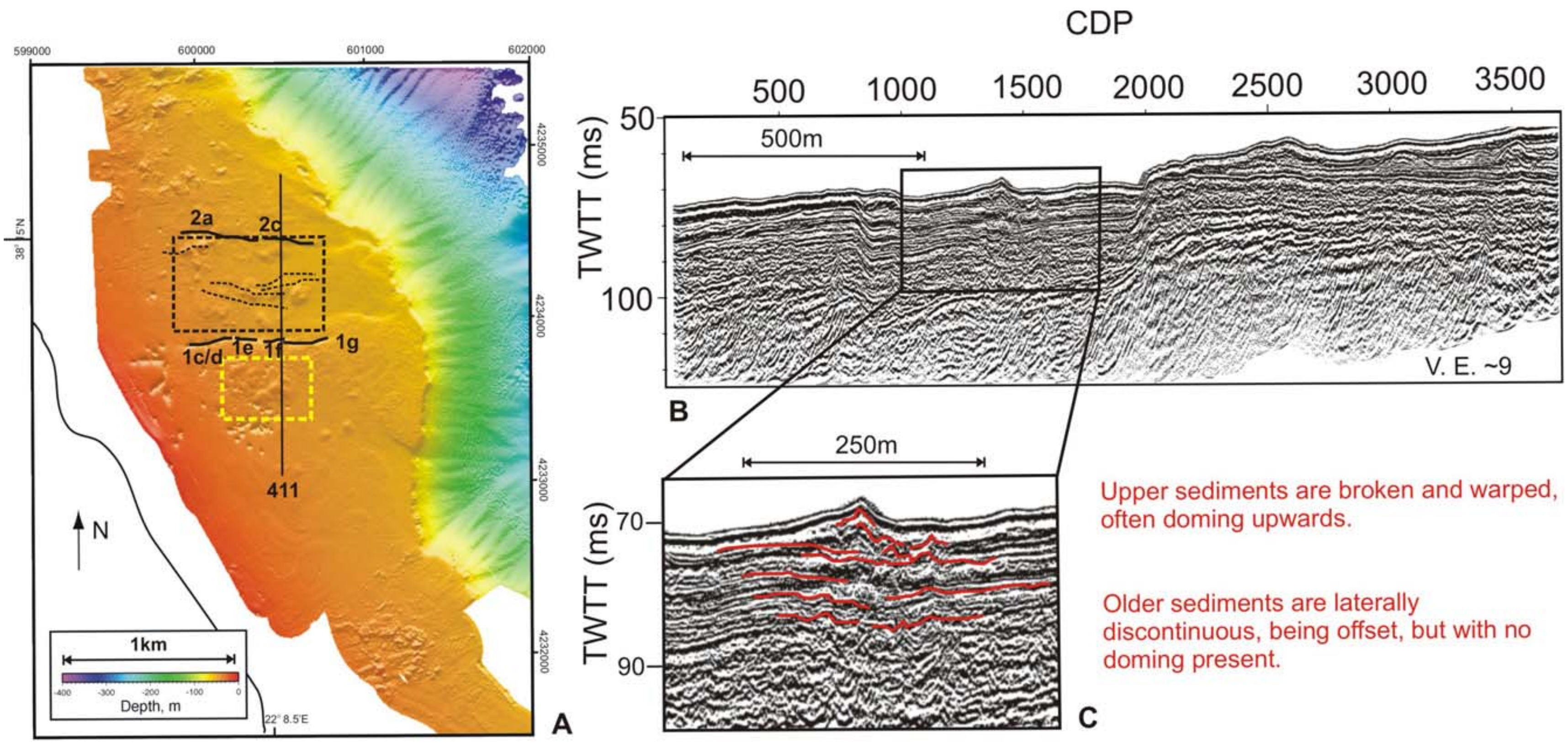

**igure 7.3:** Surface mound features. **A**) Multibeam bathmetry showing the seafloor mounds. The black rectangle highlights the mounds located within the graben, that are underlain by sub-surface faults indicated. The yellow rectangle highlights the mounds located on the footwall of the Aigion Fault, located within a cluster of pockmarks, but with no sub-surface faults underlying them. **B**) uninterpreted Boomer MCS reflection profile line 411. The line location is indicated on the multibeam plot. **C**) enlargement showing the distortion and warping of sediments typically observed directly beneath all the mounds. **F**

The mounds in the graben appear both symmetrical, with a slight depression in the peak, and asymmetrical, appearing to tilt towards the south (Figure 7.5A & B). This variation is proposed to be a result of whether the MCS reflection survey lines crossed the mound centrally or to one side, as they have a similar morphology in plan view (Figure 7.5C). They appear to be predominantly underlain by faulting (Figure 7.3A). However, there appears to be no correlation between the size of a mound and the size of the fault in closest proximity to it.

The mounds imaged in the footwall of the Aigion Fault do not have a direct relationship to specific faults (Figure 7.3A). They are, however, located within the cluster of pockmarks previously described. This suggests that there is a common cause behind the formation of both these features.

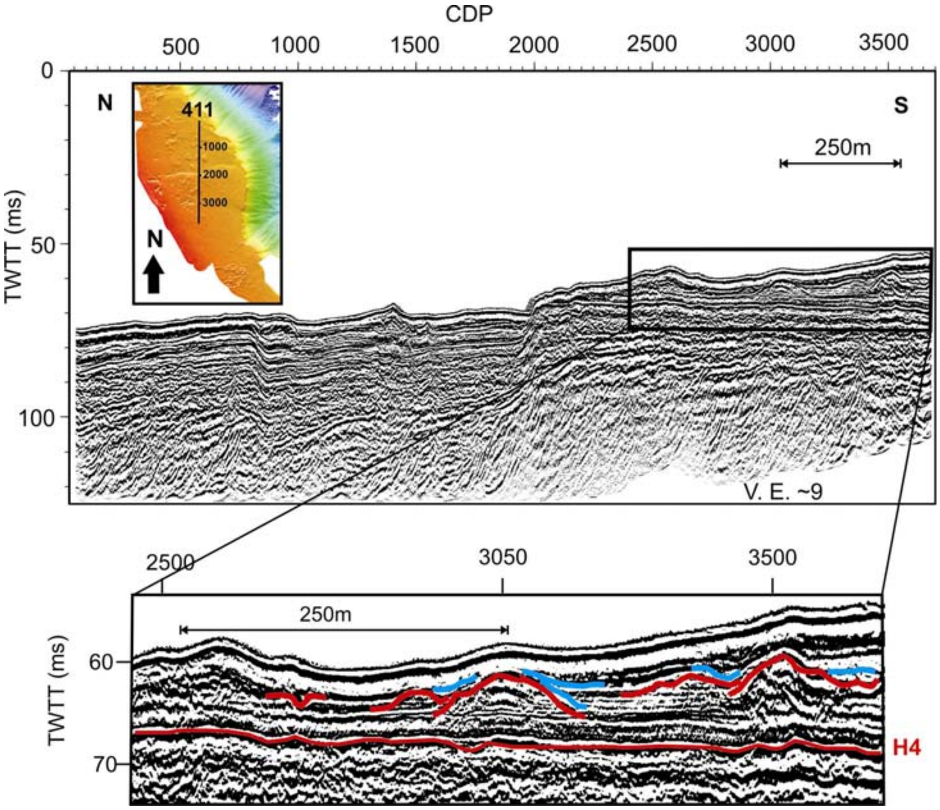

**Figure 7.4:** Boomer MCS reflection profile line 411. Multibeam inset shows the location of the uninterpreted seismic profile. The enlargement shows examples of the sub-surface mounds located within unit U1, above the transgressive horizon H4. Younger sediments are seen to initially onlap onto these buried mounds, with later sediment draping over the whole mound causing a doming of the present-day seafloor topography.

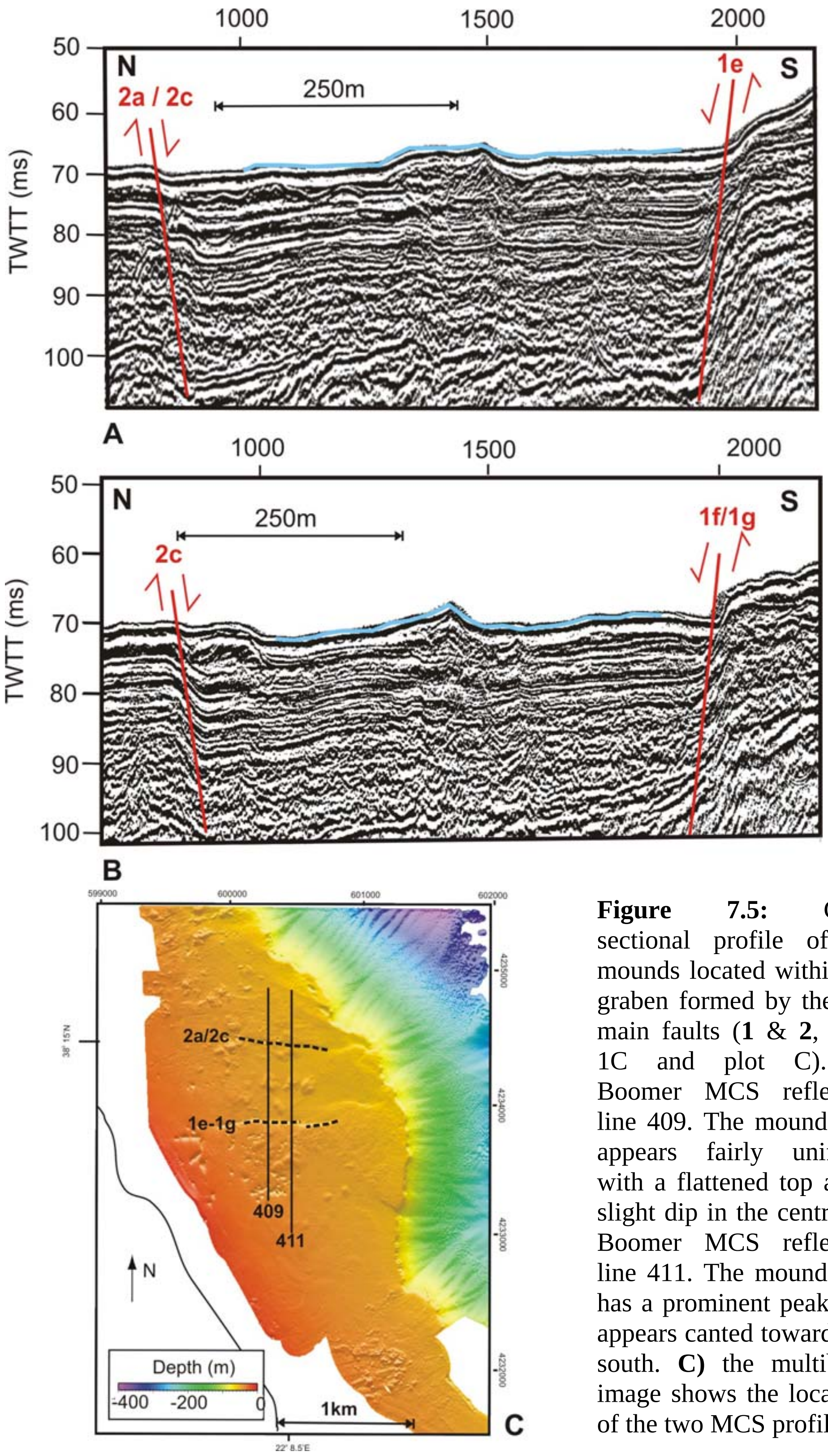

**Figure 7.5:** Cross sectional profile of the mounds located within the graben formed by the two main faults (**1** & **2**, Plate 1C and plot C). **A)** Boomer MCS reflection line 409. The mound here appears fairly uniform, with a flattened top and a slight dip in the centre. **B)** Boomer MCS reflection line 411. The mound here has a prominent peak, and appears canted towards the south. **C)** the multibeam image shows the locations of the two MCS profiles.

## 7.3 MASS WASTING

Data collected across the shelf edge show it to be undergoing significant mass wasting (Figure 7.6). In the MCS reflection profiles, it appears that the slope of the shelf is steepest at the top (Figure 7.6A & B). The highstand unit (<11.5 ± 1 ka) appears to abruptly terminate against slump scars (Figure 7.6B & C). Further down-slope, the slope angle decreases, more closely mirroring the angle of the internal clinoforms forming U3 ($30^o$). This may indicate that the clinoforms laid down at the angle of repose for coarse grained deltaics are acting as planes of weakness along which failure can occur. Defined chutes, ranging from c. 100 to 400m wide, leading away from the area of faulting and mass wasting at the edge of the Aigion Shelf (Figure 7.7) suggest that periodic mass wasting events may be contributing to the shaping of the shelf edge.

North of the graben, visible on the regional multibeam bathymetry data, lies the N-dipping Cape Gyftissa Fault (Figure 7.8). The bathymetry indicates that the hanging-wall of this fault is undergoing slope failure, and that the fault plane itself is dictating the position of the northern edge of the Aigion Shelf. This supports the hypothesis that the multiple faults located in close proximity to the shelf edge within the survey area may be having a major impact on the mass wasting of the shelf edge itself.

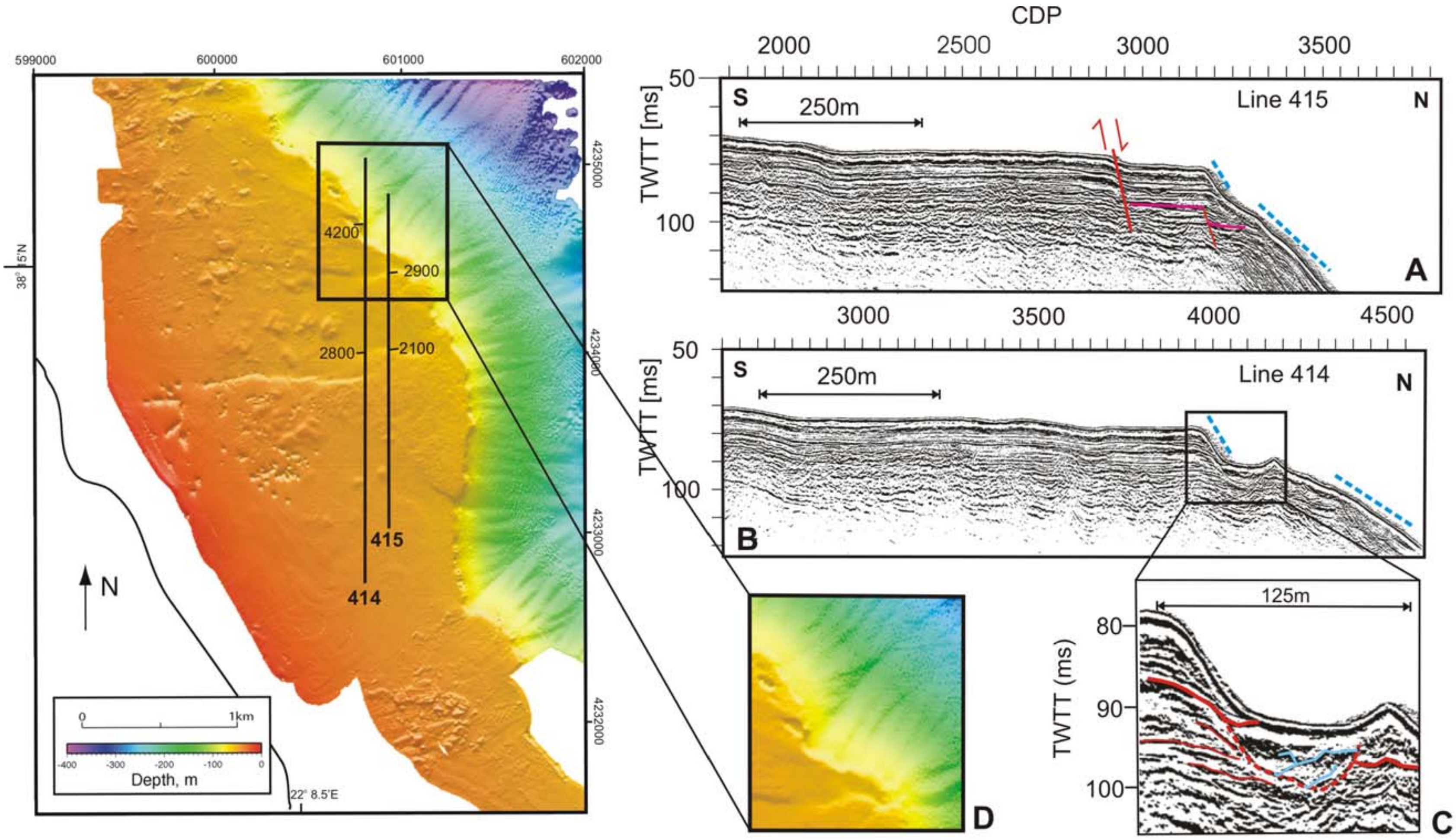

**Figure 7.6:** Boomer MCS reflection profiles lines 414 and 415, and swath bathymetry showing the mass-wasting of the shelf edge. The MCS profile locations are shown on the multibeam plot. **A)** Boomer line 415. Evidence of surface and sub-surface faulting close to the shelf edge, that may be weakening the shelf edge, contributing to the failure of the shelf. Fault number corresponds to Plate 1C. **B)** Boomer line 414. The change in the angle of the slope is indicated by the blue lines. The upper sediments terminate against a steep slope angle, whereas lower sediments terminate against a shallower slope angle, which closely matches that of the internal clinoform structure of U3. **C)** enlargement that shows a relic scarp. The scoop-like shape (dashed red line) of the failure cuts lower reflectors. **D)** uninterpreted enlargement of the multibeam image showing the shelf edge.

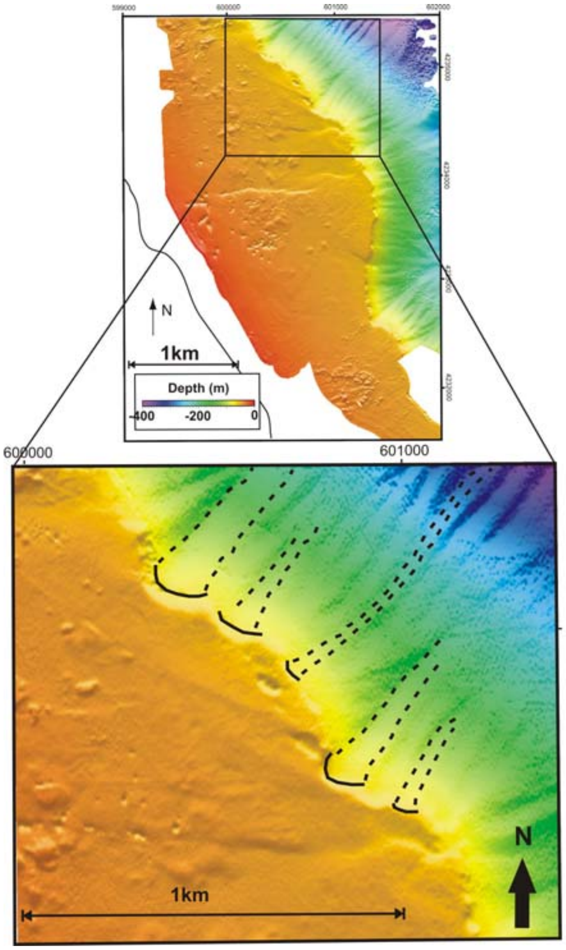

**Figure 7.7:** Multibeam bathymetry image showing the mass wasting of the Aigion Shelf. The enlargement shows clear concave shaped scars, reminiscent of landslide headwall features. From many of these scars, defined chutes run downslope towards the main canyons that feed the axial channel that runs down the centre of the Gulf (Chapter 3).

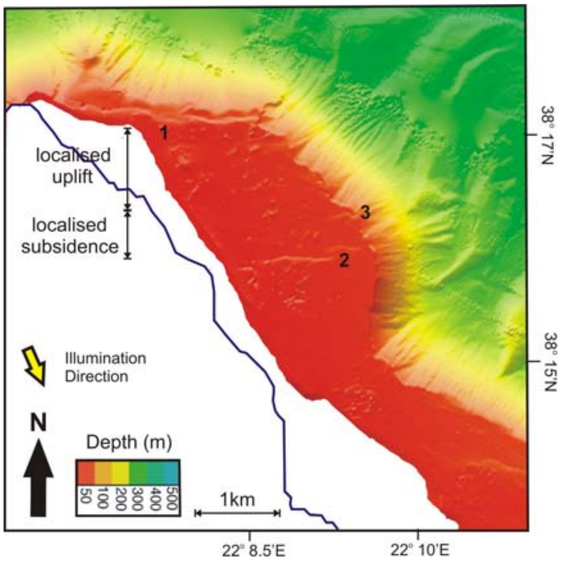

**Figure 7.8:** Multibeam bathymetry image of the Aigion Shelf and the Cape Gyftissa Fault that bounds it to the north (number 1). The offshore extension of the Aigion Fault is imaged (number 2), and the north dipping segment of the other graben bounding fault (number 3). It can be seen that the northern shelf edge is controlled by the N-dipping Cape Gyftissa Fault. Between the N-dipping Cape Gyftissa Fault and the predominantly S-dipping graben bounding fault, there will be localised uplift, whilst between the S-dipping fault and the N-dipping Aigion Fault, there will be localised subsidence.

## 7.4 DISCUSSION

### 7.4.1 Pockmarks

It is proposed that the pockmarks imaged on the Aigion Shelf form as gas is expelled or groundwater migrates up through overlying sediments. Removal of material due to fluids migrating along seepage pathways can occur as a result of changes in the balance between pore-water pressure and shear strength of the sediments. This balance is represented by equation 7.1 (Hovland and Judd, 1988):

$$\mathbf{Su = c' + (\sigma'n) \tan \phi} \qquad \mathbf{7.1}$$

Where **Su** = shear strength; **c'** = cohesion with respect to effective stress; **σ'n** = effective normal stress (balance between total normal stress (σn) and pore-fluid pressure (μ) = σn-μ); ϕ = angle of internal friction.

Harrington (1985) proposed a mechanism for the formation of pockmarks by groundwater expulsion that relied on an external trigger such as an earthquake. This process will continue as long as there is pore water to be expelled. Complete drainage of an area will halt pockmark formation until re-charge of the sediments occurs. Papatheodorou et al. (1993), Soter (1999) and Hasiotis et al. (2002a) have all documented examples of enhanced gas expulsion occurring in the Gulf of Corinth and the Gulf Of Patras coincident with earthquake activity, whilst Christodoulou et al. (2003) document continuous freshwater groundwater seepage forming pockmarks in Elaiona Bay, SE of the Aigion Shelf. Pressure variations, either from external triggering or from changes in the pressure gradients due to localised fluid movement such as onshore hydrostatic head, may therefore be causing release of over-pressured interstitial fluids / gas (Hovland and Judd, 1988), resulting in the formation of pockmarks across the Aigion Shelf.

Dimitrov and Woodside (2003) state that there is a primary relationship between normal faults and pockmark features. Structural features such as microfissures, fractures and faults provide migration pathways for fluids and gas (Dimitrov and Woodside, 2003). Bonatti (1987) reported the results of a laboratory based experiment indicating that migration of fluids along a fault plane resulted in the formation of strings of regularly spaced pockmarks, similar in appearance to those seen de-lineating the location of sub-surface faults on the Aigion Shelf.

Figure 7.9 illustrates how this relationship might translate to the Aigion shelf, where a number of faults offset the transgressive surface (H4). The variability in size between the pockmarks within the cluster on the Aigion Fault footwall can be explained by back-tilting of the transgressive horizon towards the south and thinning of the sediments towards the fault. Reservoirs form as the sediments become less consolidated (Dimitrov and Woodside, 2003). Fluids migrating through the upper unconsolidated sediments will form progressively smaller pockmarks with thinning of the source sediments and increasing distance from any shallow reservoirs, as seismic activity enhances fluidisation. The mounds however appear to be sourced from deeper, below horizon H4, with fluidised sediments using faults as migratory pathways. Liquefaction of the beach topsets from below H4 results in building of mounds, as opposed to shallow expulsion of fluid / gases causing collapse of overlying sediments and resulting pockmarks.

Similar fault and pockmark relationships were imaged by Yin et al. (2003) in the East China Sea. In this continental shelf area, sea-level fall during the Last Glacial Maximum (LGM) caused exposure of areas of the shelf. A high sedimentation rate combined with fluvial deposition during the LGM resulted in deposition of sediments with a high pore water and air content. These gas / fluids were trapped beneath the Maximum Flooding Surface (MFS) laid down during the transgression. Beneath the MFS, the seismic unit showed a chaotic character, which the authors believe was due to trapped fluids / gas. A similar chaotic unit, located beneath the transgressive surface (H4), is observed on the Aigion Shelf (U2). The fault planes on the Aigion shelf may therefore be providing a pathway for any gas / fluids past the transgessive barrier to the surface.

This hypothesis is supported by the findings of Hasiotis et al. (1996), who stated that the gas being expelled at locations in the Gulf of Corinth would often migrate up an inclined horizon that was acting as an impermeable barrier, until it reached a fault plane that would provide a pathway upwards through the barrier. In addition, Lemeille et al. (2004) found trapped gas in a sand layer within the AIG10 borehole. It was contained by

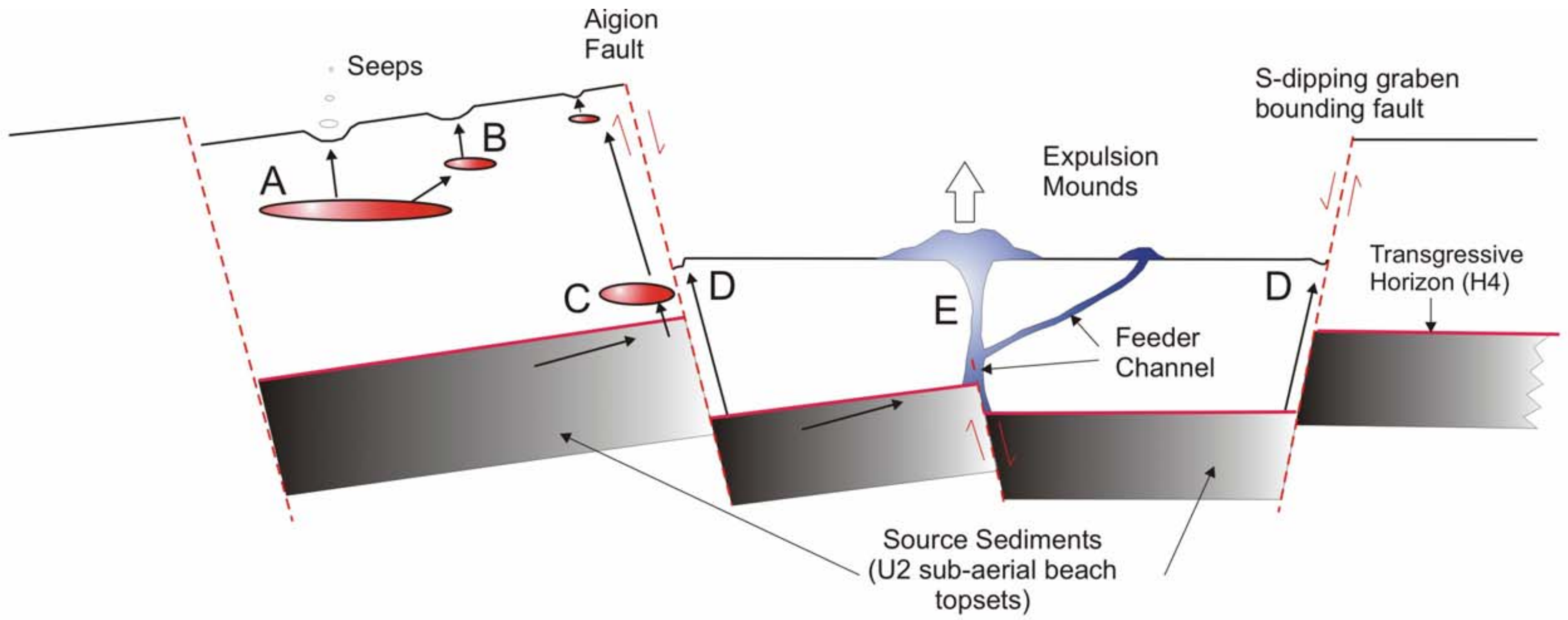

**Figure 7.9:** Cartoon illustrating the relationship between the normal faults and the pockmarks and mound features. A = Larger reservoirs form in nearsurface unconsolidated sedimentsr. These reservoirs in turn feed smaller ones (B). Seepage from these reservoirs can form pockmarks in the overlying seafloor, despite not being located directly above a fault. Fluids and gas also migrate up the inclined transgressive barrier (H4), forming reservoirs when they finally breach it at a fault plane (C), or surface pockmarks directly over the fault trace (D). Where the fault terminates in the sub-surface, the migrating fluids can form a preferential migratory pathway through the overlying sediments over time, creating feeder channels (E). Material can then be expelled directly up these pathways, creating seafloor mounds.

impermeable clay layers on either side of it, and was using the Aigion Fault as a migratory pathway through this sedimentary barrier. This may explain the close proximity of the majority of pockmarks to normal faults planes, if a similar stratigraphy containing impermeable clay layers as that found in the AIG10 borehole is projected onto the Aigion Shelf, causing trapped fluids to use the faulting across the Shelf as migratory pathways.

### 7.4.2 Mounds

Liquefaction, and resultant sand volcano formation in the sub-aerial environment, is a well documented feature in this region (e.g Schmidt, 1875 following the 1861 Eliki earthquake, and Lekkas et al., 1996 following the 1995 Aigion earthquake). McNeill et al (2005b) document sand dykes in the sub-aerial environment, which may indicate the position of feeder pipes for now eroded sand volcanoes, however, no sub-aerial examples of actual sand volcanoes have been preserved. The features seen in the MCS reflection and multibeam datasets may therefore represent modern submarine examples of soft sediment deformation features that have not yet been subjected to significant erosion following uplift into the sub-aerial environment.

Similar associations between submarine mounds, pockmarks and faulting have been documented at various locations in the Eastern Mediterranean (Zitter et al., 2005), whilst Dimitrov and Woodside (2003) describe mud volcanoes located in close proximity to normal faults at Eratosthenes Seamount and Anaxiamander Mountains in the Eastern Mediterranean.

A change in reservoir pressure, exceeding that of the overburden, causes sediments to liquefy and be expelled, resulting not only in the building of mounds, but also the reduction of sediment volume at depth, leading to collapse at seepage sites, causing depressions to form (Yin et al., 2003). This change in pressure can occur due to re-charge of a reservoir from beneath, as with the constant groundwater percolation suggested by Christodolou et al. (2003), or as a result of cyclical loading due to earthquakes, causing periodic and enhanced expulsion (Hovland and Judd, 1988). Liquefaction could therefore funnel sediments up to the near surface and surface via feeder pipes which form above sub-surface faults (Figure 7.9). Once such a pathway is established it will become the preferential route for further expulsion of material (Dimitrov and Woodside, 2003), so enabling large structures to form above the minor sub-surface faults on the Aigion Shelf.

The shore-face topsets from the lowstand unit (U3 into U2) are a possible source for the sediments liquefying and forming these mounds in the offshore environment. The MCS reflection profiles show that in the majority of cases, these shallow dipping deposits are absent where seafloor mounds are present, and still in-situ where there is no mound above.

It is believed that the disturbance and warping of reflectors beneath these mounds may be caused by the upward mobilisation of these sandy shore-face deposits. The presence of un-deformed younger sediments onlapping onto the mounds, progressively burying them, suggests that there are periods of quiescence in their formation. Hovland and Judd (1988) observed that periods of inactivity often follow shallow reservoir depletion, again suggesting a link between episodic earthquake activity, liquefaction and the formation of these features

### 7.4.3 Link Between Sedimentary Features and the Earthquake Cycle

Initial conclusions drawn from the multibeam data suggested that the 1995 earthquake activated many of the pockmarks imaged in the footwall of the Aigion Fault. Records document the sea bubbling prior to the earthquake (Soter, 1999), suggesting that fluids or gases were being expelled. However, comparison between the multibeam data collected in 2003 with sidescan data collected in 1988 (Soter, 1999), prior to this earthquake, shows no major morphological change in the pockmark cluster (Figure 7.10). It is therefore suggested that whatever caused these pockmarks to form initially occurred prior to the 1995 earthquake, and that the earthquake itself resulted in enhancing expulsion of fluids through pathways that were already established.

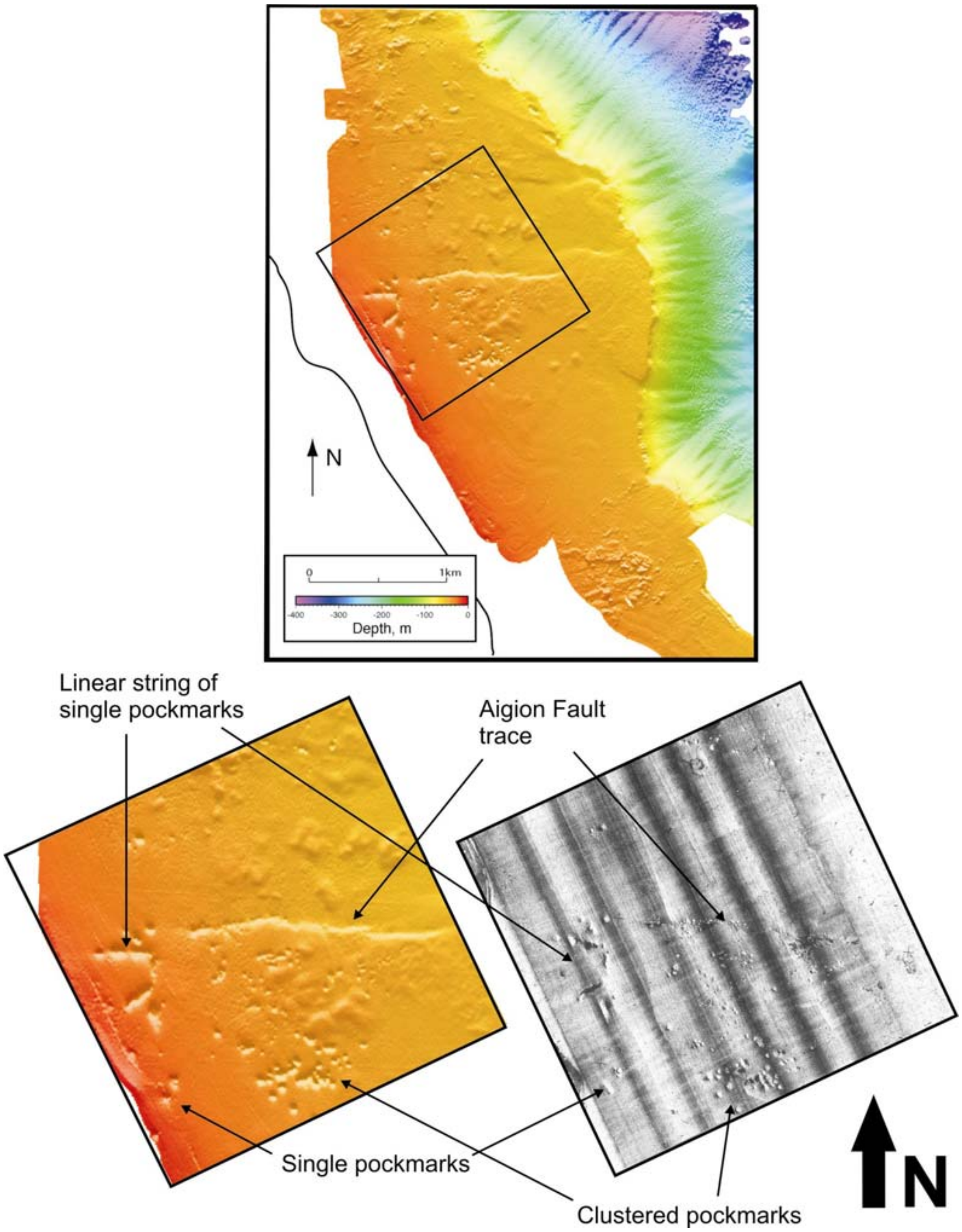

**Figure 7.10:** Comparison between the multibeam bathymetry survey data collected in 2003, after the 1995 Aigion earthquake, and sidescan sonar data collected by Soter and Katsonopoulou (1995), pre the 1995 Aigion earthquake. Both images clearly show the linear string of pockmarks, the cluster of pockmarks in the Aigion Fault footwall, and the seafloor expression of the Aigion Fault. The pockmarks are clearly imaged in both datasets. However the mounds are not clear in the sidescan, indicating that they might have formed post 1988. The major features appear to have been established before the 1995 earthquake, and although there are subtle morphological changes to the pockmark fields, there is no evidence of new fields starting.

The similarity between the dip of the clinoforms in unit U3 (lowstand unit), and the gradient of the offshore slope down to the basin floor, suggests that the clinoforms are acting as glide planes upon which failure occurs. Papatheodorou & Ferentinos (1997) andHasiotis et al (2002b) have documented examples of sediment failure at various locations in the Gulf of Corinth. In three of those, sediment failure appeared to be directly linked to liquefaction on a particular horizon as a result of increased pore water pressures resulting from seismic activity, forming a glide plane. This suggests that mass wasting of the Aigion Shelf may be accelerated by the earthquake cycle.

## 7.5 CONCLUSIONS

- There is significant surface and sub-surface soft sediment deformation across the Aigion Shelf. Pockmarks are seen to form linear strings or clusters, whilst the mounds appear to be orientated in an E-W trend. Both features appear to be intrinsically linked to the normal faulting that is occurring across the Aigion Shelf (Figure 7.10).

- The similarity between the data imaged in this survey, and examples from other locations, supports the hypothesis that these features are closely linked to the fault planes that offset the impermeable trangressive barrier H4, creating migratory pathways for mobilised sediments, fluids or gas. There is also a strong suggestion that earthquakes act as triggers for periods of enhanced gas and fluid expulsion.

- The similarity between the sidescan image from pre 1995, before the Aigion earthquake, and the multibeam image obtained in this survey after the 1995 earthquake (Figure 7.11) suggest that the same pockmarks are being used for any gas or fluid expulsions. This supports Hasiotis et al's (1996) and Dimitrov and Woodside's (2003) observation that once a pathway is set up, it will become the preferential route for further migration, both following earthquake activity, and during periods of seismic quiescence.

- The buried mound features suggest that this process has been ongoing for at least 11.5 kyr. Buried examples appear to be predominantly smaller than the more modern day seafloor features. This suggests that either preservation in the submarine environment is also limited, or that whatever is causing these features to form has increased in amplitude during the most recent highstand period, creating larger examples that are visible on the present day seafloor.

- Mass wasting of the shelf edge appears to be intrinsically linked to the internal structure and deposition style of the deepest imaged unit (U3), combined with the effects of normal faulting causing additional structural weakness.

# Chapter 8

# Discussion

Following analysis of high-resolution multichannel seismic reflection Boomer profiles and multibeam bathymetry datasets collected across the offshore Aigion Fault system, the results were integrated with previously published datasets for the onshore component of the Aigion Fault system. The findings revealed that the Aigion Fault system is a complex, segmented normal fault system. This chapter will address the geometry and evolution of this fault system, looking at structural links between the onshore and offshore environments, causes of the spatial and temporal displacement variability and interaction between different components of the Aigion Fault system, and its relationship with other fault systems in the western Gulf of Corinth.

## 8.1 GEOMETRY OF THE AIGION FAULT SYSTEM

The Aigion Fault system is composed of a number of different onshore and offshore faults or fault segments. Figure 8.1 shows the locations of the fault and fault segments that will be discussed in this chapter, along with the nomenclature that will be adopted during discussion of the entire fault system.

Interpretation of the data in this thesis has shown that although the offshore fault zone is proposed to have an onshore component, it is not believed that the offshore fault is linked directly to the main Aigion Fault (AF1 and 2, Figure 8.1). The reasoning behind this hypothesis will be discussed in more detail later in this chapter. However, in order to differentiate between the two faults, the offshore fault will be identified as the Aigion Shelf Fault in this discussion (Figure 8.1).

All of the faults and segments comprising the Aigion Fault system (onshore Aigion Fault and Aigion Shelf Fault) have an E-W orientation. The Aigion Fault has a measured dip of ~55$^{o}$ (Rettenmaier et al. 2004). Whilst the limited penetration of the MCS reflection profiles prevents seeing fault dips to depth, the estimated dip of 50-60$^{o}$ of the Aigion Shelf Fault in the youngest sediments appears to be consistent with Rettenmaier et al. (2004) and with other Gulf of Corinth faults.

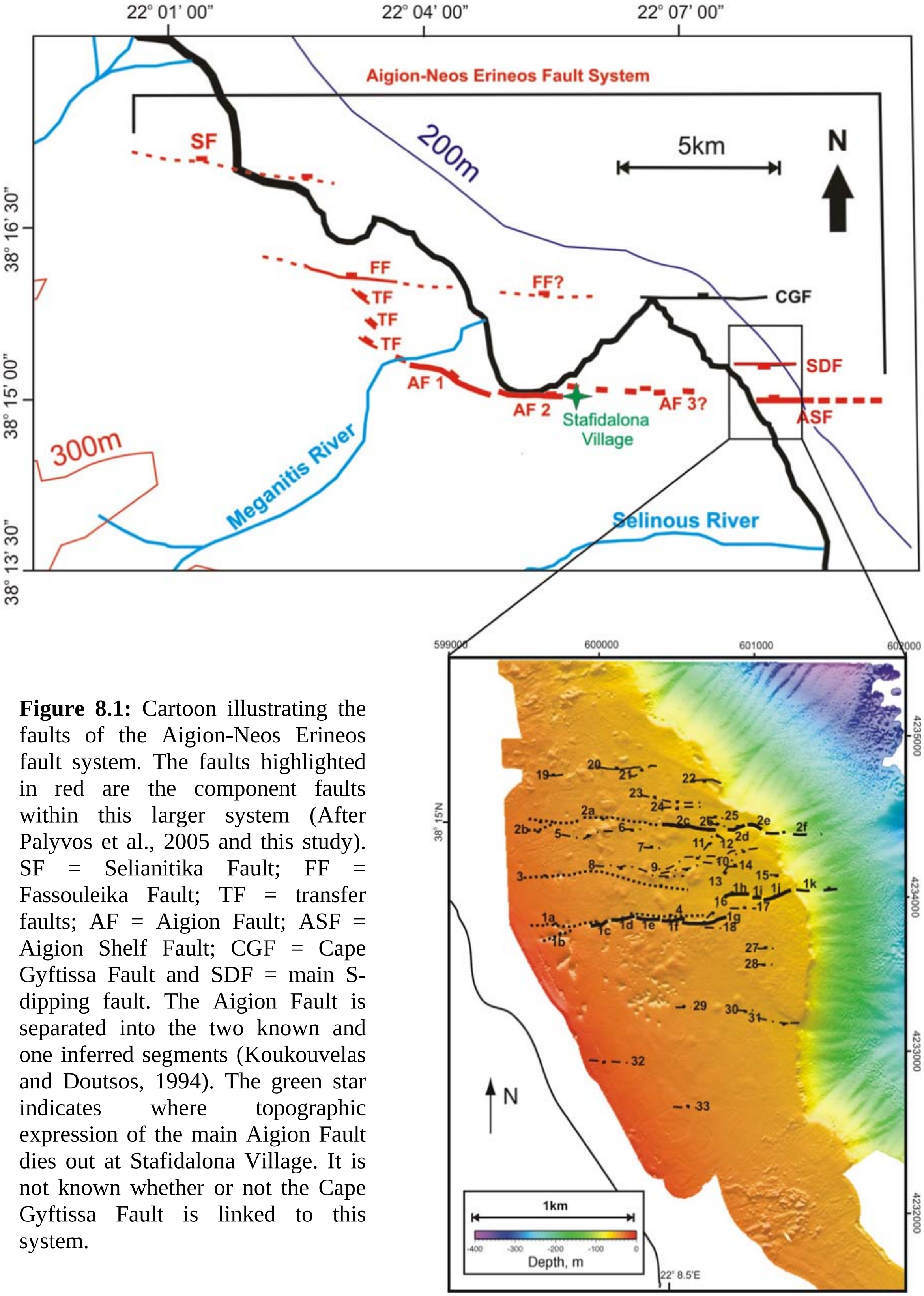

**Figure 8.1:** Cartoon illustrating the faults of the Aigion-Neos Erineos fault system. The faults highlighted in red are the component faults within this larger system (After Palyvos et al., 2005 and this study). SF = Selianitika Fault; FF = Fassouleika Fault; TF = transfer faults; AF = Aigion Fault; ASF = Aigion Shelf Fault; CGF = Cape Gyftissa Fault and SDF = main S-dipping fault. The Aigion Fault is separated into the two known and one inferred segments (Koukouvelas and Doutsos, 1994). The green star indicates where topographic expression of the main Aigion Fault dies out at Stafidalona Village. It is not known whether or not the Cape Gyftissa Fault is linked to this system.

The Aigion Shelf Fault (ASF, Figure 8.1) has a complex surface geometry composed of numerous distinct segments as short as ~100 m. Displacement profiles suggest that many of these segments are linked at depth, forming second order segments of ~1.5 km in length. In total, the Aigion Shelf Fault is >2 km in length. This offshore segmented fault is surrounded by several other faults, including the segmented S-dipping fault (Figure 8.1). These subsidiary faults range in length from ~100 m - >1 km, forming a complex, asymmetrical damage zone, that covers an area ~500 m south and >1 km north of the Aigion Shelf Fault. The evolution of this fault population will be addressed in more detail in section 8.4.

Previously published data describing the Aigion Fault (Koukouvelas and Doutsos, 1994) indicates two known segments with clear topographic signature (AF1-2, Figure 8.1), and a further hypothesised segment defined from surface ruptures (AF3, Figure 8.1), with lengths of 2 – 8 km, that are linked to form a through-going fault of ~12 km length (including the hypothesised segment). Identification of smaller segment lengths onshore is inhibited by lack of sub-surface data, and surface effects such as vegetation.

Recent data presented by Palyvos et al. (2005) suggests that the Aigion Fault forms part of a larger fault system that incorporates two additional faults, the Fassouleika and Selianitika Faults (Figure 8.1). The N-dipping Fassouleika Fault is ~3 km long, located ~1 km north of the western end of the Aigion Fault, overlapping it by ~1 km. Palyvos et al. (2005) suggest that there may be an offshore extension to the Fassouleika Fault located in Aigion Harbour (Figure 8.1), however no such structures are observed from data collected in this study. The ~2 km long N-dipping Selianitika Fault is located ~1 km north of the Fassouleika Fault, also overlapping it for ~1 km. Together, the Aigion, Fassouleika and Selianitika Faults form the larger Aigion-Neos Erineos system (Palyvos et al., 2005). This would bring the total length of the onshore, topographically distinct system to ~12 km, (omitting AF3, Figure 8.1).

The central segment of the Aigion Fault (AF2, Figure 8.1) has a clear topographic signature, with a scarp that increases in height westwards from zero displacement at Stafidalona village (Figure 8.1 and 8.2) to ~150 m in Aigion town, 1 – 2 km west of Stafidalona. Micarelli et al. (2003) suggest that the displacement continues to increase

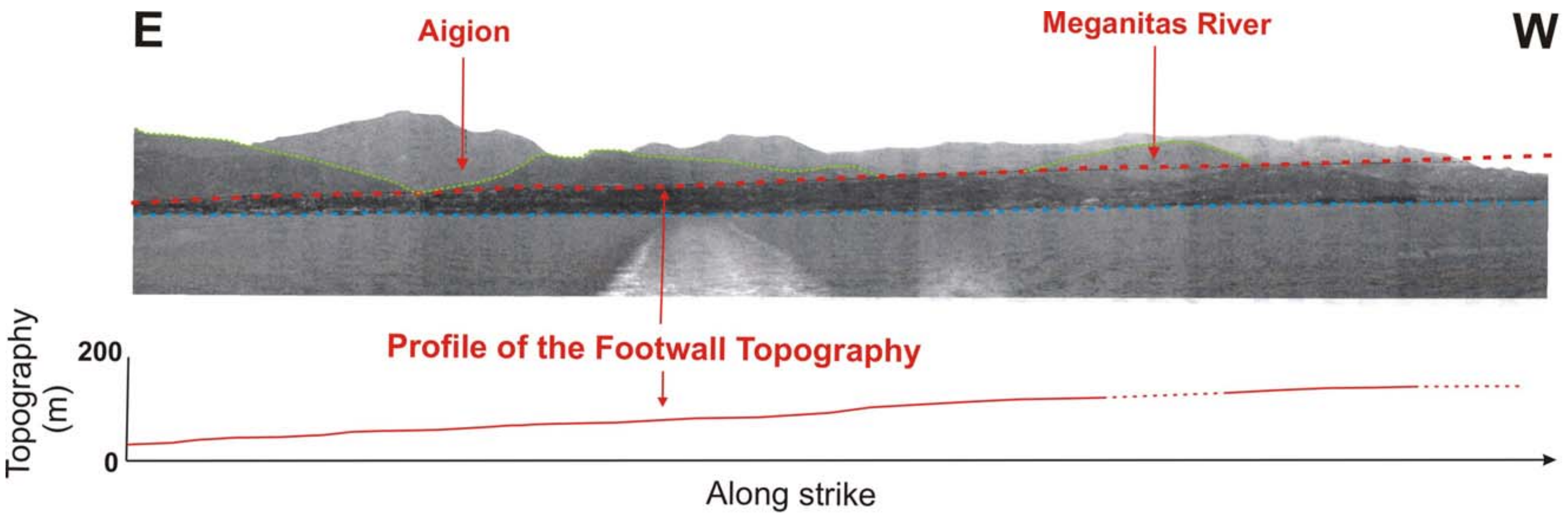

**Figure 8.2:** Photograph of the Aigion Fault viewed from the North, showing the steady E to W trend of increasing displacement. The easternmost tip corresponds to Stafidalona Village, where displacement on the visible fault scarp reaches zero. Photograph from Micarelli et al. (2003).

west of the Meganitis River (Figure 8.2), beyond where Palyvos et al. (2005) place the western tip of the Aigion Fault (AF1, Figure 8.1), transferring faulting to the Fassouleika Fault (FF, Figure 8.1). This supports the idea that the Aigion Fault links up with other faults to the west, forming the Aigion-Neos Erineos system proposed by Palyvos et al. (2005), which is the preferred interpretation of the fault geometry in this region. However, available datasets cannot conclusively confirm that these faults are linked at depth, and so the assumptions that the faults are interacting are based predominantly on morphology, proximity and overlap.

The link between the hypothesised third segment of the Aigion Fault (AF3, Figure 8.1) and the Aigion Shelf Fault (ASF, Figure 8.1) is not clearly defined. Studies by Koukouvelas and Doutsos (1996), Micarelli et al. (2003), De Martini et al. (2004) and Palyvos et al. (2005) show segment 3 of the Aigion Fault starting east of Aigion town, and continuing across the delta, and yet there is no topographic evidence to support this assumption. Identifying the existence of this fault segment has previously been reliant on interpretation of 1:5,000 topographic maps, aerial photographs and field observations.

The displacement profile taken from the longest period of observation (~11.5 kyr) suggests that the offshore Aigion Fault continues onshore to some extent (Figure 8.3A). If the polynomial curve applied to that dataset is projected, then this extension should continue ~ 700 m onshore (Figure 8.3B). The assumed displacement profile would be a typical bell shaped profile predicted by the post-yield model of Cowie and Scholtz (1992).

Evidence along the coastline of the offshore segment coming onshore is very limited due to construction. However some features were observed that are suggestive of small scarps. These were: **1)** offset of a beachside pavement of ~20 cm was observed at 38$^o$ 14’48.6”N / 22$^o$ 08’01.8”E; **2)** a break in the slope of a road, in an otherwise flat area, at 38$^o$ 14’46.1”N / 22$^o$ 07’ 51.1”E; **3)** a break in slope of a road inside a holiday resort, at 38$^o$ 14’ 48.6”N / 22$^o$ 07’ 53.4”E (Figure 8.4). These features are all orientated E-W, slightly north of the Aigion Shelf Fault, with the sense of displacement indicating they were N-dipping.

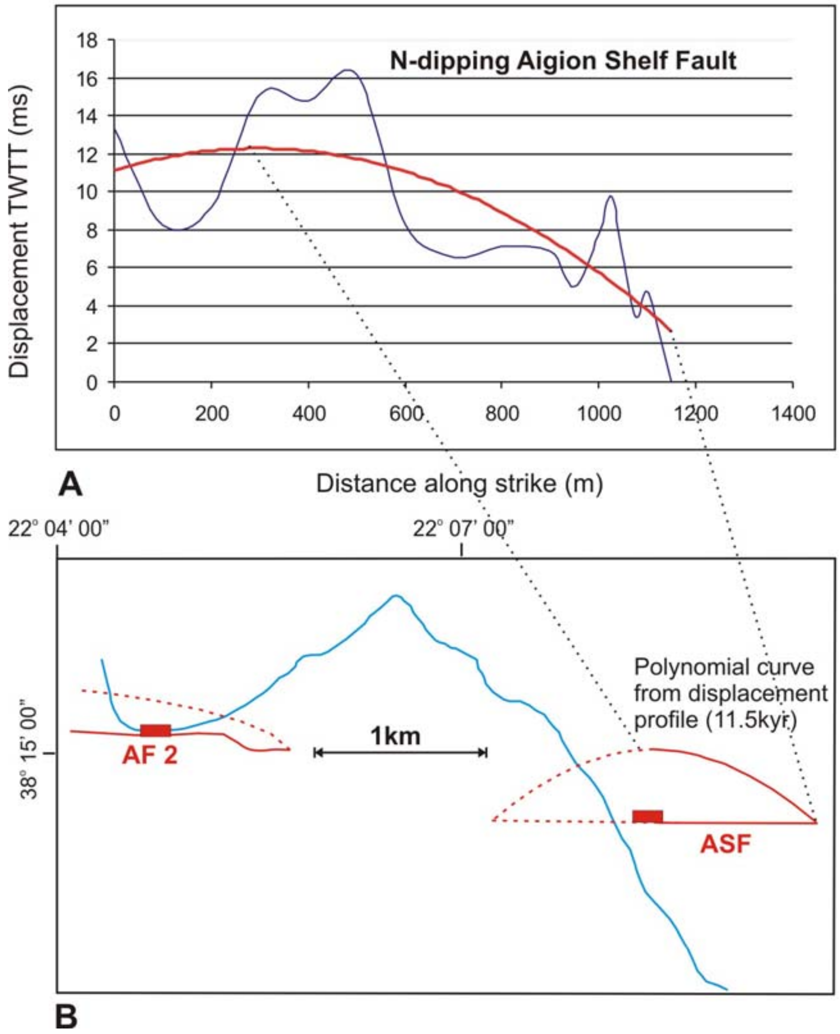

**Figure 8.3: A)** Polynomial curve applied to the displacement profile for the longest period of observation (~11.5kyr), suggests that the Aigion Shelf Fault is part of a larger fault. **B)** Extending the polynomial curve to form a symmetrical profile gives an indication of the extent of this fault to the west.

The presence of small scarp features at the coastline, occurring in locations where offset of man-made structures preserves the evidence of minor faulting, supports the hypothesis of an onshore extension of the Aigion Shelf Fault. Figure 8.4 shows these three features in relation to the Aigion Shelf Fault, and the Aigion Fault. The dashed red line in Figure 8.4 is the proposed extension of the Aigion Shelf Fault, running through the scarp features at the coast. Despite being located ~1 km south of the original position suggested by Koukouvelas (1998) for this "segment" (AF3, Figure 8.1), the position suggested in Figure 8.4 provides a better fit with the actual data.

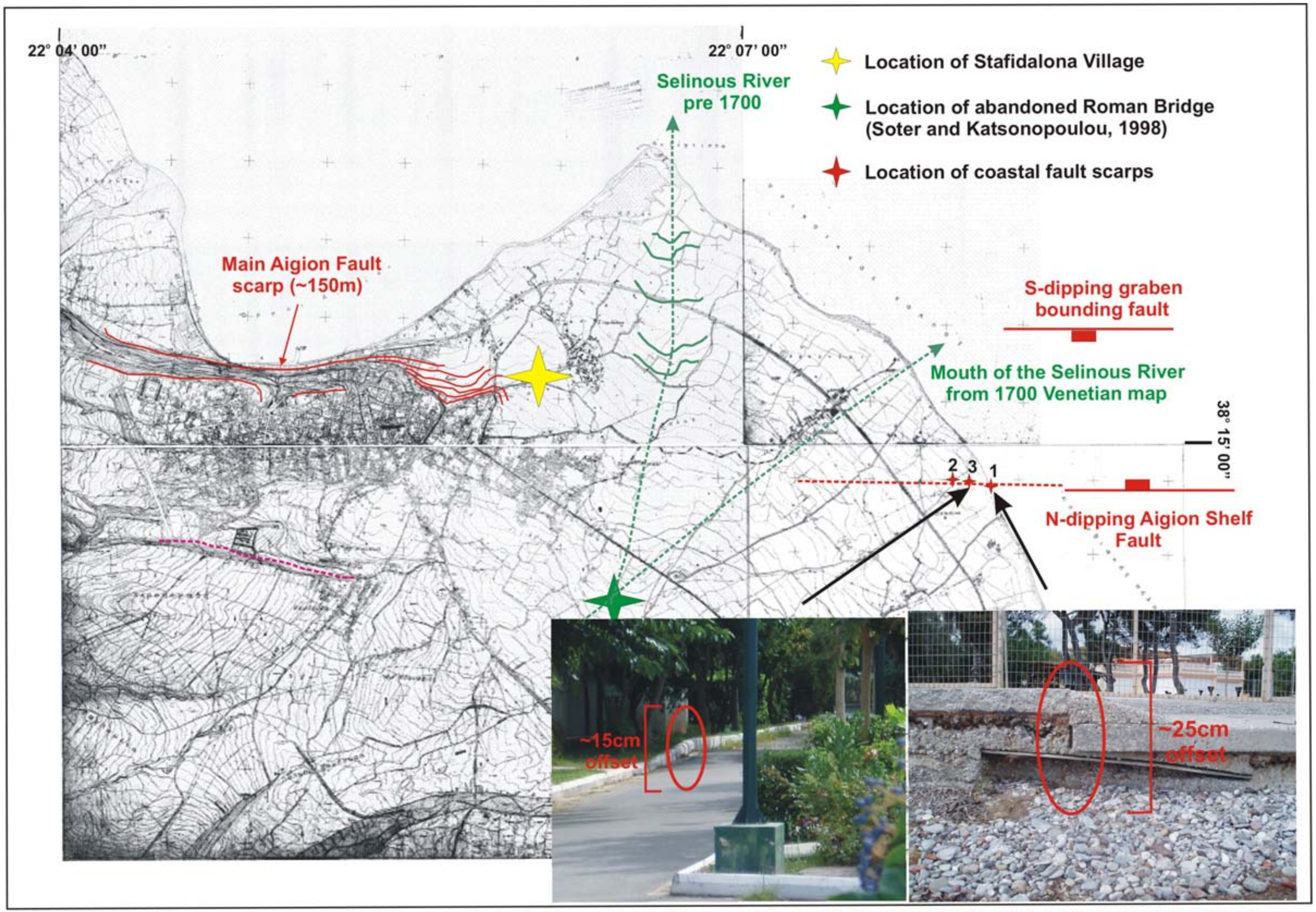

**Figure 8.4:** 1:5,000 topographic maps of the Aigion Delta, indicating the positions of features discussed in the main text. The relationship between the offshore Aigion Shelf Fault imaged in this survey, and onshore features that suggest possible minor offset due to faulting, support the hypothesis that there is an onshore extension to the Aigion Shelf Fault. Paleoriver channel positions based on abandoned bridges and historical maps (Soter and Katsonopoulou, 1998), indicate rapid shifting of channel positions on the deltaic plain.

The offset at the seafloor in the survey area was ~3 m, although this is believed to have been reduced by the effects of erosion. If the Aigion Shelf Fault not only links to the immediate onshore, but continues westwards across the delta to link up with the known Aigion Fault segments, we would expect to see displacement across the delta that was at least commensurate with that observed offshore. However this is not observed at any point, assuming such displacement would persist through the erosional actions of the river and the depositional draping as sediments were laid down.

It is possible that anthropogenic activity has altered the landscape, removing any evidence of larger scarps that may be present on the Aigion delta. It is also possible that avulsion of the Selinous River has eradicated any minor fault scarps. Soter and Katsonopoulou (1998) propose that the delta has been shaped by anastomising channels and serious flooding in the past, with some events having a significant impact on the top few metres of the delta surface. Figure 8.4 indicates the known recent locations of the Selinous River, indicating the area that may have been affected by repeated river migration. Although these locations sit within the apparent “gap” between the eastern tip of the Aigion Fault and the western tip of the Aigion Shelf Fault, the magnitude of scarp that would have to be removed suggests that the Aigion Shelf Fault is an isolated structure.

There is therefore no evidence that a further structure links the Aigion Fault to the Aigion Shelf Fault across the delta, as proposed by Koukouvelas (1998). It is possible that the western onshore tip of the Aigion Shelf Fault (Figure 8.3B) may be propagating towards the main Aigion Fault. However, a lack of data from this area, combined with the apparent lack of propagation of the eastern offshore section, suggests that this has not been occurring during the Holocene. The separation between the proposed western tip of the Aigion Shelf Fault, and the eastern tip of the Aigion Fault at Stafidalona is therefore ~1.2 km E-W and 0.5 km N-S (Figure 8.4).

When considering the similarities between the geomorphology, and the degree of overlap and proximity between structures, it appears that the Aigion-Neos Erineos fault system is composed of several discrete faults (Figure 8.1), including the Aigion Shelf Fault, that together form a stepped fault system. The Aigion Shelf Fault (which is proposed to extend onshore), represents one separate complex, comprised of an extensive damage zone, which as yet does not appear to have hard linked to the main Aigion Fault (AF1 & 2, Figure 8.1); the Aigion Fault, from the topographic profiles, appears to be linked via transfer faults to the N-dipping Fassouleika Fault (Palyvos et al. 2005). North of the Fassouleika Fault lies the N-dipping Selianitika Fault, which again appears to have morphological similarities to the Fassouleika and Aigion structures (Palyvos et al., 2005), suggesting it may be linked to them. Beyond this fault system are two major basin bounding faults (Eliki and Psathapyrgos Faults), each of which have lateral continuity of ≥15 km (Figure 8.5), and ~5 km N-S separation from the Aigion-Neos Erineos system.

What is unusual about the geometry of the Aigion-Neos Erineos system in comparison to other fault systems along the southern margin of the Gulf of Corinth, is the number of component faults, the degree of overlap between each of the component faults (Figure 8.1), the N-S separation of component faults, and the total N-S extent of the system (~5 km).

Between the Fassouleika, Selianitika and Aigion faults there is ~1 km overlap, whilst between the Aigion and Western Eliki Faults this is almost 5 km. However, overlap of major faults is not observed at any other point along the southern margin of the Gulf of Corinth, until the Alkyonides Gulf, where there is significant overlap between the Skinos and Pisia Faults (Collier et al., 1992; Leeder et al., 2005). The N-S separation between the Aigion-Neos Erineos component faults is 0.5-1 km, whereas between this system and other basin bounding systems it increases significantly to ~5 km. The overlap and separation observed in the Aigion-Neos Erineos fault system therefore suggests there is a significant change to the fault geometry in this localised area. (The spacing of GPS stations to date is such that this very localised change cannot be resolved).

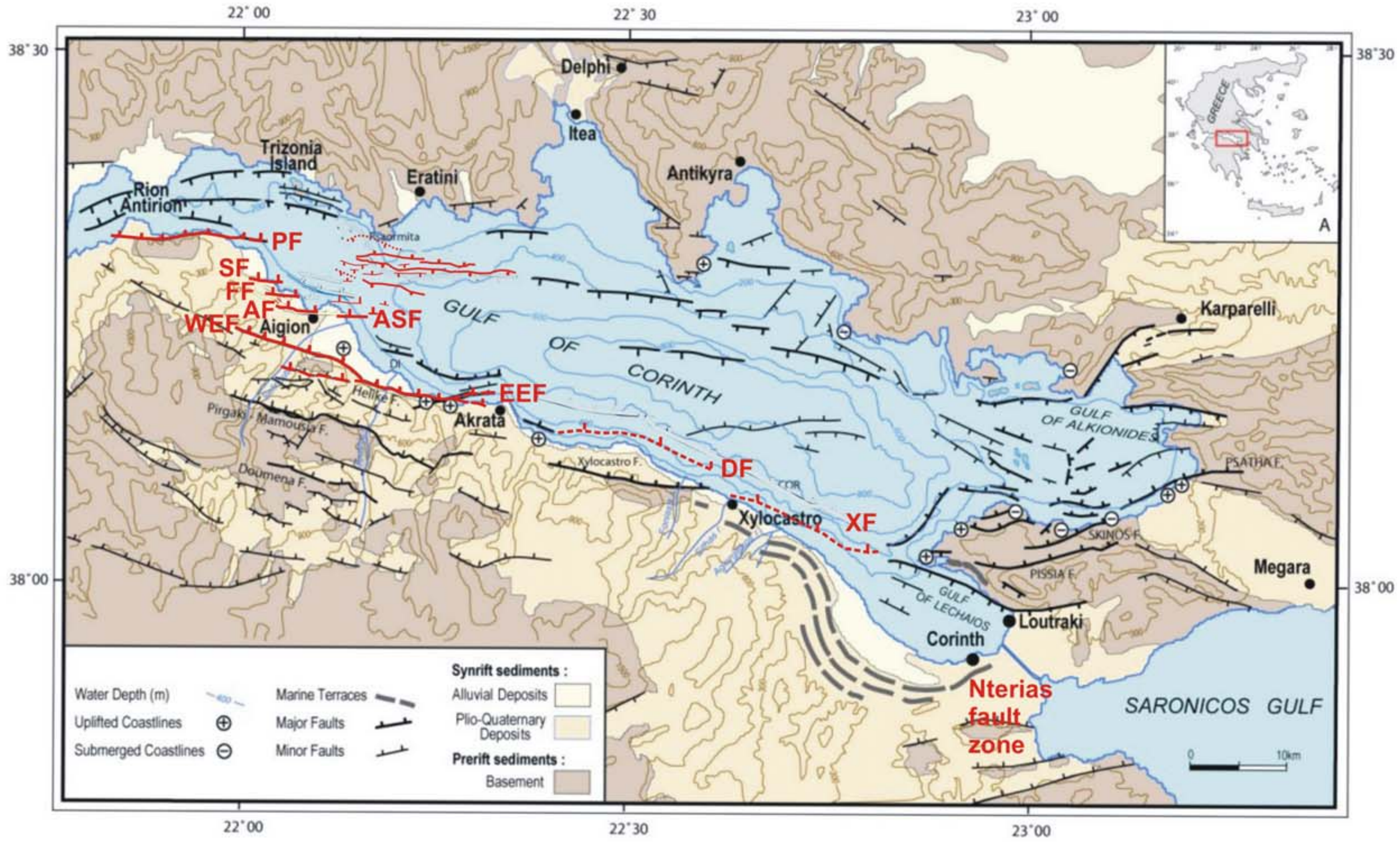

**Figure 8.5:** Gulf of Corinth basin. Major basin bounding faults discussed in the text are delineated in red. Offshore faults identified in the regional survey (Chapter 3) are also highlighted in red. Other faults in black are from Ghisetti et al. (2001); Stefatos et al. (2002); Sakellariou et al. (2001) and Armijo et al. (1996). PS - Psathopyrgos Fault; SF - Selianitika Fault; FF - Fassouleika Fault; AF - Aigion Fault; ASF - Aigion Shelf Fault; WEF and EEF - Western and Eastern Eliki Faults; DF - Derveni Fault; XF - Xylokastro Fault. (After Moretti et al., 2003).

However, the total E-W length of the Aigion-Neos Erineos system, when the overlap between the four component structures is considered, is ~15 km, which is consistent with the length of both the Psathapyrgos and Western Eliki Faults that bound the system, and other major faults in the Gulf. This supports the hypothesis that the Aigion Shelf, Aigion, Fassouleika and Selianitika faults are combining to form one fault system.

**Comparison of the Aigion-Neos Erineos Fault Geometry to Regional Fault Geometry**

The MCS reflection Sparker profiles, and regional multibeam bathymetry presented in Chapter 3 provided the basis for the fault map of the western Gulf (Figure 3.4; McNeill et al., 2005a). This figure, and further investigation, shows a greater number of faults offset the basement in the part of the western Gulf of Corinth between the Aigion delta and the northern coastline than elsewhere in the western and central Gulf. It is accepted that deformation is generally being distributed over a number of faults across the Gulf of Corinth (e.g. McNeill et al., 2005a; Stefatos et al., 2002; Leeder et al., 2005; Sachpazi et al., 2003), instead of being concentrated onto single basin bounding faults that dominate the southern margin. However new data suggests that the high density of basement displacing faults observed in this part of the Gulf is specific to this area (McNeill, Pers. Comm.). The unusual geometry of the Aigion-Neos Erineos fault system may therefore reflect this anomaly.

Possible causes behind this localised change in fault geometry could be the narrowing of the Gulf between the Aigion delta and Cape Psaromita (Figure 8.5) and associated E-W changes in crustal thickness due to the underlying geological nappe, or changes to the subduction angle of the African Plate (Leeder et al., 2005). Le Pourheit et al. (2003) present results from a thermomechanical numerical model that incorporates changes in subduction angle of the African Plate with changes in crustal thickness and variations in heat flow, to explain the E-W changes in extension observed along the Gulf. They suggest that changes in fault geometry observed in the Aigion area result from the location of inhomogeneous heat flow associated with the subducting slab, combined with proximity to thinned continental crust. Le Pourheit et al. (2003) propose that the change in angle of subduction moves from shallow to steep close to the northern margin of the western Gulf, whereas it lies on the southern margin of the eastern Gulf. This results in shallow subduction and significant extension and northward migration of normal faulting occurring across the western Gulf, whilst the eastern Gulf shows a very different tectonic regime, supporting the findings of Leeder et al. (2003). However, the exact locations and extent of changes in slab geometry are poorly resolved.

## 8.2 EVOLUTION AND AGE OF THE AIGION-NEOS ERINEOS FAULT SYSTEM

### Age of the Aigion-Neos Erineos Fault System

One of the principal questions raised by this study is whether or not the geometry of the Aigion Fault system represents an early phase in typical fault development in the Gulf of Corinth, or a departure from the usual geometry exhibited by other faults. Many of the major faults bordering the southern coastline in the Gulf of Corinth are believed to have been active for at least 1Ma (Armijo et al. 1996; Goldsworthy and Jackson, 2001; McNeill and Collier, 2004), therefore determining the age of the Aigion Fault may help define its relative maturity.

The sloping onshore displacement profile, (contrasting with that of other Gulf faults), and subdued footwall topography (Figure 8.2) suggest that the Aigion Fault is young. Further evidence to support this assumption can be gained from analysis of uplifted marine terraces.

De Martini et al. (2004) mapped Late Pleistocene marine terraces uplifted in the footwall of the Aigion and Western Eliki faults (Figure 8.6). Terraces located in the footwall of the Western Eliki Fault were dated to ~300 ka (oxygen isotope stage 9), providing a baseline from which to date older and younger terraces mapped. Terraces in the Aigion Fault footwall stretch south for ~4 km, before abutting against the Western Eliki Fault. The oldest terraces located between the Aigion and Western Eliki Faults were assigned to marine oxygen isotope stage 7, giving an approximate maximum age of 200 ka (De Martini et al., 2004), suggesting that the Aigion Fault has been active for at least 200 kyr, uplifting these terraces to their present day height of 220 m above sea-level.

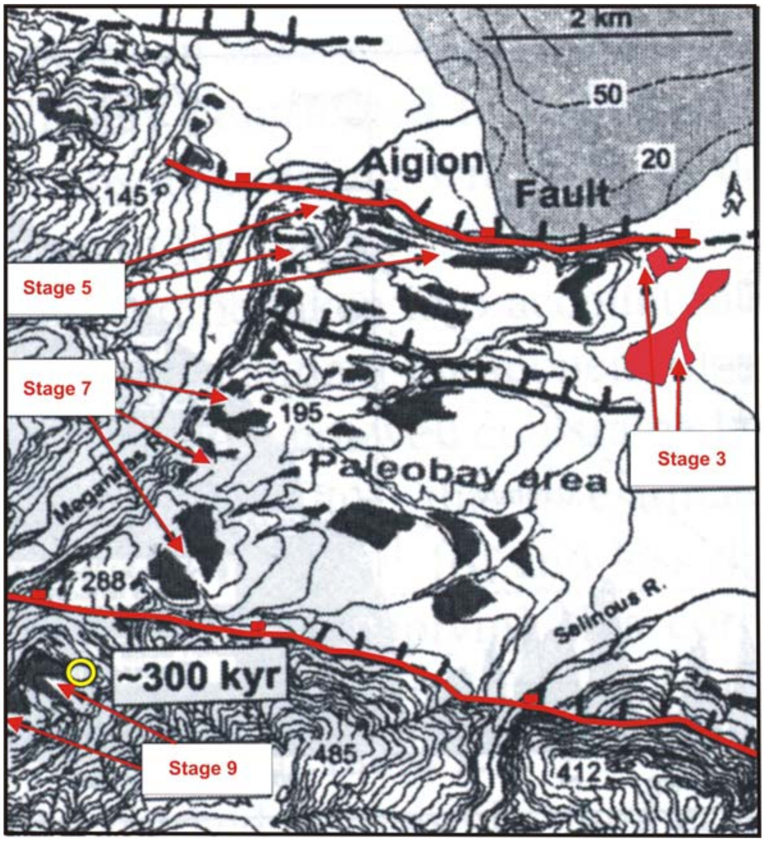

**Figure 8.6:** Map of the marine terraces located between the Aigion and Western Eliki Faults, taken from De Martini et al. (2004), and correlation to sea-level highstand. Stage 3 terraces located at the eastern tip of the main Aigion Fault segment have been highlighted. Open circle (yellow) shows the location of dated material.

It is possible that the Aigion Fault has been active for longer, contributing to the uplift of the stage 9 terraces, with subsidence of the Western Eliki footwall counter-acting any initial uplift of the Aigion Fault footwall, so enabling the stage 7 terraces to form. However, as it is not possible to distinguish the effects of uplift on one fault from subsidence on the other, and the fit of the terraces identified by De Martini et al. (2004) with sea-level highstands seems reasonable, the De Martini et al. (2004) results have been adopted.

De Martini et al. (2004) document uplift rates on the Aigion Fault of between 1 – 1.2 mm yr$^{-1}$ over the past 200-250 kyr. The stage 7 terraces give an overall rate of 1mm yr$^{-1}$

whilst the younger stage 5 terraces yield a faster rate of 1.2 mm yr$^{-1}$. The differences may represent a true variability in uplift rate over the longer term. However, distance from the Aigion Fault trace and terrace erosion may cause decay in uplift rates, whilst proximity to the WEF may have enhanced the effect of subsidence associated with the hanging-wall, causing the older terraces to indicate lower uplift rates. Nevertheless, both these rates are consistent with (within likely errors) those suggested by Koukouvelas (1998), De Martini et al. (2002) and Pantosti et al. (2004), that range from 1–1.5 mm yr$^{-1}$.

The De Martini et al. (2004) uplift rates give an age range of ~185 – 210 kyr for the oldest terrace to be uplifted to its present height through activity on the Aigion Fault alone. This suggests that the Aigion Fault is significantly younger than the Eliki Fault (~1 Ma), and other basin bounding faults in the Gulf of Corinth (Armijo et al., 1996; McNeill and Collier, 2004). Therefore, its present day morphology and activity is likely to represent a stage in the development of an immature fault system.

## Growth of the Aigion Fault System

Isopachs of the time intervals between the four horizons mapped offshore indicate that sediment deposition is being primarily controlled by faulting (Chapter 5). However, neither the isopachs, nor the fault structure plots indicate lateral growth of depocentres occurring as a result of propagation of fault segments, suggesting that there was no resolvable lateral propagation of the Aigion Shelf Fault during the last 12 kyr.

It is possible to try and evaluate fault growth over time using the same marine terraces, combined with present day topography. Uplift of marine terraces, whose formation can be correlated to a specific time period, can be used to track lateral fault growth or increasing displacement on a fault plane.

De Martini et al. (2004) identify Stage 3 terraces, formed between ~25-50 ka, located at the eastern tip of the central segment of the Aigion Fault (AF2, Figure 8.1), coincident with where there is zero topographic displacement (Figure 8.4). If a fault segment had been propagating across the Aigion delta prior to 25-50 ka, it would be expected that uplift of the segments' footwall would inhibit formation of Stage 3 terraces, raising the area above sea-level. Therefore, propagation was either very rapid after terrace formation, or did not occur at all.

It is clear that the Aigion Shelf Fault, and several other faults on the shelf area, offset the horizon formed during sea-level fall associated with the Last Glacial Maximum, suggesting that faulting on the Aigion shelf was active at the same time the Stage 3 terraces were forming. This rules out rapid propagation across the Aigion delta of the hypothesised third segment of the Aigion Fault (AF3, Figure 8.1), supporting the hypothesis that the Aigion Shelf Fault is an isolated structure, established prior to formation of the Stage 3 terraces, and that there is no third segment that links the Aigion Fault to the Aigion Shelf Fault across the delta.

This supports the idea proposed in section 8.1 that the Aigion-Neos Erineos fault system is formed through linkage of isolated fault structures. Many of these are already proposed to have linked, such as the central and western onshore Aigion Fault segments (AF1 and 2, Figure 8.1), and potentially the Aigion Fault with the Fassouleika and Selianitika faults. However, as yet, there is no link between the Aigion Shelf Fault, and the Aigion Fault (Figures 8.3 and 8.4), supporting the immaturity of the system.

It is possible that the present-day configuration of the Aigion Fault system was established prior to ~12 ka. This would support the model proposed by Walsh et al. (2003), and observations by Poulimenos (2000), Meyer et al. (2002) and Nicol et al. (2005), who suggest fault length is established rapidly at depth, often in <0.5 Myr, with subsequent slip events serving to predominantly increase displacement on the fault, with only minimal changes in fault length. This would therefore suggest, from the calculated age of the Aigion Fault, that the fault system reached its present day length in <0.2 Ma.

## 8.3 DISPLACEMENT VARIABILITY

### Variability in the Offshore Fault System

The displacement analysis (Chapter 6) showed high variability in both temporal and spatial displacement rates along the offshore faults imaged. The greatest vertical displacement (~15 m) on the Aigion Shelf Fault (Figure 8.1) is observed on the oldest horizon (H4). Displacement on all four mapped horizons gradually increases westwards, suggesting extension of the fault onshore (see previous section).

Where segments have linked (1a – 1g, Plate 1C), producing a displacement profile that is reminiscent of a single fault over long time periods, displacement minima remain, indicating the locations of past segment overlap and points of linkage (Figure 6.20). Even over the longest time period (~11.5 kyr), displacement profiles from the Aigion Fault indicate that these points continue to inhibit full rupture, suggesting that despite through-going linkage, segmentation can continue to influence displacement.

Displacement on the Aigion Shelf Fault appears to increase from $0.5 \pm 0.1$ mm $yr^{-1}$ pre ~$4.5 \pm 0.6$ ka (H2), to $0.9 \pm 0.1$ mm $yr^{-1}$ after this time. This increase is maintained to the present day. A similar increase was observed on the major S-dipping graben bounding fault at the same time, from $0.3 \pm 0.1$ mm $yr^{-1}$ to $1.4 \pm 0.2$ mm $yr^{-1}$. However, this increase was not maintained, with displacement rates reverting back to pre ~$4.5 \pm 0.6$ ka levels at ~3.5 ka, suggesting that the simultaneous, differential increase in displacement at ~4.5 ka was not solely due to a change in sedimentation rates.

Taking the contributions from all the mapped faults, the average displacement rate across the Aigion Shelf is $2.3 \pm 0.2$ mm $yr^{-1}$ over the longest time period of observation ($11.5 \pm 1$ ka), whilst between $4.5 \pm 0.6$ ka and the present day, the average displacement rate is $1.9 \pm 0.4$ mm $yr^{-1}$. As both these rates are within error, it suggests that there has been no increase in the total strain being accommodated across the Aigion Shelf. The increase observed on the Aigion Shelf Fault post 4.5 ka must be offset by a decrease on minor faults to maintain constant strain rate across the shelf. This would fit with the apparent decrease in length and numbers of minor faults observed across the Aigion Shelf, between ~11.5 ka and the present day.

### Displacement behaviour along the Aigion-Neos Erineos Fault System

The spatially averaged vertical displacement rate over ~11.5 kyr for the Aigion Shelf Fault is $0.6 \pm 0.1$ mm $yr^{-1}$. This is significantly lower than the displacement rates of 2 – 3.5 mm $yr^{-1}$ suggested from data onshore (Koukouvelas, 1998; De Martini et al., 2004; Palyvos et al., 2005). It does however compare to the paleoseismologically derived rates of 0.3 – 1.5 mm $yr^{-1}$ suggested by Pantosti et al. (2004) for the eastern tip of the western segment of the onshore Aigion Fault (1, Figure 8.1).

However, if the faults mapped on horizon H4 converge onto a single structure at depth, and the deformation associated with that structure is being distributed, then the contribution from each fault should be taken into account. This increases the spatially averaged vertical displacement rate on the Aigion Shelf Fault system, over 11.5 kyr, to 2.3 ± 0.2 mm $yr^{-1}$, bringing it into line with rates on the Fassouleika and Aigion Faults.

**Causes of Displacement Rate Variability**

It is possible that the choice of methodology used can give rise to variability between results. Using the Pantosti et al. (2004) and Palyvos et al. (2005) studies as the most directly comparable with regards to timescale (1 kyr and 4 kyr respectively), the displacement rates they suggest for the Aigion Fault alone are still much higher than the rates obtained in this study of the Aigion Shelf Fault of 0.6 ± 0.1 mm $yr^{-1}$.

However, the Pantosti et al. (2004) study also showed variability when looking at displacement on the main fault versus associated splays. The rate of 0.3-0.4 mm $yr^{-1}$, increased to 1 – 1.5 mm $yr^{-1}$ when including the effects from the splays. Likewise, the offshore Aigion Shelf Fault rate of 0.6 ± 0.1 mm $yr^{-1}$ increased to 2.3 ± 0.2 mm $yr^{-1}$ when the contributions of all the splays were included. This brings it into line with the rates given by Palyvos et al. (2005) for displacement on the Fassouleika Fault, although it is not known whether or not that study included the contribution from any damage zone.

It is possible that trenching is not able to resolve the contributions from multiple splays if they are widely distributed, leading to an under-estimation of displacement over the whole fault system. Comparing results gained from analysis of different methodologies could therefore be misleading.

The displacement results from this study suggest that the Aigion Fault and Aigion Shelf Fault have similar Holocene displacement rates, but displacement is distributed over a much broader and complex damage zone on the Aigion Shelf, as may be expected at the tip of a fault. This raises the question of whether or not the effect of significant damage zones should be incorporated into the analysis of displacement behaviour on a specific fault, if the degree of linkage between structures within that damage zone cannot be fully constrained.

Another major factor when comparing the displacement rates between the offshore and onshore faulting is the observation period used. Pantosti et al. (2004) used a period of 1 kyr, whilst this survey looked at the last ~11.5 kyr, and the results were comparable between these two surveys. However, longer periods of observation (>200 kyr), such as the De Martini et al. (2004) study gave different rates. It is difficult to constrain whether or not the variability arises from comparing Late Pleistocene rates with Holocene rates, and the relative timescales involved, or whether it is a factor of the methodologies used.

Displacement rates obtained through palaeoseismology are often under-estimated, as these surveys only sample a few events, leading to high variability. Longer-term displacement rates, calculated using uplifted marine terraces, provide a better indication of the stable behaviour of a fault system, although in doing so, it smoothes out the shorter-term variability that can help identify periods of enhanced activity.

### Displacement Variability – Comparison to the Eliki Fault System

As the Eliki Fault system is in close proximity to the Aigion Fault, it is a useful comparison when addressing whether the Aigion Fault and Aigion Shelf Fault displacement profiles are “normal” for faults in the Gulf of Corinth. It may be expected that following initiation of the Aigion Fault, displacement on the overlapping Western Eliki Fault would begin to decrease, as strain was transferred. A difficulty with testing this hypothesis arises from the methodology used to investigate uplift along the Western Eliki Fault.

Micarelli et al. (2003) present a topographic displacement profile that uses the offset between the present day footwall and hangingwall (Figure 8.7). The displacement profile obtained from these surface offsets, shown in Figure 8.7B, is bell-shaped, suggesting that the Eliki Fault is behaving as an isolated structure. However, it is not clear how Micarelli et al. (2003) define where the top of the footwall is located, and how they are accounting for any erosion effects. In addition, topographic maps, and the consistent elevation of an uplifted terrace, appear to suggest that the footwall is flat-topped, and not domed as suggested in Figure 8.7A.

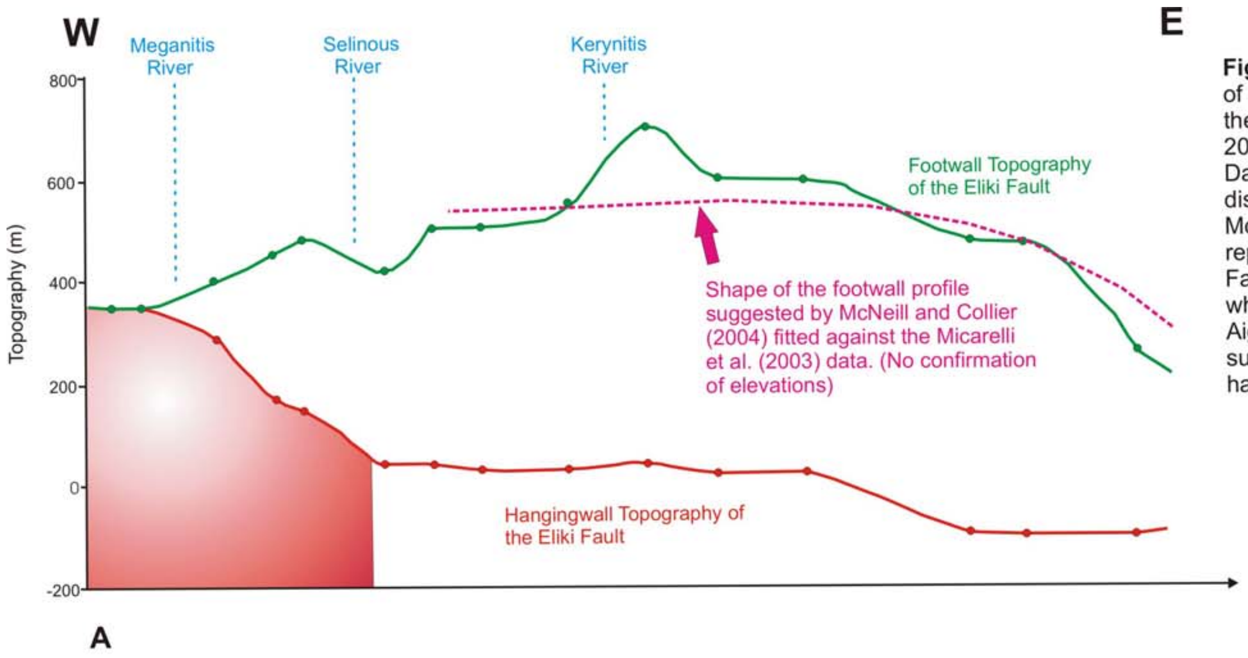

**Figure 8.7: A)** Topographic profile of the footwall and hangingwall of the Eliki Fault (After Micarelli et al., 2003).
Dashed magenta line indicates the displacement shape suggested by McNeill and Collier (2004). Shading represents the area where the Aigion Fault overlaps the Western Eliki Fault, where uplift in the footwall of the Aigion Fault may be offsetting subsidence of the Western Eliki Fault hangingwall.

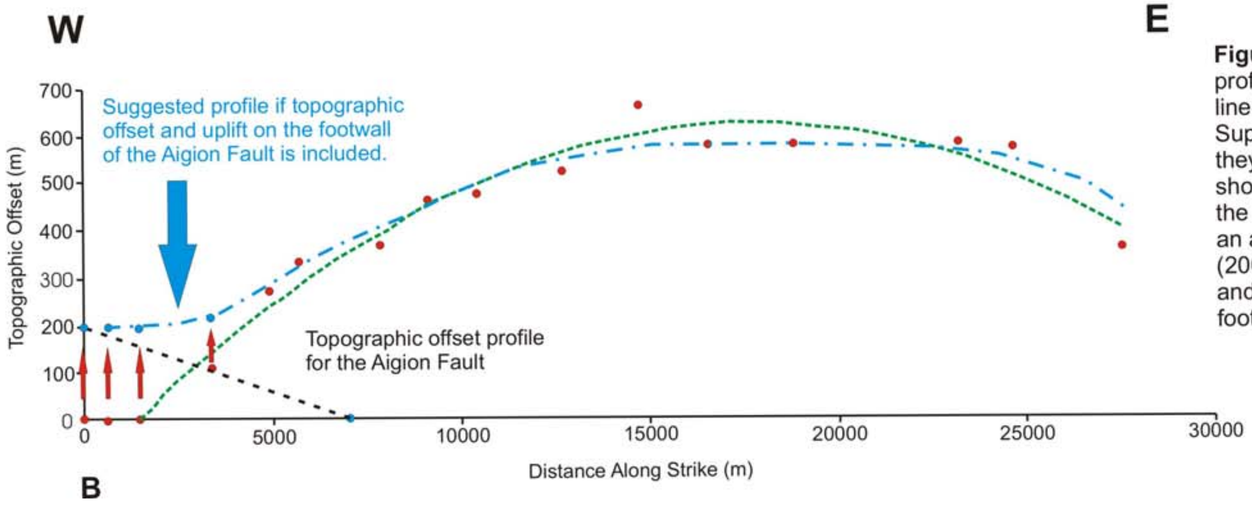

**Figure 8.7: B)** Inferred displacement profile for the Eliki Fault (green dashed line) (After Micarelli et al., 2003).
Superimposed is the topographic profile they present for the Aigion Fault (black), showing the degree of overlap between the two systems. The blue line indicates an alternative interpretation of Micarelli et al. (2003) offset data, based on terrace analysis, and including the influence of uplift on the footwall of the Aigion Fault.

The Micarelli et al. (2003) profile (Figure 8.7) also does not account for the balance between uplift of the Aigion Fault footwall and subsidence of the Western Eliki hangingwall. The apparent decrease to zero total offset between the Western Eliki footwall and hangingwall is caused by the hangingwall topography increasing in height, due to uplift occurring on the Aigion Fault footwall. The contribution from the Aigion Fault suggested in Figure 8.7B indicates that it does not fully compensate for the decrease in topographic offset at the western tip of the Eliki Fault (~0-4000 m along strike). However, it does raise the survey positions that apparently reach zero displacement (red circles) to an offset that is more comparable with the eastern end of the Eliki Fault (blue circles). Therefore, there are significant areas of concern associated with the Micarelli et al. (2003) study that need to be taken into account when comparing the profile they present for the Eliki Fault with that of the Aigion and Aigion Shelf faults.

A uniform flat-topped displacement profile, based on results from McNeill & Collier (2004), who trace a prominent marine terrace along the footwall of the Eastern and onto the Western Eliki Fault segments located ~100 m above present day sea-level, is believed to be more representative of actual behaviour on the Eliki Fault. This flat-topped hypothesis is also consistent with uplift rates suggested by De Martini et al. (2004) and McNeill and Collier (2004) who found that rates did not vary between the Western and Eastern Eliki Faults. The apparent uniformity along strike is also similar to displacement profiles observed by Contreras et al. (2000) in the East African Rift, and Bull et al. (in review) in New Zealand, for mature faults, where despite differential displacement profiles for individual segments, the total displacement profile becomes flattened towards the centre of a mature fault system. It is believed that the method employed by Micarelli et al. (2003) is more liable to biasing as a result of anthropogenic activity, erosion and deposition, and incorrectly portrays footwall topography.

Figure 8.2 shows that the displacement profile decreases on the Aigion Fault W to E. Displacement on the Aigion Shelf Fault increases towards the coastline, and is proposed to extend onshore, forming a bell shaped profile indicative of an isolated structure. Therefore neither the Aigion nor the Aigion Shelf Fault, both of which overlap the Western Eliki Fault, show the flat topped profile of established faults in the Gulf of

Corinth. This supports the hypothesis that the differences observed between the Eliki and Aigion and Aigion Shelf faults may be age related. However, it is also possible that much of the apparent discrepancy between the flat-topped Eliki Fault profile and the profiles exhibited by the Aigion and Aigion Shelf faults is connected to interaction between the two systems.

A lack of datable material has meant that variability of displacement rates due to interaction between the two fault systems over the last 200 kyr could not be resolved. However, assuming constant displacement rates over the whole 200-300 kyr does produce a good fit with eustatic sea-level highstand curves, suggesting that the profile differences are more liable to be related to age and system maturity.

## 8.4 DEVELOPMENT OF THE OFFSHORE FAULT POPULATION

The Aigion Shelf Fault (1a-1j, Plate 1C) is surrounded by numerous other minor faults, ranging in length from <300 m to ~1 km, and a major S-dipping segmented fault of ~1.5-2 km length (2a-2f, Plate 1C). The majority of the minor faults are blind and only displace the oldest datable horizon (H4), not affecting the youngest sediments. The faults can be divided into three distinct arrays or sub-populations. There appears to be a positive relationship between segment length and maximum displacement (Figure 6.19), although it is not possible to define whether it is power-law or linear due to limitations in the spread and lateral extent of the data.

Figure 8.8 shows a cross section taken through the two main fault arrays (S-dipping and Aigion Fault arrays). It indicates that if the faults are projected to depth using the suggested dip for the onshore Aigion Fault of 55°, proposed by Rettenmaier et al. (2004), then the faults would converge onto a single structure at ~650 m depth. Therefore the offshore zone of faulting, situated between the Aigion Shelf Fault and the main S-dipping graben bounding fault, is interpreted as being a damage zone that formed as a result of early stage, lateral growth of the Aigion Shelf Fault system across the Aigion shelf.

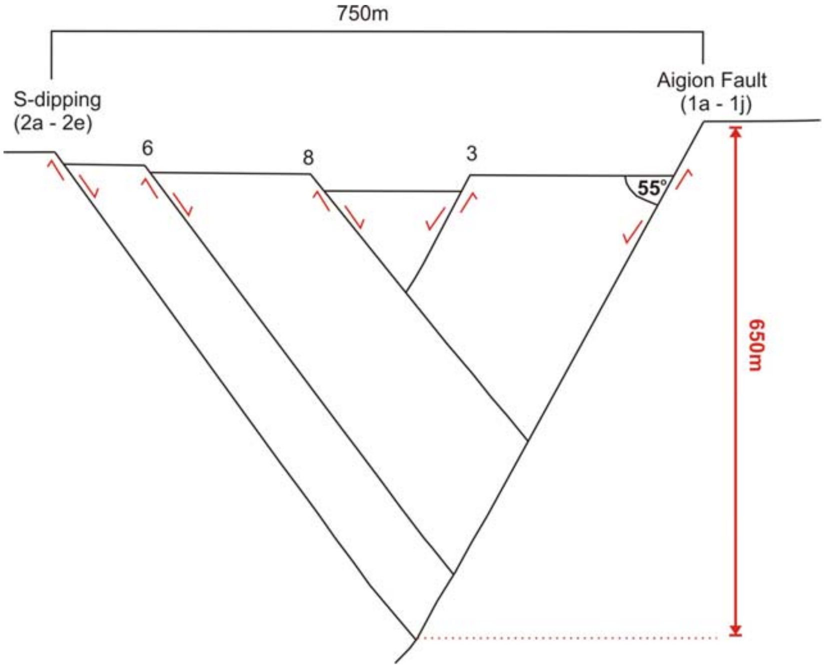

**Figure 8.8:** Cartoon illustrating the proposed connection between the numerous fault splays identified, and the main Aigion Fault strand. Fault numbers relate to the scheme shown in Plate 1C.

Heterogeneity in the rock structure, combined with non-uniformity of stress fields at segment tips, can result in upward bifurcation of splays from a single structure at depth, often referred to as tip-line bifurcation (Childs et al., 1996; Walsh et al., 2003). This initially distributes deformation over a number of smaller structures. The size of a damage zone can vary both temporally and spatially along a fault (Berg and Skar, 2005) with changes in lithology, rheology, distribution of strain and displacement distribution (Aarland and Skjerven, 1998) causing differences between the hangingwall and footwall of a fault.

The damage zone imaged in the multibeam bathymetry shows that the deformation is primarily concentrated within the graben, forming an asymmetrical damage zone about the dominant Aigion Shelf Fault. The footwall damage zone only encompasses fault 18 (Plate 1C), lying <100 m from the main Aigion Shelf Fault, whereas the deformation in the hangingwall is ≤750 m wide. The minor faults that make-up the footwall array are not believed to form a significant part of the damage zone. The two main arrays have a high density of minor faults within a small area, whereas the footwall array is much more widespread, and predominantly composed of faults that are <300 m in length. Therefore the footwall array has not been included in the assessment of damage zone width.

Micarelli et al. (2003) identify damage zones associated with the two main faults that lie south of the Aigion Fault, based on structural analysis at several survey sites. They use the definition of Caine et al. (1996) whereby the damage zone is distinguished by the density of faulting and fracturing. The Eliki Fault zone is defined as ~60-80 m wide in total, whilst the Pirgaki Fault zone is ~100 m wide. Both are asymmetrical, with damage predominantly seen in the hangingwall.

From analysis of the damage zones in the AIG10 core, and correcting for the angle between the borehole and the inclined fault plane, Micarelli et al. (2003) estimate that the damage zone associated with the Aigion Fault is ~25 m wide, which seems much smaller than the two older faults, and significantly smaller than the ~750 m zone imaged offshore. It is believed that as the estimation of the Aigion Fault damage zone is based solely on analysis of the borehole, with no supporting field surveys, that the extent of the damage zone has been under-estimated. It is also possible that the criteria adopted by Micarelli et al. (2003) for defining the damage zone has led to under-estimation due to the gradational changes between the fractured and undamaged country rock. However, it is expected that deformation would be greater towards a fault tip, where strain is spread over a number of faults prior to coalescing onto the main through-going system, resulting in a larger damage zone forming.

Other field studies in extensional settings have also shown this type of damage zone asymmetry. Berg and Skar (2005) observed an asymmetrical damage zone associated with normal faulting, where the hangingwall damage zone was three times the width of the footwall one, and was composed of many minor faults that had an opposing dip sense to the dominant fault. Koestler and Ehrmann (1991) and Aarland and Skjerven (1998) document similar findings from observations of faulting in the North Sea, whilst Taylor (2003) shows a similar pattern from the Whakatane Graben, New Zealand.

Koukouvelas et al. (1999) analysed a series of parallel fault strands in the Nterias Fault Zone in the Gulf of Corinth (Figure 8.5), and found that in cross section, the population had a “Y” shape, as splays converged onto a single fault plane. In the Nterias study, asymmetry between the footwall and hangingwall of the dominant fault was caused by differential accrual of displacement between faults with opposing dip directions. However, it is also possible that collapse of the hangingwall into the fault plane could also result in multiple minor faults radiating up into the hangingwall fault block.

Findings from the Koukouvelas et al. (1999) study also indicated that there was a significant decline in fault numbers as the length of faults increased. The strong parallels between the fault population observed at Nterias, and that on the Aigion Shelf, suggest that the development of such a fault population is not geographically unusual in the Gulf of Corinth, with the studies being located at the eastern and western ends respectively. What makes the fault geometry unique in the Aigion region is the geometry of the larger Aigion-Neos Erineos fault system, as discussed in previously.

Analysis of displacement and sedimentary sequences in chapters 5 and 6 has shown the influence of fault segmentation in controlling depocentre formation and fault interaction. Irregular displacement profiles over short timescales show evidence of positions along strike that experience minimal / zero displacement, suggesting the earthquakes in this region are not always capable of full along strike rupture. This matches the Cowie and Shipton (1998) model that predicts partial rupture along faults. High displacement gradients at fault tips, associated with fault interaction, and the transference of displacement across faults also agrees with the results from models of segmented fault systems (e.g. Peacock and Sanderson, 1996), as opposed to the more linear tapering of displacement predicted for isolated fault structures (e.g. Young-Seog and Sanderson, 2005).

The pattern of fault segments maintaining their individual displacement profiles following linkage, observed on the Aigion Shelf Fault, is also found in the Sofiko range, south of Korinthos, in the Gulf of Corinth. Koukouvelas et al. (1999) document 17 faults >4 km in length that take up 85% of the strain across the locality. They compare this region to the Aigion region, suggesting that as the faults formed through linkage of segments, each segment retains a degree of freedom. This individuality despite being part of a larger linked system is also shown through modeling by Anders and Schlische (1994), whereby larger faults do not show the simple length / displacement relationship shown in many simple models, as they are formed of coalesced segments that can still move independently.

Interpretation of thickened wedges in the hangingwalls of both the major offshore faults suggests that each fault was dominant over particular time periods and at certain locations. The displacement data specifically suggests that displacement was predominantly taken up by the Aigion Shelf Fault, but that periodically this switched onto the S-dipping fault. This flipping of displacement between faults has been documented by Trudgill and Cartwright (1994), King et al. (1994) and Goldsworthy and Jackson (2001), where sub-parallel faults temporarily act as bypass structures around areas where displacement may be inhibited due to locking at a segment boundary or interacting stress fields (D’Alessio and Martel, 2004).

However, this pattern may also be observed in the Gulf of Corinth on a much larger scale. Stefatos et al. (2002) and Sachpazi et al. (2003) suggest the polarity of the central Gulf of Corinth switched, with dominance moving from a S-dipping northern margin fault onto a N-dipping southern margin one. With switching of polarity on this scale, it is not believed that temporary transference of displacement past a locked boundary was the driving force. Instead, more regional processes related to rift evolution and crustal thickness are more likely causes. However, it is interesting that a similar type of fault behaviour is observed on different scales and over different time periods within the same rift.

# Chapter 9

# Conclusions and Future Work

The data presented in this thesis describe the short-term behaviour of the normal fault population of the Aigion Shelf. The geometry of this fault zone in relation to the onshore Aigion-Neos Erineos and Eliki fault systems that have previously been described, is analysed in order to assess whether or not the offshore fault zone is linked to, or behaving independently of, the onshore basin bounding fault systems.

- **Rift Strain Distribution:** Analysis of MCS reflection profiles and multibeam bathymetry data has confirmed that strain is being distributed across a number of major offshore fault systems in the western Gulf. Quantification of slip rates, based on seismic stratigraphy, has shown that the contributions from these faults, when combined with known onshore fault systems, total 8 – 16 mm $yr^{-1}$ extension, thereby reconciling the previous discrepancy between geodetic and geologic extension (McNeill et al., 2005a).

- **Western Gulf of Corinth Rift Morphology:** The western Gulf of Corinth is dominated by an E-W axial channel, into which a network of canyons from the southern margin feed. Both the canyon and channel morphology disappears in the central Gulf, approaching the abyssal plain province. The southern margin is characterised by a narrow shelf, steep slope and mass wasting, whilst the northern margin shows evidence of uplifted sub-basins and a more gradual slope.

- **Holocene Aigion Shelf Deposition:** Three main units with distinct seismic characteristics have been identified on the Aigion Shelf. Due to the influence of the Rion Sill, these units can be correlated to changes in eustatic sea-level from the nature of their internal geometry. The deepest unit imaged is composed of dipping clinoforms deposited during sea-level fall. This is overlain by shallow dipping beach topsets. The next unit represents sub-aerial deposition and early stage transgression, when the Gulf of Corinth was an isolated lacustrine basin and the Aigion Shelf was exposed. The youngest unit represents late stage transgression, when sea-level over-topped the Rion Sill and the Aigion Shelf was inundated, with highstand progradation occurring in the last ~6 kyr. Inundation of the Aigion Shelf has been estimated at ~11.5 ± 1 ka.

- **Horizon Identification:** Four laterally continuous horizons were used for quantitative fault displacement analysis. Using the transgressive horizon as the oldest and most reliably dated synchronous marker, it was possible to assign ages to three younger, laterally extensive horizons, based on their relative depth within the sequence imaged, and assuming a constant sedimentation rate. The dates obtained for each horizon were H4 - ~11.5 ± 1 ka; H3 – 7.5 ± 1.1 ka; H2 – 4.5 ± 0.6 ka and H1 – 3.5 ± 0.5 ka. A comprehensive error analysis incorporating errors associated with horizon picking, velocity analysis, age assignment and estimation of depth was conducted. Cumulative errors on the horizons range from 9-14%, whilst errors related to specific time periods range from 9 – 17%.

- **Sedimentary Deformation Features:** Pockmark and mound features appear to be intrinsically linked to faulting occurring across the Aigion Shelf. Migrating fluids and gases are using the fault planes as migratory pathways past impermeable layers. Other studies have suggested that the trangressive horizon may be a significant barrier, whilst analysis of the Aigion borehole indicates that there are significant clay layers in the Holocene deposits which may also be acting as sedimentary barriers.

- **Offshore Fault Geometry:** The Aigion Shelf Fault (1, Plate 1C) has a complex damage zone associated with it, comprising numerous smaller faults and one other major S-dipping segmented fault (2, Plate 1C). There is a graben structure between the Aigion Shelf Fault and the S-dipping fault, within which the majority of the minor faulting is concentrated (Plate 1C). It is believed that the majority of the faults converge at depth onto a single N-dipping fault structure.

- **Aigion Shelf Fault Geometry:** The Aigion Shelf Fault, is a segmented normal fault, that has a complex seafloor morphology, and an E-W orientation (1, Plate 1C). Displacement profiles indicate that the segments are linked at depth, causing the fault to behave as a coherent unit over the long-term. Short-term spatial variability is associated with the independent behaviour of segments within the linked system, with preserved displacement minima indicating segment boundaries.

- **Evolution of the Offshore Fault Population:** Displacement profiles and analysis of sedimentary deposition has shown that maximum displacement, and fault dominance, switches back and forth between the Aigion Shelf Fault and the S-dipping graben bounding fault, corresponding to specific segments that were more active over particular time periods. This mirrors the larger scale switching along the rift observed by Sachpazi et al. (2003) and Stefatos et al. (2002), who show a change from a S-dipping border fault on the northern margin dominating sedimentation, to a N-dipping fault on the southern margin of the Gulf of Corinth.

- **Isopach Analysis:** Isopachs from five specific time periods indicate that the predominant control on depocentre formation during the last 11.5kyr has been faulting. The change from sub-aerial to marine conditions following the last post-glacial transgression is assumed to have occurred rapidly, based on the topographic expression of the shelf and biota zoning in a reef (Kershaw et al., 2005). Therefore the trangressive horizon is assumed to be synchronous in this study. This move from sub – aerial to marine transgression and continued sea – level rise is accompanied by a change in depocentre location from the shelf edge to inshore, between 11.5 – 7.5 ka. Following sea-level stabilisation, the Aigion Shelf Fault and S-dipping graben bounding fault dominated the development of the graben depocentre, whilst uplift of the footwalls of both these faults created significant depocentre minima. From ~4.5 ka, the influence of coastal progradation is observed in both the multibeam and sub-surface seismic datasets.

- **Age of the Aigion Fault System:** Evidence from marine terraces suggests that the Aigion Fault is ~200 ka, whilst displacement of the oldest imaged horizon on the Aigion Shelf indicates that the Aigion Shelf Fault population is at least 25 ka. Both the faults are therefore significantly younger than other established border faults in the Gulf of Corinth (~1Ma), such as the Eliki Fault system (McNeill and Collier, 2004).

- **Lateral Propagation:** There is no evidence of lateral propagation of the Aigion Shelf Fault and associated splays during the Holocene. Studies by Taylor et al. (2004) and Leeder et al. (2005) have both suggested that fault growth through lateral propagation occurs relatively early in the history of a fault system, suggesting the observed period in this study post dates any significant lateral propagation. The lack of propagation during the Holocene may indicate that the most significant period of fault growth occurs in <200 kyr of a fault initiating, and that subsequent activity serves to establish the displacement profile that the mature faults exhibit.

- **Future Fault Evolution:** The 11.5 kyr displacement profile suggests that the offshore Aigion Shelf Fault extends onshore. There is no geomorphological evidence however that the Aigion Shelf Fault is linked to the main onshore Aigion Fault, supporting the immaturity of the fault and suggesting that this survey has imaged the first stage of a two stage process. The first phase involved the nucleation of the Aigion and Aigion Shelf faults as discrete structures, which is observed through the displacement profiles and geomorphology. At a later date, as the fault system as a whole develops further, they may link up to form a through-going fault of ~15 km length, that spans the entire delta region.

- **Fault Maturity:** Comparisons of the displacement profiles from the mature Eliki Fault system (flat-topped and uniform), and the Aigion and Aigion Shelf faults (asymmetrical and bell-shaped respectively), combined with evidence from uplifted marine terraces, suggest that the Aigion and Aigion Shelf faults are immature compared to other basin bounding fault systems in the Gulf of Corinth. Spatial displacement variability along the Aigion Fault system indicates that it is still establishing a stable profile. It is believed that this will not occur until all component structures have hard-linked, establishing the larger system's final length and geometry.

- **Slip Rate:** The Holocene slip rate for the Aigion Shelf population is 2.6 ± 0.2 mm $yr^{-1}$. This is significantly lower than slip rates proposed for the onshore Aigion Fault by De Martini et al. (2004) of 9-11 mm $yr^{-1}$. However, a lower rate would be expected if the Aigion Shelf population represents either a smaller isolated fault, or the eastern tip of the larger Aigion Fault system.

- **Aigion-Neos Erineos System:** Previously published work suggests that the onshore Aigion Fault is linked to the Fassouleika and Selianitika Faults (Palyvos et al., 2005), forming the 5 km wide (N-S) Aigion-Neos Erineos system. The similarity between the displacement profiles from the onshore and offshore fault zones, combined with the vertical displacement data from segment tips, suggests that the Aigion Shelf Fault forms the eastern part of this larger Aigion-Neos Erineos Fault system. The geometry of the stepping configuration of the four closely spaced and overlapping faults that comprise the Aigion-Neos Erineos system is significantly different from that of the other major basin bounding fault systems in the Gulf of Corinth. It occurs over a very localised area, and may result from rift narrowing, inhomogeneous crustal heat flow and thickness, and the angle of slab subduction, as well as the fault system's immaturity.

## FUTURE WORK

Although this study clearly identified variability associated with fault activity and interaction between segments, there was a degree of uncertainty associated with the assignment of ages to horizons, and so to the displacement rates calculated. Coring or drilling of this shelf region, to a depth of ~50 m below the seabed, would not only provide accurate constraints for the horizons H4 – H1 and displacement analysis already conducted, but would provide a date at a specific location for horizon H5. This would mean that the detailed analysis could be extended to cover between 11.5 - ~50ka, providing a detailed record of one complete sea-level cycle, and testing the hypothesis that slip rates vary through time.

The MCS reflection survey line spacing was too far apart to resolve whether or not there had been any lateral growth of the Aigion Shelf Fault or its component segments at rates of <3 mm yr$^{-1}$. A more closely spaced / 3D survey may resolve the debate between there being lateral growth, but at below the resolution limitations of this study, or no propagation due to the fault length being established prior to the transgression of ~11.5ka. If it was resolved that there had been no propagation over the Holocene, it may help to further define a timeframe with regards to fault evolution and the establishing of fault length.

It was noted that there was significant attenuation of the seismic signal below 120 ms TWTT. This prevented full analysis of fault dip and geometry of the fault population at depth. The use of a lower frequency seismic source, combined with the line spacings conducted in this study, would enable greater analysis of the fault geometry, identifying whether or not the multiple faults converge onto a single structure at depth. This method may also help identify when periods of lateral fault growth and segment linkage occurred.

However, it is acknowledged that the nature of the stratigraphy, and the internal dip of some reflectors may mask deeper structure even if a lower frequency source is used.

In order to fully address the evolution of the Aigion-Neos Erineos fault system, it is necessary to confirm or deny the existence of a fault segment crossing the Aigion delta, connecting the onshore and offshore fault zones. Sub-surface data would provide the most reliable means for identifying such a feature, even if other factors have caused any surface expressions to be eradicated. Clay and high water content may inhibit any clear resolution of a fault on the delta. However, Ground Penetrating radar (GPR) or trenching over the features observed at the coastline may help quantify how much surface offset there would be from a known displacement on a fault at depth. This would help establish whether or not we would expect to see surface morphological evidence across the delta if there was a buried segment.

Recent work conducted by Bull et al. (in press) and within this thesis, has shown the viability of conducting a variance analysis on fault displacement data in order to ascertain the time period of observation over which long-term behaviour can be identified from within short-term irregularities. The similarity in results between two different locations suggests that there may be an approximate timescale over which activity on normal fault systems will begin to reveal long-term behavioural patterns. However, further variance analysis of different datasets from extensional regimes is required before this can be confirmed.

In order to fully address the possible changes in deformation and distribution of strain throughout the Gulf of Corinth, it is necessary to compile a detailed map of all offshore faults. Not only will this show whether or not the Aigion Shelf Fault, and larger scale Aigion-Neos Erineos fault system is an anomaly in terms of its geometry, it will also help identify whether or not this is a unique location within the Gulf of Corinth, or if the pattern of composite faulting is repeated elsewhere in the offshore environment.

# Appendix A

# Multibeam Bathymetry Master Database Settings

This appendix details the settings used within the master database file of the Reson 8160 multibeam bathymetry acquisition system.

### B.1 Multibeam Database Information:

| | |
|---|---|
| Heading Offset | 2.800 |
| Roll Offset | -1.050 |
| Pitch Offset | -0.950 |
| Max No. beams per ping | 240 |

### B.2 Navigation / Equipment Information:

| | |
|---|---|
| IMU | x direction = 0m |
| | y direction = 0m |
| | z (ref to water line) = -2.348m |
| 8160 sonar head | x (ref to IMU) = -3.830m |
| | y (ref to IMU) = -8.939m |
| | z (ref to water line) = -2.340m |
| Antenna 1 | x (ref to IMU) = +3.180m |
| | y (ref to IMU) = -2.049m |
| | z (ref to IMU) = +6.598m |

| | |
|---|---|
| Distance to the stern (ref to IMU) | y = -14.209m |
| POS/MV accuracy | 0.011 degree |
| Lat/Long accuracy | 0.66m |
| Rotation convention pitch | Positive Bow up |
| Rotation convention roll | Positive heeling to starboard |

### B.3 Geodetic Information:

| | |
|---|---|
| Zone | 34N |
| Projection | UTM (North orientated) |

UTC to GPS time correction = 13.00s

# Appendix B

# Multichannel Seismic Reflection Processing

This appendix details the processing steps and relevant parameters used in processing the MCS reflection dataset. Section 2.4 details data acquisition, and Figure 2.6 shows the processing flow used.

### A.1 Bandpass Filtering

Interactive Spectral Analysis' were run for each line. From the results, parameter tests were run to identify the four corners chosen for the minimum phase Ormsby Bandpass Filters applied to both the Boomer and Sparker profiles. The maximum Nyquist frequency for the Boomer data is 4000Hz, however in order to maximise the detail revealed, and due to the very clear images produced from the un-processed data, it was decided to adopt corner frequencies of 100-200-5000-6500Hz, thus ensuring all high frequency signals were passed through the filter. The best corner frequencies for the Sparker data were 50-150-2200-3600Hz. Bandpass filters were run both pre and post migration.

### A.2 Automatic Gain Control

An Automatic Gain Control of 25ms was initially used to aid image visualisation during the processing by balancing the amplitude differences down the trace, and enhancing weaker reflectors. However True Amplitude Recovery was found to work, and so this was chosen to use during the stacking of the traces.

### A.3 Geometry Assignment

Navigational and seismic log information were combined. First arrival times were analysed using a Normal Moveout Correction to adjust the geometry spacing between each receiver and the source. The data was then binned, with the pseudo 3D Boomer survey CDP interval being 0.5m and the regional Sparker survey CDP interval at 1m.

### A.4 True Amplitude Recovery

A True Amplitude Recovery with a time power constant of 2 was applied to the data, applying gain to correct for loss of energy due to geometric spreading and absorption of the original signal.

### A.5 Predictive Deconvolution

Minimum phase predictive deconvolution was applied to remove convolution effects due to the source signal, geophones and the effects of the Earth itself. An operator length of 4ms with a predictive distance of 1ms was applied to all of the Boomer and Sparker traces within the pseudo 3D survey area. A post migration deconvolution of 1.5ms over a gate of 0.75ms was tried, but found to have negligible effect.

The regional Sparker survey was found to benefit from the application of two separate minimum phase predictive deconvolution filters. The first, with an operator length of 15ms and a gate distance of 1.5ms removed any streamer ghost. The second, with an operator length of 8ms and a gate distance of 3.5ms reduced any remaining intrinsic effects.

### A.6 Velocity Analysis

Velocity analyses were conducted every 50 CDP’s (25m) on the pseudo 3D survey lines, resulting in between 35-80 analyses per line. This was only possible by running each line twice doing the analysis every 100 CDP’s, with a 50 CDP offset between runs. (Running analysis every 50 CDP’s caused the software to crash.) However this generated spikes in the analysis at depth as reflectors became less distinct below the seabed multiple. Individual spikes were removed in PROMAX using the velocity viewer/points editor, and the lines then smoothed within velocity manipulation, to obtain an RMS stacking velocity profile that could be used in the migration.

The analyses were conducted every 500 CDP's for the regional Sparker lines, decreasing to every 100 CDP's where the lines entered the pseudo 3D survey area. This ensured continuity between the pseudo 3D survey and the regional survey lines.

### A.7 Normal Moveout Correction (NMO)

This compensates for the delay in arrival times from a horizontal reflector due to the offset between the source and the different receivers.

### A.8 CDP/Ensemble Stack

Vertical mean stack of the ensembles of traces, using a square root scaling of the samples contributed. Using the square root scaling method avoids excessive amplification of shallow reflectors, but increases the signal to noise ratio over the whole trace.

### A.9 Stolt F-K Migration

A Stoltz F-K Migration (in the time domain) was applied, using 105% stacking velocities obtained during the velocity analysis flow. The Stoltz stretching algorithm used in this migration accounts for lateral and vertical velocity variations. Individual lines were later converted into the depth domain following analysis in the 3D LandMark IESX package.

# Appendix C

# Mulibeam Bathymetry Processing

This appendix details the filters used during the processing of the multibeam bathymetry dataset. Section 2.5, Chapter 2, details the data acquisition.

### C.1 Brightness Filter

This evaluates the brightness of the seafloor soundings compared to the background brightness. If the seafloor is >1.5 times brighter than the ambient background, it has good brightness and the sounding is accepted.

### C.2 Colinearity Filter

This examines five adjacent soundings to determine if any four lie in line (<7% of the range of the middle most point of the five). Spikes above this range are removed.

### C.3 Depth Filter

This filter excludes random data points caused by interference, such as soundings from objects within the water column or the keel of the survey vessel. This filter can be modified in real-time by the operator whilst surveying, and will be recorded if producing a qpd file immediately. However if producing a qpd file by re-playing the data post cruise, as with this survey, the initial depth filters applied at the start of each line re-played are the only ones taken and flagged.

### C.4 Single Spike Filter

This examines and removes a spike amongst three soundings, where the difference between the first and second sounding has a difference of opposite value to that between the second and third sounding.

## C.5 Range Filter

This sets up the depth ranges within which surveying is taking place. Works with the depth filter, and can also be altered in real-time by the operator. The same restrictions apply to this filter as to the depth filter when creating the qpd file post-cruise.

## C.6 Excluded Filter

This filter excludes beams from the swath that may be corrupted. In this cruise these beams were the outermost 3 – 5 starboard beams, which were clipping the keel of the survey vessel. The same restrictions apply to this filter as to the depth filter when creating the qpd file post-cruise.

## C.7 Butterworth Filter

This filter identifies low and high frequency noise values. The degree of smoothing ranges from very low to very high, and can operate in either the horizontal (x,y) direction, or the vertical depth (z) direction.

# Bibliography

Aarland, R.K., and Skjerven, J., Fault and fracture characteristics of a major fault zone in the northern North Sea: analyses of 3D seismics and orientated cores in the Braga Field (Block 31/4), in *Structural Geology in Reservoir Characterisation*, edited by Coward, M.P., Daltaban, T.S., and Johnson, H., pp. 209 - 229, 1998.

Ambraseys, N.N., and Jackson, J.A., Seismicity and associated strain of central Greece between 1890 and 1988., *Geophysical Journal International*, *101*, 663 - 708, 1997.

Anders, M.H., and Schlische, R.W., Overlapping faults, intrabasin highs, and the growth o fnormal faults., *Journal of Geology*, *102*, 165 - 180, 1994.

Armijo, R., Meyer, B., Hubert, A., and Barka, A., Westward propagation of the North Anatolian fault into the northern Aegean: Timing and kinematics., *Geology*, *27* (3), 267 - 270, 1999.

Armijo, R., Meyer, B., King, G.C.P., Rigo, A., and Papanastassiou, D., Quaternary evolution of the Corinth Rift and its implications for the Late Cenezoic evolution of the Aegean., *Geophysical Journal International*, *126*, 11 - 53, 1996.

Avallone, A., Briole, P., Agatza-Balodimou, A.M., Billiris, H., Charade, O., Mitsakaki, C., Nercessian, A., Papazissi, K., Paradissis, D., and Veis, G., Analysis of eleven years of deformation measured by GPS in the Corinth Rift Laboratory area., *Comptes Rendus Geoscience*, *336*, 301 - 311, 2004.

Bagnold, R.A., *The physics of blown sand and desert dunes.*, Methuen, London, 1941.

Berg, S.S., and Skar, T., Controls of damage zone asymmetry of a normal fault zone: outcrop analyses of a segment of the Moab Fault, SE Utah., *Journal of Structural Geology*, *27* (10), 1,803 - 801,822, 2005.

Bernal, A., Hardy, S., Gawthorpe, R.L., and Finch, E., Stratigraphic expression of the lateral propagation and growth of isolated fault-related uplifts., *Basin Research*, *16*, 219-233, 2004.

Bernard, P., Briole, P., Meyer, B., Lyon-caen, H., Gomez, J.M., Tiberi, C., Berge, C., Cattin, R., Hatzfeld, D., Lachet, C., Lebrun, B., Deschamps, A., Courboulex, F., Larroque, C., Rigo, A., Massonnet, D., Papadimitriou, P., Kassaras, J., Diagourtas, D., Makropoulos, K., Veis, G., Papazisi, E., Mitsakaki, C., Karakostas, V.G., Papadimitriou, E., Papanastassiou, D., Chouliaras, M., and Stavrakakis, G., The Ms=6.2, June 15, 1995 Aigion earthquake (Greece): evidence for low angle normal faulting in the Corinth rift., *Journal of Seismology*, *1*, 131 - 150, 1997.

Billiris, H., Paradissis, D., Veis, G., England, P., Featherstone, W., Parsons, B., Cross, P.A., Rands, P., Rayson, M., Sellers, P., Ashkenazi, V., Davison, M., Jackson, J.A., and Ambraseys, N.N., Geodetic determination of tectonic deformation in central Greece from 1900 to 1988., *Nature*, *350*, 124 - 129, 1991.

Boccaletti, M., Bonini, M., Mazzuoli, R., Abebe, B., Piccardi, L., and Tortorici, L., Quaternary oblique extensional tectonics in the Ethiopian Rift (Horn of Africa). *Tectonophysics*, *287*, 97 - 116, 1998.

Bonatti, E., The rifting of continents., *Scientific American*, *256* (3), 75-81, 1987.

Briole, P., Rigo, A., Lyon-Caen, H., Ruegg, J.C., Papazissi, K., Mitsakaki, C., Balodimou, A., Veis, G., Hatzfeld, D., and Deschamps, A., Active deformation of the Corinth rift, Greece: Results from repeated Global Positioning System surveys between 1990 and 1995., *Journal of Geophysical Research*, *105* (B11), 25,605 - 625, 625, 2000.

Bull, J.M., Barnes, P.M., Lamarche, G., Sanderson, D.J., Cowie, P.A., Taylor, S.K., and Dix, J.K., High-Resolution Record of Displacement Accumulation on an Active Normal Fault: Implications for Models of Slip Accumulation during Repeated Earthquakes, *Journal of Structural Geology*, in press.

Bull, J.M., Minshull, T.A., Mitchell, N.C., Dix, J.K., and Hardardottir, J., Magmatic and tectonic history of Iceland's western rift zone at Lake Thingvallavatn., *Geological Society of America Bulletin*, *117* (11/12), 1451 - 1465, 2005.

Burgmann, R., Pollard, D.D., and Martel, S.J., Slip distributions on faults: effects of stress gradients, inelastic deformation, heterogeneous host rock stiffness, and fault interaction., *Journal of Structural Geology*, *16*, 1675 - 1690, 1994.

Caine, J.S., Evans, J.P., and Forster, C.B., Fault zone architecture and permeability structure, *Geology*, *11*, 1,205 - 201,028, 1996.

Cartwright, J., Mansfield, C., and Trudgill, B., The growth of normal faults by segment linkage., in *Modern developments in Structural Interpretation, Validation and Modelling.*, edited by Buchanan, P.G., and Nieuwland, D.A., pp. 163-177, Geological Society Special Publication, 1996.

Cartwright, J., Trudgill, B., and Mansfield, C., Fault growth by segment linkage: an explanation for scatter in maximum displacement and trace length data from the Canyonlands Grabens of SE Utah., *Journal of Structural Geology*, *17* (9), 1319-1326, 1995.

Childs, C., Nicol, A., Walsh, J.J., and Watterson, J., The growth and propagation of synsedimentary faults., *Journal of Structural Geology*, *25* (4), 633-648, 2003.

Childs, C., Watterson, J., and Walsh, J.J., Fault overlap zones within developing normal fault systems., *Journal of the Geological Society, London*, *152*, 535-549, 1995.

Childs, C., Watterson, J., and Walsh, J.J., A model for the structure and development of fault zones., *Journal of the Geological Society, London*, *153*, 337-340, 1996.

Christodoulou, D., Papatheodorou, G., Ferentinos, G., and Masson, M., Active seepage in two contrasting pockmark fields in the Patras and Corinth gulfs, Greece., *Geo-Marine Letters*, *23*, 194-199, 2003.

Chronis, G., Piper, D.J.W., and Anagnostou, C., Late Quaternary evolution of the Gulf of Patras, Greece: Tectonism, deltaic sedimentation and sea-level change., *Marine Geology*, *97*, 191-209, 1991.

Cladouhos, T.T., and Marrett, R., Are fault growth and linkage models consistent with power-law distributions of fault length?, *Journal of Structural Geology*, *18* (2/3), 281-293, 1996.

Clarke, P.J., Davies, R.R., England, P.C., Parsons, B., Billiris, H., Paradissis, D., Veis, G., Cross, P.A., Denys, P.H., Ashkenazi, V., Bingley, R., Kahle, H.G., Muller, M.V., and Briole, P., Crustal strain in central Greece from repeated GPS measurements in the interval 1989 - 1997., *Geophysical Journal International*, *135*, 195 - 214, 1998.

Clarke, P.J., Davies, R.R., England, P.C., Parsons, B.E., Billiris, H., Paradissis, D., Veis, G., Denys, P.H., Cross, P.A., Ashkenazi, V., and Bingley, R., Geodetic estimates of seismic hazard in the Gulf of Korinthos., *Geophysical Research Letters*, *24* (11), 1,303 - 301,306, 1997.

Clifton, A.E., Schlische, R.W., Withjack, M.O., and Ackermann, R.V., Influence of rift obliquity on fault-population systematics: results of experimental clay models., *Journal of Structural Geology*, *22*, 1491-1509, 2000.

Collier, R.E.L., and Dart, C.J., Neogene to Quaternary rifting: sedimentation and uplift in the Corinth Basin, Greece., *Journal of the Geological Society, London*, *148*, 1049 - 1065, 1991.

Collier, R.E.L., Leeder, M.R., Rowe, P.J., and Atkinson, T.C., Rates of Tectonic Uplift in the Corinth and Megara basins, Central Greece., *Tectonics*, *11* (6), 1159-1167, 1992.

Collier, R.E.L., Leeder, M.R., Trout, M., Ferentinos, G., Lyberis, E., and Papatheodorou, G., High sedimentary yields and cool, wet winters: Test of last glacial paleoclimates in the northern Mediterranean.. *Geology*, *28*, 999 - 991,002, 2000.

Collier, R.E.L., Pantosti, D., D'Addezio, G., De Martini, P.M., Masana, E., and Sakellariou, D., Paleoseismicity of the 1981 Corinth earthquake fault: Seismic contribution to extensional strain in cnetral Greece and implications for seismic hazard., *Journal of Geophysical Research*, *103* (B12), 30,001 - 030,019, 1998.

Contretras, J., Anders, M.H., and Scholtz, C.H., Growth of a normal fault system: observations from the Lake Malawi basin of the east African rift., *Journal of Structural Geology*, *22* (2), 159-168, 2000.

Cowie, P.A., Gupta, S., and Dawers, N.H., Implications of fault array evolution for synrift depocentre develoment: insights from a numerical growth model., *Basin Research*, *12*, 241-261, 2000.

Cowie, P.A., and Roberts, G.P., Constraining slip rates and spacings for active normal faults., *Journal of Structural Geology*, *23*, 1901-1915, 2001.

Cowie, P.A., and Scholz, C.H., Physical explanation for the displacement-length relationship of faults using a post-yield fracture mechanics model., *Journal of Structural Geology*, *14* (10), 1133-1148, 1992.

Cowie, P.A., and Shipton, Z.K., Fault tip displacement gradients and process zone dimensions., *Journal of Structural Geology*, *20* (8), 983-997, 1998.

D'Alessio, M.A., and Martel, S.J., Fault terminations and barriers to fault growth., *Journal of Structural Geology*, *26* (10), 1885 - 1896, 2004.

Dart, C.J., Collier, R.E.L., Gawthorpe, R.L., Keller, J.V.A., and Nichols, G., Sequence stratigraphy of (?) Pliocene-Quaternary synrift, Gilbert-type fan deltas, northern Peloponnesos, Greece., *Marine and Petroleum Geology*, *11* (5), 545-560, 1994.

Davies, R., England, P., Parsons, B., Billiris, H., Paradissis, D., and Veis, G., Geodetic strain of Greece in the interval 1892 - 1992., *Journal of Geophysical Research*, *102* (B11), 24,571 - 524,588, 1997.

Dawers, N.H., Anders, M.H., and Scholtz, C.H., Growth of normal faults: Displacement-length scaling., *Geology*, *21*, 1107-1110, 1993.

De Martini, P.M., Pantosti, D., Palyvos, N., Lemeille, F., McNeill, L.C., and Collier, R.E.L., Slip rates of the Aigion and Eliki Faults from uplifted marine terraces, Corinth Gulf, Greece., in *EGS XXVII General Assembly*, Geophysical Research Abstracts, Nice, France, 2002.

De Martini, P.M., Pantosti, D., Palyvos, N., Lemeille, F., McNeill, L.C., and Collier, R.E.L., Slip rates of the Aigion and Eliki Faults from uplifted terraces, Corinth Gulf, Greece., *Comptes Rendus Geoscience*, *336*, 325-334, 2004.

Dia, A.N., Cohen, A.S., O'Nions, R.K., and Jackson, J.A., Rates of uplift investigated through $^{230}$Th dating in the Gulf of Corinth (Greece). *Chemical Geology*, *138* (1171 - 184), 1997.

Dimitrov, L., and Woodside, J.M., Deep sea pockmark environments in the eastern Mediterranean., *Marine Geology*, *195*, 262-276, 2003.

Doutsos, T., and Kokkalas, S., Stress and deformation patterns in the Aegean region., *Journal of Structural Geology*, *23*, 455 - 472, 2001.

Doutsos, T., Kontopoulos, N., and Poulimenos, G., The Corinth-Patras rift as the initial stage of continental fragmentation behind an active island arc (Greece). *Basin Research*, *1*, 177 - 190, 1988.

Doutsos, T., and Piper, D.J.W., Listric faulting, sedimentation, and morphological evolution of the Quaternary eastern Corinth rift, Greece: first stages of continental rifting., *Geological Society of America Bulletin*, *102* (6), 812 - 829, 1990.

Doutsos, T., and Poulimenos, G., Geometry and kinematics of active faults and their seismotectonic significance in the western Corinth-Patras rift (Greece). *Journal of Structural Geology*, *14* (6), 689 - 699, 1992.

Ferentinos, G., Papatheodorou, G., and Collins, M.B., Sediment transport processes on an active submarine fault escarpment: Gulf of Corinth, Greece., *Marine Geology*, *83*, 43 - 61, 1988.

Flerit, F., Armijo, R., King, G.C.P., and Meyer, B., The mechanical interaction between the propagating North Anatolian Fault and the back-arc extension in the Aegean., *Earth and Planetary Science Letters*, *224* (3/4), 347 - 362, 2004.

Gautier, S., Latorre, D., Virieux, J., Deschamps, A., Skarpelos, C., Sotiriou, A., Serpetsidaki, A., and Tselentis, A., A New Passive Tomography of the Aigion Area (Gulf of Corinth, Greece) from the 2002 Dataset., *PAGEOPH*, *in press*, 2005.

Gawthorpe, R.L., Sharp, I., Underhill, J.R., and Gupta, S., Linked sequence stratigraphy and structural evolution of propagating faults., *Geology*, *25* (9), 795 - 798, 1997.

Ghisetti, F., and Vezzani, L., Plio-Pleistocene sedimentation and fault segmentation in the Gulf of Corinth (Greece) controlled by inherited structural fabric., *Comptes Rendus Geoscience*, *336*, 243-249, 2004.

Goldsworthy, M., and Jackson, J.A., Migration of activity within normal fault systems: examples from the Quaternary of mainland Greece., *Journal of Structural Geology*, *23*, 489 - 506, 2001.

Goodliffe, A., Weiss, J., Taylor, B., Sachpazi, M., Hirn, A., Stefatos, A., and Laigle, M., Variations in the distribution and control of syn-rift deformation in the Gulf of Corinth, Greece., *Geophysical Research Abstracts*, *5* (no. 04697), 2003.

Gupta, S., Cowie, P.A., Dawers, N.H., and Underhill, J.R., A mechanism to explain rift-basin subsidence and stratigraphic patterns through fault-array evolution., *Geology*, *26* (7), 595-598, 1998.

Hardy, S., and Gawthorpe, R.L., Effects of variations in fault slip rate on sequence stratigraphy in fan deltas: Insights from numerical modelling., *Geology*, *26* (10), 911-914, 1998.

Harrington, P.K., Formation of Pockmarks by Pore-Water Escape., *Geo-Marine Metters*, *5*, 193-197, 1985.

Hasiotis, T., Papatheodorou, G., Bouckovalas, G., Corbau, C., and Ferentinos, G., Earthquake-induced coastal sediment instabilities in the western Gulf of Corinth, Greece., *Marine Geology*, *186* (319-335), 2002*b*.

Hasiotis, T., Papatheodorou, G., and Ferentinos, G., A string of large and deep gas-induced depressions (pockmarks) offshore Killini peninsula, western Greece., *Geo-Marine Letters*, *22*, 142-149, 2002*a*.

Hasiotis, T., Papatheodorou, G., Kastanos, N., and Ferentinos, G., A pockmark field in the Patras Gulf (Greece) and its activation during the 14/7/93 seismic event., *Marine Geology*, *130*, 333-344, 1996.

Hatzfeld, D., On the shape of the subducting slab beneath the Peloponnese, Greece., *Geophysical Research Letters*, *21* (3), 173 - 176, 1994.

Hatzfeld, D., Karakostas, V.G., Ziazia, M., Kassaras, I., Papdimitriou, E., Makropoulos, K., Voulgaris, N., and Papaioannou, C., Microseismicity and faulting geometry in the Gulf of Corinth (Greece), *Geophysical Journal International*, *141*, 438 - 456, 2000.

Hatzfeld, D., Kementzetzidou, D., Karakostas, V.G., Ziazia, M., Nothard, S., Diagourtas, D., Deschamps, A., Karakaisis, G., Papadimitriou, P., Scordilis, M., Smith, R., Voulgaris, N., Kiratzi, S., Makropoulos, K., Bouin, M.P., and Bernard, P., The galaxidi earthquake of a8 November 1992: A Possible Asperity within the Normal Fault System of the Gulf of Corinth (Greece). *Bulletin of the Seismological Society of America*, *86* (6), 1,987 - 981,991, 1996.

Heezen, B.C., Ewing, M., and Johnson, G.L., The Gulf of Corinth floor., *Deep-Sea Research*, *13*, 381 - 411, 1966.

Hicks, S., A high resolution geophysical study of the west Gulf of Corinth's northern margin with regard to offshore faulting., University of Southampton, 2004.

Houghton, S.L., Roberts, G.P., Papanikolaou, I.D., and McArthur, J.M., New $^{234}$U$^{230}$Th coral dates from the western Gulf of Corinth: Implications for extensional tectonics., *Geophysical Research Letters*, *30* (19), doi:10.1029/2003GL018112, 2003.

Hovland, M., and Judd, A.G., *Seabed Pockmarks and Seepages. Impact on Geology, Biology and the Marine Environment.*, 293 pp., Graham and Trotman, London, 1988.

Jackson, J.A., Active normal faulting and crustal extension., in *Continental Extensional Tectonics*, edited by Coward, M.P., Dewey, J.F., and Hancock, P.L., pp. 3 - 17, Geological Society of London Special Publication, London, 1987.

Jackson, J.A., Fault death: a perspective from actively deforming regions., *Journal of Structural Geology*, *21*, 1,003 - 001,010, 1999.

Jackson, J.A., Gagnepain, J., Houseman, G., King, G.C.P., Papadimitriou, P., Soufleris, C., and Virieux, J., Sesimicity, normal faulting, and the geomorphological development of the Gulf of Corinth (Greece): the Corinth earthquakes of February and March 1981., *Earth and Planetary Science Letters*, *57*, 377 - 397, 1982.

Jensen, F.B., Kuperman, W.A., Porter, M.B., and Schmidt, H., *Computational Ocean Acoustics*, American Institute of Physics, 1994.

Keraudren, B., and Sorel, D., The Terraces of Corinth (Greece) - A detailed record of eustatic sea-level variations during the last 500,000 years., *Marine Geology*, *77*, 99 - 107, 1987.

Kershaw, S., and Gui, L., Marine notches in coastal cliffs: indicators of relative sea-level change, Perachora Peninsula, central Greece., *Marine Geology*, *179*, 213 - 228, 2001.

Kershaw, S., Guo, L., and Braga, J.C., A Holocene coral-algal reef at Mavra Litharia, Gulf of Corinth, Greece: structure, history, and applications in relative sea-level change., *Marine Geology*, *215*, 171 - 192, 2005.

King, T.A., Mechanisms of Isostatic Compensation in Areas of Lithospheric Extension: Examples from the Aegean., University of Leeds, 1998.

Knott, S.D., Beach, A., Brockbank, P.J., Brown, J.L., McCallum, J.E., and Welbon, A.I., Spatial and mechanical controls of normal fault populations., *Journal of Structural Geology*, *18* (2/3), 359-372, 1996.

Koestler, A.G., and Ehrmann, W.U., Description of brittle extensional features in chalk on the crest of a salt ridge (NW Germany). in *The Geometry of Normal Faults.*, edited by Roberts, A.M., Yielding, G., and Freeman, B., Geological Society of London Special Publication, London, 1991.

Koukouvelas, I.K., The Egion Fault, Earthquake-Related and Long-Term Deformation, Gulf of Corinth, Greece., *Journal of Geodynamics*, *26* (2-4), 501 - 513, 1998.

Koukouvelas, I.K., Asimakopoulos, M., and Doutsos, T.T., Fractal characteristics of active normal faults: an example of the eastern Gulf of Corinth, Greece., *Tectonophysics*, *308*, 263 - 274, 1999.

Koukouvelas, I.K., and Doutsos, T., Implications of structural segmentation during earthquakes: the 1995 Egion earthquake, Gulf of Corinth, Greece., *Journal of Structural Geology*, *18* (12), 1,381 - 381,388, 1996.

Koukouvelas, I.K., Stamatopoulous, L., Katsonopoulou, D., and Pavlides, S., A palaeoseismological and geoarchaeological investigation of the Eliki fault, Gulf of Corinth Greece., *Journal of Structural Geology*, *23*, 531-543, 2001.

Lamarche, G., Barnes, P.M., and Bull, J.M., Faulting and Extension Rate over the last 20,000 years in the offshore Whakatane graben, New Zealand Continental Shelf., *Tectonics*, in press.

Lascaratos, A., Salusti, E., and Papageorgaki, G., Wind-induced upwellings and currents in the gulfs of Patras, Nafpaktos and Korinthos, Western Greece., *Oceanologica Acta*, *12* (3), 159 - 164, 1989.

Le Pichon, X., and Angelier, J., The Aegean Sea, *Philosophical Transactions of the Royal Society of London A*, *300*, 357 - 372, 1981.

Le Pourhiet, L., Burov, E., and Moretti, I., Initial crustal thickness geometry controls on the extension in a back arc domain: Case of the Gulf of Corinth., *Tectonics*, *22* (4), doi:10.1029/2002TC001433, 2003.

Leeder, M.R., Collier, R.E.L., Aziz, L.H.A., Trout, M., Ferentinos, G., Papatheodorou, G., and Lyberis, E., Tectono-sedimentary processes along an active marine/lacustrine half-graben margin: Alkyonides Gulf, Gulf of Corinth, Greece., *Basin Research*, *14*, 25 - 41, 2002.

Leeder, M.R., and Gawthorpe, R.L., Sedimentary models for extensional tilt-block/half-graben basins., in *Continental Extensional Tectonics*, edited by Coward, M.P., Dewey, J.F., and Hancock, P.L., pp. 139 - 152, Geological Society of London, Special Publications, 1987.

Leeder, M.R., McNeill, L.C., Collier, R.E.L., Portman, C., Rowe, P.J., Andrews, J.E., and Gawthorpe, R.L., Corinth rift margin uplift: New evidence from Late Quaternary marine shorelines., *Geophysical Research Letters*, *30* (12), doi:10.1029/2003GL017382, 2003.

Leeder, M.R., Portman, C., Andrews, J.E., Collier, R.E.L., Finch, E., Gawthorpe, R.L., McNeill, L.C., Perez-Arlucea, M., and Rowe, P.J., Normal faulting and crustal deformation:Alkyonides Gulf and Perachora peninsula, eastern Gulf of Corinth rift basin, Greece., *Journal of the Geological Society, London*, *162*, 549 - 561, 2005.

Lekkas, E., Lozios, S., Skoutsos, E., and Kranis, H., Liquefaction, ground fissures and coastline change during the Egio earthquake (15 June 1995: Central-Western Greece). *Terra Nova*, *8*, 648-654, 1996.

Lemeille, F., Chatoupis, F., Foumelis, M., Rettenmaier, D., Unkel, I., Micarelli, L., Moretti, I., Bourdillon, C., Guernet, C., and Muller, C., Recent syn-rift deposits in the hangingwall of the Aigion fault (Gulf of Corinth, Greece). *Comptes Rendus Geoscience*, *336*, 425-434, 2004.

Lykousis, V., Sakellariou, D., and Pananikolaou, D., Sequence stratigraphy in the N. margin of the Gulf of Corinth: Implications to upper Quaternary basin evolution., *Geological Society of Greece Bulletin*, *32*, 157 - 164, 1998.

Machette, M.N., Personius, S.F., Nelson, A.R., Schwartz, D.P., and Lund, W.R., The Wasatch fault zone, Utah-segmentation and history of Holocene earthquakes., *Journal of Structural Geology*, *13* (2), 137 - 149, 1991.

Maniatis, G., Lempp, C., and Heinisch, H., 3D strain monitoring of onshore active faults at the eastern end of the Gulf of Corinth (Greece). *Journal of Geodynamics*, *36*, 95 - 102, 2003.

Manighetti, I., King, G.C.P., Gaudemer, Y., Scholtz, C.H., and Doubre, C., Slip accumulation and lateral propagation of active normal faults in Afar., *Journal of Geophysical Research*, *106* (B7), 13,667-613,696, 2001.

Mansfield, C., and Cartwright, J., Fault growth by linkage: observations and implications from analogue models., *Journal of Structural Geology*, *23*, 745-763, 2001.

Mansfield, C.S., and Cartwright, J.A., High-resolution displacement mapping from three-dimensional seismic data: evidence for dip linkage during fault growth., *Journal of Structural Geology*, *18* (249 - 263), 1996.

McClay, K., and White, M.J., Analogue modelling of orthogonal and oblique rifting., *Marine and Petroleum Geology*, *12*, 147 - 151, 1995.

McClusky, S., Balassanian, S., Barka, A., Demir, C., Ergintav, S., Georgiev, I., Gurkan, O., Hamburger, M., Husrt, K., Kahle, H., Kastens, K., Kekelidze, G., King, R., Kotzev, V., Lenk, O., Mahmoud, S., Mishin, A., Nadariya, M., Ouzounis, A., Paradissis, D., Peter, Y., Prilepin, M., Reilinger, R., Sanli, I., Seeger, H., Tealeb, A., Toksoz, M.N., and Veis, G., Global Positioning System constraints on plate kinematics ad dynamics in the eastern Mediterranean and Caucasus., *Journal of Geophysical Research*, *105* (B3), 5,695 - 695,719, 2000.

McLeod, A., Dawers, N.H., and Underhill, J.R., The propagation and linkage of normal faults: insights from the strathspey-brent-statfjord fault array, northern north sea., *Basin Research*, *12*, 263 - 284, 2000.

McMurray, L.S., and Gawthorpe, R.L., Along-strike variability of forced regressive deposits; late Quaternary, northern Peleponnesos, Greece., in *Sedimentary responses to forced regressions.*, edited by Hunt, D., and Gawthorpe, R.L., pp. 363 - 377, Geological Society of London, Special Publication, London, 2000.

McNeill, L.C., and Collier, R.E.L., Uplift and slip rates of the eastern Eliki fault segment, Gulf of Corinth, Greece: inferred from Holocene and Pleistocene terraces., *Journal of the Geological Society, London*, *161*, 81-92, 2004.

McNeill, L.C., Collier, R.E.L., Pantosti, D., De Martini, P.M., and D'Addezio, G., Recent history of the Eastern Eliki Fault: Geomorphology, paleoseismology and impact on paleoenvironments., *Geophysical Journal International*, *16* (1), 154 - 166, 2005*b*.

McNeill, L.C., Cotterill, C.J., Henstock, T.J., Bull, J.M., Stefatos, A., Collier, R.E.L., Papatheodorou, G., Ferentinos, G., and Hicks, S., Active faulting within the offshore Gulf of Corinth, Greece: Implications for models of continental rift deformation., *Geology*, *33* (4), 241-244, 2005*a*.

Meyer, V., Nicol, A., Childs, C., Walsh, J.J., and Watterson, J., Progressive localisation of strain during the evolution of a normal fault population., *Journal of Structural Geology*, *24*, 1215-1231, 2002.

Miall, A.D., *Principles of Sedimentary Basin Analysis.*, 616 pp., Springer-Veralg, New York, 1999.

Micarelli, L., Moretti, I., and Daniel, J.M., Structural properties of rift-related normal faults: the case study of the Gulf of Corinth, Greece., *Journal of Geodynamics*, *36* (1-2), 275 - 303, 2003.

Moretti, I., Lykousis, V., Sakellariou, D., Reynaud, J., Benziane, B., and Prinzhoffer, A., Sedimentation and subsidence rate in the Gulf of Corinth: what we learn from the *Marion Dufresne*'s long-piston core., *Comptes Rendus Geoscience*, *336*, 291 - 299, 2004.

Moretti, I., Sakellariou, D., Lykousis, V., and Micarelli, L., The Gulf of Corinth: an active half graben?, *Journal of Geodynamics*, *36* (1-2), 323-340, 2003.

Morewood, N.C., and Roberts, G.P., Lateral propagation of the surface trace of the South Alkyonides normal fault segment, central Greece: its impact on models of fault growth and displacement-length relationships., *Journal of Structural Geology*, *21* (6), 635-652, 1999.

Moriya, S., Childs, C., Manzocchi, T., and Walsh, J.J., Analysis of the relationships between strain, polarity and population slope for normal fault systems., *Journal of Structural Geology*, *27*, 1113-1127, 2005.

Nicol, A., Walsh, J.J., Berryman, K., and Nodder, S., Growth of a normal fault by accumulation of slip over millions of years., *Journal of Structural Geology*, *27*, 327 - 342, 2005.

Nicol, A., Walsh, J.J., Manzocchi, T., and Morewood, N.C., Displacement rates and average earthquake recurrence intervals on normal faults., *Journal of Structural Geology*, *27*, 541 - 551, 2005.

Nicol, A., Walsh, J.J., Watterson, J., and Gillespie, P.A., Fault size distributions - are they really power-law?, *Journal of Structural Geology*, *18* (2/3), 191-197, 1996.

Nicol, A., Walsh, J.J., Watterson, J., and Underhill, J.R., Displacement rates of normal faults., *Nature*, *390*, 157-159, 1997.

Nicol, A., Watterson, J., Walsh, J.J., and Childs, C., The shapes, major axis orientations and displacement patterns of fault surfaces., *Journal of Structural Geology*, *18* (2/3), 235-248, 1996.

Ori, G.G., Geologic history of the extensional basin of the Gulf of Corinth (?Miocene-Pleistocene), Greece, *Geology*, *17*, 918 - 921, 1989.

Palyvos, N., Pantosti, D., De Martini, P.M., Lemeille, F., Sorel, D., and Pavlopoulos, K., The Aigion-Neos Erineos coastal normal fault system (Western Corinth Gulf Rift, Greece): geomorphological signature, recent earthquake history and evolution., *Journal of Geophysical Research*, *110* (B09302), doi:10.1029/2004JB003165, 2005.

Pantosti, D., De Martini, P.M., Koukouvelas, I.K., Stamatopoulous, L., Palyvos, N., Pucci, S., Lemeille, F., and Pavlides, S., Palaeoseismological investigation of the Aigion Fault (Gulf of Corinth, Greece). *Comptes Rendus Geoscience*, *336*, 335 - 342, 2004.

Papatheodorou, G., and Ferentinos, G., Submarine and coastal sediment failure triggered by the 1995, $M_s$ = 6.1R Aegion earthquake, Gulf of Corinth, Greece., *Marine Geology*, *137*, 287-304, 1997.

Papatheodorou, G., Hasiotis, T., and Ferentinos, G., Gas-charged sediments in the Aegean and Ionian Seas, Greece., *Marine Geology*, *112*, 171-184, 1993.

Papazachos, B.C., Karakostas, V.G., Papazachos, C.B., and Scordilis, E.M., The geometry of the Wadati-Benioff zone and lithospheric kinematics in the Hellenic arc., *Tectonophysics*, *319*, 275 - 300, 2000.

Peacock, D.C.P., Propagation, interaction and linkage in normal fault systems., *Earth-Science Reviews.*, *58*, 121-142, 2002.

Peacock, D.C.P., and Sanderson, D.J., Displacements, segment linkage and relay ramps in normal fault zones., *Journal of Structural Geology*, *13* (6), 721-733, 1991.

Peacock, D.C.P., and Sanderson, D.J., Effects of propagation rate on displacement variations along faults., *Journal of Structural Geology*, *18*, 311-320, 1996.

Perissoratis, C., Piper, D.J.W., and Lykousis, V., Alternating marine and lacustrine sedimentation during late Quaternary in the Gulf of Corinth rift basin, central Greece., *Marine Geology*, *167*, 391-411, 2000.

Pickering, G., Peacock, D.C.P., Sanderson, D.J., and Bull, J.M., Modelling Tip Zones to Predict the Throw and Length Characteristics of Faults., *AAPG Bulletin*, *81* (1), 82-99, 1997.

Piper, D.J.W., Kontopoulos, N., Anagnostou, C., Chronis, G., and Panagos, A.G., Modern fan deltas in the Western Gulf of Corinth, Greece., *Geo-Marine Letters*, *10*, 5 - 12, 1990.

Pirazzoli, P.A., Stiros, S.C., Arnold, M., Laborel, J., Laborel-Deguen, F., and Papageorgiou, S., Episodic uplift deduced from Holocene shorelines in the Perachora Peninsula, Corinth area, Grecce., *Tectonophysics*, *229*, 201 - 209, 1994.

Pollard, D.D., and Segall, P., Theoretical displacements and stresses near fractures in rock: with applications to faults, joints, veins, dikes and solution surfaces., in *Fracture Mechanics of Rock*, edited by Atkinson, B., Academic Press, London, 1987.

Poulimenos, G., Scaling properties of normal fault populations in the western Corinth Graben, Greece: implications for fault growth in large strain settings., *Journal of Structural Geology*, *22*, 307 - 322, 2000.

Poulimenos, G., Zelilidis, A., Kontopoulos, N., and Doutsos, T., Geometry of trapezoidal fan deltas and their relationship to extensional faulting along the south-western active margins of the Corinth rift, Greece., *Basin Research*, *5*, 179-192, 1993.

Rettenmaier, D., Giurgea, V., Hotzl, H., and Fortser, A., The AIG10 drilling project (Aigion, Greece): interpretation of the litho-log in the context of regional geology and tectonics., *Comptes Rendus Geoscience*, *336*, 415-423, 2004.

Rietbrock, A., Tiberi, C., Scherbaum, F., and Lyon-Caen, H., Sesimic slip on a low angle normal fault in the Gulf of Corinth: Evidence from high-resolution cluster analysis of microearthquakes., *Geophysical Research Letters*, *23* (14), 1817 - 1820, 1996.

Rigo, A., Lyon-Caen, H., Armijo, R., Deschamps, A., Hatzfeld, D., Makropoulos, K., Papadimitriou, P., and Kassaras, I., A microseismic study in the western part of the Gulf of Corinth (Greece): implications for large-scale normal faulting mechanisms., *Geophysical Journal International*, *126*, 663 - 688, 1996.

Roberts, G.P., and Koukouvelas, I.K., Structural and seismological segmentation of the Gulf of Corinth Fault System: implications for models of fault growth., *Annali di Geofisica*, *XXXIX*, 619 - 646, 1996.

Roberts, S., and Jackson, J.A., Active normal faulting in central Greece: an overview, in *The Geometry of Normal Faults*, edited by Roberts, A.M., Yielding, G., and Freeman, B., pp. 125 - 142, Geological Society Special Publication, London, 1991.

Sachpazi, M., Clement, C., Laigle, M., Hirn, A., and Roussos, N., Rift structure, evolution, and earthquakes in the Gulf of Corinth, from reflection seismic images., *Earth and Planetary Science Letters*, *216*, 243-257, 2003.

Schlische, R.W., and Anders, M.H., Stratigraphic effects and tectonic implications of the growth of normal faults and extensional basins., in *Reconstructing the History of Basin and Range Extension using Sedimentology and Stratigraphy.*, edited by Beratan, K.K., pp. 183-203, Geological Society of America Special Publication, Boulder, Colorado, 1996.

Schmidt, J.F.J., Studienuber Erdbeben, Leipzig, 1875.

Scholz, C.H., *The mechanics of Earthquakes and Faulting*, 471 pp., Press Syndicate of the University of Cambridge, Cambridge, 2002.

Scholz, C.H., and Cowie, P.A., Determination of the total strain from faulting using slip measurements, *Nature*, *346*, 837 - 839, 1990.

Schwartz, M.L., and Tziavos, C., Geology in the Search for Ancient Helice., *Journal of Field Archaeology.*, *6*, 243-252, 1979.

Segall, P., and Pollard, D.D., The mechanics of discontinuous faults., *Journal of Geophysical Research*, *73*, 1,417 - 411,432, 1980.

Siddall, M., Rohling, E.J., Almogi-Labin, A., Hemleben, C., Meischner, D., Schmelzer, I., and Smeed, D., Sea-level fluctuations during the last glacial cycle., *Nature*, *423*, 853 - 858, 2003.

Sorel, D., A Pleistocene and still-active detachment fault and the origin of the Corinth-Patras rift, Greece., *Geology*, *28* (1), 83 - 86, 2000.

Soter, S., Macroscopic seismic anomalies and submarine pockmarks in the Corinth-Patras rift, Greece., *Tectonophysics*, *308*, 275-290, 1999.

Soter, S., Blackwelder, P., Tziavos, C., Katsonopoulou, D., Hood, T., and Alvarez-Zarikian, C., Environmental Analysis of Cores from the Helike Delta, Gulf of Corinth, Greece., *Journal of Coastal Research*, *17* (1), 95-106, 2001.

Soter, S., and Katsonopoulou, D., The Search for Ancient Helike, 1988-1995: Geological, Sonar and Bore Hole Studies., in *Ancient Helike and Aigialeia*, edited by Katsonopoulou, D., Soter, S., and Schilardi, D., pp. 68 - 114, Aigion, 1995.

Spakman, W., Wortel, M.J.R., and Vlaar, N.J., The Hellenic Subduction Zone: A Tomographic Image and its Geodynamic Implications., *Geophysical Research Letters*, *15* (1), 60 - 63, 1988.

Stefatos, A., Study of sedimentary processes and tectonic structure in the Gulf of Corinth with marine geophysical methods., Patras, 2005.

Stefatos, A., Papatheodorou, G., Ferentinos, G., Leeder, M.R., and Collier, R.E.L., Seismic reflection imaging of active offshore faults in the Gulf of Corinth: their seismiotectonic significance., *Basin Research*, *14*, 487-502, 2002.

Stewart, I.S., and Vita-Finzi, C., Coastal uplift on active normal faults: The Eliki fault, Greece., *Geophysical Research Letters*, *23* (14), 1853-1856, 1996.

Taylor, S.K., A Long-timescale High-Resolution Fault Activity History of the Whakatane Graben, Bay of Plenty, New Zealand., University of Southampton, Southampton, 2003.

Taylor, S.K., Bull, J.M., Lamarche, G., and Barnes, P.M., Normal Fault Growth and Linkage in the Whakatane Graben, New Zealand, during the last 1.3 Million Years., *Journal of Geophysical Research*, *109* (B2), doi: 10.1029/2003JB002412, 2004.

Taymaz, T., Jackson, J.A., and McKenzie, D.P., Active tectonics of the north and central Aegean sea., *Geophysical Journal International*, *106*, 433 - 490, 1991.

Tiberi, C., Diament, M., Lyon-Caen, H., and King, T., Moho topography beneath the Corinth Rift area (Greece) from inversion of gravity data., *Geophysical Journal International*, *145*, 797 - 808, 2001.

Tiberi, C., Lyon-caen, H., Hatzfeld, D., Achauer, U., Karagianni, E., Kiratzi, A., Louvari, E., Panagiotopoulos, D., Kassaras, I., Kaviris, G., Makropoulos, K., and Papdimitriou, P., Crustal and upper mantle structure beneath the Corinth rift (Greece) from a teleseismic tomography study., *Journal of Geophysical Research*, *105* (B12), 28,159 - 128,171, 2000.

Trudgill, B., and Cartwright, J., Relay-ramp forms and normal-fault linkages, Canyonlands National Park, Utah., *Geological Society of America Bulletin*, *106*, 1143-1157, 1994.

Twiss, R.J., and Moores, E.M., *Structural Geology*, 532 pp., W. H. Freeman, New York, 1992.

Walsh, J.J., Bailey, W.R., Childs, C., Nicol, A., and Bonson, C.G., Formation of segmented normal faults: a 3-D perpsective., *Journal of Structural Geology*, *25*, 1251-1262, 2003*b*.

Walsh, J.J., Childs, C., Imber, J., Manzocchi, T., Watterson, J., and Nell, P.A.R., Strain localisation and population changes during fault system growth within the Inner Moray Firth, Northern North Sea., *Journal of Structural Geology*, *25*, 307-315, 2003*a*.

Walsh, J.J., Childs, C., Meyer, V., Manzocchi, T., Imber, J., Nicol, A., Tuckwell, G., Bailey, W.R., Bonson, C.G., Watterson, J., Nell, P.A.R., and Strand, J., Geometric controls on the evolution of normal fault systems., in *The Nature and Tectonic Significance of Fault Zone Weakening.*, edited by Holdsworth, R.E., Strachan, R.A., Magloughlin, J.F., and Knipe, R.J., pp. 157-170, Geological Society Special Publication, London, 2001.

Walsh, J.J., Nicol, A., and Childs, C., A new model for the growth of faults., in *EAGE 64th Conference and Exhibition*, Florence, Italy, 2002*a*.

Walsh, J.J., Nicol, A., and Childs, C., An alternative model for the growth of faults., *Journal of Structural Geology*, *24*, 1669-1675, 2002*b*.

Walsh, J.J., and Watterson, J., Distributions of cumulative displacement and seismic slip on a single normal fault surface., *Journal of Structural Geology*, *9*, 1,039 - 031,046, 1987.

Walsh, J.J., and Watterson, J., Analysis of the relationship between displacements and dimensions of faults., *Journal of Structural Geology*, *10* (3), 239-247, 1988.

Withjack, M.O., and Jamison, W.R., Deformation produced by oblique rifting., *Tectonophysics*, *126*, 99 - 124, 1986.

Yielding, G., Needham, T., and Jones, H., Sampling of fault populations using sub-surface data: a review., *Journal of Structural Geology*, *18* (2/3), 135-146, 1996.

Yin, P., Berne, S., Vagner, P., Loubrieu, B., and Lie, Z., Mud volcanoes at the shelf margin of the East China Sea., *Marine Geology*, *194*, 135-149, 2003.

Young-Seog, K., Peacock, D.C.P., and Sanderson, D.J., Fault Damage Zones., *Journal of Structural Geology*, *26*, 503 - 517, 2004.

Young-Seog, K., and Sanderson, D.J., The relationship between displacement and length of faults: a review., *Earth-Science Reviews.*, *68*, 317-334, 2005.

Zitter, T.A.C., Huguen, C., and Woodside, J.M., Geology of mud volcanoes in the eastern Mediterranean from combined sidescan sonar and submersible surveys., *Deep-Sea Research*, *52*, 457-475, 2005.

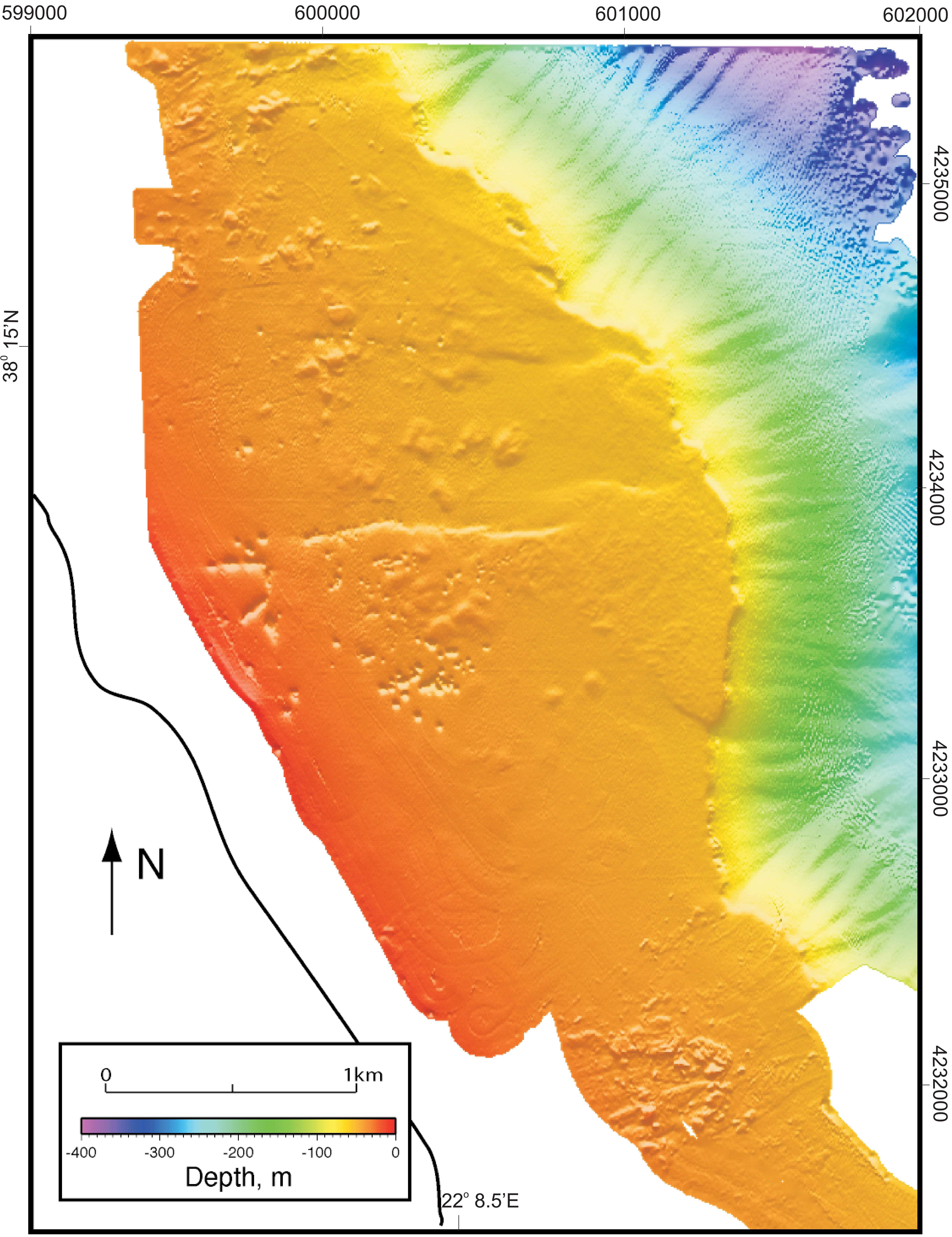

Plate 1A: Multibeam bathymetry of the Aigion Shelf, collected using the Reson Seabat 8160 swath bathymetry system. Gridded at 1.5 x 1.5m cell size. Illuminated from NNW.

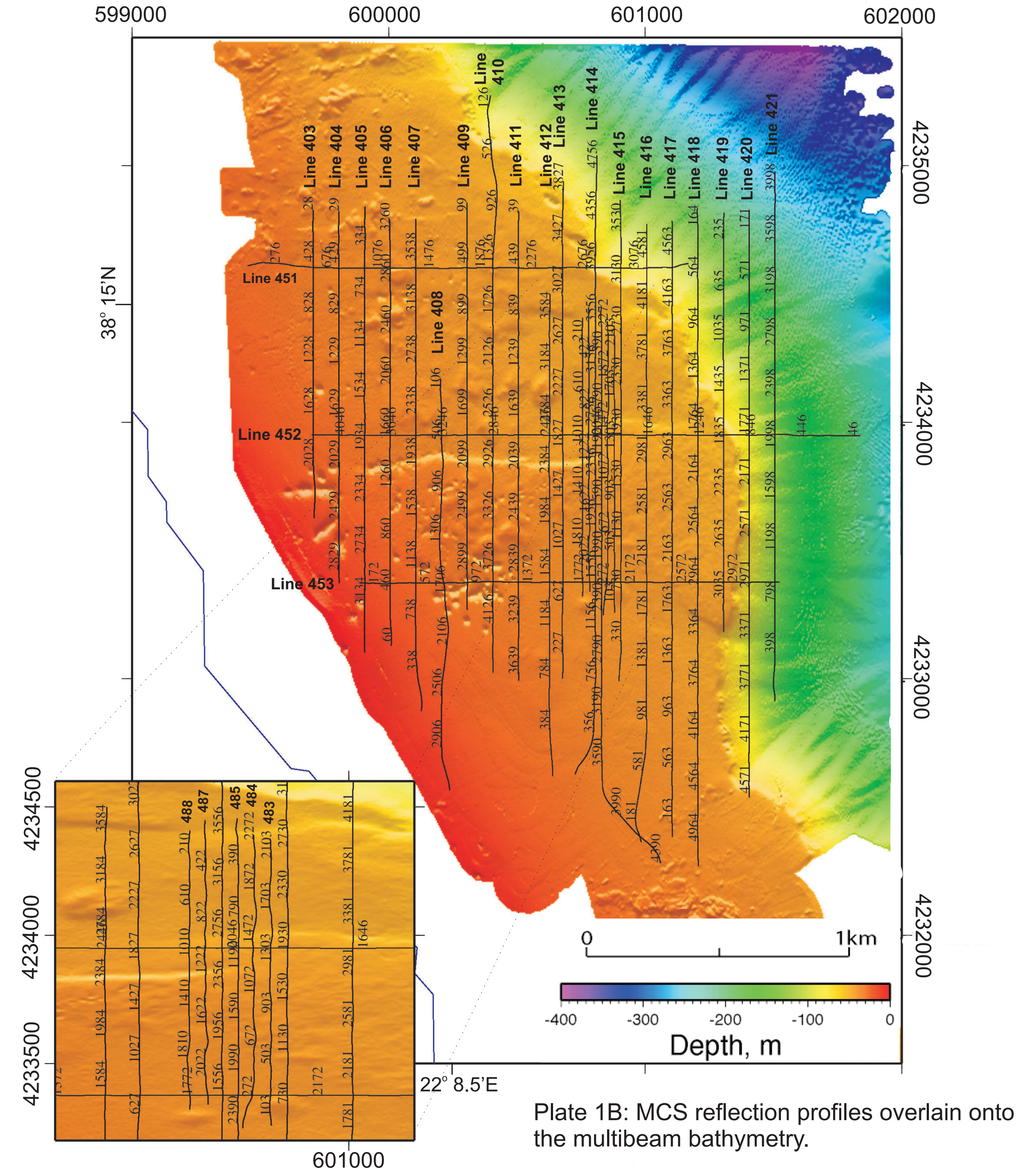

Plate 1B: MCS reflection profiles overlain onto the multibeam bathymetry.

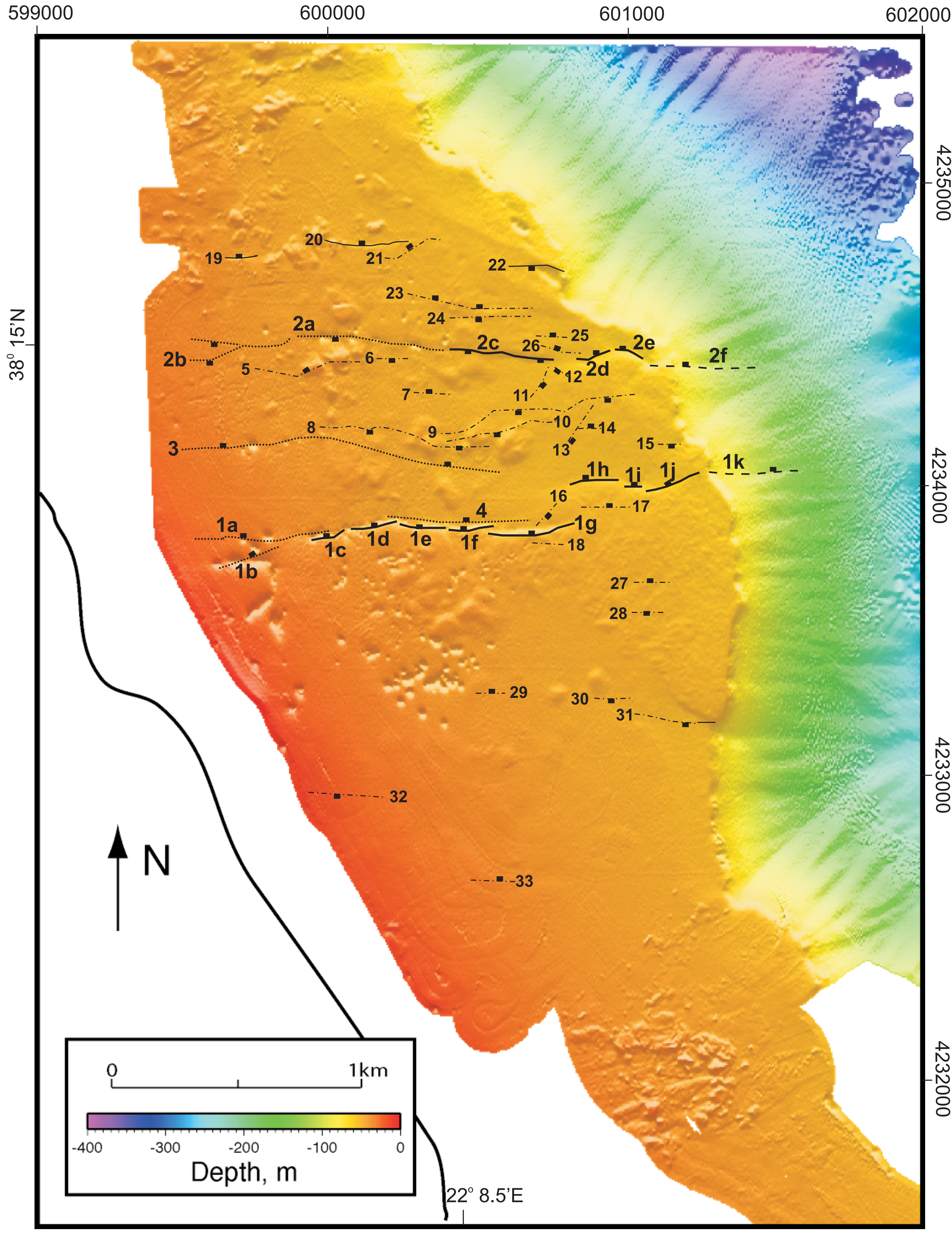

Figure 1C: Interpretation of both surface and sub-surface faults overlain onto the multibeam bathymetry.

Plate 2: MCS Reflection Boomer Profiles. Multibeam bathymetry inset **A** shows the locations of each profile. Inset **B** shows the fault interpretation of both surface and sub-surface faults. All MCS profiles are lined up using tieline 452, indicated by the dashed red line. Red arrows and numbers indicate the location of the major faults / segments identified. Fault numbers refer to the fault map shown. Lateral distances along strike between each of the MCS reflection profiles are indicated. Compass relates to the orientation of the MCS reflection profiles.
V.E. ~4.5

Plate 3: MCS Reflection Boomer Profiles. Multibeam Bathymetry inset **A** shows the locations of each profile. Inset **B** shows the interpretation of surface and sub-surface faults. All MCS profiles are lined up using tieline 452, indicated by the dashed red line. Red arrows and numbers indicate the location of the major faults / segments identified. Fault numbers refer to the fault map shown. Lateral distances along strike between each of the MCS reflection profiles are shown. Compass relates to the orientation of the MCS reflection profiles. An example of a tie-line is shown as the last MCS reflection profile. Line 451 was chosen as it best illustrates the dipping clinoforms in Unit 3.
V.E. ~4.5